Dissertations, Master's Theses and Master's Reports

2017

DEVELOPMENT OF A MULTI-ZONE CATALYZED PARTICULATE FILTER MODEL AND KALMAN FILTER ESTIMATOR FOR SIMULATION AND CONTROL OF PARTICULATE MATTER DISTRIBUTION OF A CPF FOR ENGINE ECU APPLICATIONS

Boopathi Singalandapuram Mahadevan

DEVELOPMENT OF A MULTI-ZONE CATALYZED PARTICULATE FILTER MODEL
AND KALMAN FILTER ESTIMATOR FOR SIMULATION AND CONTROL OF
PARTICULATE MATTER DISTRIBUTION OF A CPF FOR ENGINE ECU
APPLICATIONS

By

Boopathi Singalandapuram Mahadevan

A DISSERTATION

Submitted in partial fulfillment of the requirements for the degree of

DOCTOR OF PHILOSOPHY

In Mechanical Engineering – Engineering Mechanics

MICHIGAN TECHNOLOGICAL UNIVERSITY

2017

This dissertation has been approved in partial fulfillment of the requirements for the Degree of DOCTOR OF PHILOSOPHY in Mechanical Engineering – Engineering Mechanics.

Department of Mechanical Engineering – Engineering Mechanics

Dissertation Co-Advisor: *Dr. John H. Johnson*

Dissertation Co-Advisor: *Dr. Mahdi Shahbakhti*

Committee Member: *Dr. Jeffrey D. Naber*

Committee Member: *Dr. Sunil S. Mehendale*

Department Chair: *Dr. William W. Predebon*

Contents

List of Figures

List of Tables

Preface

Part of the work presented in this PhD dissertation has been published in references [1,2,3] by Journal of Emissions Control Science and Technology.

The first paper [1] covers the development of the multi-zone particulate filter model developed in this work and presented in parts of chapters 2, 3, 4 and 5 of this dissertation. This paper was titled as "Development of a Catalyzed Diesel Particulate Multi-zone Model for Simulation of Axial and Radial Substrate Temperature and Particulate Matter Distribution" and was published on the Journal of Emissions Control Science and Technology in May, 2015. The authors of this publication are Boopathi S. Mahadevan, Dr. John H. Johnson and Dr. Mahdi Shahbakhti. Boopathi S. Mahadevan was responsible for the development of the model. Dr. John H. Johnson provided the technical guidance regarding the experimental data and catalyzed particulate filter modeling aspects and Dr. Mahdi Shahbakhti provided the technical guidance on the catalyzed particulate filter modeling and analysis of the simulation results.

The Second paper [2] covers the detailed MPF model validation and simulation analysis with the experimental data and presented in parts of chapters 2, 3, 4 and 5 of this dissertation. This paper was titled as "Experimental and Simulation Analysis of Temperature and Particulate Matter Distribution for a Catalyzed Diesel Particulate Filter" and was published on July 2015 in the Journal of Emissions Control Science and Technology. The authors of this publication are Boopathi S. Mahadevan, Dr. John H. Johnson and Dr. Mahdi Shahbakhti. Boopathi S. Mahadevan was responsible for the development of the model. Dr. John H. Johnson provided the technical guidance regarding the experimental data and catalyzed particulate filter modeling aspects and Dr. Mahdi Shahbakhti provided the technical guidance on the catalyzed particulate filter modeling and analysis of the simulation results.

The third paper [3] covers the development of pressure drop model using the newly developed cake permeability model in this research work and presented in parts of chapters 4 and 5. This paper is titled as "Predicting Pressure Drop, Temperature and Particulate Matter Distribution of a Catalyzed Diesel Particulate Filter using a Multi-zone Model including Cake Permeability" and has been approved for publication in the Journal

of Emissions Control Science and Technology. Boopathi S. Mahadevan was responsible for the development of the model. Dr. John H. Johnson provided the technical guidance regarding the experimental data and catalyzed particulate filter modeling aspects and Dr. Mahdi Shahbakhti provided the technical guidance on the catalyzed particulate filter modeling and analysis of the simulation results.

The parts of chapter 4 include the joint development efforts by Boopathi S. Mahadevan and Venkata R. Chundru. Boopathi S. Mahadevan was responsible for developing models in section 4.1, 4.2, 4.3, 4.4, 4.5 and 4.6. Venkata R. Chundru was responsible for developing model explained in section 4.6 and also helped in improving the accuracy of the models in sections 4.2 and 4.3. Dr. Gordon G. Parker developed the architecture for SCR-F/CPF high fidelity model and provided the technical guidance in developing the Matlab® based code used in the SCR-F/CPF high fidelity model.

Acknowledgements

This PhD thesis was made possible by the support of several important people and organizations. I would like to take this opportunity to sincerely thank all of them for their great support and guidance during my PhD research.

I would like to thank my PhD advisors Dr. John H. Johnson and Dr. Mahdi Shahbakhti whose dedication, expertise and attention to the detail have helped me to become a better researcher. I would like to thank Dr. Jeffrey Naber and Dr. Sunil Mahendale for being on my graduate defense committee and providing valuable advice during various stages of my research work. I would like to thank Dr. Gordon Parker for his valuable advice during various stages of my research work. I would like to thank Marlene Lappeus for the great support during the course of my degree work. I would also like to thank the opportunity to be involved in various meetings of Diesel Engine Aftertreatment Consortium at Michigan Tech.

I would like to thank John Hoehne and Joe Reynolds of Cummins Engine Company for their valuable support during my degree work.

I would also like to extend my gratitude to fellow researchers and graduate students for their help and support at various stages of my PhD research work. The following are people that I would like to acknowledge by name: Venkata Chundru, Dr. Kiran Premchand, Dr. Harsha Surenahalli, Ryan Foley, Ken Shiel and James Pidgeon.

I would also like to thank my family and dear friends for all the love and support that they have shown over the years. I would like to dedicate this thesis to my mother Sellammal Mahadevan and my wife Renuga Mani.

List of Symbols

a   Width of the clean outlet channel [m]

a*   Effective width of the clean inlet channel loaded with PM [m]

A   Heat transfer area normal to the gas flow [m²]

A_{amb} Surface area of outer surface [m²]

$\bar{A}$ Average cross-sectional area [m²]

A_f Cross-sectional area perpendicular to direction of heat transfer [m²]

A_r Area normal to direction of heat transfer in the radial direction [m²]

A_{NO_2} Pre-exponential for NO_2 assisted PM oxidation [m K⁻¹ s⁻¹]

$A_{NO2\ cake}$ Pre-exponential for NO_2-assisted PM oxidation used in filtration and pressure drop models [m K⁻¹ s⁻¹]

$A_{NO2\ cake\ temp\ solver}$ Pre-exponential for NO_2-assisted PM oxidation used in temperature model [m K⁻¹ s⁻¹]

$A_{NO2\ wall}$ Pre-exponential for NO_2-assisted PM oxidation used in filtration and pressure drop models [m K⁻¹ s⁻¹]

A_{O_2} Pre-exponential for thermal (O_2) PM oxidation [m K⁻¹ s⁻¹]

$A_{O2\ cake\ temp\ solver}$ Pre-exponential for thermal (O_2) PM oxidation used in the temperature model [m K⁻¹ s⁻¹]

As   Combined surface area of both Inlet and outlet channels [m²]

$As_{i\ i,j}$ Surface area of inlet channels at each zone [m²]

$As_{o\ i,j}$ Surface area of outlet channels at each zone [m²]

b   Wall unit cell diameter [-]

C Constant notation used for temperature factor [-]

c_f Specific heat of filter material [J kg⁻¹ K⁻¹]

C_{NO_2} CPF inlet NO_2 concentration [mg m⁻³]

C_{O_2} CPF inlet O_2 concentration [mg m⁻³]

c_p Constant pressure specific heat [J kg⁻¹ K⁻¹]

C_{PM} CPF inlet PM concentration [mg m⁻³]

c_s Specific heat of PM cake [J kg⁻¹ K⁻¹]

C3   Reference pressure for wall permeability correction factor [kPa]

C4 Wall permeability correction factor [-]

C5 Cake permeability correction factor [-]

C6 Reference pressure for lambda correction [kPa]

C7 Reference temperature for lambda correction [^{o}C]

$C8_{NO2}$ Slope of delta mass offset for NO_2- assisted PM oxidation [s-g]

$C8_{th}$ Slope of delta mass offset for thermal PM (O_2) oxidation [s-g]

$C9_{NO2}$ Constant of the delta mass offset for NO_2- assisted PM oxidation [-]

$C9_{th}$ Constant of the delta mass offset for thermal (O_2) PM oxidation[-]

C10 Slope for post loading cake permeability [-]

C11 Constant for post loading cake permeability [-]

d   Side length of square channels [m]

D   Overall diameter of the CPF [m]

d Damage variable [-]

$d_{c,s_{i,j}}$ Instantaneous wall collector diameter at each zone [m]

$d_{c0,s}$ Initial wall collector diameter [m]

$d_{pore,wall}$ Diameter of pore in the substrate wall [m]

dP Differential pressure [kPa]

ds Length [m]

Ed_{dyn} Final modulus of elasticity of damaged porous media [N m^{-2}]

E_{NO_2} Activation energy for NO_2 assisted PM oxidation [J gmol^{-1}]

E_{O_2} Activation energy for thermal (O_2) PM oxidation [J gmol^{-1}]

$E0_{dyn}$ Initial modulus of elasticity of porous media [N m^{-2}]

F Friction factor in the inlet and outlet channel of the particulate filter [-]

F3-1 Radiation view factor between inlet of the channel to filter wall [-]

F3-2 Radiation view factor between outlet of the channel to filter wall [-]

h_{amb} Ambient convective heat transfer coefficient [W m^{-2} K^{-1}]

h_g Convective heat transfer coefficient [W m^{-2} K^{-1}]

ΔH_{reac} Heat of reaction for carbon oxidation via O_2 [J kg^{-1}]

J1 Radiosity of channel inlet surface [W m^{-2}]

J2 Radiosity of filter wall surface [W m^{-2}]

J3 Radiosity of channel outlet surface [W m^{-2}]

k Permeability of the solid medium [m^2]

$k_{cake_{i,j}}$ Permeability of PM cake layer at each zone [m²]

$k_{cake\ ref}$ Reference cake permeability used for the permeability ration calculation [m²]

k_d Permeability of the damaged porous media [m²]

$k_{est.cake}$ Estimated average cake permeability of the CPF [m²]

k_g Thermal conductivity of channel gas [W m⁻¹ K⁻¹]

K_k Optimal Kalman gain matrix

k_{NO_2} Rate constant for NO_2 assisted PM oxidation [m s⁻¹]

$k_{NO_2_{i,j}}$ Rate constant for NO_2 assisted PM oxidation at each zone [m s⁻¹]

k_{O_2} Rate constant for O_2 assisted PM oxidation [m s⁻¹]

$k_{O_2_{i,j}}$ Rate constant for O_2 assisted PM oxidation at each zone [m s⁻¹]

$k_{p_{i,j}}$ Permeability of PM cake layer accounting for the change in gas mean free path length [m²]

$k_{s_{i,j}}$ Permeability of substrate wall due to change in wall collector diameter at each zone [m²]

$k_{wall_{i,j}}$ Wall permeability at each zone [m²]

k_0 Permeability of the undamaged porous media [m²]

L Axial length [m]

L_t Total length of CPF [m]

$\dot{m}$ Instantaneous exhaust mass flow rate [kg s⁻¹]

$\dot{m}$ Instantaneous exhaust mass flow rate [kg s⁻¹]

$m_{cake.initial}$ Initial mass of the undamaged PM cake [g]

$m_{cake.corr}$ Mass of the PM cake after applying delta mass offset value at current time step [g]

$mc_{i,j}$ Mass of cake PM in each zone [kg]

$\dot{m}_{i,j}$ Mass flow rate at each zone [kg s⁻¹]

$ms_{i,j}$ Mass of PM in each zone [kg]

ms_t Mass of total PM to the CPF [kg]

$\dot{m}_{total}$ Total mass flow rate into CPF [kg s⁻¹]

$[mw_{i,j}]_n$ Mass of PM in each zone for slab n [kg]

n Wall slab index [-]

n_{max} Maximum number of wall slabs [-]

Nc_i Number of cells in each radial zone [-]

Nc_t Total number of cells [-]

$N_{p_{i,j}}$ Number of pores at each zone [-]

Nu   Nusselt number [-]

Pe$_w$ Peclet number of wall [-]

P_{in} CPF inlet gas pressure [kPa]

P_k^- Error covariance matrix of previous time step

$P_1|_{i,j}$ Absolute pressure at the inlet channel of each zone [kPa]

$P_2|_{i,j}$ Absolute pressure at the outlet channel of each zone [kPa]

$\dot{Q}_{cond,axial}$ Axial conduction [W]

$\dot{Q}_{conv}$ Convection between channels gases and filter wall [W]

$\dot{Q}_{cond,radial}$ Radial conduction [W]

$\dot{Q}_{gas\,i,j}$ Net convection heat transfer through the inlet and outlet channel gas [W]

$Q_{inlet-wall\,i,j}$ Heat energy flowing into the wall at each zone [W]

$\dot{Q}_{intlet-conv\,i,j}$ Convection heat transfer between inlet channel gas and the filter wall [W]

$\dot{Q}_{outlet-conv\,i,j}$ Convection heat transfer between outlet channel gas and the filter wall

$\dot{Q}_{rad}$ Radiation between channel surfaces [W]

$\dot{Q}_{reac,HC}$ Energy released during oxidation of HC in the inlet gas [W]

$\dot{Q}_{reac,PM}$ Energy released during oxidation of PM [W]

$\dot{Q}_{wall-flow\,i,j}$ Net heat transfer through the wall at each zone [W]

$Q_{wall-outlet\,i,j}$ Heat energy flowing out of the wall at each zone [W]

Q_1 Exhaust gas flow undamaged porous media [kg s^{-1}]

Q_2 Exhaust gas flow cracked impermeable media [kg s^{-1}]

r   Radial distance of zone from centerline [m]

r Characteristic particle size of the PM cake [m]

Δr   Effective zone radius [m]

R_k Covariance matrix for the state estimator

RR_{ov} Overall reaction rate [s^{-1}]

R_u Universal gas constant [J mol^{-1} K^{-1}]

$\dot{S}_{c_{(th)}}$ Thermal (O_2) assisted PM cake oxidation rate [kg C(s) m^{-3} s^{-1}]

$\dot{S}_{c_{(NO2)}}$ NO_2 assisted PM cake oxidation rate [kg C(s) m^{-3} s^{-1}]

$smax$ Number of ways of calculating the inlet pressure at each radial section [-]

S_p Specific surface area of PM ($5.5*10^7$) [m^{-1}]

t   Time [s]

T   Average gas temperature of channels [K]

T_{amb} Ambient temperature [K]

T_{exit} Filter exit gas temperature [K]

Tf Temperature of combined filter and PM cake [K]

$Tf_{i,j}$ Temperature of combined filter and PM cake at each zone [K]

T_{in} CPF inlet temperature [K]

$T_{in,4}$ CPF inlet temperature to state estimator at location 4 [K]

$T_{inlet\ i,j}$ Temperature of the gas at the inlet channel at each zone [K]

T_m Mean exhaust gas temperature [K]

$T_{n,k}$ Temperature estimate from CPF state estimator at location n for current time step [K]

$T_{out,20}$ CPF outlet temperature measured by a sensor at location 20 [K]

$T_{outlet\ i,j}$ Temperature of the gas at the outlet channel at each zone [K]

T_r Temperature at a given radial location [K]

T_s Wall inner surface temperature [K]

ts   PM cake thickness [m]

$\overline{ts}$ Average PM cake thickness across entire CPF [m]

$\overline{ts_i}$ Average PM cake thickness in each radial zone [m]

u_k State estimator inputs matrix

u_I Average inlet channel velocity [m s^{-1}]

u_{II} Average outlet channel velocity [m s^{-1}]

u_s Average velocity through PM layer [m s^{-1}]

u_{s_i} Average velocity through PM layer in each radial zone [m s^{-1}]

u_w Average velocity through wall layer [m s^{-1}]

u_{w_i} Average velocity through wall layer in each radial zone [m s^{-1}]

$u_{wall_{i,j}}$ Wall layer velocity in each zone [m s^{-1}]

$u_{inlet\ i,j}$ Inlet channel velocity at each zone [m s^{-1}]

$u_{outlet\ i,j}$ Outlet channel velocity at each zone [m s^{-1}]

v Velocity of fluid [m s^{-1}]

$v_{cake\ avg}$ Average velocity of gas in the PM cake layer of the CPF [m s^{-1}]

v_k State estimator observation noise matrix

$v_{s\,i,j}$ Velocity of gas through PM cake layer at each zone [m s^{-1}]

$v_{w\,i,j}$ Velocity of gas through substrate wall at each zone [m s^{-1}]

V Total volume of a zone [m^3]

Ve   Empty volume in each zone [m^3]

$V_{es\,i,j}$ Empty volume in each zone while accounting for average PM cake layer

            thickness [m^3]

$V_{eo\,i,j}$ Empty volume of the substrate wall [m^3]

V_f Volume of filter in each zone [m^3]

VF_i Volume fraction at each axial section of the CPF[-]

$V_{f_{i,j}}$ Volume of filter in each zone [m^3]

$V_{i,j}$ Volume at each zone [m^3]

V_{inlet} Volume of inlet channel [m^3]

$V_{s\,i,j}$ PM cake volume in each zone [m^3]

V_t Total volume of CPF [m^3]

W   Exhaust gas molecular weight [kg kmol^{-1}]

W_C Molecular weight of carbon [kg kmol^{-1}]

w_k State estimator process noise matrix

W_{NO_2} Molecular weight of nitrogen dioxide [kg kmol^{-1}]

W_{O_2} Molecular weight of oxygen [kg kmol^{-1}]

$w_{p_{i,j}}$ PM cake layer thickness at each zone [m]

w_p Average PM cake layer thickness of the CPF [m]

w_s Substrate wall thickness [m]

x   Diameter Ratio of CPF or DOC [-]

x_k States in the CPF state estimator

x_k^+ State vector, current time step

x_k^- State vector, previous time step

Y   Mass fractions [-]

$Y_{i,j_{NO_2}}$ Mass fraction of inlet NO_2 at each zone [-]

$Y_{i,j_{O_2}}$ Mass fraction of inlet O_2 at each zone [-]

y_k State estimator output matrix for temperature estimator

z_k State estimator output matrix for pressure drop estimator

Subscripts and Superscripts

i Radial Direction

j Axial Direction

n Wall slab index

s Stream line index

Greek variables

α_{NO_2} NO₂ oxidation partial factor [-]

α_{k,NO_2} Multiplicative constant for cake permeability model of NO₂ assisted PM oxidation [-]

α_{O_2} O₂ oxidation partial factor [-]

α_{k,O_2} Multiplicative constant for cake permeability model of thermal (O₂) PM oxidation [-]

β_{k,NO_2} Power constant for cake permeability model of NO2 assisted PM oxidation [-]

β_{k,O_2} Power constant for cake permeability model of thermal (O2) PM oxidation [-]

ΔP_{CPF} Total pressure drop across CPF [kPa]

$\Delta P_{cake_{i,j}}$ PM cake pressure drop at each zone [kPa]

$\Delta P_{channel\ MPF\ model}$ Total pressure drop of the inlet and outlet channels of the CPF [kPa]

ΔP_{exp} Total pressure drop across CPF measured during experiment [kPa]

$\Delta P_{est.cake}$ Estimated total PM cake pressure drop across CPF [kPa]

ΔL   Effective zone length [m]

Δr   Effective zone radius [m]

$\Delta P_{wall_{i,j}}$ Wall pressure drop at each zone [kPa]

Δt Solver time step [s]

Δx Discretization length in axial direction [m]

$\varepsilon_{s_{i,j}}$ Porosity of the substrate wall [-]

$\varepsilon_{0,s}$ Clean wall porosity [-]

$\rho_{i,j}$ Exhaust gas density at each zone [kg m^{-3}]

ρ_f Filter substrate density [kg m^{-3}]

ρ_s PM cake density [kg m^{-3}]

σ Stefan-Boltzmann constant [W m^{-2} K^{-4}]

μ Dynamic viscosity of exhaust gas [Ns m^{-2}]

$\mu_{avg\ gas}$ Average dynamic viscosity of exhaust gas in the CPF [Ns m^{-2}]

$\mu_{i,j}$ Dynamic viscosity of exhaust gas at each zone [Ns m^{-2}]

η_{cake} PM cake layer filtration efficiency [-]

$\eta_{cake\ loaded_{i,j}}$ Loaded PM cake layer filtration efficiency [-]

$\eta_{wall,m}$ Wall filtration efficiency at each slab [-]

$\eta_{wall_{i,j}\ slab\ n}$ Wall filtration efficiency at each slab [-]

$\eta_{D_{i,j}}$ Collection efficiency of a single unit collector due to Brownian diffusion

           mechanism [-]

$\eta_{R_{i,j}}$ Particle Collection efficiency of a single unit collector due to interception [-]

λ Effective thermal conductivity of PM cake and filter [W m^{-1} K^{-1}]

λf Thermal conductivity of filter [W m^{-1} K^{-1}]

λs Thermal conductivity of PM cake [W m^{-1} K^{-1}]

η_{total} Total filtration efficiency [-]

$\lambda_{i,j}$ Mean free path length of the gas [m]

λ_{ref} Mean free path length of the gas at reference condition [m]

Φ Partition coefficient [-]

Ψ Percolation factor [-]

Abbreviations

AR	Active regeneration
B10	Diesel blend (ULSD) with 10% Biodiesel
B20	Diesel blend (ULSD) with 20% Biodiesel
CFD	Computational fluid dynamics
CPF	Catalyzed particulate filter
CO	Carbon monoxide
CO_2	Carbon dioxide
DOC	Diesel oxidation catalyst
DPF	Diesel particulate filter
ECU	Electronic control unit
EKF	Extended Kalman filter
EPA	Environmental Protection Agency
FESEM	Field emission scanning electron microscopy
GB	Gigabyte
HC	Hydrocarbons
LDA	Laser Doppler Anemometer
LKF	Linear Kalman filter
MPF	Multi-zone particulate filter
MTU	Michigan Technological University
NO_2	Nitrogen dioxide
NO	Nitrogen monoxide
O_2	Oxygen
OBD	On-board diagnostics
PO	Passive oxidation
PM	Particulate matter
RAM	Random access memory
RMS	Root mean square
RU	Ramp up
SCR	Selective catalytic reduction
SCR-F	Selective catalytic reduction within filter

SEM   Scanning electron microscopy

ULSD   Ultra-low-sulfur fuel

ΔP Pressure drop

1-D   One-dimensional

3-D   Three-dimensional

Abstract

A multi-zone particulate filter (MPF) model along with the extended Kalman filter (EKF) based catalyzed diesel particulate filter (CPF) estimator was developed. The model has the potential to run in real-time within the engine control unit (ECU) to provide feedback on temperature and PM loading distribution within each axial and radial zone of the filter substrate. A high-fidelity SCR-F/CPF (selective catalytic reaction in a PM filter – the model was applied to CPF) model was developed. A new cake permeability model was also developed based on fundamental research findings in the literature to account for the potential damage in the PM cake layer during PM oxidation as well as the damage recovery of the PM cake layer during post loading of the CPF. This high-fidelity SCR-F/CPF model was calibrated with eighteen runs of data from a 2007 Cummins ISL engine that consisted of passive and active regeneration sets of data for ULSD, B10 and B20 fuels. The model had a maximum root mean square (RMS) error of $5^{\circ}C$ for predicting temperature distribution along with the RMS error of 2 g for PM loading and 0.2 kPa for the pressure drop.

A reduced order MPF model was developed to reduce the computational complexity. The reduced order model using a 5x5 zone was selected to develop an EKF based CPF state estimator. The real-time estimator calculates the unknown states of the CPF such as temperature and PM distribution and pressure drop of the CPF using the ECU sensor inputs and the reduced order model in order to determine when to do active regeneration. A DOC estimator was also integrated with the CPF estimator in order to provide estimates of the DOC outlet concentrations and temperature for the CPF estimator. The EKF based DOC-CPF estimator was validated on one of the active regeneration experiments and results show that the estimator provides improved accuracy compared to the reduced order model by taking the feedback of the CPF outlet temperature measurement. Similarly, the pressure drop and its components estimation accuracy improved with the CPF estimator compared to the reduced order model using the delta-P sensor feedback.

1 Introduction

Fuel combustion in an internal combustion engine results in several key air pollutants that are known to affect human health. These pollutants are regulated by various environmental agencies in the world. In the United States, the Environmental Protection Agency (EPA) has regulations to control the exhaust emissions from mobile and stationary sources. The major pollutants that are controlled by EPA are oxides of nitrogen (NOx), carbon monoxide (CO), total hydrocarbons (THC) and particulate matter (PM). For compression ignited diesel engines, the nitrogen oxides and PM emissions are the major pollutants. This is mainly because of the lean operating condition of the diesel engines and direct injection of fuel (no premixing with the intake air like conventional spark ignited engines) into the combustion chamber. The brake specific NOx emission (BSNOx) and brake specific PM (BSPM) emission standards set forth by EPA for on-highway heavy duty diesel engines over time is shown in Figure 1.1[4].
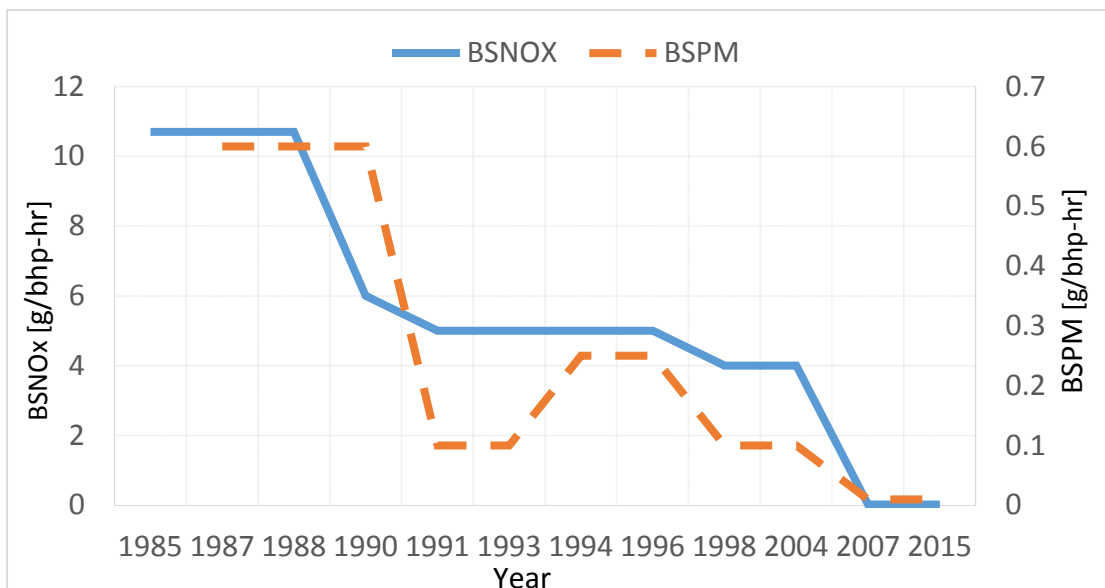
Figure 1. 1 EPA emission standards for BSNOX and BSPM for HD diesel on-highway engines [4]

Several engine technologies and aftertreatment systems have been developed to meet these emission standards. To meet earlier emission standards (before 2004), several in-cylinder methods were used such as turbocharging, reducing the charge temperatures, injection timing modulation, high pressure fuel injection system, internal and external exhaust gas recirculation. The near zero PM emissions starting from the year 2007 is

commonly achieved through aftertreatment systems. The DOC-DPF-SCR systems are the most commonly used aftertreatment configuration to meet the 2010 EPA emissions standards. In the selective catalytic reduction (SCR) systems, the selective catalytic reduction of NOx is achieved through injection of urea into the exhaust gas. The diesel oxidation catalyst (DOC) is a flow through device and it is used to oxidize HC, NO and CO emissions. By oxidizing NO into NO_2, the oxidation of PM in the CPF (NO_2 assisted oxidation) results in passive oxidation of the PM retained in the CPF. The DOC also acts to oxidize fuel dosed in upstream of the catalyst, in order to increase the temperature of the exhaust gas into the CPF for active regeneration of the particulate filter. CPFs are wall flow devices (both ends of the filter are plugged) and they capture PM emissions on the substrate walls initially and then through cake filtration. This causes an increase in engine exhaust back pressure over a period time as PM accumulates in the filter, which results in increased fuel consumption. The excess loading of PM in the filter also causes the temperature exotherms which could damage the substrate material. Hence, the regeneration of the CPF is critical for the optimum performance and durability of the filter. Rose et al. conducted experiments that showed that overall fuel consumption increased due to the increase in back pressure and extra fuel required for regeneration is up to 3.3% for Euro 5 compliant 1.4 liter turbocharged diesel engine with B10 fuel during the New European Driving Cycle [5].

The regeneration of the CPF can be achieved via passive oxidation and active regeneration modes. In passive oxidation mode, PM is oxidized using the NO_2 in the exhaust gas at temperatures as low as 300 to 450° C [6]. In the active regeneration mode, the PM is oxidized using the oxygen in the exhaust gas at approximately 550 to $600^{o}C$. The passive oxidation consumes no extra fuel as it uses the NO_2 concentration present in the exhaust gas whereas the active regeneration requires high exhaust gas temperatures which are usually achieved by dosing the diesel fuel (secondary injection) in the exhaust stream or through post injection from the primary injectors. In both cases, there is extra fuel consumed to achieve the required temperature conditions for active regeneration. Hence, optimum active regeneration frequency would help in improving the fuel consumption of the engine. This task is managed by the electronic control unit (ECU) of an engine.

The knowledge of PM mass retained as function of time is the vital input for an effective and efficient active regeneration strategy. The current engine ECU controls the PM loading using an internal PM estimator model. The PM estimator model relies on the calibrated engine maps, pressure drop across the CPF and temperature measurements to determine PM mass retained and regeneration frequencies [7]. Advanced regeneration strategies involve simplified CPF models that run real time within the ECU to provide more accurate feedback on current PM loading of the filter substrate. By applying simplified models that are similar to the ones used during design, development and application of CPFs, the regeneration frequency and duration can be optimized based on vehicle operating conditions which determine engine operating conditions. This would lead to fuel consumption savings and resulting CO_2 emissions reduction and also an increase in the durability of the CPF.

The optimum regeneration frequency and duration rely on the accurate prediction of temperature distribution within the filter. Due to the heat transfer, cake and wall PM oxidation and oxidation hydrocarbon species in the exhaust gas, the CPF filter temperature varies spatially (both axial and radial direction) and affects the regeneration efficiency of the filter as the PM oxidation reactions are highly temperature dependent. Hence, the accurate prediction of temperature distribution within the filter substrate will aid in optimizing the regeneration frequency and duration. The prediction of temperature distribution within the filter also provides robust diagnostics capability by monitoring the CPF temperature (as a virtual sensor) at several locations within the filter. The other use of the temperature distribution prediction could be as an alternative to a conventional CFD model to calculate axial and radial temperature distribution of the substrate. This could reduce significant simulation time and reduce computational resources required during the design and development phase of diesel particulate filters.

Catalyzed particulate filters are used to filter the PM from the diesel exhaust gasses. The accumulation of PM within the substrate wall and cake of a CPF leads to a increase in pressure drop (back pressure) across the CPF which increases the fuel consumption of the engine. In order to reduce the impact of the excess CPF pressure drop on engine fuel consumption, the CPF is periodically actively regenerated. Hence, the knowledge of the pressure drop across CPF is essential for optimizing the regeneration events (duration and frequency of regeneration) of a CPF. Post 2013 engines with selective catalytic

reduction (SCR) control also have increased engine-out NOx and NO_2 into the CPF which results in passive oxidation of the PM [8]. Therefore, these new systems need the pressure drop (ΔP) monitoring and ECU computation of PM loading and control of active regeneration time so that the ΔP is within the bounds expected for the engine operating condition and excessive active regenerations are not carried out. The heavy-duty emission regulations require on-board diagnostics (OBD) to monitor the performance of the emission control system during in-use vehicle operating conditions. The ΔP, temperature and PM mass distribution are the key performance indicators of the CPF condition. The ΔP from a model is necessary for developing an ECU based state estimator that uses the vehicle on-board experimentally measured ΔP along with the model ΔP. This is because the model can breakdown sources of the ΔP, so wise control action can be taken.

1.1 Objectives

The main objective of the research is to develop a computationally efficient CPF state estimator that runs fast enough (model run time faster than real time i.e. real time factor < 1) in the engine ECU to predict the filter substrate loading and temperature distribution and the pressure drop across the CPF. This goal was accomplished by developing high fidelity SCR in filter/CPF (SCR-F/CPF) model that closely simulates the experimental temperature distribution data and followed by the development of a reduced order MPF for the purpose of optimum CPF state estimation. The high fidelity SCR-F/CPF model developed in this thesis is the detailed CPF model without SCR reactions involving of ammonia and it is intended for design and development applications of the CPF as a replacement to 3-D CFD tools. The SCR reactions for SCR-F filter is being developed by Venkata Chundru through his PhD thesis work. The reduced order MPF model is the simplified version of SCR-F/CPF model to improve computational efficiency without affecting the model accuracy significantly (RMS temperature error < 10^oC, PM loading error < 3 g and pressure drop error < 0.5 kPa) for aftertreatment control applications. The CPF state estimator developed using the reduced order MPF model aids in determining the regeneration frequency for the CPF regeneration which reduces the fuel consumption and improves the durability of the CPF. The specific objectives of the proposed research are:

1. Develop a high fidelity SCR-F/CPF model to
   a. Simulate temperature distribution within filter
   b. Simulate filter loading distribution within filter
   c. Simulate Pressure drop across the filter
   d. Develop a calibration procedure and experimental validation of the high fidelity SCR-F/CPF model
2. Carry out a parametric study to determine the required number of zones in the reduced order MPF model for aftertreatment control applications
3. Develop a reduced order MPF model to
   a. Predict temperature distribution within filter
   b. Predict PM loading distribution within filter
   c. Predict pressure drop across the filter
   d. Validate the performance of the reduced order MPF model as compared to the high fidelity SCR-F/CPF model
4. Develop an extended Kalman Filter (EKF) based CPF state estimator that connects to a extended Kalman filter based DOC state estimator that uses DOC outlet model NO_2 concentration and sensor data to
   a. Estimate temperature distribution within the filter
   b. Estimate PM loading distribution within the filter
   c. Estimate pressure drop across the filter
   d. Evaluate the performance of the state estimator with high fidelity SCR-F/CPF model for steady state and transient test conditions with test cell experimental data

1.2 Overview of Thesis

This dissertation describes the research efforts towards the development of computationally efficient CPF state estimator for engine ECU application to predict the temperature and PM mass distribution within the CPF and pressure drop across the CPF. This Thesis is organized into seven chapters. They are as follows: 1) Introduction; 2) Background and Literature Review; 3) Experimental Setup and Data; 4) SCR-F/CPF High Fidelity Model Development; 5) CPF Reduced Order Model Development; 6) CPF State Estimator Development; 7) Summary and Conclusions.

2 Background and Literature Review[1]

The overall objective of this thesis is to develop a computationally-efficient high fidelity SCR-F/CPF model and a reduced order MPF model for predicting CPF temperature and PM distribution and pressure drop of the CPF for aftertreatment design, development and control applications. To fulfill the above objective, a detailed study of the published literature was carried out. This chapter provides a review of the relevant literature and the papers are organized in to six subparts: 1) Simplified models (0-D and 1-D) for ECU based controls from previous studies are explored including heat transfer models and their assumptions, 2) Study of simplified multi-dimensional CPF modeling efforts (2-D and 3-D) 3) Research work in the area of multi-dimensional temperature and PM distribution modeling efforts 4) Review of experimental investigations related to PM distribution 5) Review of research in modeling of CPF pressure drop including wall and PM cake permeability 6) Review of efforts in developing state estimators (DOC, SCR state estimators) and their experimental validation methods.

2.1 Simplified Models (0-D and 1-D) for ECU Based Controls

CPF models can be incorporated in the ECU to monitor and optimize CPF performance along with the engine performance. Such a model for CPF regeneration was described by Kladopoulou et al. [9] using a lumped parameter model approach. This was a 0-D model and the simulation relied on time dependence of input parameters. The spatial dependence (axial and radial direction) was assumed to be negligible. This lumped model included an external heat transfer mechanism by considering conduction through the packing material and the can and external ambient heat transfer through convection. Subsequently, further advanced model based control techniques were explored by many researchers to simplify conventional 1-D models for real time ECU application with reasonable accuracy and computational speed compared to conventional map based control approaches as presented by Rose et al. [7].

---

[1] Parts of the material contained in this chapter are based on references [1, 2,3] with permission of Springer.

The real time implementation of a 0-D CPF model along with 1-D DOC model were presented by Nagar et al. [10] and showed that the 0-D CPF model was able to predict the average filter substrate temperature within $25^{o}C$. They also highlighted the difficulty of initiating regeneration based on ΔP (difference between inlet and outlet pressure of CPF) measurement and concluded that PM loading provides more reliable criterion to trigger CPF filter regeneration than using ΔP values.

The 0-D CPF model developed by Nagar et al. assumed internal convective heat transfer from filter substrate to exhaust gas as a mechanism to dissipate the energy release during PM oxidation. However, the model ignores any conductive heat transfer within the substrate. Mulone et al. presented the 1-D CPF model for ECU application for steady state [11] and transient operating conditions [12]. The model is based on the single channel representation of the CPF. The model was able to predict axial variation in the PM loading. However, the model ignored radial temperature gradients in the CPF and hence the radial PM loading distribution.

The resistance node methodology presented by Depcik et al. [13] provides a simplified and computationally efficient modeling approach to predict axial and radial temperatures of the filter. However, this model assumes uniform inlet temperature and ignores the inlet temperature variation along the radial direction of the CPF. This model also ignored the oxidation of inlet hydro carbons within the CPF and its effect on the substrate temperature and PM distribution within in the CPF. The model also neglected the heat transfer through the packing material and can. This model also assumed all the PM in the inlet is deposited as a PM cake (100 % filtration efficiency) and ignores the wall PM accumulation and overall filtration efficiency of the substrate. Recently, Depcik et al. [14] developed an improved ECU based model that combines classical filtration model [15] with the lumped model to include PM filtration within the substrate wall which improved the pressure drop prediction capability. The classical filtration model developed by Konstandopoulos and Johnson along with the newly developed cake permeability model in this research is used to develop the multi-zone pressure drop model for the CPF estimator.

2.2 Multi-dimensional CPF Modeling Efforts (2-D and 3-D)

Konstandopoulos et al. [16] developed a multichannel model using a multiphase continuum approach to simulate spatial non-uniformities in the filter (axial and radial

directions). The multiphase continuum model was derived from the discrete multichannel description of the CPF. The model worked in a CFD code framework to include the partial differential equations in the CPF model. The conduction, convection and radiation heat transfer within the filter were considered in the model. This continuum model is computationally expensive as it involved a system of several ordinary and partial differential equations and the equations have to be solved in a 3-D domain.

Miyairi et al. [17] developed 2-D thermal conduction model to predict temperature distribution within the CPF. This 2-D thermal conduction model was developed by placing several quasi 1-D models in radial direction to predict temperature distribution along the radial direction. Only the thermal conductance through the solid wall was taken into account. This simplified 2-D model was developed to predict temperature distribution during regeneration and temperature distribution data was used to carry out thermal stress analysis of the substrate. This simplified 2-D model accounted for the thermal PM oxidation. However, the NO_2 assisted PM oxidation, PM filtration and wall PM oxidation models were not included. The energy release due to the oxidation of hydrocarbon in the filter was also not included in this model.

Yi [18] developed a 3-D macroscopic model for predicting PM loading within the filter. The model was based on grouping the channels with reasonably uniform inlet conditions and solving each group using 1-D model equations. This established a link between 1-D and 3-D models and reduced the complexity of detailed 3-D simulations. The model did not consider PM oxidation (NO_2 assisted and thermal O_2) within the filter and also neglected heat losses from the substrate can of the filter.

2.3 Multi-dimensional Temperature and PM Distribution Modeling Efforts

Konstandopoulos et al. [16] developed a continuum based multichannel model and used varying PM loading distribution profiles to study PM loading non-uniformities and their effect on the regeneration process (duration and maximum filter temperature). This study shows that the regeneration time was shorter (20-30% faster regeneration) when the filter was loaded more towards the front compared to the uniform loading case for an identical total PM loading. The maximum filter substrate temperature between both cases (more loading at front versus uniform loading) were close to each other. With inlet radial non-uniformities in velocity and temperature, the model showed non-uniform temperature

distribution as shown in Figure 2.1. This non-uniform temperature distribution resulted in partial oxidation of the PM in the filter as shown in Figure 2.2. The partial regeneration mainly occurred at the periphery of the filter as the PM at the periphery of the CPF was not oxidized due to lower temperatures in this region.
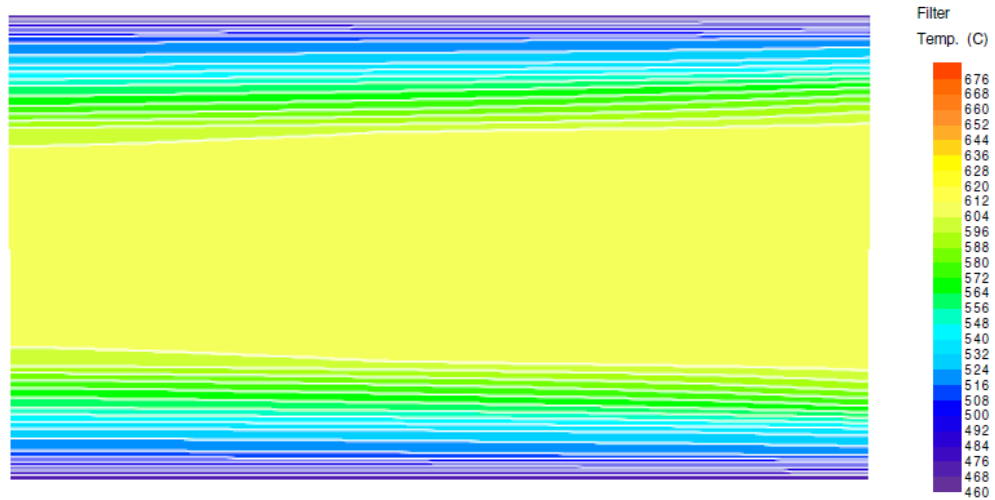
Figure 2. 1 Wall temperature evolution in the filter [16] – Reprinted with permissions from SAE International, SAE Paper No. 2001-01-0908.
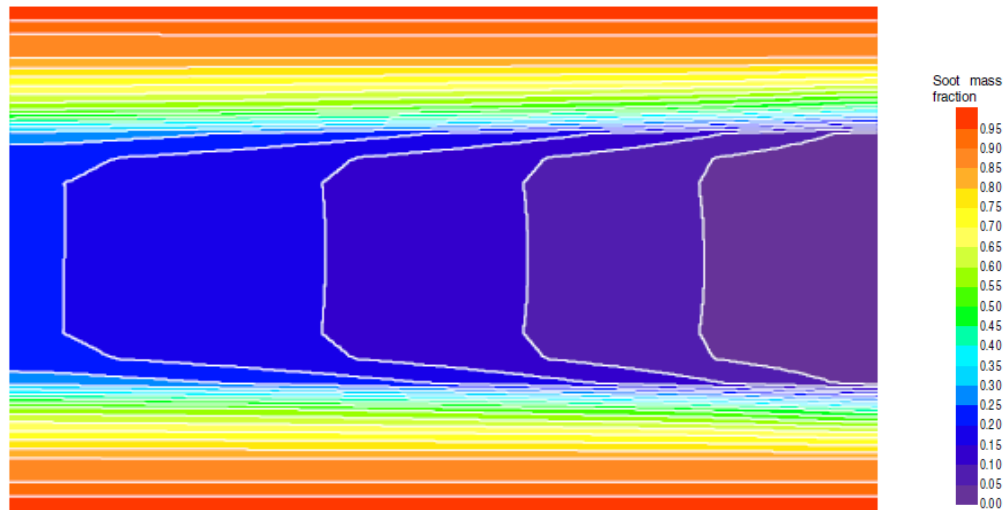
Figure 2. 2 PM mass fraction evolution of the filter [16] – Reprinted with permissions from SAE International, SAE Paper No. 2001-01-0908.

Yi [18] developed a 3-D macroscopic model to simulate PM loading distribution within the filter. This study shows that the PM accumulation is more near the centerline of the filter

compared to other sections due to the higher exhaust flow rate at the center section for the given test geometry as shown in Figure 2.3. The colors represent local porosity within the filter. Lower porosity (blue color) indicates more PM accumulation.
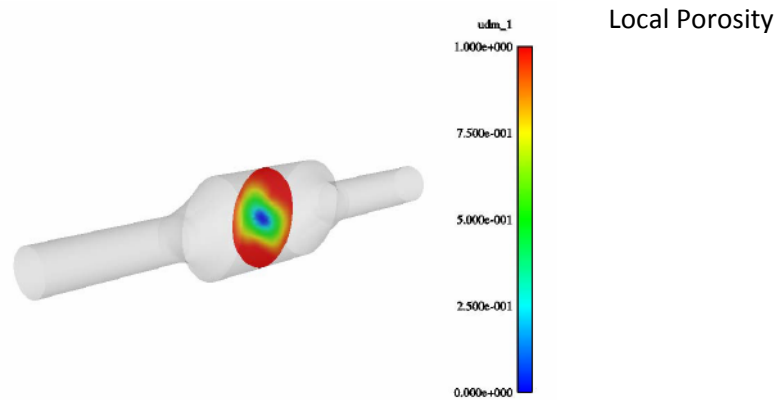
Figure 2. 3 PM loading distribution on a vertical plane [18] — Reprinted with permissions from SAE International, SAE Paper No. 2006-01-0264.

Miyairi et al. [17] developed a 2-D thermal conduction model to predict temperature distribution within the CPF. The model was validated using the regeneration test run on the regeneration test burner. The regeneration test was carried out at a temperature of $600^{\circ}C$ and a flow rate of 0.014 kg/sec. From Figures 2.4a and 2.4b, the simulated temperature was higher than the measured temperature at the center of the filter as shown in Figure 2.4. The temperature gradient simulated between the center and periphery of the filter was closely matching with the experimental results.
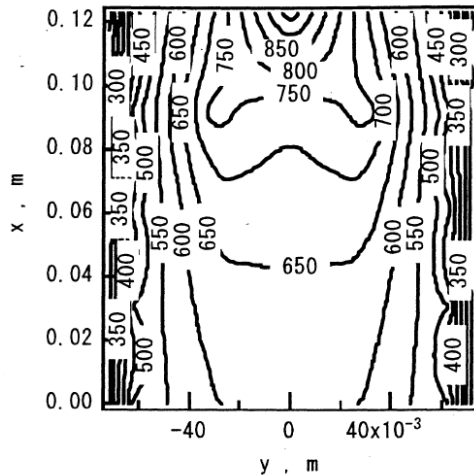
[a] Experimentally measured result for Cordierite
Cell density: 200 cpsi, Wall thickness:14 mil
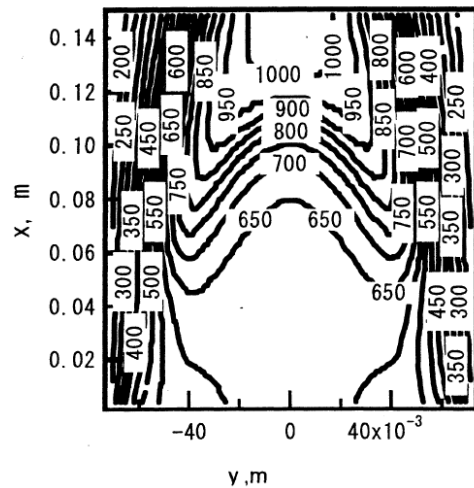
[b] Model calculation result for Cordierite
Cell density:200 cpsi, Wall thickness: 14mil

Figure 2. 4 Measured and calculated temperature distribution for Soot loading of 10 g/l, Inlet gas temperature of 600ºC, gas flow rate of 0.014 kg/sec and O2 concentration of 10% [17] — Reprinted with permissions from SAE International, SAE Paper No. 2001-01-0912.

Ranalli, Hossfeld, Kaiser, Schmidt and Elfinger [19] also showed similar findings with 3-D CFD simulations that PM loading is maximum at the central regions of the filter attributing it to higher mass flow rate and flow velocity in that section compared to other places for the given test geometry. Kostoglou et al. [20] used the continuum based multichannel model to illustrate how PM regeneration is affected by the non-uniformities in inlet flow and temperature, local hot spots and heat losses from a filter can. The study shows that, with the non-insulated filter can and with radially uniform flow and temperature conditions, the regeneration efficiency is lower at the outer surfaces of the filter due to lower exhaust gas temperature (caused by the thermal boundary layer). Koltsakis, Haralampous, Depcik, and Ragonoe [21] presented a comprehensive summary of 3-D filter modeling and used PM loading distribution plots to highlight the effect of flow maldistribution on filter loading. The 1-D model in references [22,23,24] simulated the axial variation in PM cake layer thickness assuming the PM deposition rate is proportional to wall flow velocity and showed the increased PM cake layer thickness towards end of CPF compared to other sections for the PO and AR cases studied in the reference [23]. The 1-D model developed in references [22, 23] also needed the corrections to the input data while simulating the AR engine experimental data. This is mainly to account for the temperature and PM maldistribution and potential PM cake damage during PM oxidation

within the CPF. The model developed in this thesis has the potential to overcome the problem of the 1-D model not being able to predict delta P under AR transient conditions as was shown by Premchand et al. [22] and Premchand [23].

2.4 Experimental Investigations to Characterize PM Distribution

Several experimental techniques have been developed to determine PM distribution within the filter. They include both destructive and non-destructive methods. The non-destructive methods are advantageous as they allow for repeat tests. Ranalli et al. [19] developed a methodology for a qualitative assessment of radial PM distribution of a loaded filter using Laser Doppler Anemometer (LDA) analysis and thermographic analysis. This method was not capable of analyzing the axial PM distribution within the filter substrate. The LDA analysis of the loaded filter showed that the low flow and velocity test conditions yield uniform loading of the filter and the higher flow and velocity conditions resulted in non-uniform loading. This was illustrated with the flow velocity distribution measurements using LDA. Figure 2.5 shows the flow velocity distribution measured by LDA at the outlet of the CPF for low flow conditions at 9.3 g/L. The velocity peaks indicate the PM distribution at various locations of the filter. From Figure 2.5, the velocity peaks are homogeneous across the filter and similar to the distribution measured using the empty filter. At high flow conditions, the velocity distribution is non-homogenous as shown in Figure 2.6. From Figure 2.6, the PM distribution is more at the center of the filter compared to the outer sections of the filter.
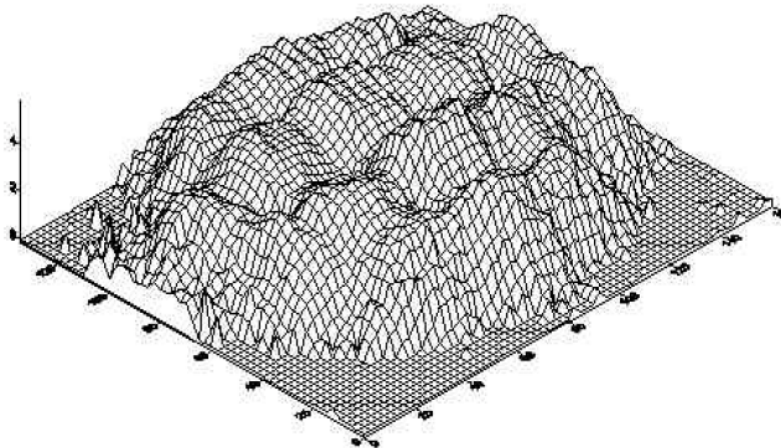
Figure 2. 5 LDA measured velocity distribution with low mass flow at 9.3 g/l loading [19] – Reprinted with permissions from SAE International, SAE Paper No. 2002-01-2158.
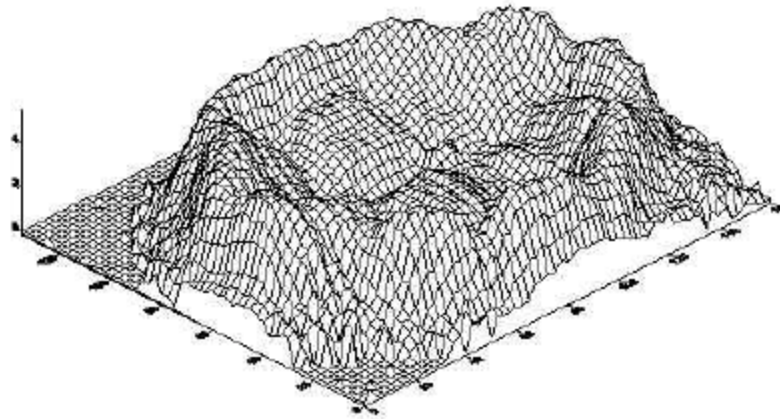
Figure 2. 6 LDA measured velocity distribution with high mass flow at 9.7 g/l loading [19] – Reprinted with permissions from SAE International, SAE Paper No. 2002-01-2158.

Pinturaud et al. [25] used velocity profiles determined from the anemometer to show the radial PM distribution. Based on the experimental study, during loading and active regeneration, the PM distribution is uniform in the radial direction. The radial PM distribution is more uniform at lower filter loading (<0.7 g/L) and it was 'quasi-uniform' at the higher level of loading (6.6 g/L). This was attributed to the cone in front of the filter causing more PM loading (flow and velocity) towards the center of filter compared to other surfaces radially. The axial PM distribution studies were also carried out using scanning electron microscopy (SEM). The study shows that PM cake loading is maximum at the end of the channel and minimum at the entrance when the filter was loaded to 7 g/L under steady state conditions with an exhaust temperature of 250°C. The PM loading of > 1.3 g/L shows a transition from deep bed filtration to cake filtration. The axial PM distribution tends to become more uniform at higher loading compared to lower loading. The study also shows that during active regeneration, the PM oxidization tends to homogenize the PM distribution along the axial direction. Bensaid et al. [26] carried out an experimental study using field emission scanning electron microscopy (FESEM) to determine the axial and radial PM distribution of a whole DPF during the loading process. The study shows that the PM cake layer thickness along the radial direction is affected by the inlet pipe geometry due to the inlet flow distribution. Foley et al. [27, 28, 29] developed a methodology to quantify the 3-D PM distribution measured using a terahertz wave scanner which is used as the reference in this thesis to compare PM loading trends predicted by

13

the SCR-F/CPF model. Unlike the SEM measuring technique, the terahertz wave scanner is one of the non-destructive experimental techniques available to quantify 3-D PM distributions within the filter and hence reducing the experimental variations.

2.5 CPF Pressure Drop Modeling

The pressure drop across the CPF is mainly due to the flow frictional losses in the inlet and outlet channels, the PM filtered within the substrate wall through deep bed filtration and the PM filtered in the cake layer. The original formulation for pressure drop across the wall flow filters using the packed bed filtration theory was developed by Konstandopoulos and Johnson [15]. Further, Kladopoulou et al. [9] developed a lumped version of CPF model for the pressure estimation for ECU based applications. Haralampous et al. [30, 31] derived improved analytical expressions from the 1-D pressure drop model ('inverse' calculation approach) for on-board assessment of PM mass loading using the on-board pressure drop, exhaust flow rate and temperature measurements. These simplified analytical expressions accounted for the PM cake permeability dependence on the gas mean free path due to slip phenomena. However, the temperature gradient within the CPF was not accounted (isothermal model) which affects the pressure drop model and on-board PM assessment during transients. Recently, Premchand et al. [22-23] developed a 1-D model for CPF pressure drop prediction. This model used axial momentum equations for solving pressure drop across the inlet and outlet channels and Darcy's equations for estimating the pressure drop across the PM cake layer and substrate wall. The instantaneous permeability of the substrate wall was estimated using the filtration sub models, developed based on packed bed filtration theory [15]. This model discretized the substrate wall into several sub-layers and the filtration model was applied at each sub-layer. Oxidation of the PM within the substrate wall was also modeled [22] in order to account for the PM oxidation effect on the substrate wall pressure drop. The 1-D model developed by Premchand et al. [22-23] also used the concept of transition permeability to determine a start of transition (i.e. cake formation) from the deep bed filtration of PM into cake filtration. This model assumed constant cake permeability during loading, PM oxidation and post loading phases of the experiment. This 1-D model showed a good agreement in predicting the pressure drop characteristics of a CPF. However, the model had to use correction factors to simulate experimental pressure drop during PM oxidation

to account for the changing cake permeability. In continuation with the above efforts, this thesis focuses on developing a multi-zone pressure drop model using packed bed filtration theory along with a cake permeability model [3] for engine ECU applications. Also, the correction factors applied in earlier 1-D model [23] was eliminated by applying the newly developed cake permeability model developed in this work.

2.5.1 Wall Permeability

Pressure drop in the wall and cake is affected by the change in permeability as defined in the Darcy's equation. In differential form Darcy's flow equation can be written as

$$-k\frac{dP}{ds} = \mu v \tag{2.1}$$

Where dP is the differential change in pressure over length of ds. μ is the dynamic viscosity of flowing fluid and v is the velocity of fluid. The constant k is assumed to be the permeability of the solid porous medium. k is not affected by the fluid medium and depends on the properties of the solid medium such as porosity, pore size distribution and surface area [32]. However, larger values of k have been obtained for gas flow than for liquid flows and the value of k varied for each gas. This was attributed to 'slip' conditions present when the gas flows through the small porous media. The slip flow condition is observed for the porous media when the mean free path length of the gas molecules approaches the pore size of the porous medium such as substrate wall and PM cake. Pulkrabek et al. [32] showed that the permeability of the gases through the porous aluminum oxide increases with temperature. The gases (air, nitrogen, and argon) that have non-polar molecules of about the same size show similar flow characteristics as a function of temperature whereas helium, with its much smaller molecules showed variation in flow characteristics compared to the other three gases as shown in Figure 2.7.
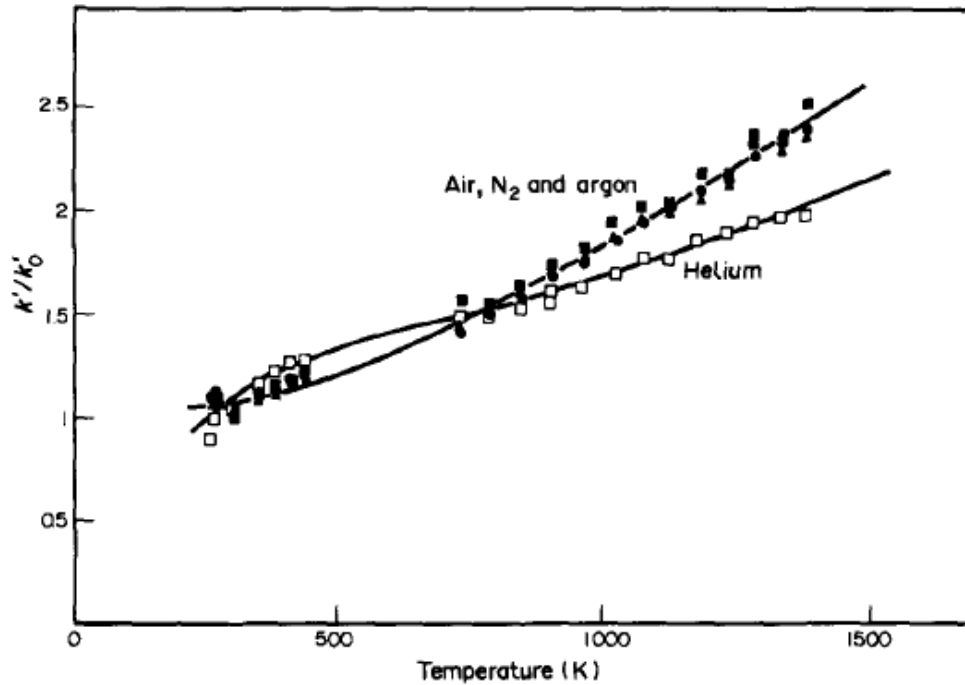
Figure 2. 7 Apparent permeability ratio (dimensionless) [32]

2.5.2 Cake Permeability

Versaevel et al. [33] developed an empirical correlation to predict pressure drop for the PM cake layer. The empirical relation was based on the assumption that the product of the PM cake layer permeability and PM cake layer density is proportional to the mean free path length of the gas. From references [32-33], the permeability of the substrate wall and cake is affected by the change in mean free path length of the gas. Hence, permeability evolution as a function of mean free path length of the gas is considered in the SCR-F/CPF model.

Konstandopoulos et al. [34] performed in situ permeability experiments on partially reacted PM cakes. The experiments showed the evolution of the hydrodynamic resistance ($\rho \times k$) of the PM cake as a function of remaining PM cake mass in the sample filter during PM oxidation (with 10% O_2) for catalyzed and unanalyzed filter. The experiments showed that the hydrodynamic resistance of the filter increased rapidly at PM cake mass load of 1 $\frac{g}{m^2}$ ($\cong \frac{1}{3}$ of initial mass).

16

Daido et al. [35] visualized PM deposition and oxidation in the DPF wall and analyzed the oxidation results with the experimental pressure drop measurement. From the visualization, it was observed that the PM accumulated inside the wall was oxidized first while the cake layer oxidizes simultaneously. This leads to decrease in pressure drop of the DPF at the early stages of PM oxidation. Further into the PM oxidation, as the PM cake layer thins, the surface accumulation layer suddenly breaks and falls into the DPF wall due to intolerable gas flow pressure as shown in Figure 2.8 [35]. This leads to further decrease in the pressure drop of the DPF before the pressure drop becomes constant.
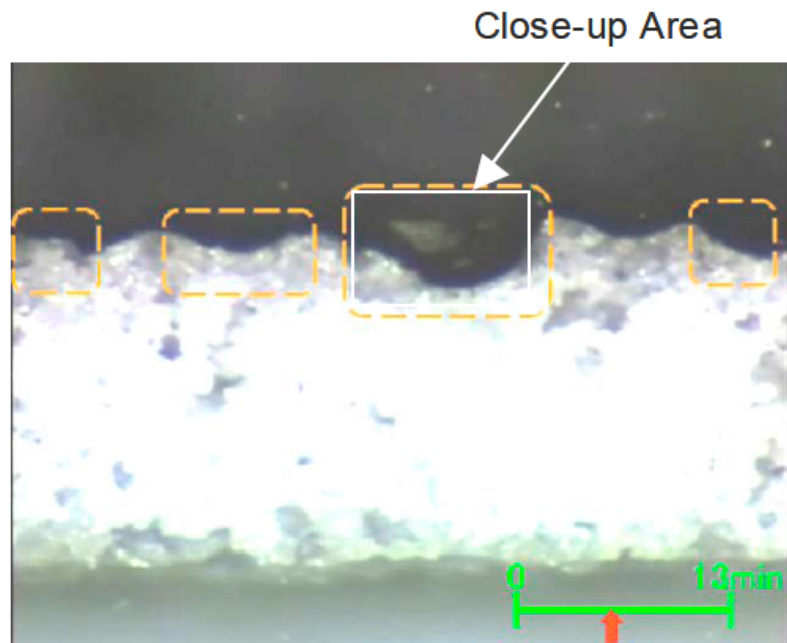
Figure 2. 8 Sudden depressions of the PM cake in cordierite DPF [35] – Reprinted with permissions from SAE International, SAE Paper No. 2009-01-1473.

Recently, Choi et al. [36] examined the PM deposition and oxidation in the DPF using a bench-scaled DPF test system equipped with an optically accessible DPF reactor and a micro-imaging system. They analyzed the correlation between the PM filtration/regeneration processes on the filter porous wall and pressure drop across the filter. From the experiments, three distinct regeneration stages were observed, each showing linear decrease in normalized pressure drop as shown in Figure 2.9. The majority of the pressure drop occurred during the second stage of the regeneration with the opening of effective pores causing increased wall permeability of the exhaust gas. During

the second stage of oxidation, several small holes in the cake were also found by the white spots in the image indicating open effective pores.
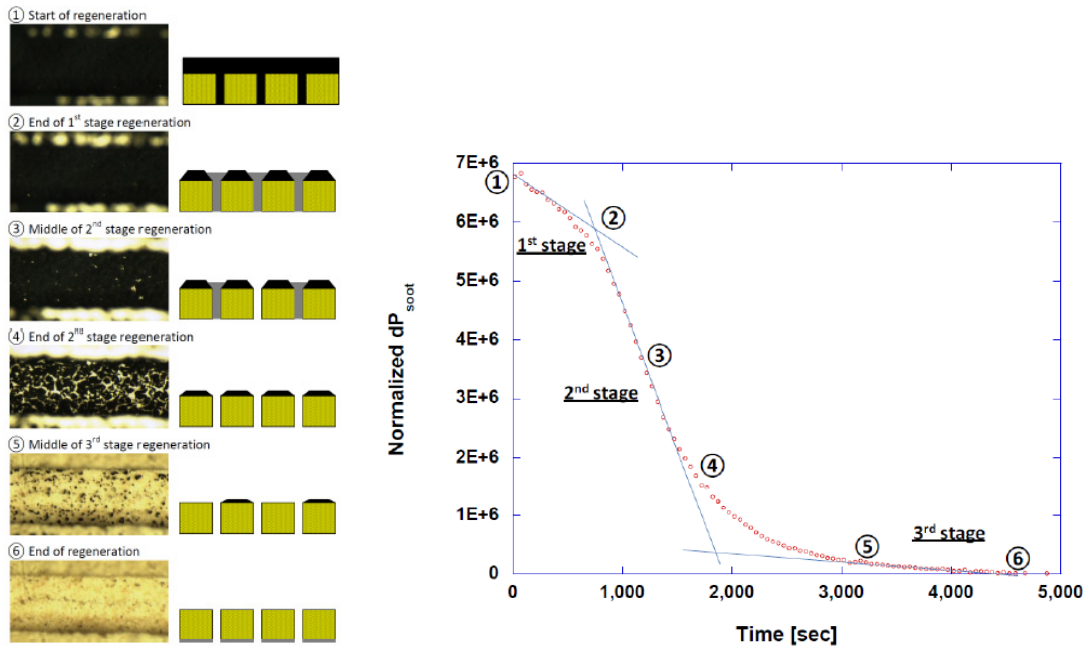
Figure 2. 9 Pressure drop traces during regeneration (with NO₂ assist at 400ºC) and corresponding visualized images and schematic drawings of PM deposition at different stages [36] – Reprinted with permissions from SAE International, SAE Paper No. 2013-01-0528.

From the above references [35-36], there is a potential that the PM cake layer breaks and several holes and cracks are formed within the cake layer during PM oxidation which leads to microscopic (affecting microstructure such as local porosity, packing density, particle size etc.) and macroscopic (affecting overall thickness of the PM cake layer, PM mass distribution etc.) damage in the PM cake layer. The interaction between PM cake deposits, its oxidation and resultant change in microstructure of the PM cake is very complex and only a few papers in the literature attempted to model this. Shadman [37] proposed evolving particle diameter model to account for the PM cake microstructure (thickness, density and surface area) evolution during PM oxidation. The PM cake in the model is assumed to consist of column of spherical particles stacked one on to top of the other and each particle surface shrinks during PM oxidation and losses its height. Considering discrete treatment of each particle in the PM cake, the model requires several thousand differential and algebraic equations for a typical PM cake thickness found in the heavy duty engine applications. Hence, the model is computationally demanding for ECU based

applications. Kostoglou et al. [38] proposed generalized continuum based 1-D model to describe the evolution of local PM cake microstructure using the two dimensionless parameters (α and β), as the microstructure descriptors α and β are not sufficient to infer the evolution of the characteristics particle size r during PM oxidation and hence, affecting the accuracy of the hydrodynamic resistance calculation and pressure drop. Further, the continuum based 1-D model requires discretization of the PM cake layer along its thickness to estimate the evolution of microstructural properties of the PM cake which is also computationally challenging for the model intended for ECU based applications. Picandet et al. [39] studied the gas flow through the damaged concrete discs (cracked porous medium) and observed that the cracks in the porous media increases the gas flow proportional to the damage permeability (k_d) as illustrated in Figure 2.10. From Figure 2.10, the flow thru the damaged porous media $(Q_1 + Q_2)$ can be divided in to two parts. First part is, minimum flow through the undamaged porous media (Q_1) proportional to initial permeability (k_o). Second part is, flow through the cracks in the impermeable media (Q_2) and it is proportional to the absolute increase in permeability ($k_d - k_0$).
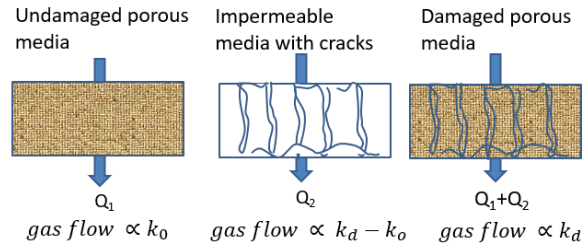
Figure 2. 10 Gas flow through damaged porous media [39]

Picandet et al. [39] developed a damage permeability function which is the result of an arbitrary choice to obtain an exponential form with a continuous increase and varying initial conditions. The relative change in dynamic elastic longitudinal modulus was used as the damage variable for analysis with porous concrete discs. In this work, in order to predict the changes in the pressure drop during the PM cake oxidation, the cake permeability during PM oxidation is estimated by using the concept of permeability evolution considering the damage in the porous media and it is explained in Chapter 4 of this thesis.

Pressure drop during PM oxidation is also affected by the inlet gas conditions (temperature, O_2 and NO_2 concentration). Choi et al. [36] also studied pressure drop trends during regeneration under three different inlet gas conditions, with and without NO_2 and at

two temperatures ($400^{\circ}C$ and $500^{\circ}C$). They observed that the NO_2 promotes a higher rate of oxidation (oxidation duration is shorted by 13 times at 1000 ppm of NO_2) and enhanced the pressure drop to decrease at about a 13 times higher rate compared to O_2 only regeneration for similar temperature conditions ($500^{\circ}C$).

From the above review, it is evident that the permeability of the substrate wall and PM cake changes during loading and oxidation and this affects the overall pressure drop of the CPF. The 1-D model developed by Premchand et al. [22-23] assumed the constant permeability during PM cake oxidation. Hence, the model had to use correction factors to simulate experimental pressure drop during PM oxidation to account for the changing cake permeability. In this research, the experimental data (measured total pressure drop) were further analyzed in combination with the simulated pressure drop components (wall and channel pressure drop) and found that the permeability of the cake layer changes significantly during PM oxidation. The findings from this research is consistent with earlier research related to PM oxidation and its effect on permeability and pressure drop [34-36]. The modeling of the cake permeability evolution during PM oxidation is using the evolving particle diameter model [37, 38] which is computationally challenging for ECU based applications. Hence, new cake permeability model (phenomenological model) was developed to account for the increase in permeability due to potential cake damage and changes in the microstructure of the PM cake. The accurate knowledge of modeled pressure drop is essential for optimizing the active regeneration event and in order to maintain the performance of the CPF. The computationally-efficient reduced order MPF model that predicts temperature and PM distribution within the CPF and ΔP has potential for using the model in a ECU based aftertreatment control system.

2.6 Kalman Filter Based State Estimators for Engine Aftertreatment Systems

Kalman filter is the widely used method for tracking and estimation due its simplicity, optimality and robustness. It is a recursive filter that can optimally estimate the states of the linear system taking into account of system dynamics and inputs [40]. An extended Kalman filter is the non-linear version of Kalman filter and retains the linear covariance and gain matrices, however uses the non-linear state propagation equations and output vector. The unique feature of the Kalman filter is that it incorporates the measurements

and measurement error statistics (approximated as Gaussian) in the estimate. It finds the stochastic relations between the model and sensor measurements, and then estimates the system states in an optimal approach.

Kalman filter based digital control techniques were explored by several researchers for optimal control of the engine and DOC-DPF-SCR based aftertreatment systems. Chauvin et al. [41] developed an air fuel ratio (AFR) estimator from a global oxygen sensor measurement using the time-varying Kalman filter model. Their work [41] demonstrated the closed loop control of fuel air ratio (FAR) for combustion control applications. Tschanz et al. [42] proposed a control scheme that integrates the feedback of the engine out emissions of NOx and PM for effective engine out emission control. This controller scheme used the model based observer to overcome the slow dynamics of the sensors (NOx and PM). This emission controller reduced the variations in emission outputs caused due to the drift and transient operating conditions. The sensor measurement of engine out NOx is the key input for the emission control of SCR aftertreatment systems. Hsieh et al. [43] developed extended Kalman filter based estimator to improve the accuracy of the NOx sensor measurement in SCR control applications.

Guardiola et al. [44] developed an online adaptive algorithm for updating the NOx look-tables used in the SCR control applications. This adaptive algorithm used simplified Kalman filtering due to its capability for tracking the system and parameters during aging. Surenahalli et al. [45] developed an extended Kalman filter based estimator for NH_3 storage, NO, NO_2 and NH_3 estimation in SCR control applications to aid OBD strategies to detect system failure modes. Further, Surenahalli et al. [46,47,48] developed an extended Kalman filter based DOC observer to estimate the internal states of the DOC such as CO, NO, NO_2, and C_3H_6 concentrations and temperatures in the catalyst. Figure 2.11 shows the schematic of a DOC estimator with all the inputs needed for DOC state estimation. The estimator uses the single outlet temperature measurement, in combination with the inlet concentrations of CO and HC, inlet exhaust gas temperature, exhaust mass flow rate from the engine ECU and the NOx concentration from a NOx sensor. Also, the estimator assumes the NO_2/NOx ratio of 0.1 to estimate the inlet NO and NO_2 concentrations.

In continuation with the above efforts, this research focuses on development of an optimal CPF estimator to function with a DOC estimator in order to predict CPF states such as PM mass retained, temperature and PM distribution within the CPF and pressure drop across CPF for comparing the model to the measured ΔP and regeneration control purposes.
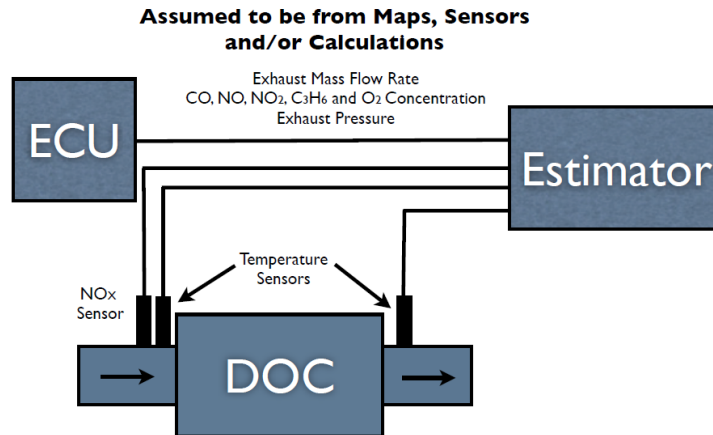
Figure 2. 11 Schematic of a DOC estimator showing all the inputs needed [48]

2.7 Summary

The relevant literature were reviewed in order to support the development of a computationally-efficient CPF model to predict temperature and PM mass distribution and pressure drop of the CPF for ECU based applications. Based on the detailed literature review, an high fidelity SCR-F/CPF model along with the reduced order MPF model and estimator are developed in this thesis to fill the knowledge gap in the literature and address the challenges for model-based estimation of CPF for control applications. Specifically, the main contribution from this thesis include:

- Multi-zone modeling approach (axial and radial zones) for ECU applications with varying inlet temperature distribution
- Multi-zone modeling of temperature and PM distribution within the CPF for ECU based applications.
- Varying CPF inlet temperature distribution using fully developed thermal boundary layer assumptions and experimental temperature distribution data.

- Consideration of the heat transfer mechanism in the high fidelity SCR-F/CPF model and the reduced order MPF model (conduction, convection within the filter and also to the ambient) intended for ECU applications.
- Calibration procedure for the multi-zone CPF models and a study of the effect of the number of axial and radial zones on model run time and accuracy as related to measured filter loading and temperature data.
- Multi-zone PM filtration and oxidation model accounting for PM accumulation and oxidation within the substrate wall and PM cake in each axial and radial zone.
- Multi-zone pressure drop model accounting for changes in mean free path length of gas in wall permeability
- <u>Development of new PM cake permeability model</u> using damage permeability concept
- <u>Development of new CPF state estimator</u> for PM loading, temperature distribution and pressure drop for multi-zone models intended for ECU applications.

3 Experimental Setup and Data[1]

This chapter describes the experimental setup, test procedure and test matrices used to record the experimental data used in this thesis. The experimental data from the eighteen experiments with three different fuels (ULSD, B10 and B20) were used for the development of cake permeability model used in the pressure drop model and calibration of PM kinetics of the high fidelity SCR-F/CPF model. The experiment temperature distribution data were also measured during these tests and were used to calibrate the heat transfer to the ambient, heating and cooling of the filter and validation of the high fidelity SCR-F/CPF model for predicting temperature distribution.

3.1 Engine, Fuel and Test Conditions

A 2007 inline 6-cylinder turbo charged direct-injection common rail Cummins ISL 8.9 L diesel engine rated at 272 kW with DOC and CPF aftertreatment devices was used for this study. Experimental data, collected by Shiel et al. [49-50] and Pidgeon et al. [51-52] at eighteen different operating conditions, was used to calibrate the high-fidelity SCR-F/CPF model. The specifications of the engine and aftertreatment system are shown in Tables 3.1 and 3.2, respectively.

---

[1] Parts of the material contained in this chapter are based on references [1, 2,3] with permission of Springer.

Table 3. 1 Specifications of engine [49, 51]

Model	Cummins ISL - 272 kW (365 HP) and 317 kW (425 HP)
Year of Manufacture	2007
Cylinders	6,inline
Bore x Stroke	115x144.5 mm
Displacement Volume	8.9 L
Aspiration	Turbocharged
Aftercooling	Charge Air Cooler
Rated Power	272 kW @ 2100 RPM
Peak Torque	1695 Nm @ 1400 RPM
EGR System	Electronically controlled and actuated

Table 3. 2 Specifications of the aftertreatment system used in the experiments [49, 51]

	DOC	CPF	Units
Substrate material	Cordierite	Cordierite	-
Cell geometry	Square	Square	-
Diameter	267	267	mm
Length	102	305	mm
Total volume	5.7	17.1	L
Number of cells per unit area	62(400)	31(200)	cells cm^{-2} (cells in^{-2})
Cell width	1.09	1.49	mm
Frontal area	81	69	%
Channel wall thickness	0.114	0.305	mm
Wall density	NA	0.45	g cm^{-3}
Specific heat	NA	891	J kg^{-1} K^{-1}
Thermal conductivity	NA	0.84	W m^{-1} K^{-1}
Porosity	35	52	%
Mean pore size	NA	13	μm

The test summary of eighteen test runs used in this research work is shown in Table 3.3 (six passive oxidation experiments) and Table 3.4 (twelve active regeneration experiments). The experiments were performed with three different fuels including ULSD,

25

B10 and B20 blends. The properties of test fuels used for the experiments are documented in references [49, 51].

Table 3. 3 Passive oxidation experiments used for the calibration of the SCR-F/CPF model [49, 23]

No	Test ID	Passive Oxidation				
		Temp	Duration	CPF Inlet NO_2/NOx	CPF inlet O_2	PM mass retained end of post loading
		(^{o}C)	(min)	(ppm/ppm)	(% Vol.)	(g)
1	PO-B10-14	253	101	112/257	12.6	50.8
2	PO-B10-15	355	81	101/194	8.9	36.9
3	PO-B10-16	408	43	61/209	7.1	35.1
4	PO-B10-17	356	80	90/178	8.7	39.4
5	PO-B20-12	350	81	109/206	9.4	37.1
6	PO-B20-13	403	42	64/204	7.3	36.1

Test ID nomenclature – PO-B10-14 means Passive Oxidation Experiment with B10 fuel type and experiment run 14.

Table 3. 4 Active regeneration experiments used for the calibration of the SCR-F/CPF model [49, 23]

No	Test ID	Active Regeneration				
		Temp	Duration	CPF Inlet NO_2/NOx	CPF inlet O_2	PM mass retained end of post loading
		(^{o}C)	(min)	(ppm/ppm)	(% Vol.)	(g)
1	AR-ULSD-1	554	15	4/106	7.2	38.4
2	AR-ULSD-2	581	6	7/141	6.9	27.7
3	AR-ULSD-4	526	21	8/122	7.6	35.9
4	AR-ULSD-5	524	22	6/131	7.7	37.1
5	AR-ULSD-6	532	21	4/130	7.7	35.8
6	AR-B10-1	530	26	4/119	7.8	27.9
7	AR-B10-2	528	19	7/110	7.8	27.4
8	AR-B10-4	554	15	3/124	7.5	29.1
9	AR-B20-1	476	35	10/152	8.8	33.0
10	AR-B20-2	503	39	4/138	8	23.0
11	AR-B20-5	528	19	7/140	8.2	18.4
12	AR-B20-6	531	16	10/124	8.2	23.1

Test ID nomenclature – AR-ULSD-1 means Active Regeneration Experiment with ULSD fuel type and experiment run 1.

3.2 Passive Oxidation Experiments

An overview of the passive oxidation experimental test procedure is shown in Figure 3.1. The passive oxidation experiment starts with the CPF clean out phase where the engine

was operated at active regeneration test condition (600°C for fifteen minutes to cleanup CPF) followed by stage 1 loading of filter with a DOC inlet temperature of 265 +/- 10°C for 30 minutes. Then the stage 2 loading starts after weighing of the filter at the end of stage 1. The engine operating conditions for stage 2 loading are the same as those in stage 1. The stage 2 loading continues to achieve a target filter loading of 2.2 +/- 0.2 g/L. At the end of stage 2 loading, the filter was weighed again and the test was continued further with the ramp up (RU) phase for 15 minutes before switching to the passive oxidation phase to achieve a stable filter temperature for PM oxidation.
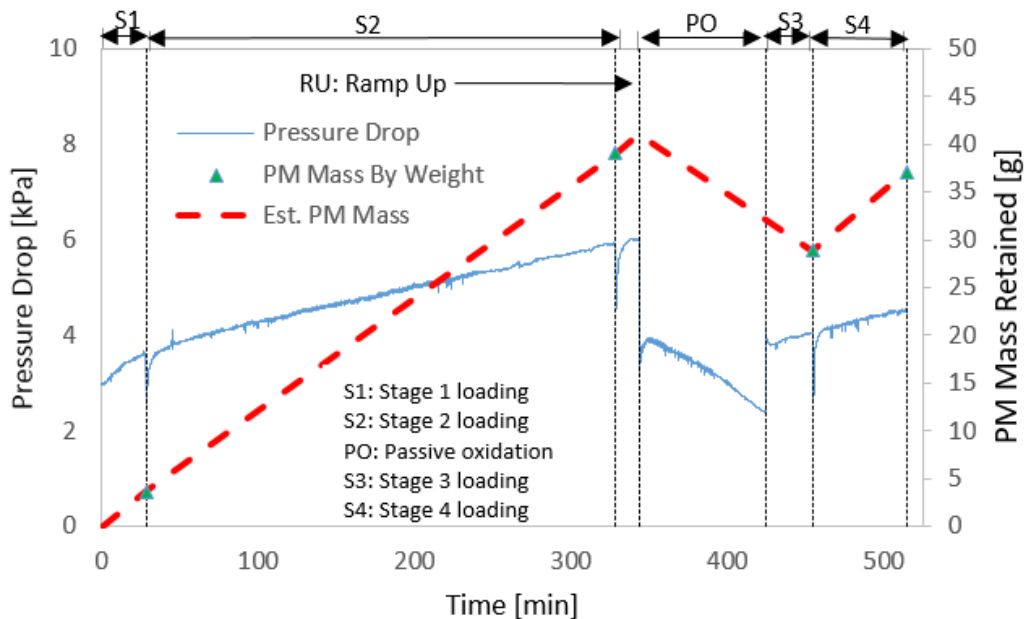
Figure 3. 1 Overview of the various stages of the typical passive oxidation experiment [50] - Reprinted with permissions from SAE International, SAE Paper No. 2012-01-0837.

The engine operating conditions for the RU phase is the same as those in stages 1 and 2 loading conditions. The purpose of the RU phase is to achieve similar substrate temperature as stage 1 and stage 2 loading before PM oxidation. During the stage 2 CPF weighing process, the CPF temperature is dropped to a lower value and hence, after reinstalling the CPF in the engine, the engine was operated at RU phase (engine operating conditions same as stage 2) for 15 minutes to achieve similar stable temperature as stage 2 loading condition before switching to the passive oxidation phase. Following the RU phase, the engine was operated at the passive oxidation test conditions (engine speed and load at which there is a significant PM, NO_2/NOx ratio and temperatures > 300°C) for a pre-determined duration and at the temperatures listed in Table 3.3. Upon completion

of the passive oxidation phase, the engine was operated at stage 3 loading conditions (engine conditions are the same as stages 1 and 2) for thirty minutes and then the filter was weighed to determine the PM loading in the CPF. Then the test was continued further with stage 4 loading for sixty minutes and then the filter was weighed again to determine post loading weight of the filter. The weighing process was carefully followed to minimize the variation in PM loading during weighing and also avoid any potential damage to the PM cake within the filter. Any change in the PM cake structure during weighing could result in change in the pressure drop trend in the subsequent loading process. There was not change in the pressure drop observed after weighing process. All the experiments followed similar procedure. The experimental data from these tests (temperature distribution, PM loading and pressure drop) are used in this study for the development of cake permeability model and for the analysis of the kinetic parameters of the model for NO_2 assisted PM oxidation, calibration of heat transfer to ambient and heating and cooling of the filter.

3.3 Active Regeneration Experiments

An overview of active regeneration experimental test procedure is shown in Figure 3.2. The CPF clean out phase, stage 1-2 loading, RU of fifteen minutes and stages 3-4 loading are similar to the passive oxidation experimental data. In the RU, the engine was operated at stage 2 loading conditions for fifteen minutes or until the DOC inlet temperature has stabilized at 265 ± 10^oC. Then the active regeneration ramp phase occurs for ten minutes or until the DOC inlet temperature has stabilized at 325 ± 10^oC . This to stabilize the CPF temperature prior at the temperature at which light-off can occur of the ignited fuel to achieve active regeneration temperature conditions. The active regeneration stage was continued for a predetermined amount of time at the specified CPF inlet temperatures listed in Table 3.4. If the active regeneration was allowed to continue for a longer period of time other than the specified durations in Table 4, then there would not be enough PM within the CPF to obtain an accurate measurement of PM mass retained and consequently accuracy of the calculation for the rate of PM oxidation will be affected.
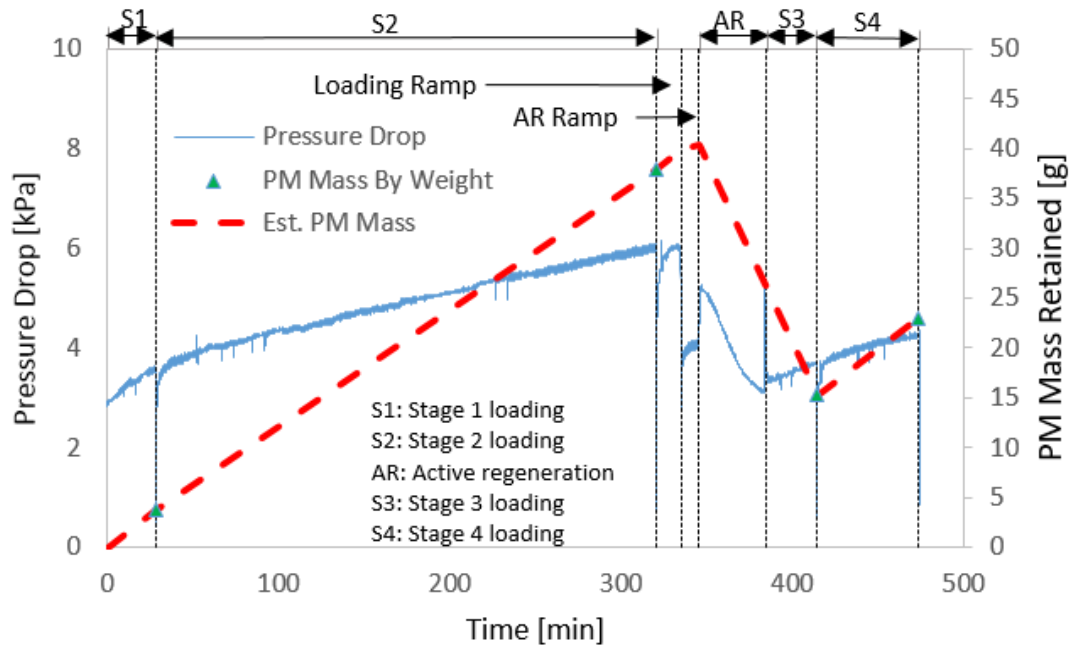
Figure 3. 2 Overview of the various stages of the typical active regeneration experiment [52] - Reprinted with permissions from SAE International, SAE Paper No. 2013-01-0521.

3.4 CPF Temperature Distribution Data

Having temperature distribution data is critical for this research for the calibration of the SCR-F/CPF model since predicting temperature distribution within the CPF is one major contribution from this research work. The experimental temperature distribution data were collected from the experimental experiments described in references [49, 51]. For each of the eighteen experiments in this study, temperature distribution within the CPF was measured using sixteen ungrounded K type thermocouples to determine temperature distribution within the filter during each test. These data were used for the heat transfer model calibration and validation of the SCR-F/CPF model. Figure 3.3 shows the thermocouple layout used for the CPF temperature distribution measurement. The thermocouples C1 to C8 were installed on the inlet channel gas flow paths and the thermocouples C9 to C16 were installed on the outlet channel gas flow paths.
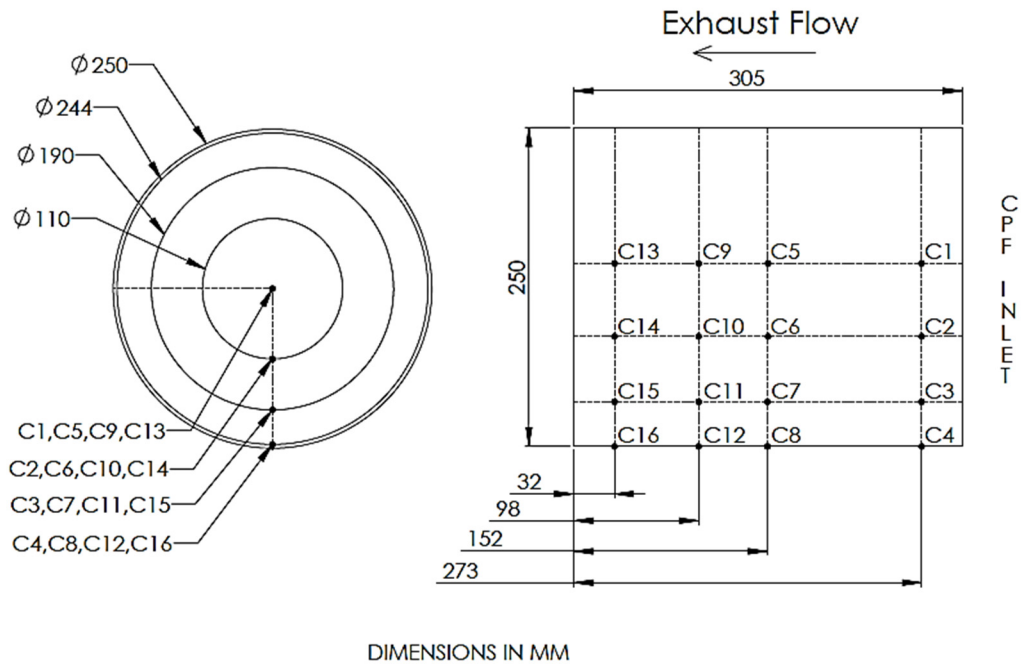
Figure 3. 3 Thermocouple layout used for the CPF temperature distribution measurement [52] - Reprinted with permissions from SAE International, SAE Paper No. 2013-01-0521.
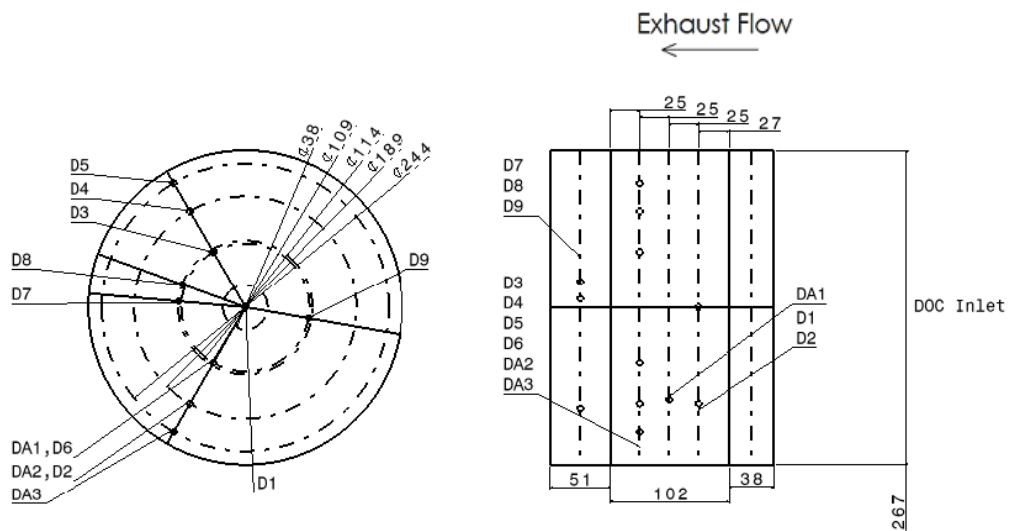
Figure 3. 4 Thermocouple layout used for the DOC temperature measurement [52] -- Reprinted with permissions from SAE International, SAE Paper No. 2013-01-0521.

The detailed specifications of the thermocouples are shown in Table 3.5.

Table 3. 5 Thermocouple specifications [49, 51]

Location	Type	Diameter (mm)	Length(s) (mm)	Watlow P/N	Body Material
DOC	K	0.508	304.8,431.8	AX1078701, PT-227664-001	Inconel
CPF	K	0.8128	304.8,431.8	AX1078801, Special Order	Inconel
Engine Exhaust	K	3.175	152.5	ACGF00Q060U40000	Inconel

The CPF thermocouples were placed at four axial locations (at a distance of 32, 98,152 and 273 mm respectively from the end of the filter) and four radial locations (at diameters of 0,110,190 and 244 mm) as shown in Figure 3.3. The thermocouples C1 to C8 were installed on the inlet channel gas flow paths and the thermocouples C9 to C16 were installed on the outlet channel gas flow paths. The temperature distribution measured by thermocouples (C1-C16) for AR-B10-1 experiment at 5.63 hrs (15 minutes after fuel dosing) is shown in Figure 3.5 [1]. Figure 3.6 shows the radial temperature distribution measured by thermocouples C1-C4 during the entire test duration.
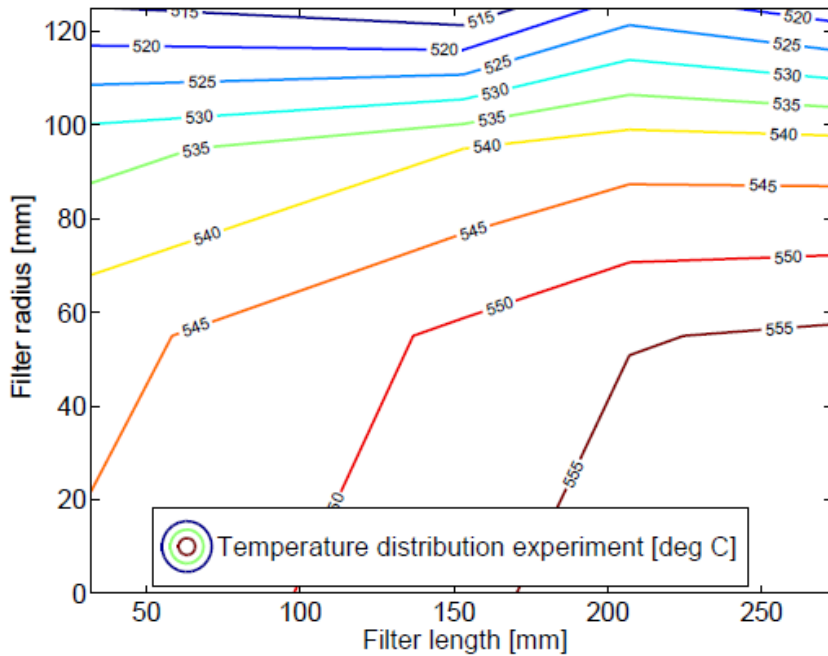
Figure 3. 5 Measured CPF temperature distribution during AR-B10-1 experiment at 5.63 hrs (15 minutes after fuel dosing)
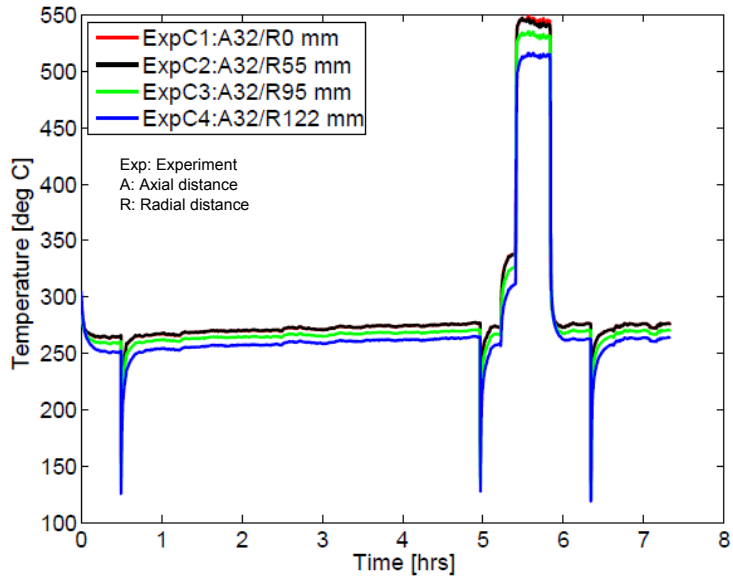
Figure 3. 6 Measured CPF temperature distribution during AR-B10-1 experiment for thermocouples C1-C4

From Figures 3.5 and 3.6, for active regeneration experiments, the temperatures are varying in both the axial and radial directions. The radial variation of temperature is comparatively higher (up to 40°C) than the axial variation in temperature (up to 12°C).
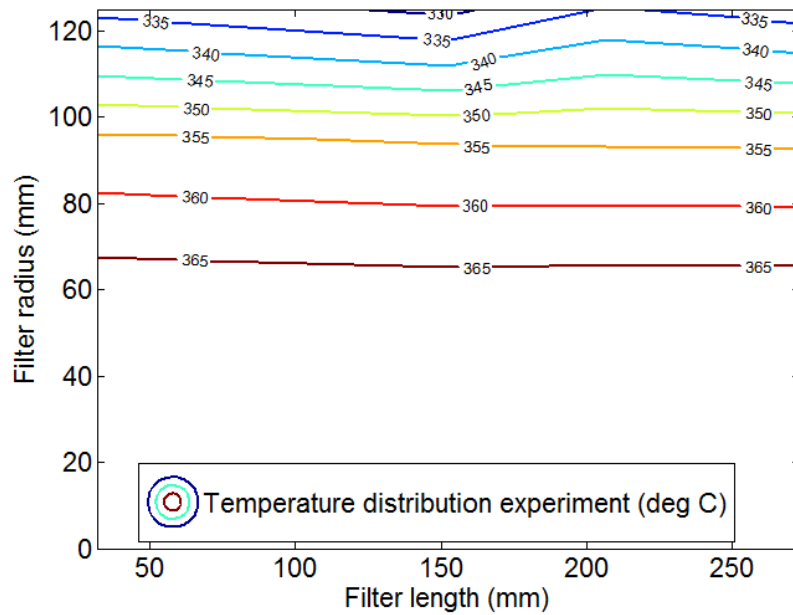
Figure 3. 7 Measured CPF temperature distribution during PO-B10-15 experiment at 4.36 hrs (15 minutes after fuel dosing)
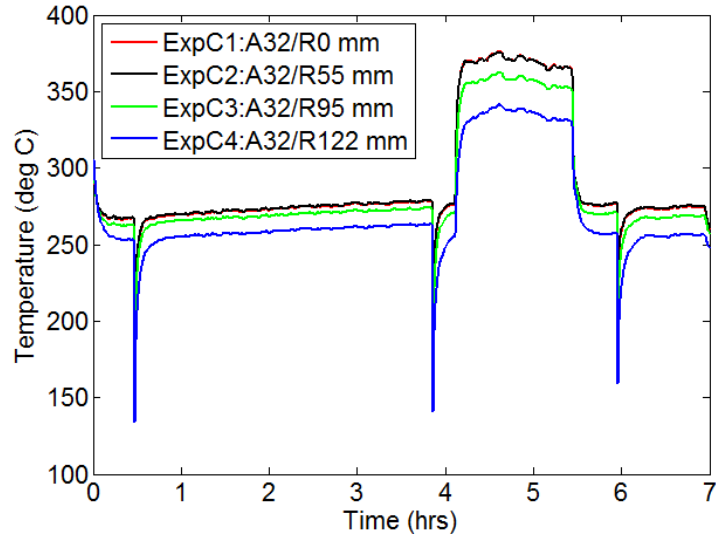
Figure 3. 8 Measured CPF temperature distribution during PO-B10-15 experiment for thermocouples C1-C4

Figure 3.7 shows the temperature distribution measured by thermocouples (C1-C16) for PO-B10-15 experiment at 4.36 hrs (15 minutes after fuel dosing). Figure 3.8 shows the radial temperature distribution measured by thermocouples C1-C4 during the entire test duration. From Figures 3.7 and 3.8, for the passive oxidation experiment, the radial variation of temperature is up to 32°C whereas the axial variation in temperature is very small and it is up to 2°C. The radially decreasing temperature is attributed to external ambient heat transfer of the filter and inlet flow/temperature maldistribution and the axially increasing temperature is attributed to the oxidation of PM and hydrocarbons (HC) within the filter during active regeneration along with the heat transfer. The axial increase in temperature is low for passive oxidation due to lower rate of PM and HC oxidation compared to active regeneration. Without the PM and HC oxidation, the temperature would drop axially due to the ambient heat transfer.

3.5 Temperature Distribution at Filter Inlet

The temperature profile at the inlet of the CPF is not constant across the radial direction for the data in Figures 3.5, 3.6, 3.7 and 3.8. This is mainly because of the thermal boundary layer development in the upstream of exhaust pipes and the DOC. The thermal boundary layer develops when the exterior surface of the pipe is exposed to a different temperature than the fluid flowing through the pipe along with a thermal resistance between the exhaust gas flow and the external ambient. If the air temperature of outer surface is lower than the

exhaust gas temperature, then the temperature of the exhaust gas in contact with the inner surface reduces and causes a subsequent drop in temperature of the exhaust gas in other regions of the pipe. This leads to the development of thermal boundary layer (similar to velocity boundary layer).

The radial temperature distribution at the inlet of the filter is affected by the thermal boundary layer development as explained in references [16, 53, 54, 55]. In order to account for the thermal boundary layer development, the empirical temperature factor profile is determined by analyzing experimental data from the eighteen runs.

For a fully developed flow, the temperature factor shown below is constant across the length (temperature profile is constant). Hence from the reference [53]

$$\frac{\partial}{\partial x}\left[\frac{T_s x - T(r,x)}{T_s(x) - T_m(x)}\right] = 0 \qquad (3.1)$$

$$Temperature\ Factor = \frac{T_s - T_r}{T_s - T_m} = C \qquad (3.2)$$

where,

T_m = Mean exhaust gas temperature

T_s = Wall inner surface temperature

T_r = Temperature at a given radial location

x = Axial location.

For this modeling work, the temperature factor at the inlet of CPF was determined by analyzing the C1, C2, C3 and C4 thermocouple measurements. Figure 3.9 shows the temperature factor calculated using Equation (3.2) for all eighteen runs at 0.42 hrs. The x axis is the CPF diameter ratio, 0 means center of the filter and 1.0 means outer diameter of the filter. The 3rd order polynomial equation was used as the curve fit to represent the temperature factor for a given diameter ratio of the CPF and it is given as

Temperature Factor (x) = -2.493x³ + 1.0585x² - 0.3285x + 1.7631 $\qquad$ (3.3)

where x is the diameter ratio at a given location.

The diameter ratio is the ratio of CPF diameter at a given measurement location to the maximum CPF diameter. From Figure 3.9, the temperature factor is almost constant up to CPF diameter ratio of 0.4 (indicating uniform temperature) and drops to 0 value (minimum

temperature) at the CPF diameter ratio of 1.0 (outer radius of the filter). The maximum gradient in the temperature factor is observed at the CPF diameter ratio of 0.8 to 1.0, attributing that 50% of the radial temperature reduction is in the 20% of the filter section close to the outer radius of the filter. From Appendix A, the minimum substrate temperature at the outer surface (R = 133 mm) is 4.3% lower than the mean substrate temperature at the inlet ($\frac{T_m}{T_s} = 1.043$).
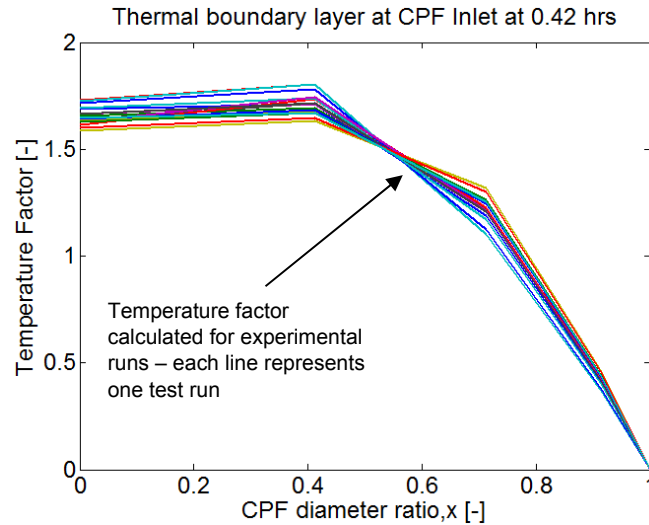
Figure 3. 9 Temperature factor profile at filter inlet for all eighteen runs at 0.42 hrs

The detailed procedure for developing the thermal boundary layer temperature factor and other coefficients used in the SCR-F/CPF model are explained in Appendix A. Using the Equations (3.2) and (3.3) and knowing the temperature at one radial location/zone of the CPF inlet, the temperatures at the other radial locations can be determined. The SCR-F/CPF model uses one CPF inlet temperature sensor data to develop thermal boundary layer profile for the remaining zones at the CPF inlet. The CPF inlet temperature was defined as the average of D7, D8 and D9 thermocouples installed at the outlet of the DOC at a diameter of 109 mm, as shown in Figure 3.4.

The experimental data in this section will be used to develop the pressure drop model including the cake permeability model and analysis of the PM kinetics (NO_2 assisted and thermal O_2) for three different fuel types, calibration of the heat transfer from filter to ambient and heating and cooling of the filter. The detailed model development, calibration and validation with the experimental data are explained in the next chapter.

4 SCR-F/CPF High Fidelity Model Development[1]

In this chapter, a high-fidelity SCR-F/CPF multi-zone model developed to predict the temperature and PM mass distribution of the CPF, pressure drop across the CPF and species concentration at each zone and at the outlet of the CPF is presented. The temperature distribution of the CPF is simulated using the filter temperature model, PM mass retained and distribution was simulated using the PM filtration and oxidation models, CPF delta pressure was simulated using the pressure drop model that includes newly developed cake permeability model and species concentration at each zone and outlet of the CPF was simulated using the species concentration model. The detailed equations used in each of the sub-model are explained in this Chapter.

The high-fidelity SCR-F/CPF model developed in this thesis is an extension of the 0-D lumped models developed by Kladopoulou et al. [9], Johnson et al. [56] and 1-D model developed by Premchand [23]. The initial version of the multi-zone particulate filter model was designed and developed to simulate temperature and PM mass distribution and pressure drop of the CPF and published in references [1, 2,3] as a part of this PhD thesis. This multi-zone particulate filter model was used as the basis for the development of high-fidelity SCR-F/CPF model with new architecture to improve computational speed intended for design applications as a replacement for complex CFD tools. The high-fidelity SCR-F/CPF model was designed to model the SCR catalyst on a DPF which is being developed by Venkata Chundru through his PhD thesis work. The species concentration solver and the improved temperature solver used in this thesis work was developed by Venkata Chundru as part of SCR-F model development.

The high-fidelity SCR-F/CPF model developed in this thesis uses the resistance node methodology developed by Depcik et al. [13] and the CPF is modeled as a user configurable number of axial and radial zones as shown in Figure 4.1. Figure 4.1 shows the schematic of the 4x4 zone model. The results presented in this chapter used the 10x10 zone version of the SCR-F/CPF model.

---

[1] Parts of the material contained in this chapter are based on references [1, 2,3] with permission of Springer.

R = Radius of the filter
L = Length of the filter
r1,r2,r3 and r4 = Radial distance of each zone from centerline
$\Delta r1, \Delta r2, \Delta r3$ and $\Delta r4$ = Effective zone radius
$\Delta L1, \Delta L2, \Delta L3$ and $\Delta L4$ = Effective zone length
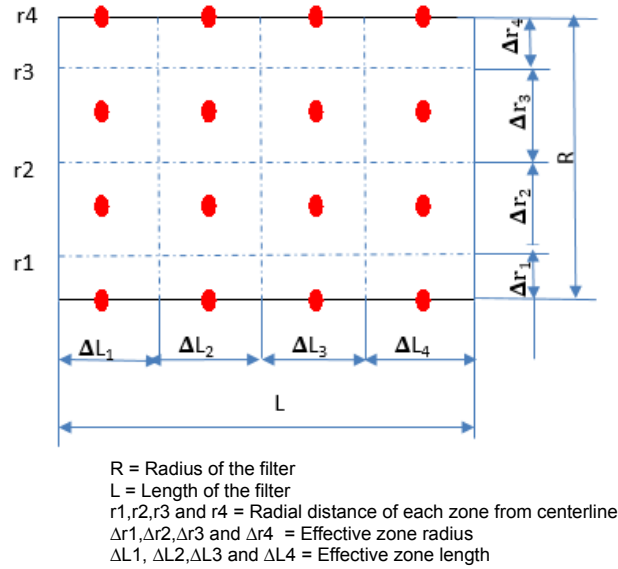
Figure 4. 1 4x4 Multi-zone CPF model schematic

The filter and gas energy equation is employed at each zone. The energy equation considers the heat transfer within the filter and external to the filter through convection, conduction and radiation heat transfer. The energy equation also includes the heat transfer to the packing material and metal can. The model also takes into account of the inlet temperature distribution assuming the fully developed boundary layer at the inlet of the CPF as explained in Chapter 3. The coefficients used for generating the temperature profile at the inlet of the filter are explained in Appendix A. The model accounts for the PM filtration and oxidation within the substrate wall and PM cake separately in each zone along with the cake permeability. The PM oxidation considers PM oxidation by thermal (O_2) and NO_2 assisted mechanisms using inlet O_2 and NO_2 concentrations. With the inclusion of species concentration solver at each zone, the reactions in the catalyst wash coat and substrate walls are also accounted. The reactions in the catalyst washcoat and substrate wall provide additional NO_2 for PM oxidation. Hence, the PM oxidation equations also accounts for the back diffusion of the NO_2 in to the PM cake layer.

The model also accounts for the HC emissions oxidation which are assumed to be within the filter. The pressure drop across the filter was calculated using the packed bed filtration theory [15]. The pressure drop model used in the SCR-F/CPF model account for the PM filtration in the wall and cake, variable wall and cake permeability accounting for the

changes in the mean free path length of the gas and permeability evolution of PM cake during PM oxidation and post loading using the newly developed cake permeability model [3]. The outputs of the high fidelity CPF model are temperature distribution within the filter substrate, inlet and outlet channels, total PM mass retained including masses in the cake and wall, PM loading distribution within the filter, species concentration at the filter outlet (NO, NO_2, CO, CO_2, O_2, HC, and PM concentration) and pressure drop across the filter. The model assumptions are outlined as follows:

1. The inlet PM deposits uniformly over the entire volume of the filter substrate.
2. The PM inlet rate into the each zone is assumed to be the ratio of volume of each zone to the total volume of the filter. In other words, no maldistribution of inlet PM is considered.
3. Species reactions are instantaneous (quasi-steady).
4. Species concentrations (O_2 and NO_2) are assumed to be uniform in the inlet channel and are equal to inlet concentrations.
5. Species concentrations at the outlet channel are equal to the concentration at the wall-outlet channel interface.
6. PM cake layer and substrate wall are at the same temperature. In other words, no temperature gradients across the PM cake layer and substrate wall are considered.
7. A fully developed boundary layer exists at the inlet of the CPF.
8. The exhaust gas mixture is assumed to be an ideal gas.
9. The exhaust gas has the same properties as air at 1 atmosphere pressure. Properties are considered as a function of temperature. CPF inlet species concentrations (CO_2, O_2, N_2 and H_2O) are used for the calculation of molecular weight of the exhaust gas.

4.1 Model Discretization

Discretization of the filter volume is done in both the axial (ΔL) and radial directions (Δr) as shown in Figure 4.1. Figure 4.2 shows the physical representation of the CPF channels with uniform deposition of PM in the cake layer along the walls of inlet channel. In the SCR-F/CPF model, the full volume of the filter is discretized into a user configurable number of axial and radial zones. Each zone is comprised of multiple inlet and outlet channels. The schematic representation of the channel geometry for each zone is shown

in Figure 4.3. Each zone consists of the filter substrate, PM cake and empty volume for inlet and outlet channels.
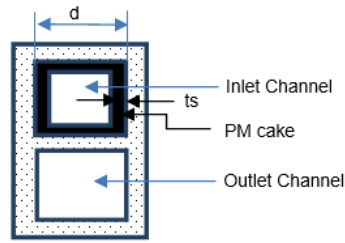
ts = Thickness of the cake layer, d = Channel width

Figure 4. 2 Schematic of the CPF channel geometry with the PM cake layer
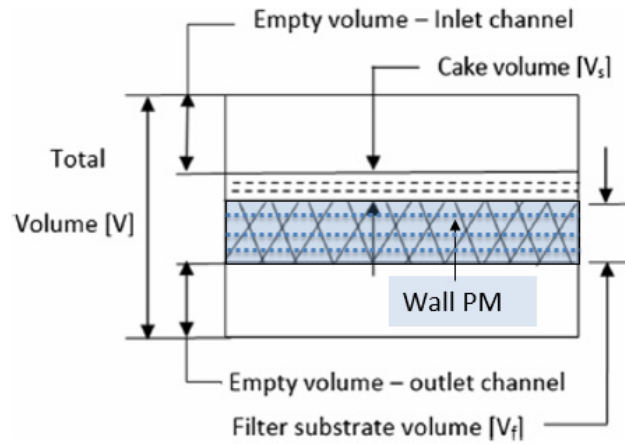
Figure 4. 3 Schematic for a zone of the SCR-F/CPF model with PM in the cake and wall

4.2 Filter Temperature Model

The energy stored in the filter is due to a) the heat conduction along the length of the filter ($\dot{Q}_{cond.axial}$), b) heat conduction along the radial direction of the filter ($\dot{Q}_{cond.radial}$), c) convection between the filter and the channel gas ($\dot{Q}_{conv}$), d) energy released during the oxidation of the PM cake ($\dot{Q}_{reac,PM}$), e) energy released during oxidation of the HC in the inlet channel gas ($\dot{Q}_{reac,HC}$) f) enthalpy transfer by the wall-flow gas ($\dot{Q}_{wall-flow}$) and g) heat transfer due to radiation exchange between channel surfaces ($\dot{Q}_{rad}$).

Hence the energy equation for the filter is:

$$(\rho_s c_s V s_{i,j} + \rho_f c_f V_{f_{i,j}}) \frac{dTf_{i,j}}{dt} =$$

$$\dot{Q}_{cond.axial} + \dot{Q}_{cond.radial} + \dot{Q}_{conv} + \dot{Q}_{reac,PM} + \dot{Q}_{reac,HC} + \dot{Q}_{rad} \tag{4.1}$$

where, Tf is the filter substrate temperature.

The detailed formulation for the terms used in Equation (4.1) is explained in Appendix B.

The convection heat transfer between the filter substrate and the channel gas is calculated using the following equation [17]:

$$\dot{Q}_{conv} = u_{wall\ i,j} \rho_{i,j} c_p A(Tf_{i,j} - T_{inlet\ i,j}) + h_g As_{i,j} (T_{outlet\ i,j} - T_{inlet\ i,j}) \Delta_j \tag{4.2}$$

where, $u_{wall\ i,j}$ is the wall layer velocity at each zone, $\rho_{i,j}$ is the density of the gas at each zone, c_p is the specific heat of the gas, A is the heat transfer area normal to the gas flow, $T_{inlet\ i,j}$ is the temperature of gas at the inlet channel at each zone, $T_{outlet\ i,j}$ is the temperature of the gas at the outlet channel at each zone, h_g is the convective heat transfer coefficient between channel gas and wall surface, $As_{i,j}$ is the combined surface area of the inlet and outlet channels at each zone and Δ_j is the axial discretization length at each zone.

The filter temperature model presented in this thesis used the improved temperature model developed by Venkata Chundru [57] as part of his PhD research. Figure 4.4 shows the schematic of the temperature solver mesh used for the SCR-F/CPF model.
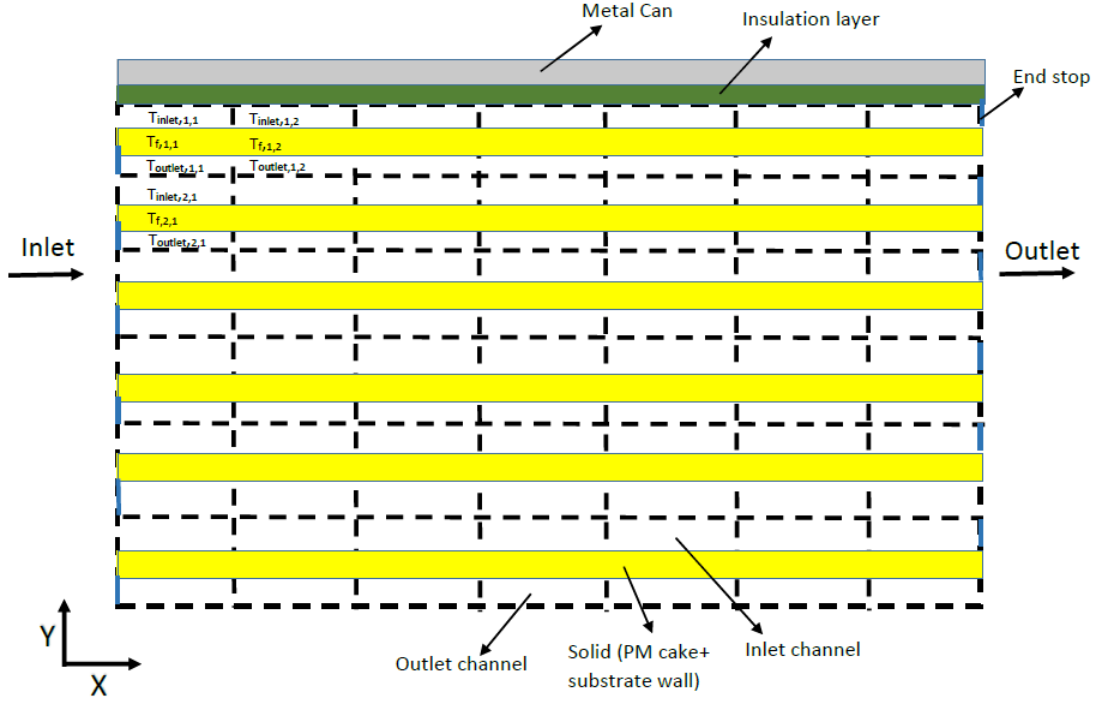
Figure 4. 4 Schematic of temperature solver mesh for SCR-F/CPF model [57]

From Figure 4.4, the new temperature solver model discretizes the each zone in to separate control volumes for inlet channels, filter and outlet channels. The filter energy equations are applied at the inlet channels (Equation 4.3), filter (Equation 4.1) and outlet channels (Equation 4.4). The model also takes in to the account of thermal resistance of the insulation and metal can. The detailed formulation of equations used for the thermal resistance calculations are explained in Appendix B.

The inlet channel energy equation is given as [17,57]:

$$\rho_{i,j} c_p V_{inlet} \frac{dT_{inlet\ i,j}}{dt} = u_{inlet\ i,j-1} \rho_{i,j-1} c_p A T_{inlet\ i,j-1} - u_{inlet\ i,j} \rho_{i,j} c_p A T_{inlet\ i,j} -$$
$$u_{wall\ i,j} \rho_{i,j} c_p A\ T_{inlet\ i,j} + h_g A s_{i\ i,j}\ (Tf_{i,j} - T_{inlet\ i,j}) \Delta_j \qquad (4.3)$$

where, V_{inlet} is the inlet channel volume, $u_{inlet\ i,j}$ is the inlet channel velocity and $T_{wall\ i,j}$ is the substrate temperature at each zone.

Similarly, the outlet channel energy equation is [17,57]:

41

$$\rho_{i,j}c_pV_{outlet}\frac{dT_{outlet\ i,j}}{dt} = u_{outlet\ i,j-1}\rho_{i,j-1}c_pAT_{outlet\ i,j-1} - u_{outlet\ i,j}\rho_{i,j}c_pAT_{outlet\ i,j} -$$

$$u_{wall\ i,j}\rho_{i,j}c_pA\ T_{outlet\ i,j} + h_gAs_{o\ i,j}\ (Tf_{\ i,j} - T_{outlet\ i,j})\Delta_j \qquad (4.4)$$

where, V_{outlet} is the outlet channel volume, $u_{outlet\ i,j}$ is the inlet channel velocity and $Tf_{\ i,j}$ is the substrate temperature at each zone.

The convective heat transfer coefficient (h_g) is calculated using the fully developed Nusselt number correlation based on the flow Peclet number and Reynolds number through the wall for a square channel configuration. Depcik et al. [58] determined Nusselt number correlations from the historical references for Prandtl number of 0.72 (approximately air). Recently, Bissett et al. [59] and Kostoglou et al. [60] derived Nusselt number correlation for wall-flow monoliths for the parameter range applicable for the diesel particulate application. From reference [59], the polynomial approximations of Nusselt numbers for $Re_w < 3$ is given as:

$$Nu_{inlet} = 2.98 + 0.60Pe_w - 0.143Re_w \qquad (4.5)$$
$$Nu_{outlet} = 2.98 - 0.40Pe_w \qquad (4.6)$$

where,

Nu_{avg} = Average Nusselt number of the inlet and outlet channel

Nu_{inlet} = Nusselt number of the inlet channel

Nu_{outlet} = Nusselt number of the inlet channel

k_g = Thermal conductivity of channel gas

Pe_w = Peclet number of wall

Re_w = Reynolds number of wall

4.3 PM Filtration Model

The PM filtration takes place within the substrate wall and the cake. The high-fidelity SCR-F/CPF model accounts for the PM filtration within the substrate wall and PM cake separately. The packed bed filtration theory [15] is applied for the substrate wall and cake. In each zone, the substrate wall is discretized into n_{max} (n_{max} = 4) number of slabs (n = 1, 2, 3 and 4) as shown in Figure 4.5. The PM filtration takes place in a sequence starting

from the slab 1 through 4. Each slab is configured as a number of spherical wall collectors. The wall collector diameter grows as the PM accumulates in the wall until the maximum loaded collector diameter. When the wall collector in the first slab is filled with PM, the transition from wall filtration to cake filtration takes place.
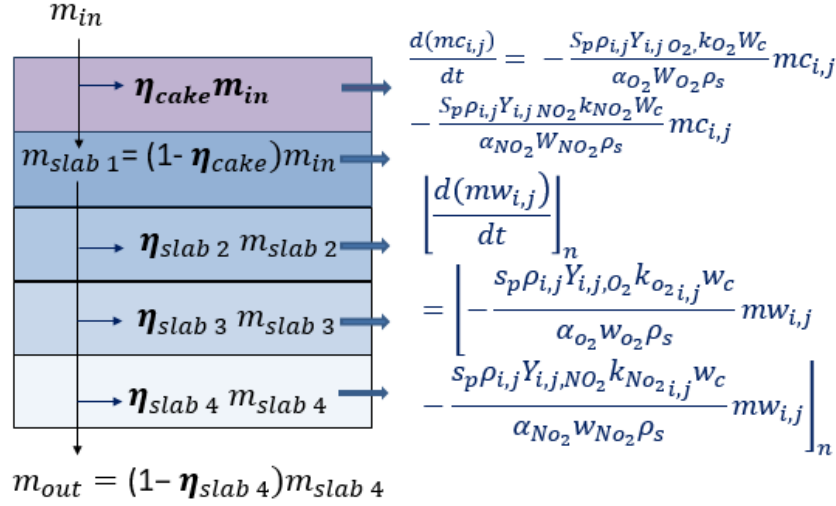
Figure 4. 5 Schematic of cake and wall filtration and PM oxidation

The overall efficiency of the filtration is equal to:

$$\eta_{total_{i,j}} = 1 - \left[(1 - \eta_{cake}) \prod_{n=1}^{n_{max}} (1 - \eta_{wall_{i,j\ slab\ n}}) \right] \tag{4.7}$$

where, $\eta_{cake_{i,j}}$ is the PM cake layer filtration efficiency and $\eta_{wall_{i,j\ slab\ n}}$ is the filtration efficiency of the each slab in the substrate wall. The detailed formulation of terms used in eqn. (4.7) is included in Appendix C and references [22, 23].

4.4 PM Oxidation Model

The PM accumulated in the substrate wall and PM cake layer are oxidized simultaneously. The PM oxidation includes NO_2 assisted and thermal (O_2) PM oxidation reactions. The oxidation of PM in the PM cake layer is equal to:

$$\frac{d(mc_{i,j})}{dt} = -\frac{s_p \rho_{i,j} Y_{i,j,O_2} k_{O_2\,i,j} W_c}{\alpha_{O_2} W_{O_2} \rho_s} mc_{i,j} - \frac{s_p \rho_{i,j} Y_{i,j,NO_2} k_{NO_2\,i,j} W_c}{\alpha_{NO_2} W_{NO_2} \rho_s} mc_{i,j} \tag{4.8}$$

where, $mc_{i,j}$ is the PM mass in the PM cake layer at each zone, s_p is the specific surface area of PM, $\rho_{i,j}$ is the density of the gas at each zone, Y_{i,j,O_2} is the mass fraction of inlet O_2 at each zone, Y_{i,j,NO_2} is the mass fraction of inlet NO_2 at each zone, $k_{O_2\,i,j}$ is the reaction rate constant for thermal (O_2) PM oxidation, $k_{NO_2\,i,j}$ is the reaction rate constant for the NO_2 assisted PM oxidation, W_c is the molecular weight of the carbon, W_{O_2} is the molecular weight of the oxygen, W_{NO_2} is the molecular weight of the NO_2, α_{O_2} is the O_2 oxidation partial factor and α_{NO_2} is the NO_2 oxidation partial factor.

Similarly, the PM mass reduction due to oxidation in each slab of the substrate wall is equal to:

$$\left|\frac{d(mw_{i,j})}{dt}\right|_n = \left|-\frac{s_p \rho_{i,j} Y_{i,j,O_2} k_{O_2\,i,j} W_c}{\alpha_{O_2} W_{O_2} \rho_s} mw_{i,j} - \frac{s_p \rho_{i,j} Y_{i,j,NO_2} k_{NO_2\,i,j} W_c}{\alpha_{NO_2} W_{NO_2} \rho_s} mw_{i,j}\right|_n \qquad (4.9)$$

where, $\left[mw_{i,j}\right]_n$ = PM mass in the nth slab of the substrate wall at each zone. The detailed formulation of terms used in equation 4.9 is explained in Appendix B.

4.5 Pressure Drop Model

The total pressure drop in the CPF is the sum of the pressure drops due to the substrate wall, PM cake layer and the frictional losses in the inlet and outlet channels. During CPF loading, the PM is initially accumulated in the substrate wall (deep bed filtration) and next a PM cake layer grows over the top surfaces of the substrate wall. The PM mass within the substrate wall and PM cake layer changes during loading, PM oxidation and post loading phases of the experiment. This affects the pressure drop of the substrate wall and the PM cake layer. In order to predict the PM retained and oxidation in the filter wall and PM cake layer, the PM filtration and PM oxidation sub-models are developed.

4.5.1 Wall and Cake Pressure Drop

The pressure drop due to the substrate wall and the PM cake layer using Darcy's flow equation is given as:

$$\Delta P_{wall_{i,j}} = \mu_{i,j} v_{w_{i,j}} \frac{w_s}{k_{wall_{i,j}}} \qquad (4.10)$$

and

$$\Delta P_{cake_{i,j}} = \mu_{i,j} v_{s_{i,j}} \frac{w_{p_{i,j}}}{k_{cake_{i,j}}}$$ (4.11)

where, $\Delta P_{wall_{i,j}}$ is the pressure drop due to the substrate wall at each zone, $\Delta P_{cake_{i,j}}$ is the pressure drop due to the PM cake at each zone, $\mu_{i,j}$ is the dynamic viscosity of the exhaust gas at each zone, $v_{w_{i,j}}$ is the velocity of gas through the substrate wall at each zone, $v_{s_{i,j}}$ is the velocity of gas through the PM cake layer at each zone, w_s is the substrate wall thickness, $w_{p_{i,j}}$ is the PM cake layer thickness at each zone, $k_{wall_{i,j}}$ is the wall permeability at each zone and $k_{cake_{i,j}}$ is the PM cake layer permeability at each zone. The detailed formulations of terms used in equations 4.10 and 4.11 are explained in Appendix B and C.

4.5.2 Channel Pressure Drop

The inlet and outlet channel absolute pressure values are calculated using the discretized axial momentum equations developed by Premchand [23] by assuming the exit pressure of the gas at the outlet of CPF is equal to the barometric pressure. The absolute pressure at the inlet and outlet channels of CPF at each zone is given as [23]:

$$P_1|_{i,j} = P_1|_{i,j+1} + \rho v_1{}^2|_{i,j+1} - \rho v_1{}^2|_{i,j} + F\Delta x \frac{\mu v_1}{a^2} \left(\frac{a*}{a}\right)^2 |_{i,j}$$ (4.12)

$$P_2|_{i,j} = P_2|_{i,j+1} + \rho v_2{}^2|_{i,j+1} - \rho v_2{}^2|_{i,j} + F\Delta x \frac{\mu v_2}{a^2} |_{i,j}$$ (4.13)

where, $P_1|_{i,j}$ is the absolute pressure at the inlet channel of each zone, $P_2|_{i,j}$ is the absolute pressure at the outlet channel of each zone, v_1 is the velocity of the gas through inlet channel, v_2 is the velocity of the gas through the outlet channel, F is the friction factor, Δx is the axial discretization length, $a*$ is the effective width of the inlet channel loaded with PM and a is the width of the clean outlet channel.

The pressure drop across each axial section of the CPF is given as

$$\Delta P_{CPF,i} = [P_1|_{x=0} - P_2|_{x=l}]_i$$ (4.14)

The total pressure drop across the CPF is given as

45

$$\Delta P_{CPF} = \frac{\sum_{s1}^{smax} \sum_{i=1}^{i=imax} VF_i \Delta P_{CPF,i}}{smax}$$
(4.15)

where, ΔP_{CPF} is the average pressure drop across the CPF based on different volumetric exhaust flow rates in each radial section of the CPF, $imax$ is the maximum number of axial discretization in the model, VF_i is the volume fraction of exhaust gas flow at each radial section of the CPF and $smax$ is the number of ways of obtaining the absolute pressure at the inlet of the inlet channel ($P_1|_{i,j+1}$) at each radial section of the filter using the stream lines approach as explained in Appendix C. The detailed formulation of the pressure drop model is provided in Appendix C.

Wall Permeability Model

The substrate wall permeability changes during loading due to the oxidation of PM in the pores of substrate wall that changes the wall collector diameter. The permeability change due to the change in collector diameter is given as [61]:

$$\left[k_{s_{i,j}}\right]_{slab\ n} = \left[k_{0,s} \left(\frac{d_{c,s_{i,j}}}{d_{c0,s}}\right)^2 \left(\frac{f(\varepsilon_{s_{i,j}})}{f(\varepsilon_{0,s})}\right)\right]_{slab\ n}$$
(4.16)

where, $k_{0,s}$ is initial permeability of the clean substrate wall, $k_{s_{i,j}}$ is the current permeability of the substrate wall due to the change in collector diameter in each zone, $d_{c,s_{i,j}}$ is the loaded collector diameter at each zone, $d_{c0,s}$ is the clean collector diameter, $f(\varepsilon_{s_{i,j}})$ is the Kuwabara geometric function of porosity for the loaded substrate wall and $f(\varepsilon_{0,s})$ is the Kuwabara geometric function of porosity for the clean substrate wall.

From eqn. (4.16), the wall permeability is minimum ($k_s = k_{0,s}$) when the filter is clean and increases proportional to the square of the change in wall collector diameter and porosity as the PM accumulates in the wall collector. Similarly, the wall permeability increases during PM oxidation as the PM in the wall collector is oxidized leading to a reduction in wall collector diameter and porosity. The change in porosity (ε_s) is given as [61]:

$$\left[\varepsilon_{s_{i,j}}\right]_{slab\ n} = \left[1 - \left(\left(\frac{dc_{s_{i,j}}}{dc_{0,s}}\right)^3 (1 - \varepsilon_{0,s})\right)\right]_{slab\ n}$$
(4.17)

where, $\varepsilon_{0,s}$ is the clean substrate wall porosity and $\varepsilon_{s_{i,j}}$ is the PM loaded porosity of the substrate wall due to the change in collector diameter in each zone.

46

The permeability of the gas flowing through the substrate wall also changes due to the change in mean free path length of the gas. Hence, permeability of the substrate wall correcting for the mean free path length of the gas is given as [32]:

$$k_{wall_{i,j}} = k_{s_{i,j}} \left(1 + C_4 \frac{P_o}{p} \mu \sqrt{\frac{T_{i,j}}{M_g}} \right) \tag{4.18}$$

Where, $k_{s_{i,j}}$ is the average permeability of the substrate wall accounting for the PM loading in the wall collectors of each slab at each zone and $k_{wall_{i,j}}$ is the average permeability of substrate wall accounting for the mean free path length of gas at each zone. The effect of mean free path lengths on the loaded wall permeability is mainly due to the presence of the PM particles in the pores. This effect is minimum for the clean wall considering the wall pore size compared to mean free path length of the gas.

4.5.3 Cake Permeability Model

Similar to the substrate wall permeability, the PM cake layer permeability also changes during PM loading and oxidation due to the change in mean free path length of the gas. Hence, the change in PM cake layer permeability due to the change in mean free path length of the gas is given as [33]:

$$\left[\rho_s k_p \right]_{i,j} = C_5 \frac{\lambda_{i,j}}{\lambda_{ref}} \tag{4.19}$$

where, $k_{p_{i,j}}$ is the PM cake layer permeability accounting for the changes in mean free path length of the gas at each zone, C_5 is the cake permeability correction factor, $\lambda_{i,j}$ is the mean free path length of the gas and λ_{ref} is the mean free path length of the gas at reference pressure (100 kPa) and temperature conditions (300 K).

Damage Permeability Hypothesis for PM Cake

During PM oxidation, the cake layer breaks as it is oxidized and holes and cracks are formed as visualized by former researchers [35, 36].

The increase in permeability of PM cake due to the potential damage in the cake can be modeled using a damage permeability function given in reference [39]:

$$k_{d_{i,j}} = k_{p_{i,j}} e^{\left[(\alpha_k d)^{\beta_k}\right]}$$
(4.20)

where, $k_{d_{i,j}}$ is the PM cake layer permeability accounting for the damage in the PM cake. The change in PM mass retained in the PM cake is used as the varying damage variable $\left(d = \frac{m_{cake,\,initial} - m_{cake\,corr}}{m_{cake,\,initial}}\right)$. The calibration coefficients $m_{cake,\,initial}$, $m_{cake\,corr}$, α_k and β_k are determined from the experimental data.

4.5.3.1 Development of Cake Permeability Model

For the development of cake permeability model, the experimental pressure drop values were analyzed along with the simulated pressure drop components (wall pressure drop and channel pressure drop) to estimate the average cake pressure drop during PM oxidation and post loading phases of the experiment. The direct experimental evidences such as visual evidences using the high speed imaging techniques shown in references [35-36] were not available for these experiments. However, the visual evidences in references [35-37] were correlated with the measured pressure drop, indicating the pressure drop is the direct evidence of change in cake permeability. Hence, in this work the measured total pressure drop values along with the simulate pressure drop from wall and channel pressure drop models are used to estimate the cake pressure drop and subsequent change in permeability of PM cake layer.

The main objective of the experimental analysis is to obtain the single value for the pressure drop components from the multi-zone (axial and radial zones) model so that measured average total pressure drop can be used to estimate the average cake pressure drop and cake permeability of the CPF.

The total experimental drop (ΔP_{exp}) is the sum of the substrate wall, PM cake layer and channel pressure drops and it is given as:

$$\Delta P_{exp} = \Delta P_{wall\,MPF\,model} + \mu_{avg\,gas} v_{cake\,avg} \left(\frac{w_{p\,avg}}{k_{cake}}\right) + \Delta P_{channel\,MPF\,model}$$
(4.21)

where, $\mu_{avg\,gas}$ is the average dynamic viscosity of the exhaust in the CPF, $v_{cake\,avg}$ is the average velocity of the exhaust gas through the cake layer in the CPF, $w_{p\,avg}$ is the average PM cake layer thickness in the CPF, k_{cake} is the average PM cake permeability

48

in the CPF, $\Delta P_{wall\,MPF\,model}$ is the volume weighted substrate wall pressure drop simulated by the SCR-F/CPF model and $\Delta P_{channel\,MPF\,model}$ is the total pressure of the inlet and outlet channels simulated by the SCR-F/CPF model.

From eqn. (4.21), PM cake layer pressure drop can be estimated as:

$$\Delta P_{est.\,cake} = \Delta P_{exp} - \Delta P_{wall\,MPF\,model} - \Delta P_{channel\,MPF\,model} \tag{4.22}$$

where, ΔP_{exp} is the experimentally measured total pressure drop and $\Delta P_{wall\,MPF\,model}$ is given as

$$\Delta P_{wall\,MPF\,model} = \sum_{i=1}^{i=10} VF_i \Delta P_{wall_i\,MPF\,model} \tag{4.23}$$

The average wall pressure at each radial section (ΔP_{wall_i}) of the filter from the SCR-F/CPF model is given as:

$$\Delta P_{wall_i} = \sum_{j=1}^{j=10} \frac{\mu_{i,j} v_{w_{i,j}} \left(\frac{w_{s\,i,j}}{k_{wall,\,i,j}}\right)}{10} \tag{4.24}$$

The estimated permeability of the PM cake layer at a given time step is calculated as:

$$k_{est.cake} = \frac{\mu\,v_{cake\,avg}\,w_{p\,avg}}{\Delta P_{est.\,cake}} \tag{4.25}$$

The relative change in the estimated permeability is calculated as:

$$Permeability\,ratio = \frac{k_{est.cake}}{k_{cake\,ref}} \tag{4.26}$$

Where $k_{cake\,ref}$ is the reference permeability value used for the permeability ratio calculation. Permeability ratio is a dimensionless number and it is the measure of the relative change in permeability from the reference permeability value. The reference permeability is selected to a value that provides close to 1 permeability ratio during stage 1 and 2 loading process. This is to aid analysis of the change in permeability during PM oxidation and post loading with reference to the stage 1 and 2 loading permeability values.

Figures 4.6 and 4.7 show the plots of permeability ratio calculated using Equations 4.22 to 4.26 during the passive oxidation and active regeneration experiments. From Figures

4.6 and 4.7, the permeability ratio is nearly constant for all experiments at the start of PM oxidation ($\cong$ 35 g for PO experiments and $\cong$ 36 to 42 g for active regeneration experiments) and remains constant during PM oxidation. Partly into the PM oxidation (i.e., below 31 g for PO experiments and 34 g for active regeneration experiments), the permeability ratio increases rapidly. This rapid increase in permeability is observed in all the experiments and it is attributed to damage in the PM cake layer causing increased gas flow with less pressure drop as explained in the literature section.
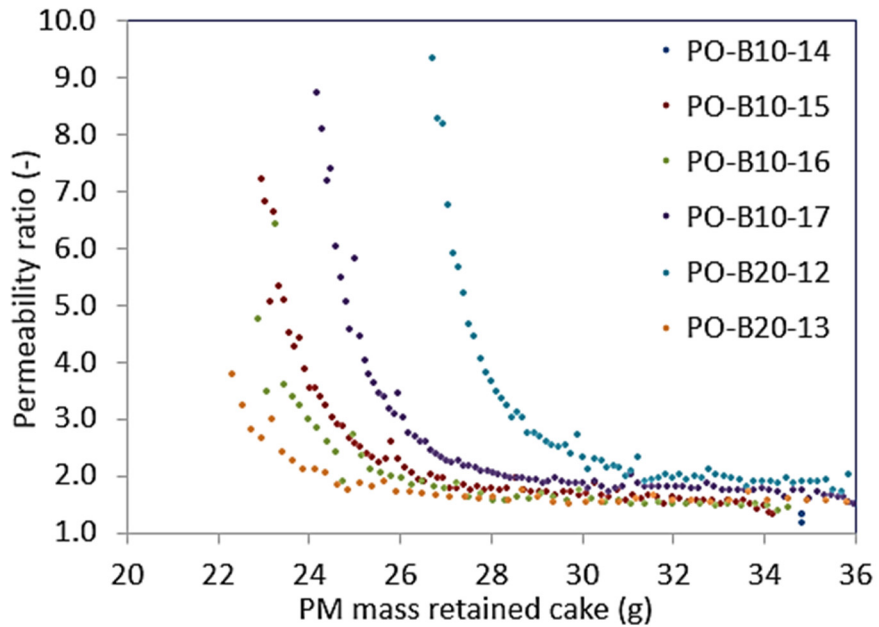
Figure 4. 6 Change in permeability ratio during the passive oxidation experiments
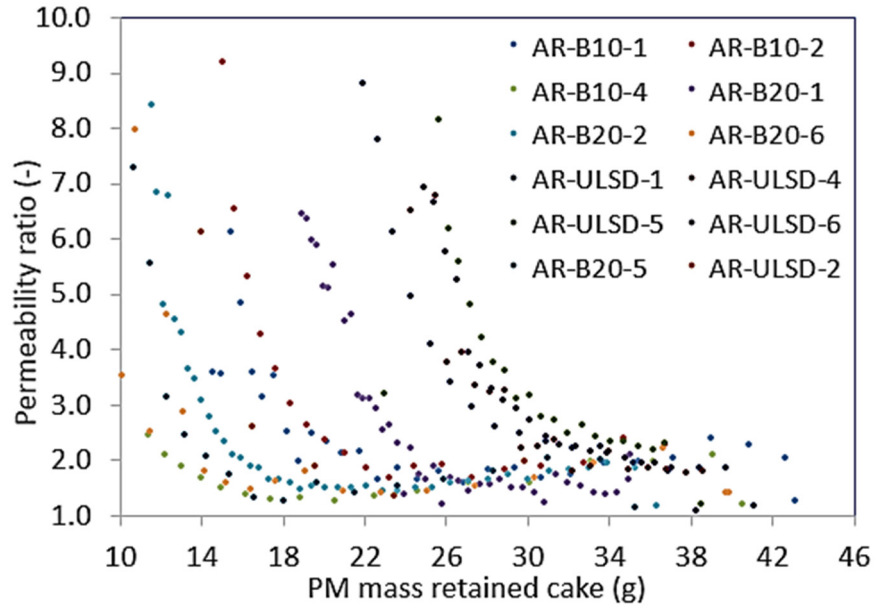
Figure 4. 7 Change in permeability ratio during the active regeneration experiments

From Figures 4.6 and 4.7, the slope of the permeability increase is also almost the same for all PM oxidation experiments indicating that the global gas flow is controlled by the similar cracks (similar sized holes, gaps and crack density) between experiments. Hence, by shifting each of the permeability curves by an x axis offset value (delta mass offset) yields one single characteristic curve which results in a single permeability ratio curve during PM oxidation for all experiments.

The PM cake permeability model developed in this work borrowed the modeling elements from the concrete permeability model developed by Picandet et al. [39]. However, there is a salient difference between the cracked concrete compared to the cracked/damage PM cake. In case of cracked concrete, the concrete slab thickness or mass is constant whereas for the PM cake the thickness and mass are dynamic variables. In case of concrete, the damage permeability model proposed by Picandet et al used the relative decrease in dynamic elastic longitudinal modulus (a dynamic variable that changes based on crack density and intensity) of a cracked concrete disc as an indicator of damage and was correlated to the increase permeability. Similarly, for the PM cake damage permeability model presented in this work, the PM cake mass retained as the damage variable coupled with PM oxidation rate as an indicator of the damaged PM cake (a set of dynamic variables that can be correlated to damage PM cake). Considering the

exponential nature of the permeability curves in Figures 4.6 and 4.7, the permeability ratio values are limited to 10 (least resistance to the flow) to avoid singularity as the PM mass retained approaches smaller values.

The delta mass offset value of the PM cake layer varies between the experiments and also based on the fuel type. Figures 4.8 and 4.9 show the delta mass offset value for the passive oxidation and active regeneration experiments for ULSD, B10 and B20 fuels. It can be attributed that the increased permeability of the PM cake layer caused by the initiation of microscopic and macroscopic cracks shows strong correlation with the PM reaction rates (time, temperature and oxidant involved in PM oxidation – NO_2 versus O_2) and hence overall PM reaction rate is used as the predictor (delta mass offset) to determine the PM cake damage initiation point in the SCR-F/CPF model. The overall PM reaction rate is given as:

$$Overall\ PM\ reaction\ rate = \frac{\sum_{i=1,j=1}^{i=imax,j=jmax}\left[\frac{sp\rho_{i,j}Y_{i,j,O_2}k_{O_2 i,j}W_c}{\alpha_{O_2}W_{O_2}\rho_s}+\frac{sp\rho_{i,j}Y_{i,j,NO_2}k_{NO_2 i,j}W_c}{\alpha_{No_2}W_{No_2}\rho_s}\right]}{imax\ jmax} \quad (4.27)$$

where, $Overall\ PM\ reaction\ rate$ is the average PM reaction rate of the CPF at each time step of the SCR-F/CPF model.

From Figures 4.8 and 4.9, the delta mass offset holds negative values at lower PM reaction rates indicating increase in PM cake permeability occurs at higher masses (early in oxidation) of the PM cake layer. Based on fuel type, experiments with ULSD fuel shows increase in PM cake permeability at higher masses of the PM cake layer compared to B10 and B20 fuels. Similarly, comparing between passive oxidation and active regeneration experiments, passive oxidation experiments show a permeability increase occurs earlier in PM cake oxidation exposure compared to the active regeneration experiments. This could be attributed to lower reaction rates associated with NO_2 assisted PM oxidation.

From the above analysis, it is assumed that the change in delta mass offset between the experiments can be attributed to the varying PM oxidation rate affected by the temperature, NO_2 and O_2 concentration in the inlet exhaust gas. At higher PM reaction rates, the PM cake layer is oxidized rapidly in a short time and allowing significant reduction in the mass of the PM cake layer before initiation of the microscopic and macroscopic cracks in the PM cake layer. At lower reaction rates, the PM cake layer

cracks are initiated at the higher mass of the PM cake layer as the cake layer is exposed to an oxidizing environment for a longer time without significant reduction in mass.
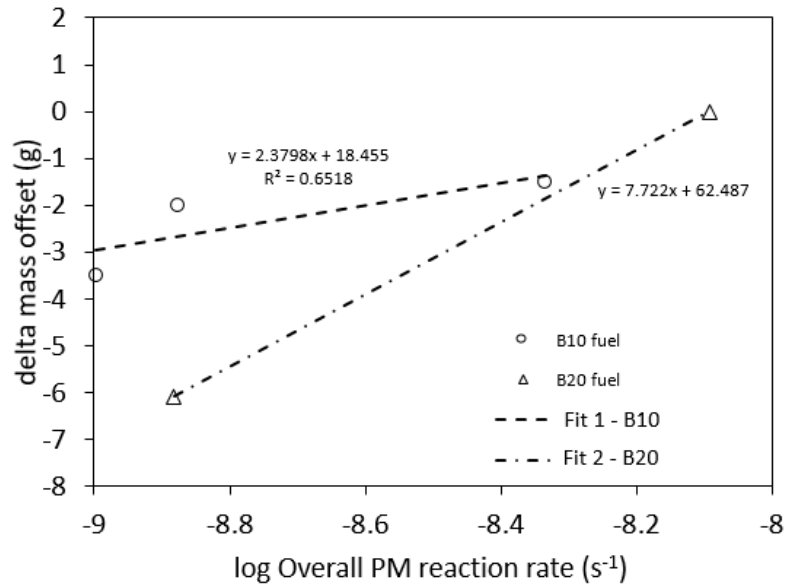
Figure 4. 8 Delta mass offset for passive oxidation experiments
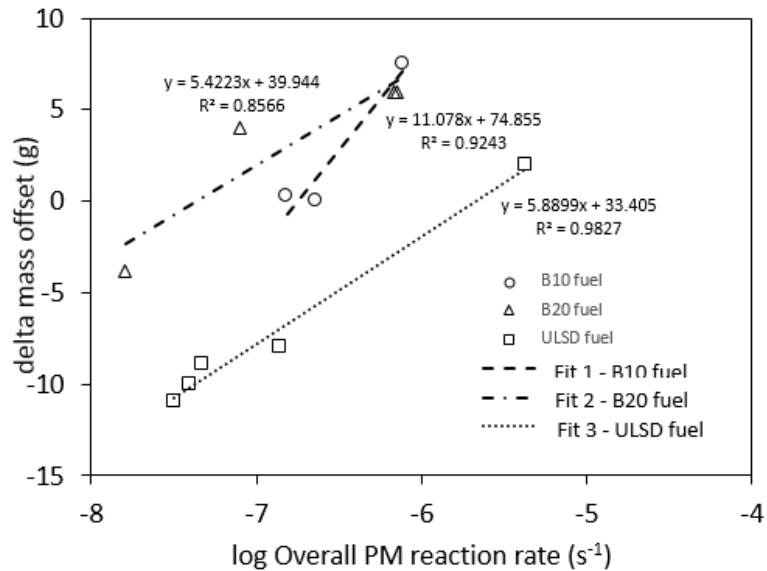
Figure 4. 9 Delta mass offset for active regeneration experiments

The delta mass offset from the above analysis is applied to each curve. Figures 4.10 and 4.11 show the resultant single set of permeability ratio curve for the passive oxidation and active regeneration experiments, respectively.
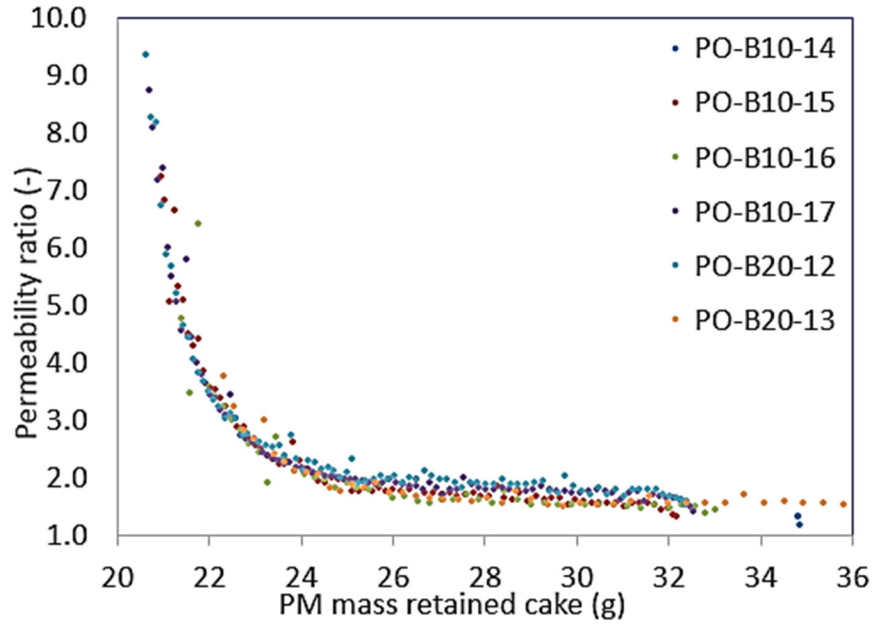
Figure 4. 10 Relative change in permeability ratio during passive oxidation experiments with delta mass offset
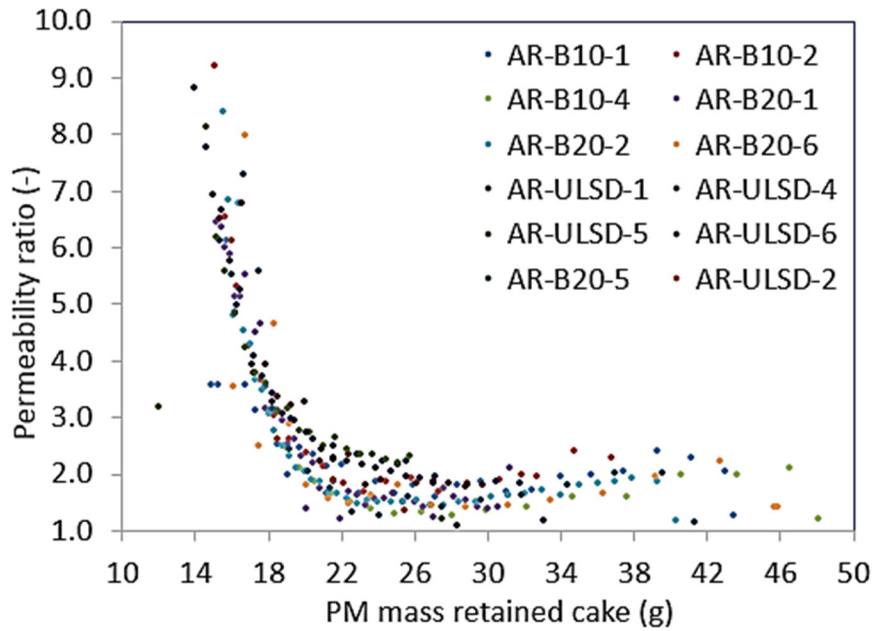
Figure 4. 11 Relative change in permeability ratio during active regeneration experiments with delta mass offset

Applying eqn. (4.20) developed by Picandet et al. [39] to the single set of permeability curves developed for the CPF, the damage permeability model coefficients

$(\alpha_{kNO_2}, \alpha_{kO_2}, \beta_{kNO_2}, \beta_{kO_2}$ and $m_{cake,initial})$ are determined by fitting it to the mass offset corrected permeability data shown in Figures 4.10 and 4.11.

Figures 4.12 and 4.13 show the damage permeability model curve fits (Eqn. 4.20) for the passive oxidation and active regeneration experiments.

The damage variable d is calculated as:

$$d = \frac{m_{cake,\,initial} - m_{cake\,corr}}{m_{cake,\,initial}} \qquad (4.28)$$

where, $m_{cake,\,initial}$ is the initial mass of the PM cake layer at the beginning of the PM oxidation and $m_{cake\,corr}$ is the current mass of the PM cake layer after applying the delta mass offset value. The delta mass offset value for each type of fuel is calculated as (from Figs. 4.8 and 4.9):

$$Delta\ mass\ offset_{th} = C8_{th}\ \ln(Overall\ PM\ reaction\ rate) + C9_{th} \qquad (4.29)$$

$$Delta\ mass\ offset_{NO2} = C8_{NO2}\ \ln(Overall\ PM\ reaction\ rate) + C9_{NO2} \qquad (4.30)$$

where, $Delta\ mass\ offset_{th}$ and $Delta\ mass\ offset_{NO2}$ are the delta mass offsets for the active regeneration and passive oxidation experiments, respectively. $C8_{th}$ and $C8_{NO2}$ are the slopes of the delta mass offset equation for the active regeneration and passive oxidation experiments determined from Figs. 4.8 and 4.9. Similarly, $C9_{th}$ and $C9_{NO2}$ are the constants of the delta mass offset equation determined from Figs. 4.8 and 4.9. The slopes and constants are obtained by fitting (linear fit) the delta mass offset values to the overall PM reaction rates.
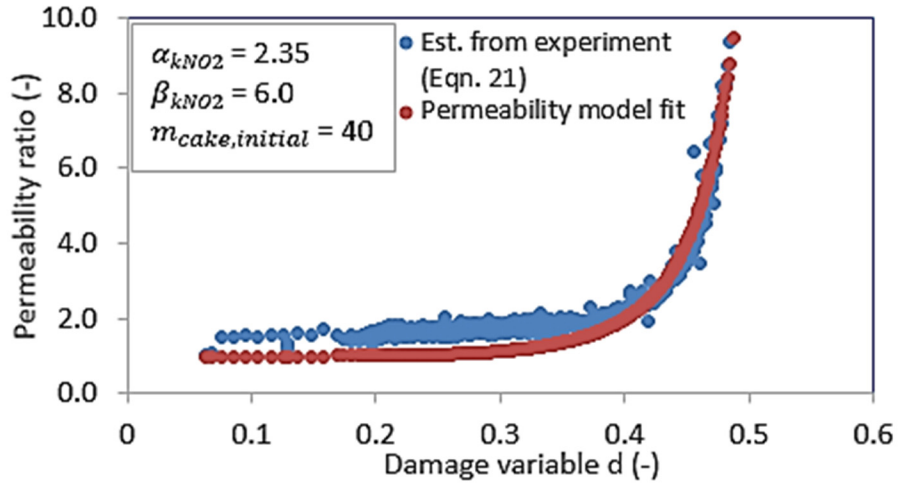
Figure 4. 12 Relative change in permeability ratio during passive oxidation experiments with delta mass offset in Fig. 4.8
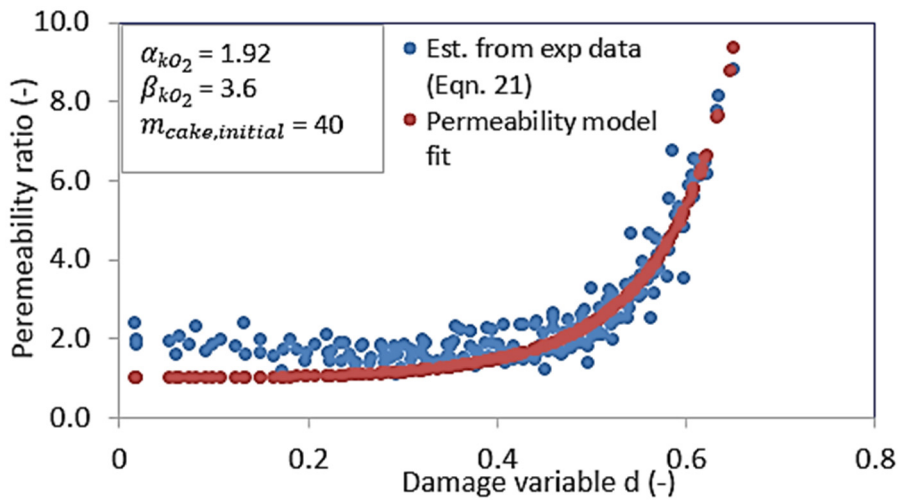
Figure 4. 13 Relative change in permeability ratio during active regeneration experiments with delta mass offset in Fig. 4.9

From Figures 4.12 and 4.13, the experimental cake permeability ratios are approximately 2 (for damage variable < 0.3) at the beginning of the PM oxidation indicating the selected reference permeability is lower than the experimental permeability by 50%. The cake permeability at the beginning of the PM oxidation varies between the experiments due to slip flow corrections in the model. However, the fitted damage permeability model using Equation (4.20) sets the undamaged PM cake permeability ratio to 1 and permeability ratio increases rapid as the damage variable increases over 0.3. This allows independent

56

application of damage permeability corrections that are separate from the other model corrections such as slip flow correction.

From Fig. 4.12, the PM cake permeability for passive oxidation experiments is calculated as:

$$k_{d_{i,j}} = k_{p_{i,j}} e^{\left[(\alpha_{kNO2}\, d)^{\,\beta_{kNO2}} \right]} \tag{4.31}$$

Similarly, from Fig. 4.13, the PM cake permeability for active regeneration experiments is calculated as:

$$k_{d_{i,j}} = k_{p_{i,j}} e^{\left[(\alpha_{kO2}\, d)^{\,\beta_{kO2}} \right]} \tag{4.32}$$

where, $k_{d_{i,j}}$ is the PM cake layer permeability accounting for the damage in the PM cake during PM oxidation (NO_2 assisted and thermal), $k_{p_{i,j}}$ is the PM cake layer permeability accounting for the changes in mean free path length of the gas at each zone, d is the damage variable, α_{kNO2} and α_{kO2} are the multiplicative constants for the passive oxidation and active regeneration experiments, respectively. Similarly, β_{kNO2} and β_{kO2} are the power constants for the passive oxidation and active regeneration experiments, respectively.

The cake permeability model parameters determined from the above analysis (Figs. 4.8, 4.9, 4.10 and 4.11) are listed in Table 4.1.

Table 4. 1 Calibrated parameters of the SCR-F/CPF model cake permeability for three different fuels for
pressure drop model

Symbol	PM cake layer permeability model parameters	ULSD	B10	B20	Units
$C8_{th}$	Slope of delta mass offset for thermal PM (O_2) oxidation	5.8899	11.08	5.422	(s-g)
$C9_{th}$	Constant of the delta mass offset for thermal PM (O2) oxidation	33.405	74.86	39.94	(-)
$C8_{NO2}$	Slope of delta mass offset for NO_2 - assisted PM oxidation	not appl.	2.38	7.722	(s-g)
$C9_{NO2}$	Constant of the delta mass offset for NO_2 assisted PM oxidation	not appl.	18.46	62.49	(-)
α_{kO2}	Multiplicative constant for cake permeability model of themal (O_2) PM oxidation	1.92			(-)
α_{kNO2}	Multiplicative constant for cake permeability model of NO_2 assisted PM oxidation	2.35			(-)
β_{kO2}	Power constant for cake permeability model of thermal (O2) PM oxidation	3.6			(-)
β_{kNO2}	Power constant for cake permeability model of NO_2 assisted PM oxidation	6			(-)
$m_{cake,initial}$	Initial mass of the undamaged PM cake	40			(g)

In the SCR-F/CPF model, the $m_{cake, initial}$ parameter defines the undamaged cake mass. This can be calibrated to higher or lower mass depending on the allowed filter loading levels for other applications. For the experiments studied in this thesis, the maximum loading is close to 40 g and the damage in the PM cake occurs at PM cake masses below $\cong$ 34 g as shown in Figures 4.6 and 4.7. For each experiment, the damage variable d is calculated and the resulting damage permeability is applied during the PM oxidation event. The damage to the PM cake occurs during the oxidation event which is tracked by the oxidation status flag which monitors the difference in the cake mass between previous and current time steps. The magnitude of the damage is determined from the damage permeability Eqns. 4.31 and 4.32. Once the oxidation is complete, the damage recovery of PM cake happens through variables (C10 & C11) during the post loading phase of the

experiments. The formulations of post loading permeability equations are explained in Appendix C.

To apply varying cake permeability model in an ECU for transient operating conditions and general drive cycles, the oxidation status flag (as explained above) along with the monitoring of the cake PM mass relative to the wall PM will aid in determining the various states of the CPF such as loading, oxidation and post loading. In the SCR-F/CPF model, the permeability of the PM cake during the loading stage is calculated using Equation 4.19. The PM cake permeability during PM oxidation is calculated using Equations 4.31 and 4.32 for passive oxidation and active regeneration experiments respectively. The post loading permeability of the PM cake is calculated using Equation D.1. This varying cake permeability model accounts for various operating conditions (loading, PM oxidation and post loading) and drive cycles of the CPF including damage in the cake during PM oxidation and should be able to be applied based on actual operating conditions of the CPF although this is not explored in this thesis. The cake permeability model also could be applied to the general occurrence of the passive oxidation during the drive cycles by monitoring the oxidation status flag along with the PM oxidation rates. The model presented in this research accounts for the varying oxidation rates using the Eqns. (4.29) and (4.30) although the model is yet to be validated on the representative drive cycles.

4.6 Species Concentration Model

The species solver used in this research was developed by Venkata Chundru [57] and is included in this thesis for complete description of the SCR-F/CPF models. In the high fidelity SCR-F/CPF model, mass conservation of chemical species are accounted at each zone. Each zone consists of inlet channel, PM cake layer, substrate wall and outlet channel. The following assumptions were used while solving the chemical species equations [23]

1. Reactions are instantaneous (quasi-steady)
2. Exhaust gas density is constant within each zone (cake, catalysts and wall control volumes)
3. Concentration of the individual chemical species at the inlet channel and PM cake layer boundary is equal to the inlet concentration of the CPF

4. Concentration of the individual chemical species at the outlet channel is equal to the substrate wall and outlet channel interface.

5. Species concentration in the cake and wall is uniform (wall and cake have uniform concentration throughout the zone)

Table 4. 2 Chemical reactions considered in the high-fidelity SCR-F/CPF model

Chemical Equations	Reaction Rate Variable
$C_{12}H_{24} + 18O_2 \rightarrow 12CO_2 + 12H_2O$	RR_{HC}
$CO + \frac{1}{2}O_2 \rightarrow CO_2$	RR_{CO}
$NO + \frac{1}{2}O_2 \leftrightarrow NO_2$	RR_{NO}
$C_{(s)} + a_{o_2}O_2 \rightarrow 2(a_{o_2} - 0.5)CO_2 + 2(1 - a_{o_2})CO$	RR_{th}
$C(s) + \propto_{NO2} NO_2 \rightarrow \propto_{NO2} NO + (2-\propto_{NO2}) CO + (\propto_{NO2} - 1) CO2$	RR_{NO_2}

The differential form of quasi-steady species conservation equation is given as [23]

$$av_w \frac{dY_l}{dy} - \frac{d}{dy}\left(D_l a \frac{dY_l}{dy}\right) = -\frac{\bar{a}}{C_{mix}}\sum_j \xi_{l\,m} R_m \tag{4.33}$$

where Y_l is the mole fraction of chemical species l in the cake+catalyst+wall control volume, D_l is the effective diffusivity of the chemical species l, the y co-ordinates denotes the traverse direction (direction normal to the gas flow) or into-the-wall direction, C_{mix} is the molecular density of the exhaust gas mixture in the cake+cat+wall control volume, $\xi_{l\,m}$ is the stoichiometric coefficient of species l in reaction m and R_m is the rate of reaction m.

The effective diffusivity D_l is given as [23]:

$$D_l = \frac{1}{\frac{\tau}{\varepsilon}\left[\frac{1}{D_{mol,l}} + \frac{1}{D_{kn\,l}}\right]} \tag{4.34}$$

where $D_{mol,l}$ is the molecular diffusivity and $D_{kn\,l}$ is the Knudsen diffusivity of the chemical species.

The detailed formulation of the terms in equation (4.33) and (4.34) are explained in reference [23].

The reaction rates for HC, CO and NO oxidation reactions are given as [23]:

$$R_{HC} = \frac{A_{HC}(T_f)^{x_{HC}} e^{\frac{-E_{a\,HC}}{RT_f}} [C_{12}H_{24}][O_2]}{G_1} \tag{4.35}$$

$$R_{CO} = \frac{A_{CO}(T_f)^{x_{CO}} e^{\frac{-E_{a\,CO}}{RT_f}} [CO][O_2]}{G_2} \tag{4.36}$$

$$R_{HC} = \frac{A_{NO}(T_f)^{x_{NO}} e^{\frac{-E_{a\,NO}}{RT_f}} \left[[NO][O_2]^{\frac{1}{2}} - \frac{[NO_2]}{K_c}\right]}{G_3} \tag{4.37}$$

where A_{HC} is the pre-exponential factor for the HC oxidation reaction, x_{HC} is the temperature order of dependence of the HC oxidation reaction, $E_{a\,HC}$ is the activation energy for HC oxidation reaction, $[C_{12}H_{24}]$ is the molar concentration of the $C_{12}H_{24}$, $[O_2]$ is the molar concentration of O_2, G_1 is the inhibition factor for the HC oxidation reaction, A_{CO} is the pre-exponential factor for the CO oxidation reaction, x_{CO} is the temperature order of dependence of the CO oxidation reaction, $E_{a\,CO}$ is the activation energy for CO oxidation reaction, $[CO]$ is the molar concentration of the CO, G_2 is the inhibition factor for the CO oxidation reaction, A_{NO} is the pre-exponential factor for the NO oxidation reaction, x_{NO} is the temperature order of dependence of the NO oxidation reaction, $E_{a\,NO}$ is the activation energy for NO oxidation reaction, $[NO]$ is the molar concentration of the NO, K_c is the equilibrium constant for the NO oxidation reaction and G_3 is the inhibition factor for the NO oxidation reaction. The detailed formulation of the terms used in equations (4.35), (4.36) and (4.37) is explained in reference [23].

4.7 Numerical Solver

The model formulation involves simulation of the time varying temperature within the CPF from node to node. Hence, an explicit solver scheme was used to determine the temperature at each time step. The explicit solver estimates the filter substrate temperature for a time step (t) using temperature values from the previous time step (t-1). This approach is relatively simple to setup and program, however Δt must be less than the limit imposed by stability constraints [62,63]. The temperature for the new time step with the explicit solver method can be expressed mathematically as (for i = 2 to imax and j = 1 to jmax)

$$Temp\_filter\_new_{i,j} \; = \; Temp\_filter\_old_{i,j} \; +$$

$$\frac{\dot{Q}_{cond.axial} + \dot{Q}_{cond.radial} + \dot{Q}_{conv} + \dot{Q}_{reac,PM} + \dot{Q}_{reac,HC} + \dot{Q}_{wall-flow} + \dot{Q}_{rad}}{(\rho_s c_s V s_{i,j} + \rho_f c_f V f_{i,j})} \; \Delta t \qquad (4.38)$$

where,

Δt is the time step for the solver.

The explicit method is easy to use but it is not unconditionally stable and the largest permissible value of Δt is limited by the stability criterion. For larger time steps, the explicit method oscillates widely and diverges from the actual solution. In general, the stability criterion is satisfied when the primary coefficients of all temperature terms in the Equation (4.41) are greater than or equal to zero for all nodes [62]. Since the time step for each term is different, the practical approach to this problem is to use the most restrictive time step. From reference [62], the 1-D convection problem for a plane wall, the time step is expressed as

$$\Delta t \; \leq \; \frac{\Delta x^2}{2\propto (1 + \frac{h\Delta x}{k})} \qquad (4.39)$$

Where, Δx is the discretization length (minimum of ΔL or Δr), α is the thermal diffusivity of the filter substrate. However, considering the heat transfer between filter and channel gas, α is minimum at the gas side and hence

$$\alpha \; = \; \frac{k_g}{\rho \, c_p} \qquad (4.40)$$

where, k_g = Thermal conductivity of exhaust gas

ρ = density of exhaust gas

c_p = Specific heat capacity of exhaust gas

$h = h_g$ = Convective heat transfer between filter substrate and channel gas.

Using the Equations (4.39) and (4.40), the initial values of time step can be determined. The high fidelity SCR-F/CPF model includes conduction, convection and radiation terms together. Further, the chemical species terms also involve advection schemes (convection + diffusion) which further reduces the time step. The multi-zone particulate filter model developed in references [1, 2,3] used the fixed step discrete solver with the model step of

0.01 seconds for temperature solver. In order to increase the speed of the simulation where in thermal gradients are small, the new SCR-F/CPF model architecture developed by Venkata Chundru and Prof. Gordon Parker used the variable time step solver with the minimum time step of 1e-8 seconds and the maximum time step of 2 to 10 seconds (varies between the experiments based on temperature or species concentration gradients with input data). Also the model outputs are treated as continuous states in the Simulink block which uses the derivatives model to determine the current state using the ODE15s stiff solver. This also reduced the model run time significantly. The relative and absolute tolerance in the solver is set as 1e-3.

4.8 High Fidelity Model Calibration Process

The high fidelity SCR-F/CPF model requires the calibration of parameters and time varying input parameters to simulate the performance of the CPF. The time varying input parameters are generated using the experimental data explained in chapter 3. The SCR-F/CPF model is calibrated using the eighteen experimental runs from references [49, 50, 51, 52].The detailed list of model inputs and model calibration process is outlined in this section.

The SCR-F/CPF model has set of input variables, constants and calibration parameters. The model needs to be parameterized in order to simulate the temperature and PM mass loading distribution within the filter substrate. The input variables include

1) Instantaneous exhaust mass flow rate ($\dot{m}$)
2) CPF inlet temperature (Tin)
3) CPF inlet concentrations including NO, NO_2, O2, CO, CO_2, N_2, HC ($C_{12}H_{24}$) and PM
4) Ambient temperature and pressure

The overall objective of the calibration process is to simulate the axial and radial PM loading distribution, temperature distribution and pressure drop of the CPF. The goal is to achieve agreement with the total experimental PM mass retained within 2 g, RMS temperature of outlet gas error within 6°C and RMS pressure drop error within 0.3 kPa. This was achieved by the three-step calibration process shown in Fig. 4.14 and described by the following steps.

1) **calibration of cake PM oxidation**: The objective of this step is to determine the initial PM kinetic parameters for cake and wall PM oxidation while simulating the PM mass retained and experimental temperature distribution data. The values of cake PM kinetic parameters ($A_{NO2\ cake}$, $E_{NO2\ cake}$, $A_{O2\ cake}$ and $E_{O2\ cake}$) are determined using the model calibration procedure explained in this section and also in reference [1]. The wall PM kinetics (A_{NO2} wall, $E_{NO2\ wall}$, $A_{O2\ wall}$ and $E_{O2\ wall}$) are set same as the cake PM kinetics.

2) **Calibration of pressure drop model**: The objective of the pressure drop model calibration is to simulate pressure drop across CPF during loading, PM oxidation and post loading phases of the experiment. The detailed pressure drop model calibration is explained in this section.

3) **Re-calibration of cake PM oxidation**: The pre-exponentials of the cake PM oxidation ($A_{NO2\ cake}$, $A_{O2\ cake}$) was re-calibrated to account for the changes in the wall PM oxidation in step 2. Nelder-Mead Simplex optimization method [64] is used to calibrate the cake PM oxidation pre-exponentials.

Determine cake PM oxidation parameters using the model calibration procedure explained in ref[1]– $A_{NO2\ cake}$, $E_{NO2\ cake}$, $A_{O2\ cake}$ and $E_{O2\ cake}$

Use cake PM oxidation parameters as initial values for wall PM oxidation – $A_{NO2\ wall}$, $E_{NO2\ wall}$, $A_{O2\ wall}$ and $E_{O2\ wall}$

Step 1

Calibration of pressure drop model – wall and cake filtration and permeability evolution models

Calibration of cake PM $A_{NO2\ cake}$ and $A_{O2\ cake}$ by closely simulating the experimental PM mass retained

Step 2

Step 3

$e_{\Delta P} < 0.3\ kPa$
$e_m < 2\ g$
$e_T < 6\ °C$

No

Yes

Calibrated model coefficients

Figure 4. 14 Model calibration flow chart

Calibration of Cake PM Oxidation

For the model calibration and results presented in this work, 10x10 SCR-F/CPF model was used. The overall objective of the calibration process was to simulate the axial and radial PM loading distribution to agree with the total experimental PM mass retained within 2 g. This was achieved by the two-step calibration process shown in Fig. 4.15.

1. Calibration of PM oxidation: PM kinetic parameters (A_{NO2}, E_{NO2}, A_{O2} and E_{O2}) are determined in this step. The calibration of PM kinetic parameters from the engine experiments are preferred over synthetic gas based lab reactor experiments because, the engine experiments provides representative PM composition, residence time and operating temperatures of the filter for calibration. Hence, the PM kinetic parameters

determined from the engine experiments can be directly used in the SCR-F/CPF model. The objective of the first step is to minimize the error between the simulation and the total experimental PM mass retained.

2. Calibration of heat transfer coefficients: Convective and radiation heat transfer coefficients (h_{amb} and $\mathcal{E}r$) are determined from this step. In addition, the filter substrate density (ρf) is found. The substrate density along with other thermo physical properties (thermal conductivity, substrate density and PM density) of the filter changes during the filter loading. Hence, in order to simulate the change in thermo physical properties of the filter, the filter substrate density is also considered as the one of the calibration variable in the SCR-F/CPF model. Depcik et al [13] showed in their model calibration efforts that the model accuracy could be improved during temperature rise portion of the experiment by optimizing the filter substrate density. The objective of this step is to minimize the RMS temperature error between the simulation and the experimental data measured by the sixteen CPF thermocouples during the loading, PO/AR and post loading phases of the experiments.
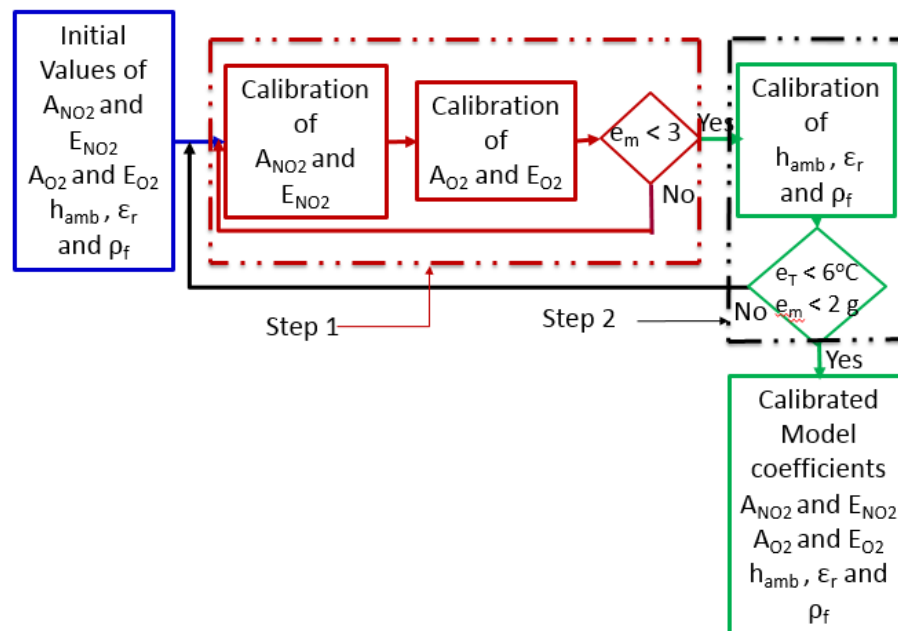
Figure 4. 15 PM oxidation calibration flow chart

The calibration process starts with the initial assumption of calibration parameters. The initial values of the calibration parameters were determined from the references [13, 21,

23 and 65]. All eighteen runs are simulated and the results are compared with the experimental data. To improve the model accuracy, the calibration process is repeated if the PM mass loading error exceeds 2 g and the RMS outlet gas temperature distribution error exceeds 6 ^{o}C. Details about the calibration process for the two steps are explained next.

Step 1: PM Kinetics Calibration Procedure

The objective of the PM kinetics calibration procedure is to simulate the experimental total PM mass retained within the filter at each of the four stages of loading. This was achieved by determining NO_2 assisted PM oxidation kinetic parameters (A_{NO2} and E_{NO2}) and thermal (O_2) assisted PM oxidation kinetic parameters (A_{O2} and E_{O2}) from the experimental runs (passive oxidation and active regeneration). The error term e_m in Fig. 4.15 represents the error between simulated and experimental PM mass retained at each of the four stages of loading. The tasks involved in the PM kinetics calibration are:

1. Determine the NO_2 assisted PM kinetics (A_{NO2} & E_{NO2}) from the passive oxidation experiments keeping other parameters constant. Optimization is done in Matlab® using Nelder-Mead Simplex method [64]. *Matlab function fminsearch* is used to minimize the error between SCR-F/CPF model simulation and the experimental PM mass retained. The error value of 1 g is used as the target for the Simulink design optimization at the end of each of the stages of loading.

2. Use the NO_2 assisted PM kinetics (from task 1) to determine the thermal (O_2) assisted PM kinetics from the active regeneration experiments keeping other parameters constant in the model.

3. From the PM kinetics determined from tasks 1 and 2, use the Arrhenius plots to determine the optimum PM kinetic parameters for each type of fuel.

4. From tasks 1, 2 and 3, determine one set of PM kinetic calibration parameters (A_{NO2}, E_{NO2}, A_{O2} & E_{O2}) for each type of fuel (ULSD, B10 & B20)

Step 2: Heat Transfer Coefficients Calibration

Similar to step 1, Nelder-Mead Simplex optimization method [64] is used to calibrate the heat transfer coefficients in the SCR-F/CPF model. The heat transfer coefficients and filter

density values are varied keeping all other parameters constant in the model. The objective of the optimization routine is to minimize the RMS temperature error between the simulation and the experimental temperature data measured by the sixteen thermocouples during loading, PO/AR and post loading phases of the experiment. The RMS error of $2^{\circ}C$ (during steady state operating condition) is used as the target for optimization.

The resulting model parameters from the 2-step calibration procedure are shown in Tables 4.3, 4.4 and 4.5. Simulation results and experimental validation of the SCR-F/CPF model with calibrated parameters are provided in the next section. The model constants C1 to C6 were determined from the thermal boundary layer formulation as explained in Appendix A.

Table 4. 3 SCR-F/CPF model constants

Symbol	Description	Units	Values
F	Radiation view factor	[-]	0.011
C1	DOC radial temperature distribution factor 1	[-]	-2.493
C2	DOC radial temperature distribution factor 2	[-]	1.0585
C3	DOC radial temperature distribution factor 3	[-]	-0.3285
C4	DOC radial temperature distribution factor 4	[-]	1.7631
C5	DOC mean to surface temperature ratio	[-]	1.0425
C6	DOC temperature sensor offset	[-]	0.0273*Tin-2.4996
ρ_{pm}	PM density	kg m^3	104
Sp	Soot Surface Area	m^{-1}	5.5x10^7
Cp$_{air}$	Specific heat of air	J kg^{-1}K^{-1}	Using Equation C.1
μ	Dynamic viscosity of air	N s m^{-2}	Using Equation C.2
λ_f	Thermal conductivity of substrate wall	W m^{-1}K^{-1}	1
λp	Thermal conductivity of PM cake layer	W m^{-1}K^{-1}	2.1
α_{O2}	O$_2$ combustion partial factor	[-]	0.8
α_{NO2}	NO$_2$ combustion partial factor	[-]	1.75

Table 4. 4 Calibrated parameters of the SCR-F/CPF model for PM kinetics for three different fuels

PM oxidation	Symbol	Description	Units	ULSD	B10	B20
NO$_2$ - assisted	A$_{NO2}$	Pre-exponential for NO$_2$-assisted PM oxidation	m K^{-1} s^{-1}	0.0070	0.0060	0.0078
	E$_{NO2}$	Activation energy for NO$_2$-assisted PM oxidation	kJ gmol^{-1}	60.8	64.1	63.1
Thermal (O$_2$)	A$_{O2}$	Pre-exponential for Thermal (O$_2$) PM oxidation	m K^{-1} s^{-1}	0.090	0.710	0.720
	E$_{O2}$	Activation energy for Thermal (O$_2$) PM oxidation	kJ gmol^{-1}	139.0	151.8	148.9

Table 4. 5 Calibrated heat transfer coefficients and filter density for the SCR-F/CPF model

Symbol	Description	Units	Values
hamb	Convection heat transfer coefficient	W m^{-2} K^{-1}	4.0
ε_{rext}	External radiation coefficient	[-]	0.08
ρ_{filter}	Filter density	kg m^{-3}	449

Calibration of Pressure Drop Model

The objective of the pressure drop model calibration is to simulate the wall filtration and cake filtration regimes and the pressure drop during loading, PM oxidation and post loading phases of the experiment. The pressure drop model is calibrated by following a eight-step calibration procedure. Figure 4.16 shows the respective region of each calibration step on a typical pressure drop data plot. Figure 4.16 shows the simulated channel, cake, wall and total pressure drop along with the total experimental pressure drop trend over the entire experiment.

The initial model calibration values for wall and cake filtration parameters (k_{0w}, k_{trans}, $k_{0,cake}$, C1$_{wpm}$, C2$_{wpm}$, C$_3$, C$_4$, $\alpha_{0,cake}$, A$_{eff\ cake}$, C$_5$, C$_6$ and C$_7$) were determined from earlier references [22, 23, 32, 33]. The parameters were further calibrated to simulate the experimental pressure drop by following the steps explained below. The following numbered steps refer to Fig. 16.

1. First, the initial wall permeability ($k_{0,w}$) is calibrated to simulate the clean wall pressure drop trend as shown in Figure 4.16 for the time periods of 0-0.2 hours.

2. The transition permeability (k_{trans}) is calibrated to simulate transition from wall permeability to cake permeability regime as shown by 2 in Figure 4.16.

3. The cake permeability correction factor C_5, cake layer porosity ($1-\alpha_{o,cake}$) and maximum cake efficiency parameter ($A_{eff\ cake}$) are calibrated to simulate the linear increase in pressure in the cake filtration regime.
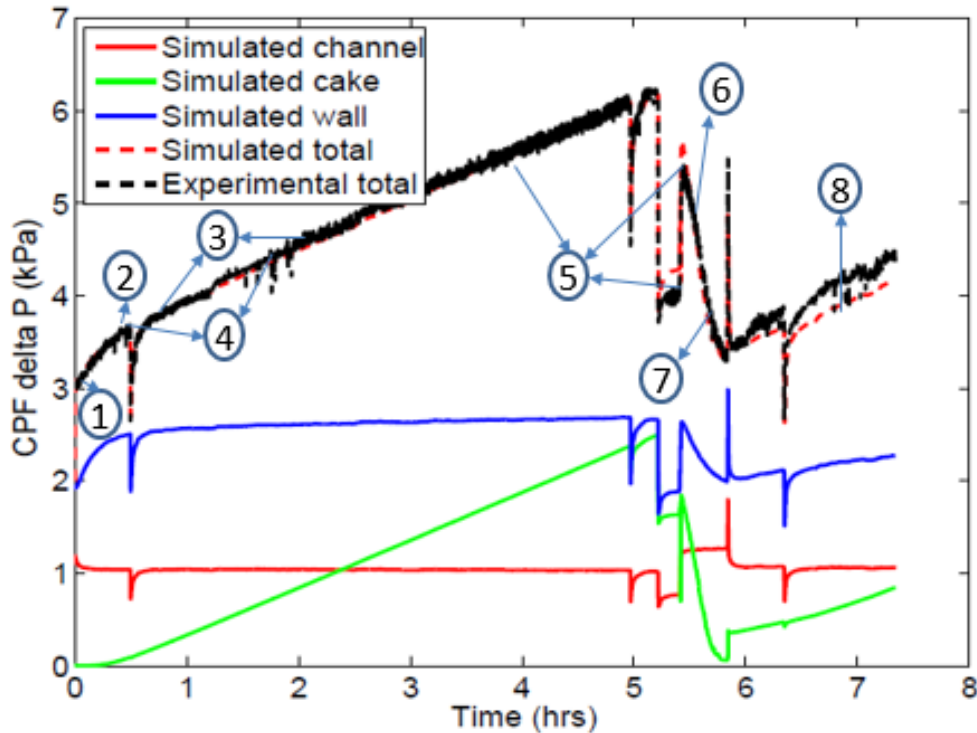
Figure 4. 16 Illustration of pressure drop model calibration steps

4. As the PM accumulates in the wall collector, the wall packing density changes which affects the total pressure drop. Hence, the wall packing density parameters $C1_{wpm}$ and $C2_{wpm}$ are calibrated based on the mass of PM in the wall collectors.

5. The permeability of the wall and cake is affected by the change in mean free path length of the gas. Hence, the wall permeability correction factor (C_4) and cake permeability correction (C_5) are applied in the model. The correction factors C_4 and C_5 for the wall and cake permeability corrections have to be optimized to minimize the pressure drop simulation error during loading as well as any change in pressure and temperature conditions of the gas considering the phenomenological nature of the model in Equations 4.18 and 4.19.

6. The wall pressure drop during PM oxidation is calibrated in this step. The wall PM oxidation pre-exponential is calibrated to simulate the pressure drop trend at the end of PM oxidation. This is mainly because, at the end of PM oxidation (passive oxidation and active regeneration), the permeability of cake layer increases significantly due to potential damage in the cake as explained in earlier sections. Also, most of the PM in the wall is oxidized in the earlier stages of PM oxidation because of the total PM in the wall pores are smaller than the cake and also increased oxidation rate of PM in the pores compared to PM cake layer [36]. Nelder-Mead Simplex optimization method [64] is used to calibrate the wall PM oxidation pre-exponentials. The objective for the optimization scheme is to minimize the pressure drop error between experimental and simulation data at the end of PM oxidation by optimizing the wall PM kinetics.

7. With calibrated wall PM oxidation, the constants of the cake PM permeability models ($C8_{NO2}$, $C8_{th}$, $C9_{NO2}$ and $C9_{th}$) are determined.

8. During post loading, the permeability of the cake layer reduces as the open holes and cracks are refilled with PM. The reduction in permeability varies between PM oxidation types (passive oxidation versus active regeneration). In the SCR-F/CPF model, it was determined to use the same post loading permeability constants for passive and active regeneration experiments as explained in Appendix C. The post loading permeability variables C_{10} and C_{11} were calibrated to simulate the pressure drop trend during the post loading phase of the experiment.

The resulting model parameters from the 3-step calibration procedure are listed in Tables 4.6, 4.7, 4.8 and 4.9. Table 4.6 also shows model parameters used in the 1D model developed in reference [1]. Simulation results and experimental validation of the SCR-F/CPF model with calibrated parameters are provided in the next section.

Table 4. 6 Pressure drop model constants

Parameter	Description	SCR-F/CPF	1-D	Units
Substrate Wall				
$k_{0,w}$	Initial permeability of substrate wall	5.42E-14	1.19E-13	(m^2)
$k_{0,trans}$	Transition permeability of substrate wall	8.00E-14	7.00E-14	(m^2)
Wall PM				
$C1_{wpm}$	First constant for wall packing density calculation	3.7	2.2	$(1/m^3)$
$C2_{wpm}$	Second constant for wall packing density calculation	0.48	1.48	(kg/m^3)
C_3	Ref. pressure for wall permeability correction	103.25	not appl.	(kPa)
C_4	Wall permeability correction factor	110	not appl.	(-)
PM cake layer				
$\alpha_{o,cake}$	Initial solidosity of PM cake layer	0.05	0.05	(-)
$k_{0,cake}$	Initial / ref. permeability of PM cake layer	7.01E-15	7.00E-15	(m^2)
$A_{eff,cake}$	PM cake maximum filtration efficiency parameter	0.95	0.95	(-)
C_5	Cake permeability correction factor	3.38E-13	not appl.	$(kg\ m^{-1})$
C_6	Ref. pressure for lambda correction	100	not appl.	(kPa)
C_7	Ref. temperature for lambda correction	300	not appl.	(K)
C_{10}	Slope for post loading cake peremeability	-0.036 (PO), -0.058 (AR)	not appl.	(-)
C_{11}	Constant for post loading cake permeability	3.087	not appl.	(-)

Table 4. 7 Calibrated parameters of the SCR-F/CPF model for cake PM kinetics for three different fuels for pressure drop model

PM Oxidation	Symbol	PM cake layer	ULSD	B10	B20	Units
NO$_2$- assisted	$A_{NO2,cake}$	Pre-exponential for NO_2-assisted PM oxidation	0.0007	0.006	0.006	m / K-s
	$Ea_{NO2,cake}$	Activationn energy for NO_2-assisted PM oxidation	60.8	64.1	63.1	kJ/gmol
Thermal (O$_2$)	$A_{th,cake}$	Pre-exponential for thermal (O_2) PM oxidation	0.09	0.71	0.72	m / K-s
	$Ea_{th,cake}$	Activationn energy for thermal (O_2) PM oxidation	139	151.8	148.9	kJ/gmol

PM Oxidation	Symbol	Substrate wall	ULSD	B10	B20	Units
NO$_2$- assisted	A$_{NO2,wall}$	Pre-exponential for NO$_2$-assisted PM oxidation	0.020	0.019	0.020	m / K-s
	Ea$_{NO2,wall}$	Activationn energy for NO$_2$-assisted PM oxidation	60.8	64.1	63.1	kJ/gmol
Thermal (O$_2$)	A$_{th,wall}$	Pre-exponential for thermal (O$_2$) PM oxidation	0.14	1.27	2.17	m / K-s
	Ea$_{th,wall}$	Activationn energy for thermal (O$_2$) PM oxidation	139	151.8	148.9	kJ/gmol

Calibration of Species Concentration Model

The objective of the species concentration model calibration is to accurately simulate the NO, NO$_2$, O$_2$, CO and CO$_2$ concentration at each zone as they affect the PM oxidation and temperature distribution at each zone. The initial values for the activation energies and pre-exponential factors were obtained from reference [23]. The pre-exponential and activation energies were further optimized to simulate experimental outlet concentration of NO, NO$_2$, CO and C$_{12}$H$_{24}$. Table 4.10 shows the optimized calibration parameters for the high-fidelity SCR-F/CPF model. The NO$_2$ back diffusion term (tortuosity of the PM cake layer) was optimized to simulate the NO$_2$ concentration at the outlet of the CPF.

Table 4. 9 SCR-F/CPF model species kinetics

Catalytic Reaction	Symbol	PM cake	ULSD	B10	B20	Units
NO oxidation	A$_{NO}$	Pre-exponential for NO oxidation		3.48E+05		m / K-s
	Ea$_{NO}$	Activationn energy for NO oxidation		1.87E+07		J/kmol
CO oxidation	A$_{CO}$	Pre-exponential for CO oxidation		5.00E+09		m / K-s
	Ea$_{CO}$	Activationn energy for CO oxidation		4.35E+04		J/kmol
HC oxidation	A$_{HC}$	Pre-exponential for HC oxidation		6.00E+08		m / K-s
	Ea$_{HC}$	Activationn energy for HC oxidation		4.35E+07		J/kmol

4.9 Simulation of High Fidelity Model

The single set of calibration parameters (Tables 4.3 – 4.10) determined from the calibration process was used for the SCR-F/CPF model simulation of passive oxidation

(PO-B10-15) and active regeneration experiment (AR-B10-1). The results are presented in the following section. The high-fidelity SCR-F/CPF model summary for PM mass retained and pressure drop for all eighteen experiments are shown in Appendix E.

4.9.1 Passive Oxidation Experiments

The parameters summary of passive oxidation experimental data used for the model calibration are listed in Table 3.3. From Table 3.3, the filter substrate temperature during passive oxidation is between 250 and 400°C. During passive oxidation, most of the PM mass retained in the filter substrate is oxidized by the NO_2 assisted PM oxidation mechanism and the PO experiments were run for 42 to 101 minutes in order to carry out the PM mass oxidation. The slower rate of PM oxidation during PO oxidation experiments affect the heat transfer, temperature and filter loading distribution within the filter. The NO_2 assisted PM oxidation also affects the wall and cake PM oxidation rates and thereby the pressure drop trends. This is mainly because of the differences in the reaction rates with NO_2 assisted PM oxidation mechanism (passive oxidation reaction rates are 7.5 to 8.5 times lower than active regeneration reaction rates) [2] and its effect on overall PM loading and temperature distribution. The SCR-F/CPF model accounts for the NO_2 assisted PM oxidation using Equations 4.8 and 4.9. The results of one such passive oxidation experiment are presented in the following section.

Filter Outlet Temperature

Figure 4.17 shows the comparison of model outlet gas temperature with the experimental outlet gas temperature along with the CPF inlet temperature measured upstream of the CPF. From Figure 4.17, the simulation prediction error is within 2°C excluding the temperature spikes related the experimental procedure and transition phase of moving in and out of the PO phase of the experiment.
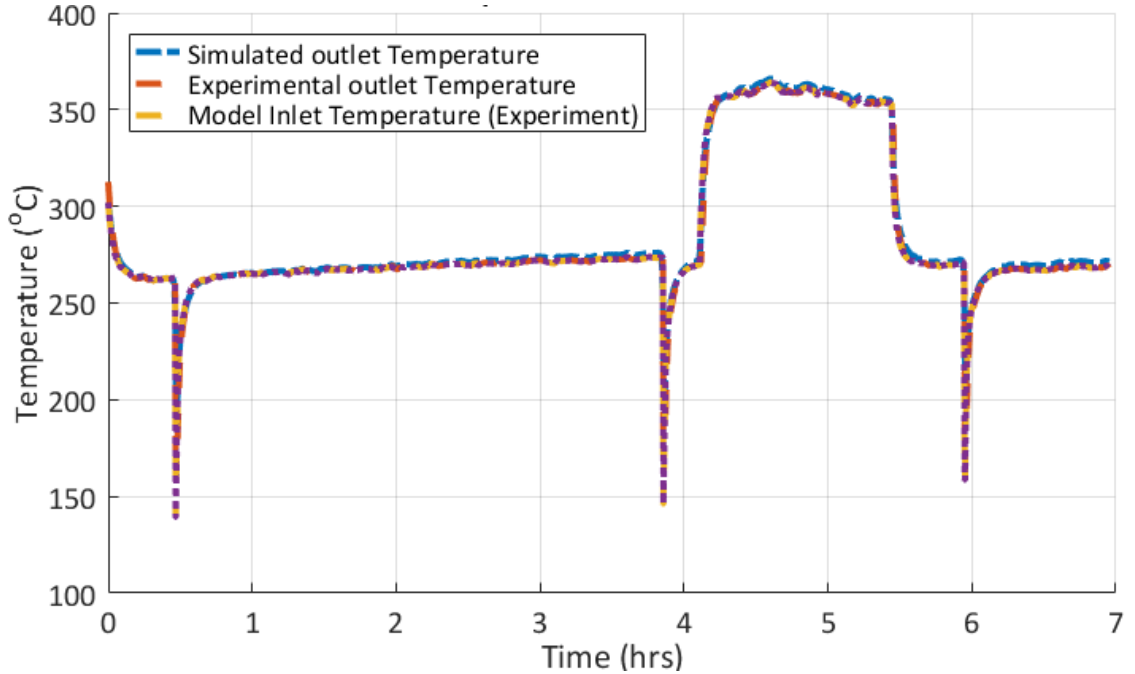
Figure 4. 17 Comparison of experimental and model CPF outlet gas temperature with model input CPF inlet gas temperature for PO-B10-15 experiment

Temperature Distribution

Figure 4.18 shows the experimental temperature distribution measured by all 16 thermocouples and Figure 4.19 shows the temperatures simulated by the high-fidelity SCR-F/CPF model at 4.36 hrs (15 minutes after switching to passive oxidation engine operating condition). The engine operating condition at 4.36 hrs is chosen to compare the model prediction accuracy at high temperature regions of the experiment. The inlet temperature to the SCR-F/CPF model was simulated using the Equation 3.3 and the inlet mass flow rate fraction was simulated using volume ratio of the inlet channels in each zone while accounting for the average PM cake layer thickness at each zone as shown in Equation (4.41).

$$\dot{m}_{i,j} = \dot{m}_{total} \frac{Ves_{i,j}}{\sum_i Ves_{i,j}} \tag{4.41}$$

where, $\dot{m}_{i,j}$ is the exhaust gas mass flow rate at each zone

$\dot{m}_{total}$ is the total exhaust mass flow rate into the CPF

75

$Ves_{i,j}$ is the empty volume in each zone while accounting for the average PM cake layer thickness.
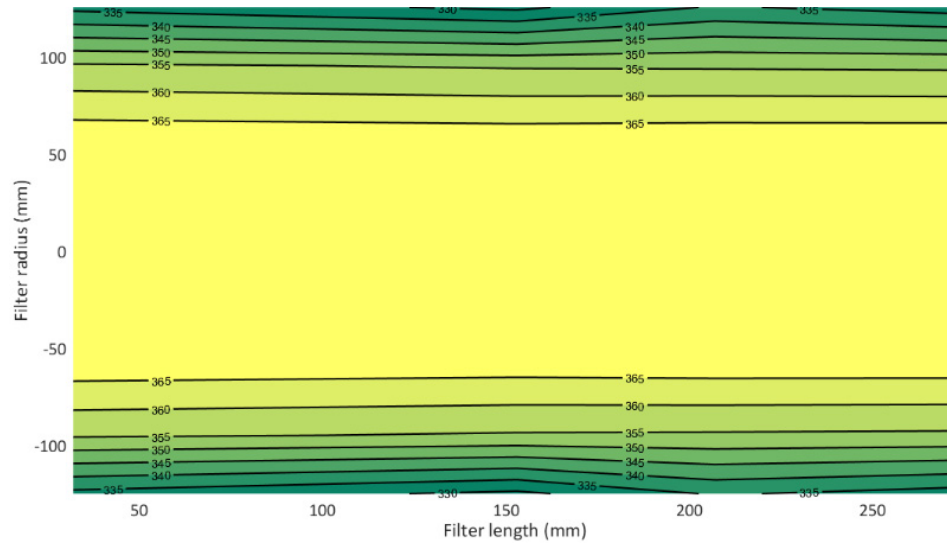
Figure 4. 18 Experimental temperature distribution in ºC for PO-B10-15 experiment at 4.36 hrs. (15 minutes after switching to PO operating condition)
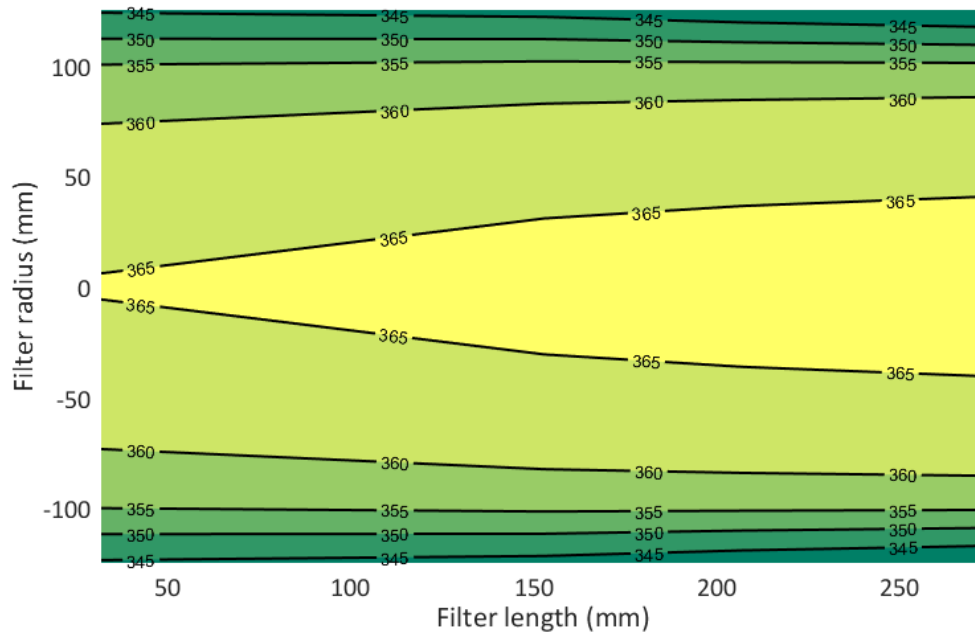
Figure 4. 19 Simulated temperature distribution in ºC for PO-B10-15 experiment at 4.36 hrs. (15 minutes after switching to PO operating condition)

From Figure 4.19, it is evident that the SCR-F/CPF model follows the experimental data. The maximum absolute temperature difference between the experimental and simulation

data is ≅ 11°C. From Figure 4.19, the filter substrate temperatures for radiuses greater than 80 mm are approximately constant as a function of axial distribution. A slight increase (1-2°C) in axial temperature is due to the local PM and HC oxidation. The substrate temperature close to the wall shows a slight decrease in temperature due to the dominant convection heat losses to the ambient compared to the local PM and HC oxidation. Comparing Figures 4.19 with 4.18, the CPF inlet temperature distribution at filter axial lengths of < 50 mm is about 5°C lower in the model compared to the experimental data. This is mainly due to the differences in estimated inlet temperature distribution using Equations 3.1 to 3.3 (thermal boundary layer equations and general curve fit for all eighteen experiments) compared to the measured temperature distribution. Figure 4.20 shows the SCR-F/CPF simulated temperature distribution by closely simulating the measured temperature distribution at the inlet of the CPF (axial length < 32 mm, C1, C2, C3 and C4 thermocouples in Figure 3.3). Comparing Figures 4.18 with 4.19, the simulated temperatures within the CPF closely matches with the experimental temperature. The maximum absolute temperature difference between the experimental and simulation data is ≅ 7°C and RMS temperature difference is ≅ 3°C. Hence, the inlet temperature distribution has to be as accurate as possible for the accurate estimate of temperature distribution within in the CPF.
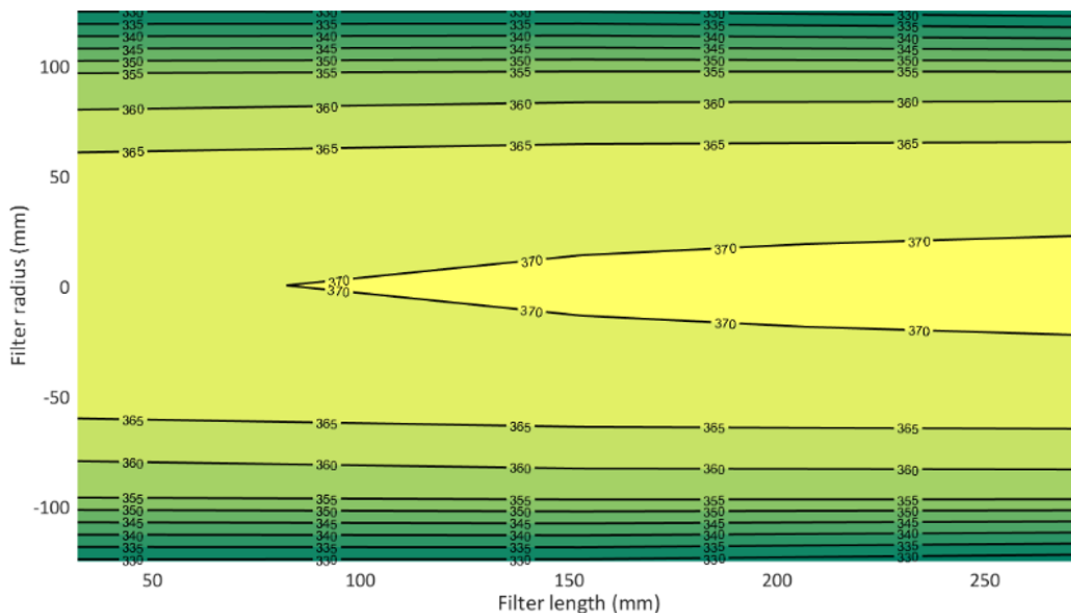
Figure 4. 20 Simulated temperature distribution in °C for PO-B10-15 experiment at 4.36 hrs. (15 minutes after switching to PO operating condition) with closely simulated measured inlet temperature distribution

Filtration

Figure 4.21 shows the comparison of the total filtration efficiency (mass basis) between the experimental data and simulation model along with the distribution of filtration efficiency into PM cake and substrate wall for PO-B10-15 experiment on mass basis. From Figure 4.21, the total filtration efficiency simulated by the SCR-F/CPF model is comparable with the experimental data measured during stage 2 loading (97% - shown as purple 'o' marker). Wall filtration efficiency at the beginning of the stage 1 loading is minimum ($\cong$ 44 % at 0.01 hrs) and increases to $\cong$ 50% at the end of wall filtration (at 0.5 hrs). During stage 2 loading, the wall filtration increases slightly (up to $\cong$ 50.3% at 3.8 hrs) due to changes in wall packing density caused by the continued loading of PM in the pores of the substrate wall. Wall filtration efficiency further increases during ramp up phase (up to $\cong$ 59% at 4.1 hrs) due to the increase in diffusion of PM into the pores of the substrate wall. Further, during PM oxidation, PM in the substrate wall is oxidized and hence, wall filtration efficiency approaches close to the clean wall filtration efficiency ($\cong$ 45 % at 5.45 hrs). During post loading, the wall filtration efficiency increases at a slower rate as most of the PM is filtered through the PM cake. The cake filtration efficiency is minimum at the beginning of the stage 1 loading ($\cong$ 5 % at 0.1 hrs). The rapid increase in cake filtration efficiency occurs during transition from wall filtration to cake filtration regimes when the top surfaces of the substrate wall are covered with PM. The cake filtration efficiency increases to $\cong$ 79 % at 0.5 hrs at the end of stage 1 loading. During stage 2 loading, the cake filtration efficiency increases to 94% and remains at 94% during the entire experiment. The loaded PM cake filtration efficiency in the SCR-F/CPF model is calibrated to simulate the overall filtration efficiency measured during experiments by calibrating the maximum PM cake filtration efficiency parameter (A_η) in Equation (4.42) [22, 23]

$$\eta_{cake\ loaded_{i,j}} = A_\eta \left(1 - e^{\left(\frac{3\eta_{cake_{i,j}}(1-\varepsilon_p)w_{p_{i,j}}}{2\ \varepsilon_p d_{c,cake}} \right)} \right) \tag{4.42}$$
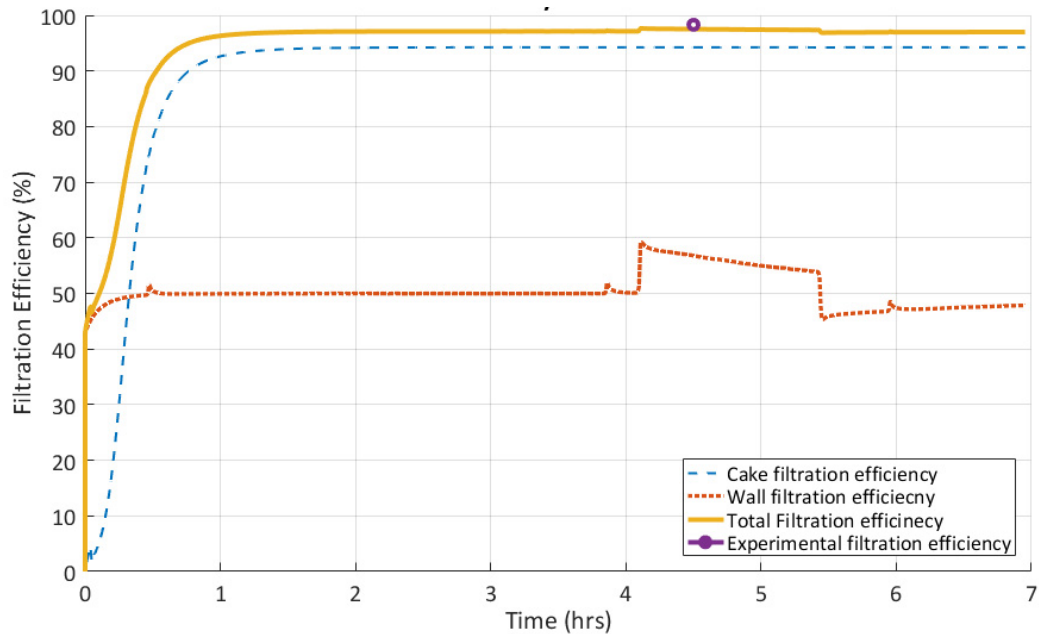
Figure 4. 21 Comparison of experimental data and simulation model total filtration efficiency and distribution of filtration efficiency into PM cake and substrate wall for PO-B10-15 experiment on mass basis

PM Mass Retained

Figure 4.22 shows the cumulative PM mass retained in the filter in comparison with the cumulative inlet PM mass, cake and wall PM masses. Most of the PM ($\cong$ 94 % at the end of stage 2 loading at 3.85 hrs) in the CPF is captured in the PM cake layer through the cake filtration as shown by the blue solid line in Figure 4.21. During stage 1 loading (< 0.5 hrs), most of the PM is captured within the pores of substrate wall (wall filtration regime) followed by the cake filtration regime (> 0.5 hrs) where in most of the incoming PM is captured as a PM cake layer on the top surface of the substrate wall. The PM mass in the substrate wall is maximum ($\cong$ 2 g) at end of stage 2 loading compared to the PM mass in the cake ($\cong$ 32.1 g). Most of the PM mass in the substrate wall is oxidized during the PM passive oxidation stage and wall PM mass is reduced to < 0.5 g. The PM accumulates at a slow rate in the substrate wall during post loading (>5.46 hrs) compared to stage 1 loading due to the presence of the PM cake layer on the top surfaces of the substrate wall which has a $\cong$ 94 % filtration efficiency shown in Figure 4.21.
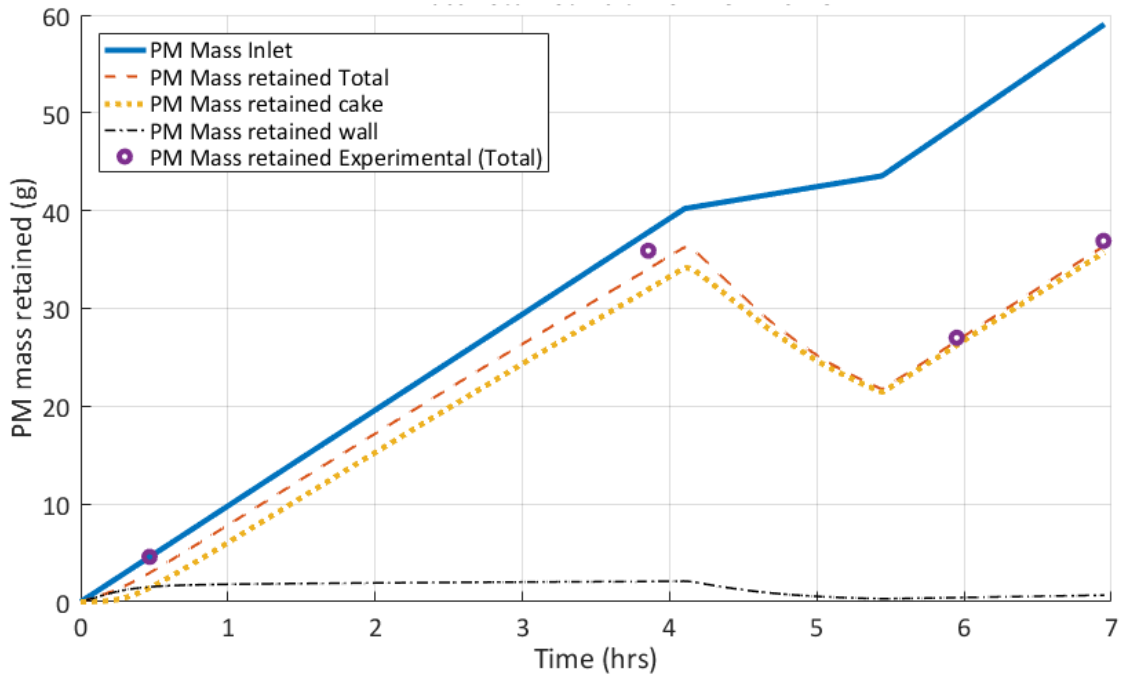
Figure 4. 22 Comparison of PM mass retained in the experimental data and simulation model along with the model cumulative for PM inlet, cake and wall PM masses for PO-B10-15 experiment.

Figure 4.23 shows the cumulative PM mass retained in the filter in comparison with the cumulative inlet PM mass and PM oxidation mass. NO_2 assisted PM oxidation (99%) is the dominant mode of PM oxidation shown by the dashed line because of the NO_2 concentration (101 ppm). The thermal (O_2) assisted PM oxidation is low (< 0.3 g) compared to NO_2 assisted PM oxidation due to the lower exhaust gas temperature during the PM oxidation (350°C). From Figure 4.23, the SCR-F/CPF model simulated the PM mass retained within the filter substrate with the maximum absolute error of 1.8 g between the experimental and the simulated PM mass retained at the end of the stage 2 loading phase of the experiment.
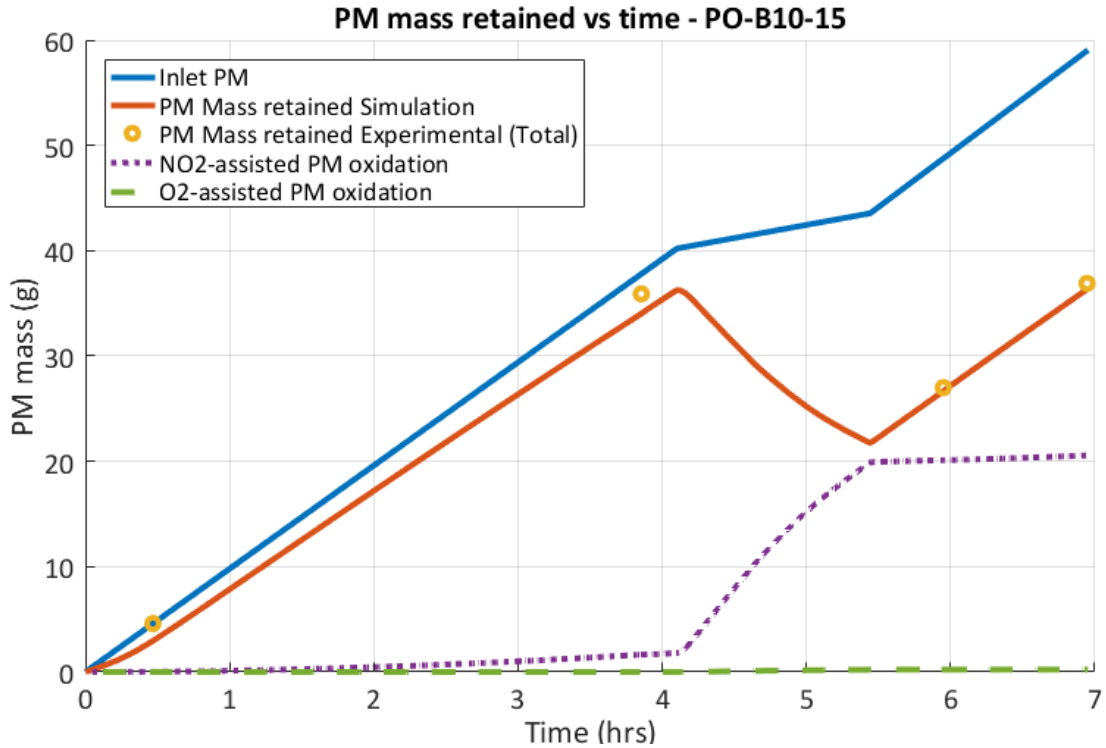
Figure 4. 23 Comparison of PM mass retained in the experimental data and simulation model along with the model cumulative for PM inlet and oxidation masses for PO-B10-15 experiment.

PM Distribution

Figures 4.24 and 4.25 show the PM mass loading distribution at the start and end of PM oxidation during the passive oxidation stage. From Figures 4.24 and 4.25, the PM loading is almost uniform (2.0 ± 0.03 g/L) at the beginning of oxidation, whereas the PM loading distribution significantly varies at the end of passive oxidation. The minimum PM mass loading is 1.1 g/L and increases to a maximum value of 1.6 g/L at the outer radius of the filter substrate. This is mainly due to the lower exhaust gas temperature at the outer radius of the filter due to the ambient convective and radiative heat transfer compared to the center of the filter substrate.
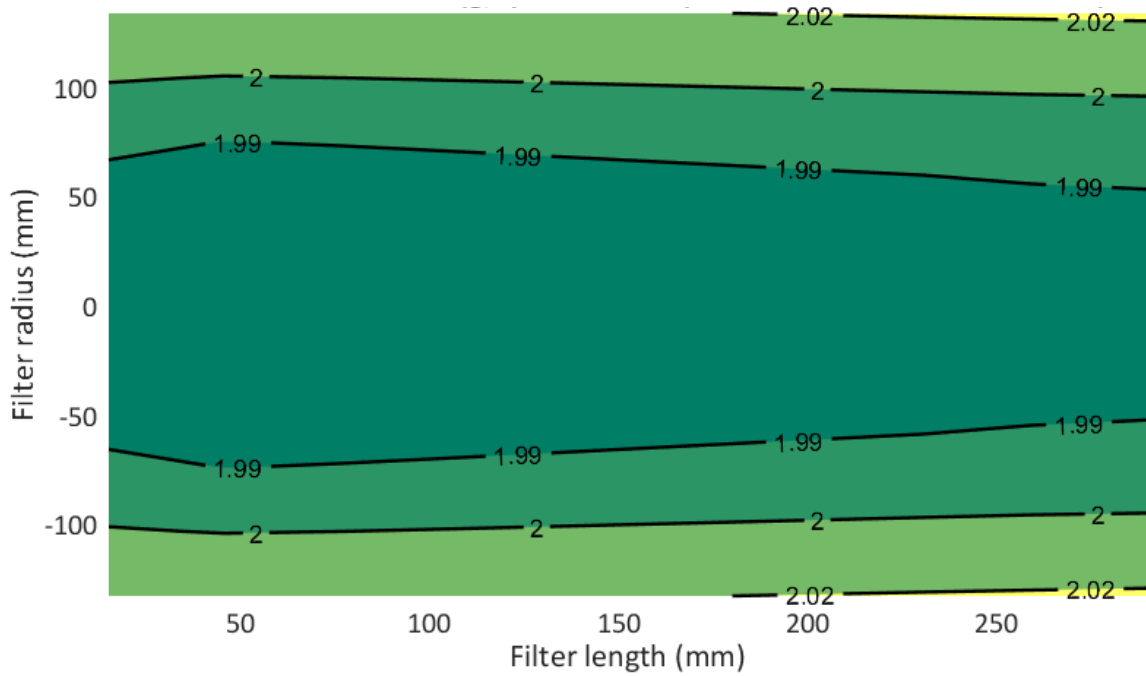
Figure 4. 24 Simulated PM mass loading distribution in g/L along axial and radial directions at 4.11 hrs. – start of passive oxidation for PO-B10-15 experiment
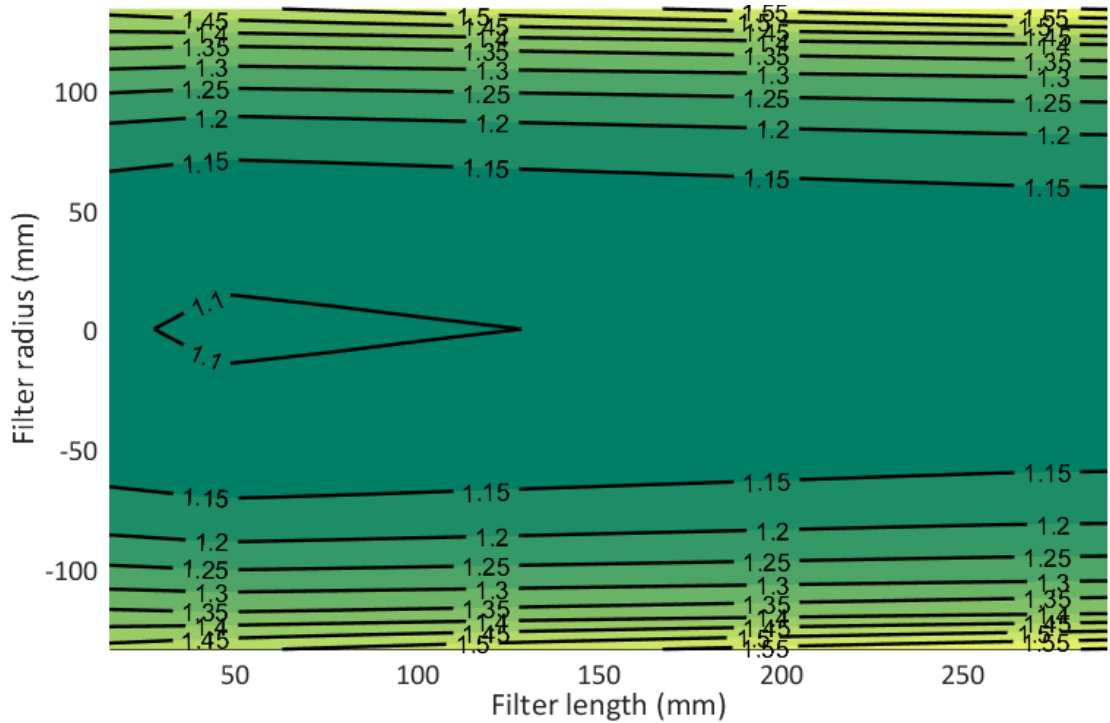
Figure 4. 25 Simulated PM mass loading distribution in g/L along axial and radial directions at 5.46 hrs - end of passive oxidation for PO-B10-15 experiment.

Figure 4.26 shows the simulated PM mass loading distribution along the axial and radial direction at the end of post loading for the PO-B10-15 experiment. From Figure 4.26, the PM loading distribution at the end of post loading is also non-uniform (1.95 to 2.4 g/L). Comparing Figure 4.25 with Figure 4.26, the non-uniform PM loading originated during PM oxidation by passive oxidation due to the temperature gradient within the filter and the non-uniform PM loading continued further during the post loading phase of the experiment.
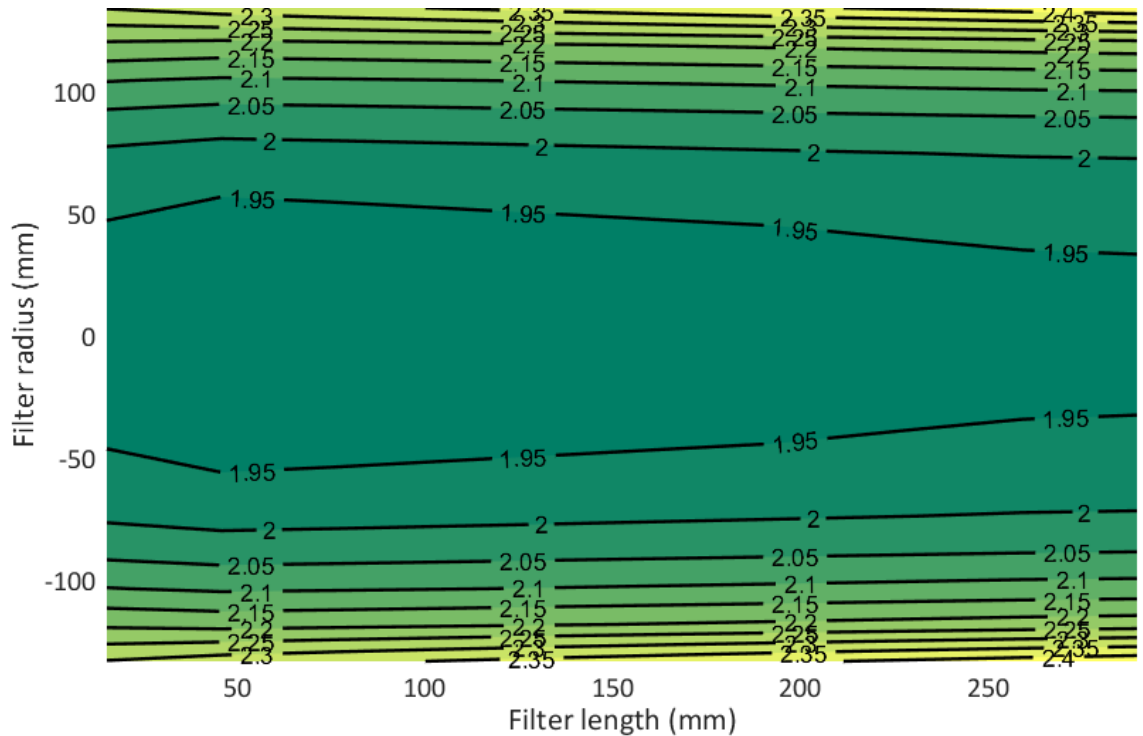
Figure 4. 26 Simulated PM mass loading distribution in g/L along axial and radial directions at 6.95 hrs -end of post loading for PO-B10-15 experiment.

Figure 4.27 shows the axial and radial distribution of PM loading measured by Foley [27] for the same engine in this study for the passive oxidation case (average CPF temperature 348°C, NO_2 concentration of 196 ppm and ULSD fuel type) with the end of passive oxidation PM mass loading of 3.25 g/L. Comparing Figures 4.27 and 4.25, the simulation model data shows the uniform filter loading along the length the filter whereas the experimental data in Figure 4.27 shows the uniform PM loading up to axial length ratios of 0.7 (filter length < 215 mm). For axial length ratios > 0.7 (filter length > 215 mm), the experimental data shows an increase in PM loading close to the outlet end of the substrate (axial length ratios > 0.7 or filter length > 215 mm). This may be explained by PM cake

and ash particle transport mechanisms (regeneration-induced and flow-induced) proposed by Sappok et al. [66] using the optically-accessible filter core sample in a catalyst bench reactor. During passive oxidation of PM, the particle in contact with washcoat oxidizes the PM cake and reduces the adhesive force [66] which aids in particle detachment and transports towards the plugged end of the filter substrate. This particle transport mechanism is not included in the SCR-F/CPF model. The PM loading experimental data close to the inlet (axial length ratios < 0.05) and outlet sections (axial length ratio > 0.97) are considered to be less accurate due to the error associated with the scanning procedure and PM loading analysis methodology around the channel plugs [28]. The radial distribution of PM loading with the experimental data shows a slight reduction in radially outward (subplot 20d - diameter of 231-267 mm) direction. This may be due to the uncertainties associated with the terahertz analyzer ability to scan at the outer surfaces [28]. Both the simulation model and experimental data show relatively uniform PM loading radially from 80 mm radius to the centerline of the filter. This is consistent with uniform temperature trends observed from the experimental data and the SCR-F/CPF model results.
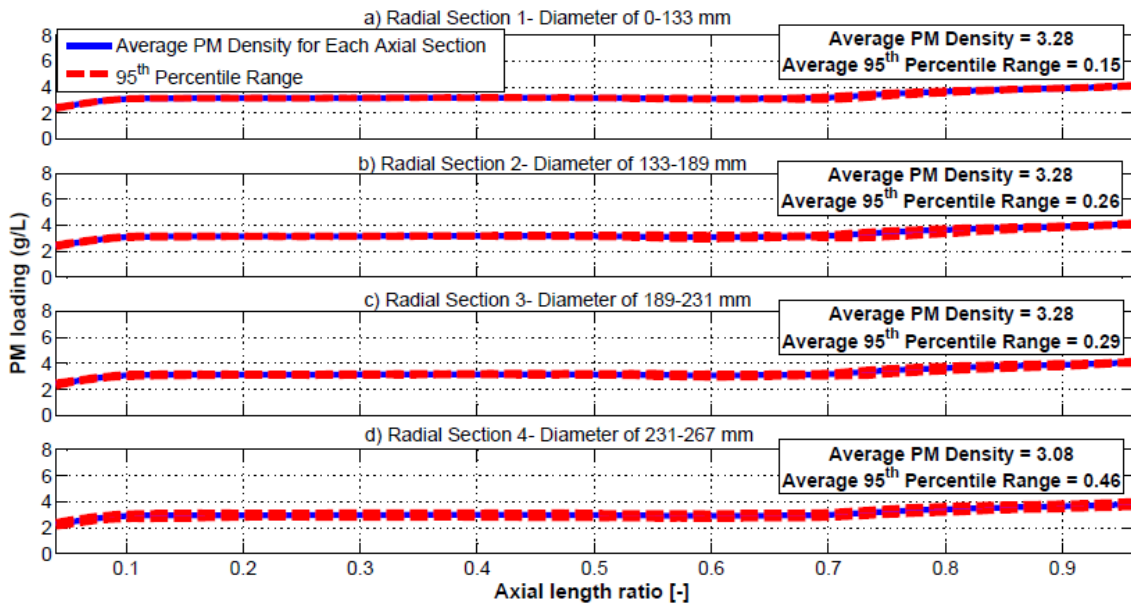
Figure 4. 27 Test 8 end of passive oxidation (PO) phase axial and radial PM distribution measured - adapted from reference [27] for 2007 ISL engine, axial length ratio of 1.0 corresponds to 305 mm filter length, axial uniformity index for plots a –d are 0.91, average radial uniformity index = 0.97 and average angular uniformity index = 0.98

Pressure Drop

Figure 4.28 shows the comparison of the experimental and simulated total pressure drop across the CPF and its components for PO-B10-15 experiment. From Figure 4.28, the simulated pressure drop values are comparable with experimental data with a maximum absolute error of $\cong 0.3$ kPa at 4.07 hrs. The wall and PM cake contribute the most to the overall pressure drop after loading to 2.5 hours. The clean wall pressure drop is $\cong 1.9$ kPa at the beginning of stage 1 loading (< 0.1 hrs) and increases to $\cong 2.5$ kPa at 0.4 hrs as the PM accumulates in the pores of the substrate wall. Once the pores in the top slab of the substrate wall is saturated with PM, the wall filtration is transitioned into cake PM filtration regime (> 0.4 hrs). During stage 2 loading, the wall pressure drop is almost constant and decreases during PM oxidation as the PM in the pores of the wall is oxidized due to NO_2 assisted PM oxidation. In the case of the cake pressure drop, during the cake filtration regime (> 0.4 hrs), the cake pressure drop value increases linearly proportional to the PM loading up to $\cong 1.9$ kPa at 4.07 hrs. During the PM oxidation by passive oxidation, the cake pressure drop decreases significantly (1.9 to 0.1 kPa). Also, the slope of the cake pressure drop curve and total pressure drop curve (simulation and experimental) changes during PM oxidation by passive oxidation. This could be attributed to varying PM oxidation rates between wall and cake as observed by earlier studies [35-36] and also the change in permeability of the PM cake layer due to the potential damage in the PM cake as described in the earlier section of this thesis. The SCR-F/CPF model is able to account for both of these effects and is able to simulate the varying pressure drop trend during the PM passive oxidation stage. Without the damage cake permeability model (i.e with constant cake permeability assumption), the simulated total pressure drop values will be over the experimental pressure drop values. From Fig. 4.28, the model showed the capability to simulate experimental pressure drop using the PM cake damage permeability model under steady state operating conditions. However, further validation of the new cake permeability model is needed to understand its capability to distinguish the variable wall oxidation rate and PM cake damage during steady state and transient drive cycles.
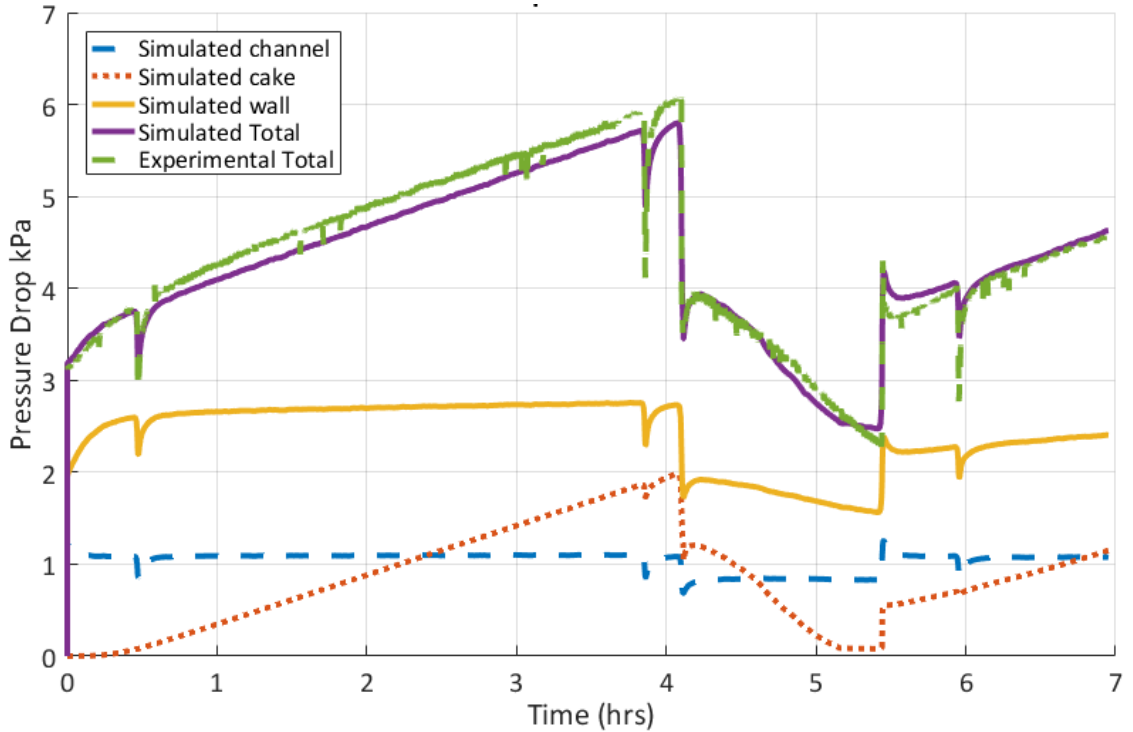
Figure 4. 28 Comparison of experimental and simulated total pressure drop across CPF and its components for PO-B10-15 experiment

Wall and Cake Permeability

Figure 4.29 shows the simulated wall and cake permeability (right axis) along with the PM mass retained (left axis) for PO-B10-15 experiment. From Figure 4.29, the wall permeability during stage 1 loading (< 0.5 hrs) decreases quickly from the clean wall permeability as the PM accumulates in the substrate wall (wall filtration). Upon filling of wall pores, during stage 2 loading, the wall permeability is almost constant (6.77E-14 m^2 @ 3.8 hrs) following the constant wall PM mass retained in the substrate wall. During the PM passive oxidation stage, the loaded wall permeability increases up to 9.2 E-14 m^2 and approaches close to the clean wall permeability due to the oxidation of PM in the substrate wall. Upon completion of PM oxidation, during stage 3 and 4 loading, the wall permeability reduces at slower rate as the PM accumulates within the substrate wall. This slow change in wall permeability is due to the presence of PM cake layer which has an $\cong$ 97% filtration efficiency over the top of the substrate wall which filters most of incoming PM to the CPF.

Comparing Figure 4.29 with Figure 4.28, the wall permeability affects the substrate wall pressure drop of the CPF. At the beginning of the loading (< 0.5 hrs), the wall pressure drop increases as the permeability of the wall reduces due the PM accumulation within the pores of the substrate wall. The wall pressure drop is almost constant due to the constant wall permeability during stage 2 loading. The wall pressure drop reduces during PM oxidation resulting in increased permeability of the substrate wall due to the oxidation of PM in the pores of the substrate wall. During stage 3 and 4 loading, the wall pressure drop increases as the wall permeability reduces due to the slow accumulation of PM in the substrate wall. From Figure 4.29, the PM cake permeability is almost constant during stage 1 and 2 loading. At the start of the PM passive oxidation stage, permeability increases slightly (from 6.6E-15 to 8.3E-15 m2) due to the change in mean free path length of the gas and was simulated using the Equation 4.19 of the cake permeability model. During PM oxidation (4.87 to 5.44 hrs), the permeability of the PM cake increases due to the damage in the PM cake layer as explained in SCR-F/CPF model development section (Section 4.5). The damage permeability model determines the initiation of the PM cake damage and the cake permeability model calculates the damage variable d (Equation 4.28) during the PM passive oxidation stage. The damage variable d is calculated using the current mass of the PM cake after applying the delta mass value ($m_{cake\ corr}$). The delta mass value for passive oxidation experiment is calculated using the Equation 4.30. The increase in permeability due to the damage in the PM cake is calculated from the Equation 4.31.
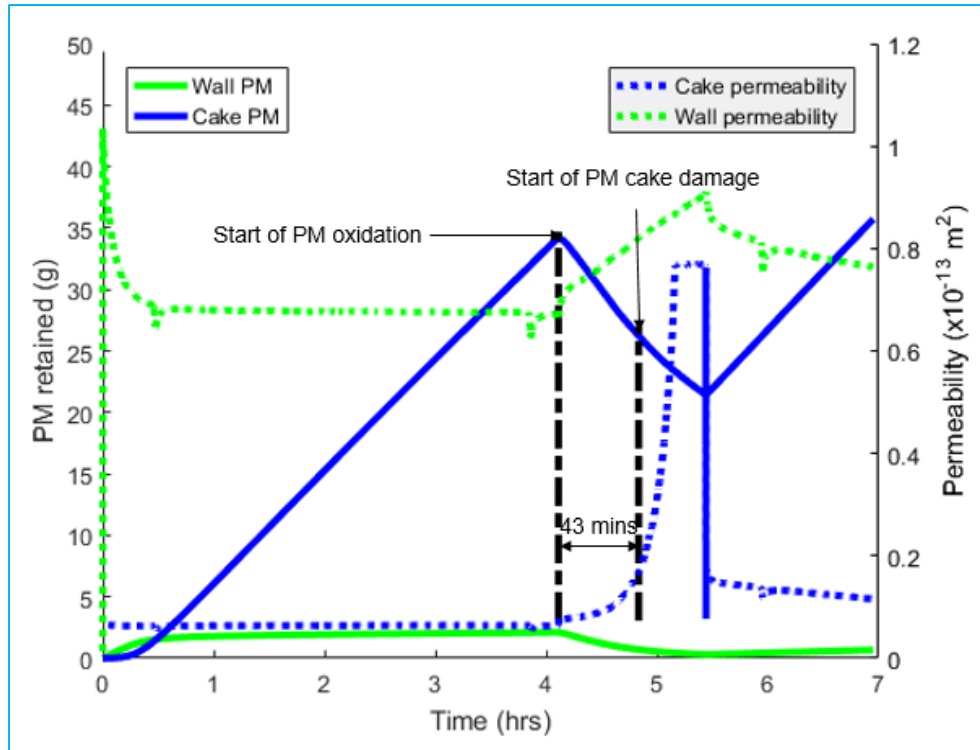
Figure 4. 29 Simulated wall and cake permeability (right axis) along with the PM mass retained (left axis) for PO-B10-15 experiment
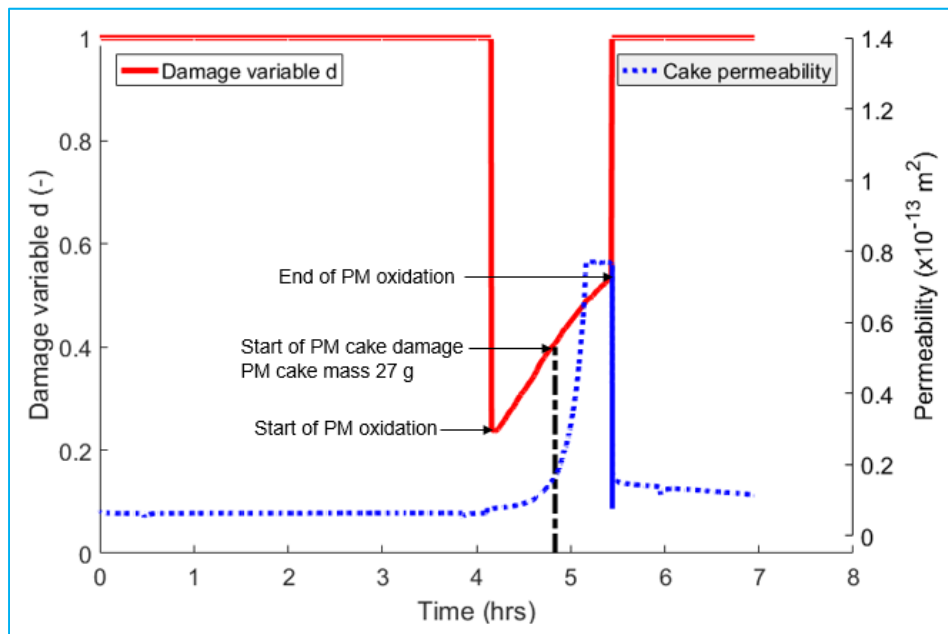
Figure 4. 30 Simulated damage variable (left axis) and cake permeability (right axis) during PM oxidation for PO-B10-15 experiment

Figure 4.30 shows the simulated damage variable (d in Equation 4.28) and PM cake permeability (defined in Equation 4.31) during the PM passive oxidation stage of PO-B10-15 experiment. The delta mass offset value for PO-B15-15 experiment is $\cong$ -2 g (at ln(Overall PM reaction rate) of $\cong$ -8.88 1/s) as shown in Figure 4.8. From Figure 4.29, the damage variable at the beginning of the PM oxidation is $\cong$ 0.22 (at 4.11 hrs, PM cake mass $\cong$ 36 g, $m_{cake\ corr}$ $\cong$ 34 g). Further into the PM oxidation, the damage variable increases proportional to the PM cake mass retained. At cake PM masses less than $\cong$ 27 g (at 4.83 hrs, start of PM cake damage, $m_{cake\ corr}$ $\cong$ 25 g) and the damage variable has values greater than $\cong$ 0.40 and the permeability values increase rapidly from 1.6E-14 to 7.71E-14 m2 ($\cong$ 5 times the initial permeability value).   This rapid increase in cake permeability is mainly due to the exponential relationship of permeability with the damage variable as shown in Figure 4.12 of the damage permeability model and it is due to the damage in PM cake layer based on the model.

The damage in the PM cake layer causes almost near zero cake pressure drop at the end of PM oxidation as shown in Figure 4.28 (Time = 5.4 hrs, cake delta P < 0.1 kPa). This is mainly due to the increased permeability of the damaged PM cake layer causing low resistance to the gas flow in the CPF. Upon completion of PM oxidation, during stage 3 and 4 loading, the PM cake permeability reduces at a slower rate. The PM cake permeability during stage 3 and 4 loading is higher than that of stage 2 loading. This increased permeability is mainly due to the presence of the damaged PM cake layer from the PM passive oxidation stage causing low flow resistance in the CPF. Further in to the stage 3 and 4 loading, the damaged PM cake layer is refilled with incoming PM causing recovery of the damaged PM cake layer. In the SCR-F/CPF model, this damage recovery was simulated using the linear permeability Eqn. D.1 explained in Appendix D.

Comparing the permeability of the wall and cake in Figure 4.29, the permeability of the cake is $\cong$ 0.11 of the wall during stage 1 and stage 2 loading. During the PM passive oxidation stage, the wall permeability increases instantly as soon as passive oxidation test conditions are achieved whereas the cake permeability is almost constant for $\cong$ 43 minutes (at $\cong$ 4.8 hrs) into the PM oxidation and then increases rapidly. This time delay is attributed to time taken to initiate damage in the PM cake layer. The increase in wall permeability is proportional to the reduction in wall PM mass whereas the cake

permeability is constant until the PM cake mass reach 27 g and then increases rapidly. During stage 3 and 4 loading, the PM cake permeability reduces as the PM cake mass loading increase and it is ≅ 15% of the wall permeability at the end of stage 4 loading (at 6.9 hrs).

Comparing Figures 4.29 with 4.28, the cake pressure drop increases during stage 1 and 2 loading as the PM accumulates in the PM cake layer at constant cake permeability. During the PM passive oxidation stage, the cake pressure drop reduces following the oxidation of PM in the cake layer and also due to the increased permeability of the PM cake layer caused by the damage in the PM cake layer. Upon completion of the PM passive oxidation stage and during stage 3 and 4 loading, the cake pressure drop increases as the PM accumulates in the cake layer and there is also reduced permeability of PM cake layer attributed to damage recovery of PM cake layer as simulated by the cake permeability model.

4.9.2 Active Regeneration Experiments

The active regeneration experimental data used for the model calibration are listed in Table 3.4. The filter substrate temperatures during active regeneration experiments are in the range of 450 - 600°C which is higher than the passive oxidation experiments explained in the previous section. The active regeneration experiments are short in duration (6 to 39 minutes) because of the high PM oxidation rates. The PM oxidation during active regeneration is governed by thermal (O_2) assisted PM oxidation mechanism. The SCR-F/CPF model simulation data are presented for one active regeneration experiment (AR-B10-1) in order to consider the higher filter substrate temperature and short PM oxidation duration and its effect on the heat transfer, temperature and filter PM loading distribution within the filter and pressure drop characteristics of the CPF. The results are presented in the following section.

Filter Outlet Temperature

Figure 4.31 shows the comparison of model outlet gas temperature with the experimental outlet gas temperature along with the CPF inlet temperature measured upstream of the

CPF. From Figure 4.31, the simulation prediction difference is within 7°C excluding the temperature spikes related to the experimental procedure and transition phase of moving in and out of the AR phase of the experiment.
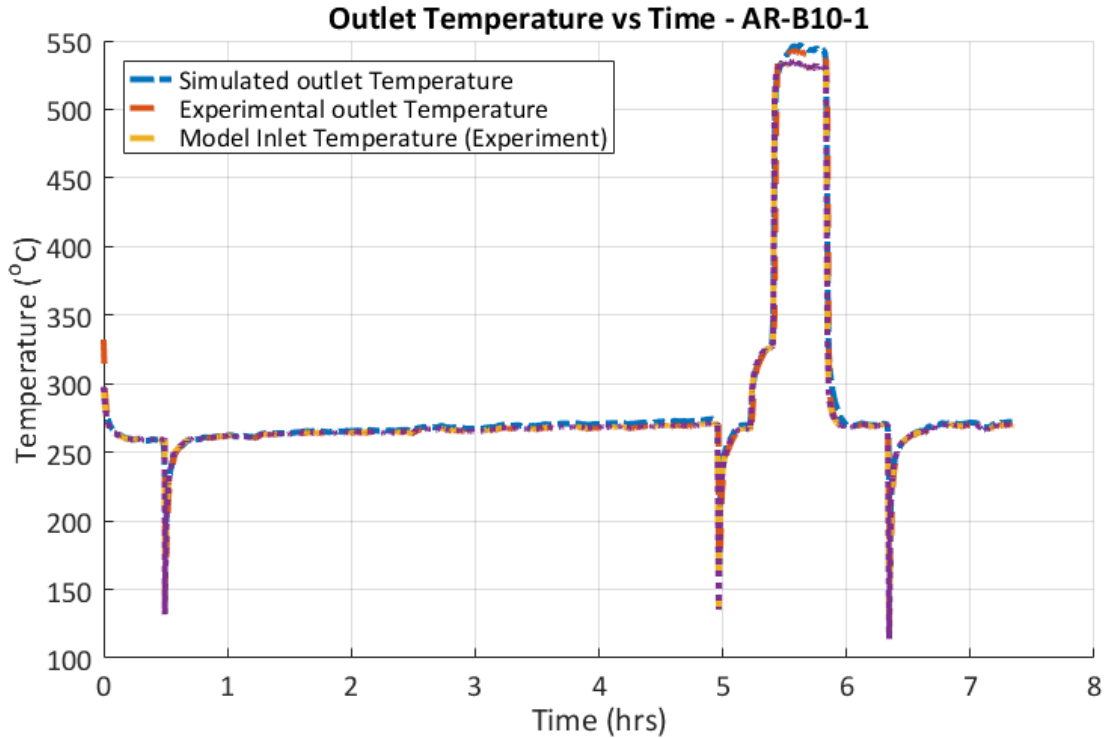
Figure 4. 31 Comparison of experimental and model CPF outlet gas temperature with model input CPF inlet gas temperature for AR-B10-1 experiment

Temperature Distribution

Figure 4.32 shows the experimental temperature distribution and Figure 4.33 shows the simulated temperature distribution for AR-B10-1 experiment at 5.63 hrs (15 minutes after start of fuel dosing). From Figure 4.32, the experimental filter substrate temperature shows an increase in temperature (10-12°C at filter radiuses below 40 mm) axially due to the local PM oxidation and the substrate temperature close to the wall shows a lower increase in temperature axially ($\cong$ 2°C) due to the dominant convection and radiative heat loss to the ambient compared to the local PM oxidation. The radial variation in temperature is up to $\cong$ 40°C. This is mainly because of the inlet temperature distribution caused by the thermal boundary layer as explained in section 3.5. From Figure 4.33, the SCR-F/CPF simulation model also shows an increase in temperature ($\cong$ 13°C) in the axial direction

due to PM and HC oxidation within the filter and the substrate temperature close to the wall shows lower increase in temperature axially ($\cong 4^{\circ}C$). The maximum variation in radial temperature distribution is up to $\cong 41^{\circ}C$. Comparing Figures 4.32 and 4.33, the simulated temperature distribution closely follows experimental data with maximum RMS error of 3.1 $^{\circ}C$.
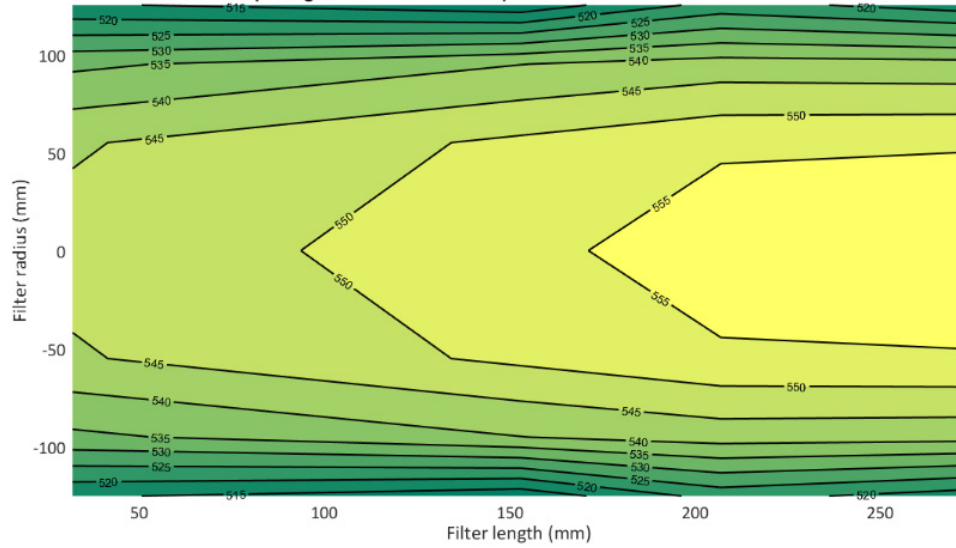
Figure 4. 32 Experimental temperature distribution in °C for AR-B10-1 experiment at 5.63 hrs. (15 minutes after start of fuel dosing)
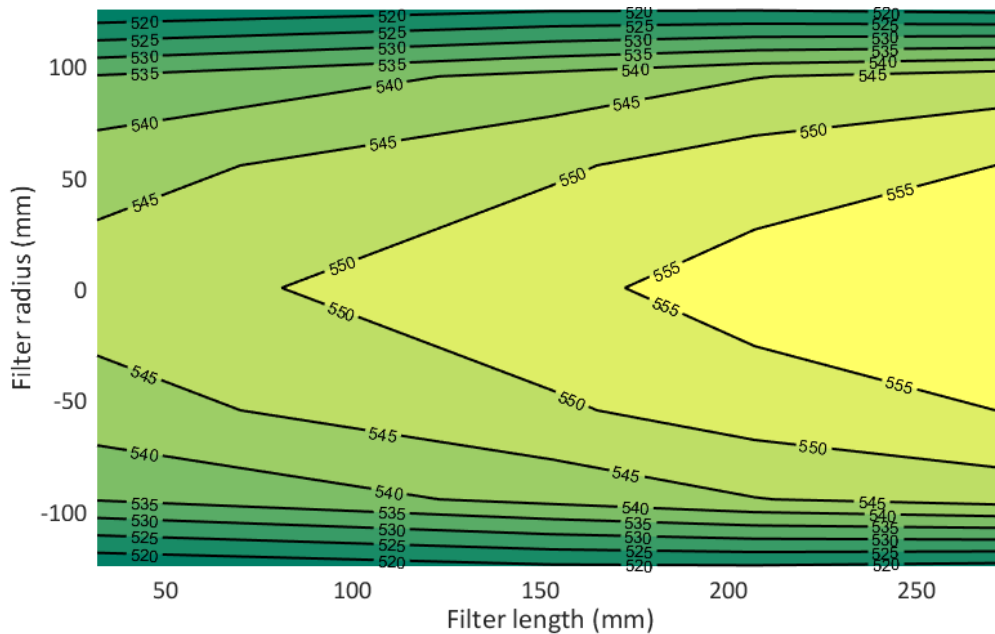
Figure 4. 33 Simulated temperature distribution in °C for AR-B10-1 experiment at 5.63 hrs (15 minutes after start of fuel dosing)

Filtration

Figure 4.34 shows the comparison of the experimental and simulation model total filtration efficiency and the filtration efficiency of the PM cake and the substrate wall for the AR-B10-1 experiment. From Figure 4.33, the total filtration efficiency simulated by the SCR-F/CPF model is 97% and it is comparable with the experimental data measured during stage 2 loading (98% - shown as purple 'o' marker). Wall filtration efficiency at the beginning of the stage 1 loading is minimum and similar to PO-B10-15 experiment ($\cong$ 44 % at 0.01 hrs) and increases to $\cong$ 50% at the end of wall filtration (at 0.5 hrs). During stage 2 loading, the wall filtration increases slightly (up to $\cong$ 50.3% at 4.9 hrs) due to changes in wall packing density caused by the continued loading of PM in the pores of the substrate wall. Wall filtration efficiency further increases during ramp up phase (up to $\cong$ 59% at 5.2 hrs) due to the increase in diffusion of PM into the pores of substrate wall. Further, during PM oxidation by active regeneration, PM in the substrate wall is oxidized and hence, wall filtration efficiency approaches close to the clean wall filtration efficiency ($\cong$ 44 % at 5.9 hrs). During post loading, the wall filtration efficiency increases at a slower rate as most of the PM is filtered through the PM cake. The PM cake filtration efficiency trends are similar to PO-B10-15 experiment and maximum efficiency observed was 94% during stage 2 loading.
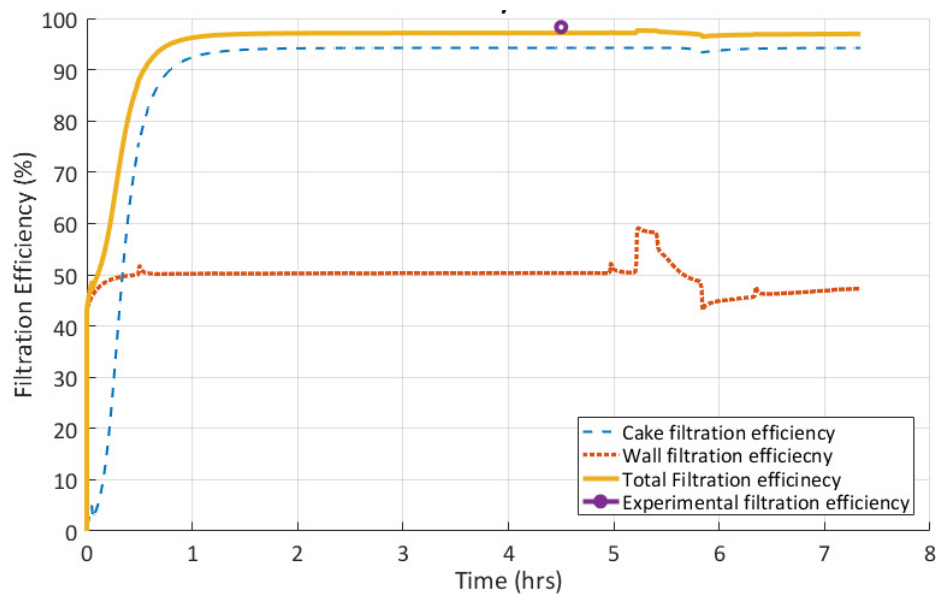
Figure 4. 34 Comparison of experimental data and simulation model total filtration efficiency and distribution of filtration efficiency into PM cake and substrate wall for AR-B10-1 experiment

PM Mass Retained

Figure 4.35 shows the cumulative PM mass retained in the filter in comparison with the cumulative inlet PM and PM oxidation masses. From Figure 4.35, thermal (O_2) assisted PM oxidation is the dominant mode of PM oxidation shown by the green dotted line because of the increased reaction rate over the loading rate due to the higher exhaust gas temperature (530^oC) and O_2 concentration(7.8 %). The overall PM oxidized (at the end of post loading at 7.33 hrs) by thermal (O_2) assisted PM oxidation is 91 % whereas the NO_2 assisted PM oxidation is 9 % due to the lower NO_2 concentration in the exhaust gas. The maximum absolute difference between the experiment and the simulation for PM mass retained is 0.9 g at the end of the stage 1 loading condition.
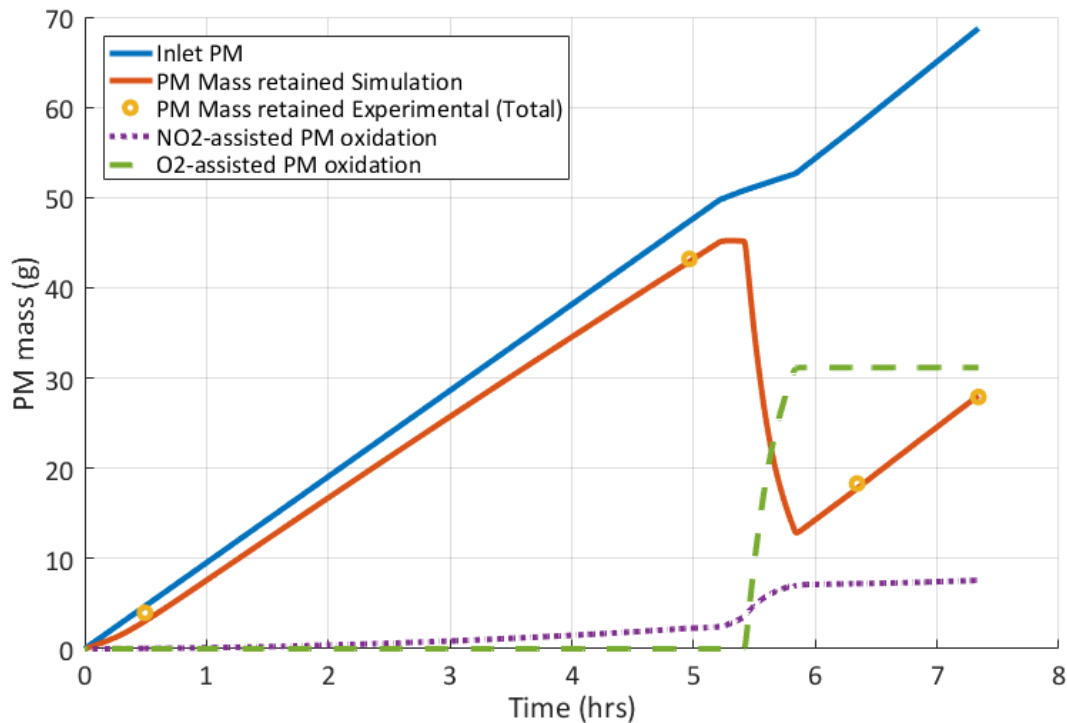
Figure 4. 35 Comparison of PM mass retained in the experimental data and simulation model along with the cumulative PM inlet and oxidation masses for AR-B10-1 experiment

Figure 4.36 shows the cumulative PM mass retained in the filter in comparison with the cake and wall PM masses. The majority of the PM filtration takes place through the cake filtration regime shown by the yellow solid line in Figure 4.36. During stage 1 loading (< 0.5 hrs), most of the PM is captured within the pores of substrate wall (wall filtration

regime) followed by the cake filtration regime (> 0.5 hrs) where most of the incoming PM is captured as a PM cake layer on the top surface of the substrate wall. The PM mass in the substrate wall is maximum ($\cong$ 2.2 g) at end of stage 2 loading compared to the PM mass in the cake ($\cong$ 41 g at 4.98 hrs). Most of the PM mass in the substrate wall is oxidized during PM oxidation and the wall PM mass is reduced to < 0.2 g. The PM accumulates at a slow rate in the substrate wall during post loading (> 5.9 hrs) compared to stage 1 loading. This is due to the presence of the PM cake layer on the top surfaces of the substrate wall.
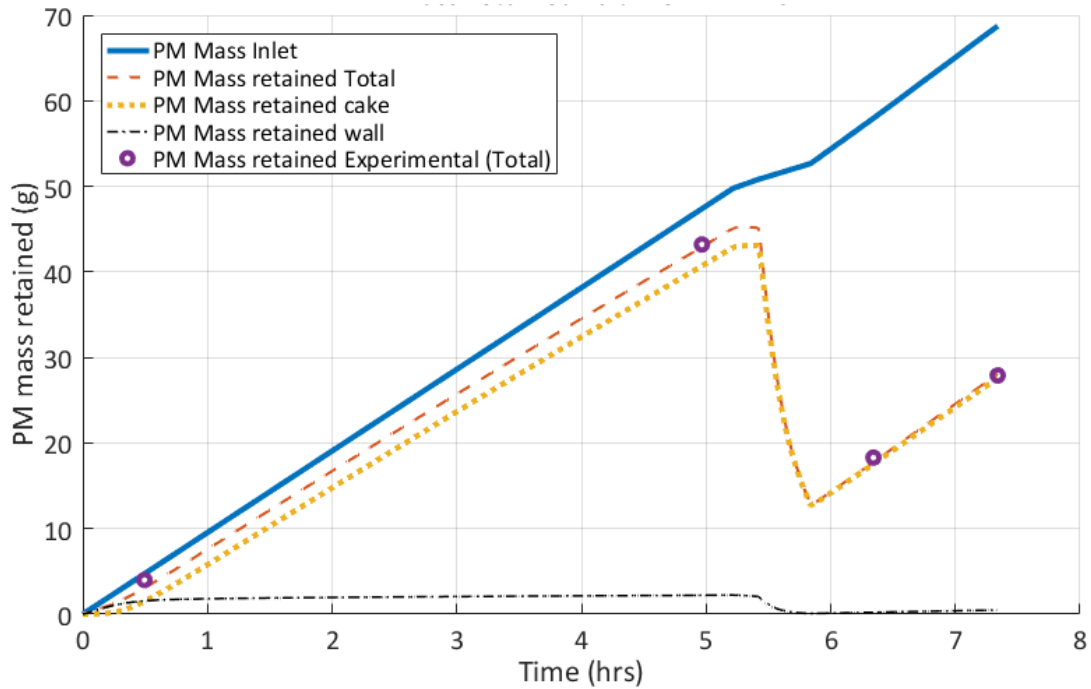
Figure 4. 36 Comparison of PM mass retained in the experimental data and simulation model along with the model cumulative for PM inlet, cake and wall PM masses for AR-B10-1 experiment

PM Distribution

Figure 4.37 shows the PM mass loading distribution along axial and radial directions at the end of PM oxidation (at 5.82 hrs) by active regeneration for AR-B101 experiment. From Figure 4.37, the PM loading distribution varies significantly along the radial direction. The PM loading is less than 0.6 g/L up to a filter radius of 80 mm and increases to a maximum value of 1.8 g/L at the outer radius of the filter. This is mainly due to the lower exhaust gas

temperature at the outer radius of the filter (as shown in Figure 4.33) due to the convective and radiative heat losses compared to the center of the CPF.
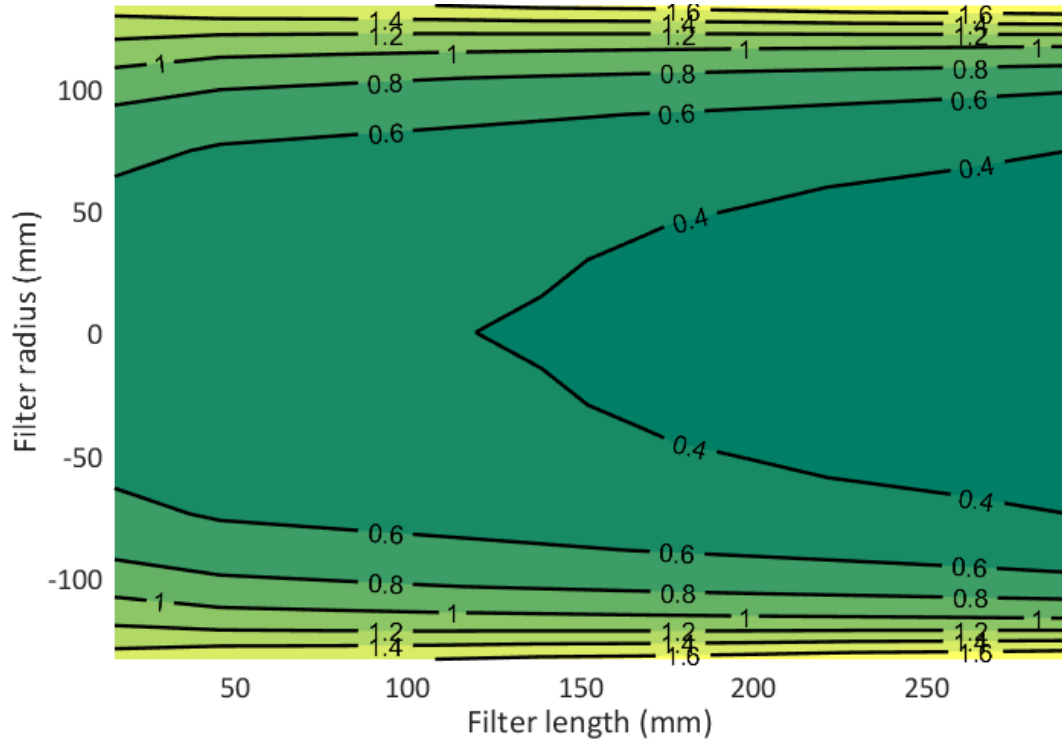
Figure 4. 37 Simulated PM mass loading distribution in g/L along the axial and radial directions at 5.82 hrs (end of PM oxidation by active regeneration) for AR-B10-1 experiment

Figure 4.38 shows the axial and radial distribution of PM loading measured by Foley [27] for a similar active regeneration experiment (526°C active regeneration temperature and 7.5% O_2 concentration at CPF inlet) with the post active regeneration PM mass loading of 2.22 g/L (PM loading before start of active regeneration was 3.06 g/L) using ULSD fuel. Comparing Figures 4.37 and 4.38, the SCR-F/CPF model and the experimental PM loading distribution shows the uniform loading of the filter substrate at the end of PM oxidation for the active regeneration experiment up to filter radius of 66 mm. The PM loading distribution in the simulation (Figure 4.37) shows the small axial gradient between 0 to 66 mm filter radiuses (0.4 to 0.6 g/L). However, it is similar to the 95% range given in Figure 4.38 (0.14 g/L for filter radiuses up to 66 mm). Hence, considering the small axial variation in the experiment and simulation data, the PM loading is uniform for simulation

and experimental data up to filter radiuses 66 mm. The experimental PM loading trend shows an increase in PM loading towards the end of the filter substrate (5 % higher than the average filter substrate loading). However, the SCR-F/CPF model shows a decrease in the PM loading ($\cong 0.3$ g/L) trend till the filter substrate radiuses < 120 mm and an increase in PM loading for the filter radiuses > 120 mm. The decrease in PM loading for filter radiuses less than 120 mm in the SCR-F/CPF model could be attributed to increased PM oxidation due to the higher temperature in the axial direction towards the middle to the end sections of the filter as shown in the temperature distribution plot (Figure 4.32). The SCR-F/CPF model shows a consistent increase in PM loading towards the outer section of the filter substrate consistent with the reduction in the filter substrate temperature. The PM loading increases towards the outlet end of the filter could be explained by PM cake and ash transport mechanisms proposed by Sappok et al [66] as explained in passive oxidation results section. The experimental PM loading towards the outer most edge of the filter substrate shows a decrease in PM loading due to the lack of measurement capability of the terahertz wave scanner close to the wall surfaces.
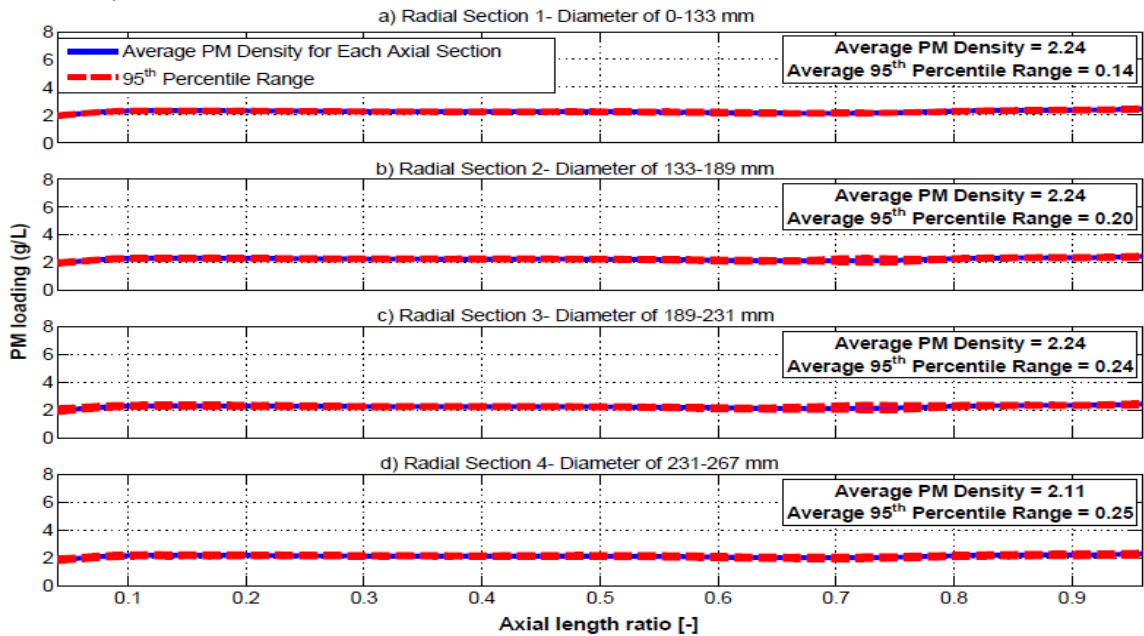
Figure 4. 38 Test 4 end of active regeneration (AR) phase axial and radial PM distribution measured - adapted from reference [27] for 2007 ISL engine, axial length ratio of 1.0 corresponds to 305 mm filter length, axial uniformity index for plots a –d are 0.97 average radial uniformity index = 0.98 and average angular uniformity index = 0.98

Pressure Drop

Figure 4.39 shows the comparison of the experimental and simulated total pressure drop across the CPF and its components for AR-B10-1 experiment. The simulated pressure drop values are in good agreement with experimental data with a maximum absolute difference of $\cong$ 0.3 kPa during the AR ramp phase of the experiment (5.3 hrs). The wall pressure drop trend during stage 1 and 2 loading is similar to the PO-B10-15 experiment. The wall pressure drop decreases (1.9 kPa at 5.8 hrs) during PM oxidation by active regeneration as the PM in the pores of the wall is oxidized due to thermal O_2 assisted PM oxidation. In the case of the cake pressure drop, time when the pores in the substrate wall are filled with PM (> 0.5 hrs), the PM cake layer begins to form over the top surface of the substrate wall and the resultant PM cake pressure drop value increases linearly proportional to PM loading during stage 1 and 2 loading phase of the experiment.
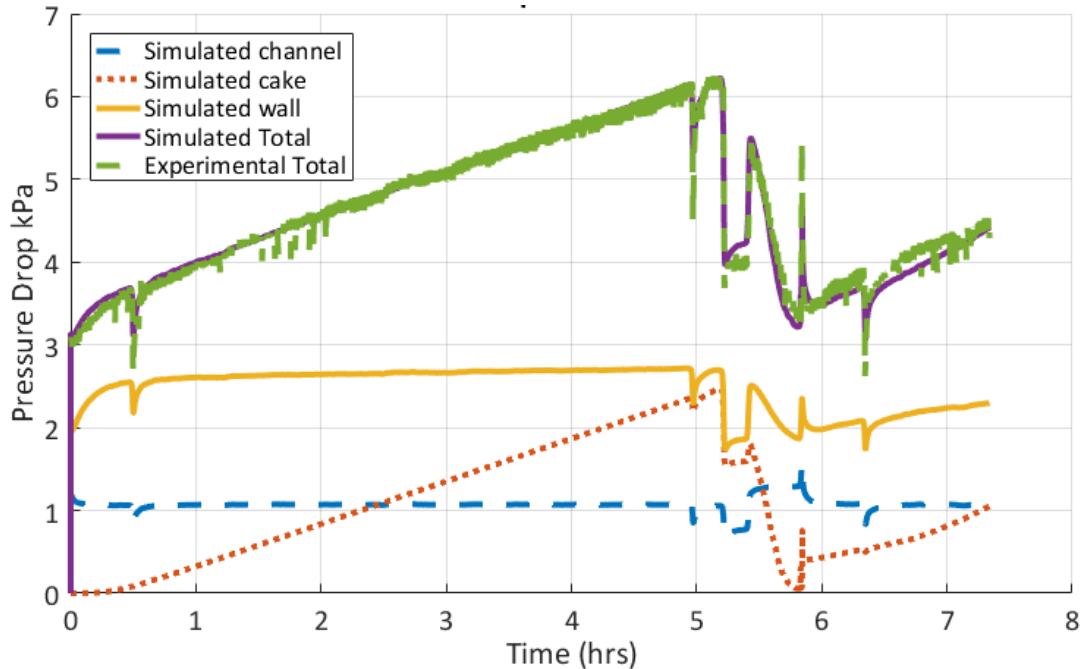
Figure 4. 39 Comparison of experimental and simulated total pressure drop across CPF and its components for AR-B10-1 experiment.
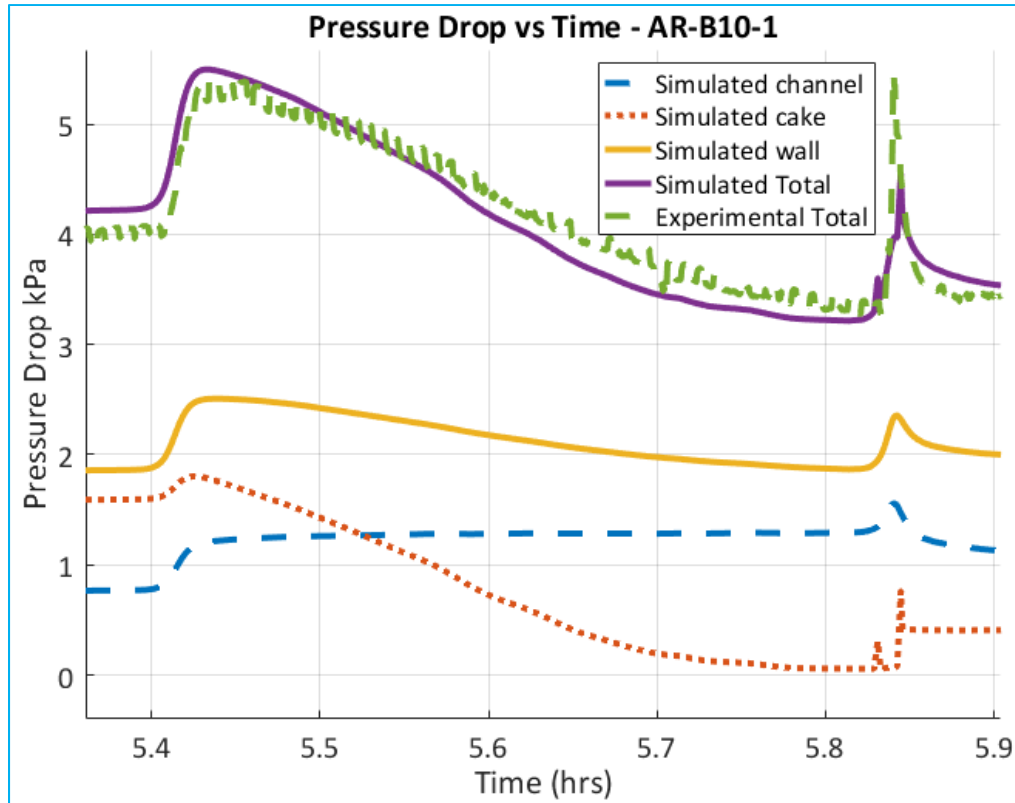
Figure 4. 40 Comparison of experimental and simulated total pressure drop across CPF and its components for AR-B10-1 experiment during PM oxidation (5.38 to 5.82 hrs)

Figure 4.40 shows the pressure drop trend during PM oxidation during active regeneration stage (5.38 to 5.82 hrs). The cake pressure drop reduces significantly (1.8 to 0.1 kPa). Also, the slope of the cake pressure drop curve and total pressure drop curve (simulation and experimental) changes during PM oxidation. This can be attributed to varying PM oxidation rates between wall and cake (5.43 to 5.7 hrs) as observed by the earlier researchers [35-36] and also due to the change in permeability of the PM cake layer due to the damage in the PM cake as described in the earlier section of this thesis (5.7 to 5.82 hrs). The SCR-F/CPF model is able to account for both of these effects and is able to simulate the varying pressure drop trend during PM oxidation.

Wall and Cake Permeability

Figure 4.41 shows the simulated wall and cake permeability (right axis) along with the PM mass retained (left axis) for AR-B10-1 experiment. From Fig. 4.41, the wall and cake

permeability curves are similar to the PO-B10-15 experiment during stage 1 and stage 2 loading as shown in Figure 4.29. During the PM oxidation by active regeneration (> 5.38 hrs), the wall permeability increases up to 1.136E-13 m^2 due to the oxidation of PM in the substrate wall. Upon completion of PM oxidation, during stage 3 and 4 loading, the wall permeability decreases at a slower rate as the PM accumulates in the substrate wall. This slow change in wall permeability is mainly due to the presence of the PM cake layer on the substrate wall which filters most of incoming PM to the CPF. Comparing Figures 4.41 and 4.39, the wall permeability and wall pressure drop curves are similar to the PO-B10-15 experiment during stage 1 and 2 loading. During PM oxidation, the wall pressure drop reduces following the increased permeability of the substrate wall due to the oxidation of PM in the pores of the substrate wall. During stage 3 and 4 loading, the wall pressure drop increases as the wall permeability reduces due to the accumulation of PM in the substrate wall.
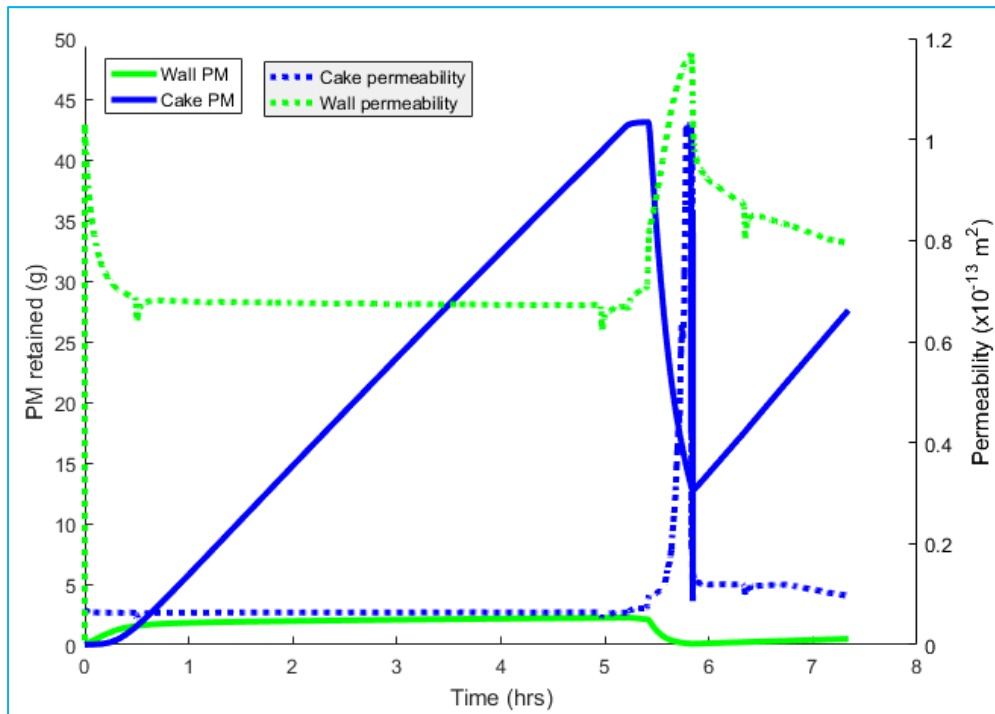
Figure 4. 41 Simulated wall and cake permeability (right axis) along with the PM mass retained (left axis) for AR-B10-1 experiment

The PM cake permeability is almost constant during stage 1 and 2 loading. At the beginning of the PM oxidation (at 5.5 hrs), the cake permeability increases slightly (from

7.3E-15 to 1.05E-14 m^2) due the changes in mean free path length of the gas. Further into the PM oxidation, at cake PM masses less than 25 g (> 5.6 hrs), permeability values increase rapidly from 1.403E-14 to 1.028E-13 m^2 ($\cong$ 7 times increase). This increase in cake permeability is attributed to the damage in the PM cake layer and was simulated using the cake permeability model. The damage in the PM cake layer causes almost near zero cake pressure drop (cake delta P < 0.1 kPa) at the end of PM oxidation as shown in Figure 4.40 ($\cong$ 5.8 hrs). Upon completion of the PM oxidation, during stage 3 and 4 loading, the PM cake permeability reduces at a slower rate attributed to damage recovery of the PM cake layer as simulated by the cake permeability model. The reduced permeability of the PM cake layer along with the PM accumulation during stage 3 and 4 loading leads to an increase in cake pressure drop as shown in Figure 4.39.

Comparing the permeability of the wall and cake, the permeability curves during stage 1, 2, 3 and 4 loading are similar to those of PO-B10-15 experiment. During the PM oxidation during active regeneration stage, the wall permeability increases as soon as the active regeneration test conditions are achieved whereas the cake permeability is constant for $\cong$ 11 minutes (at $\cong$ 5.6 hrs) into the PM oxidation and then increases rapidly. This time delay is attributed to time taken to initiate damage in the PM cake layer. The increase in wall permeability is proportional to the reduction in the wall PM mass whereas the cake permeability is constant until the PM cake mass reaches 25 g and then increases rapidly.

Comparing with the permeability data for PO-B10-15 experiment in Figure 4.29, the cake permeability increase due to the damage in the PM cake layer for AR-B10-1 experiment occurs $\cong$ 11 minutes (cake PM masses below 25 g) into the PM oxidation by active regeneration whereas for PO-B10-15 experiment it occurs $\cong$ 43 minutes (cake PM masses less than 27 g) into the PM oxidation by passive oxidation. The shorter time interval AR-B10-1 experiment is mainly due to the increased PM oxidation rate of the AR-B10-1 experiment compared to the PO-B10-15 experiment. At higher PM reaction rates, the PM cake layer is oxidized rapidly in a short time, allowing significant reduction in the mass of the PM cake layer before initiation of the microscopic and macroscopic cracks in the PM cake layer. At lower reaction rates, the PM cake layer cracks are initiated at the higher mass of the PM cake layer as the cake layer is exposed to oxidizing environment for a longer time without significant reduction in its mass.

From the analysis of the pressure drop (Figure 4.28 and Figure 4.39) and permeability curves (Figures 4.29 and 4.41) for the passive oxidation and active regeneration experiments, at fixed flow and temperature conditions, it is evident that the pressure drop across the filter is governed by several factors such as PM flow rate (PM concentration and volumetric flow rate), thickness of the PM cake layer (PM mass retained), filtration efficiency (PM within the pores of the substrate wall), wall and cake PM oxidation rate (temperature, NO_2 and O_2 concentration), permeability of substrate wall (clean wall permeability, packing density and slip flow) and permeability of cake (initial permeability, damage permeability, damage recovery and slip flow). The SCR-F/CPF model developed in this research accounts for these factors and is able to simulate pressure drop trends of passive oxidation and active regeneration experiments within pressure drop RMS error of 0.2 kPa (see Appendix E).

Overall, the comparison of the passive oxidation and active regeneration experimental results to those from the high-fidelity SCR-F/CPF model confirm that the model can predict temperature, PM mass loading and pressure drop within good agreement with the experimental measurements. The SCR-F/CPF model was also applied and compared with extensive engine experimental data for a wide range of operating conditions covering six passive oxidation and twelve active regeneration cases. The SCR-F/CPF model showed PM loading RMS error of 1.8 g (see Appendix E), pressure drop RMS error of 0.2 kPa (see Appendix E) for all eighteen experimental runs. The temperature distribution and pressure drop plots for all eighteen experiments are presented in Appendix F. From the experimental data presented in this thesis for PO-B10-15 and AR-B10-1 experiments, the maximum RMS temperature distribution error was within 3°C during PM oxidation.

4.10 Model Features Comparison with Prior Works

Table 4.10 shows the comparison of the key model features of SCR-F/CPF high fidelity model and contributions from this thesis with the models in the literature (MTU 1-D model and ECU based model by Depcik et al.). The comparison of reduced order MPF model and CPF estimator with SCR-F/CPF model is also presented in the Table 4.10. The detailed development of the reduced order MPF model is presented in Chapter 5 and the CPF state estimator in Chapter 6.

Table 4. 10 Comparison of model features and contribution from this thesis work (SCR-F/CPF model, reduced order MPF model and CPF state estimator) with prior works (MTU 1-D model and ECU based model by Depcik et al.)

Model Features	ECU Model- Depcik et al. [13, 72]	1-D Model by Kiran [23]	SCR-F/CPF Model [This Thesis]	Reduced Order MPF Model and CPF State Estimator[This Thesis]
Model architecture	CPF divided into number of axial and radial zones	Single channel representation of the CPF	**CPF divided into number of axial and radial zones**	**CPF divided into number of axial and radial zones**
Control volume for energy equation	Lumped inlet and outlet channel volumes and substrate volumes	Inlet channel, substarte and outlet channel volumes	**Inlet channel, substrate and outlet channel volumes***	**Lumped inlet and outlet channel volumes and substrate volumes**
Inlet temperature distribution	Constant inlet temperature	Constant inlet temperature	**Varying inlet temperature distribution using fully developedboundary layer equations**	**Varying inlet temperature distribution using fully developedboundary layer equations**
Heat transfer mechanism within CPF	Conduction and convection	Conduction and convection	**Conduction, convection and radiation**	Conduction and convection
Species reactions	CO, CO_2 and O_2	NO, NO_2, CO, CO_2, O_2 and HC	NO, NO_2, CO, CO_2, O_2 and HC**	**HC and PM**
PM oxidation reactions	Multizone thermal (O_2) reaction in PM cake and wall	Single channel based NO_2 assisted and thermal (O_2) reactions in PM cake and wall	**Multi-zone NO_2 assisted and thermal (O_2) reactions in PM cake and wall**	**Multi-zone NO_2 assisted and thermal (O_2) reactions in PM cake and wall**
Effect of NO_2 back diffusion on cake PM oxidation	Not accounted	Included in cake PM oxidation by assuming tortuosity of PM cake layer as 1	Included in cake PM oxidation by assuming tortuosity of PM cake layer as 1**	Effect of NO_2 back diffusion on cake PM oxidation is neglected
PM filtration	Multi-zone filtration model using filtration theory developed by Konstandopoulos and Johnson [15]	Single channel model using filtration theory developed by Konstandopoulos and Johnson [15]	Multi-zone filtration model using filtration theory developed by Konstandopoulos and Johnson [15]	Multi-zone filtration model using filtration theory developed by Konstandopoulos and Johnson [15]
Slip flow correction for wall and cake permeability	Not accounted	Not accounted	**Slip flow in the wall accounted using Pulkrabek correction [33] and slip flow in the PM cake accounted using Versaevel et al. correction [34]**	**Slip flow in the wall accounted using Pulkrabek correction [33] and slip flow in the PM cake accounted using Versaevel et al. correction [34]**
PM cake permeability evolution during PM oxidation	Not accounted	Not accounted	**Used new cake permeability model based on this thesis - Chapter 4.5.3**	**Used new cake permeability model based on this thesis - Chapter 4.5.3**
Post loading cake permeability correction	Not accounted	Not accounted	**Used new cake permeability model based on this thesis - Chapter 4.5.3 and Appendix D**	**Used new cake permeability model based on this thesis - Chapter 4.5.3 and Appendix D**
Model outputs	Temperature Distribution	Average CPF Temperature, PM loading and pressure drop	**Multi-zone temperature and PM mass distribution, PM loading and pressure drop**	**Multi-zone temperature and PM mass distribution, PM loading and pressure drop**
CPF state estimation for potential ECU controls and diagnostics	Not available	Not available	Not available	**Extended Kalman filter based state estimator for temperature and PM distribution and linear Kalman filter based estimator for pressure drop estimates**

* Jointly developed with Venkata R Chundru
** Developed by Venkata R Chundru as part of SCR-F model development
The improvements over the prior works by this theis are highleged in bold black font

From the above analysis, with the key model features shown in Table 4.10, the high-fidelity SCR-F/CPF model provides accurate prediction of temperature, PM distribution and pressure drop. However, the SCR-F/CPF model is computationally demanding. Hence, further model reduction is required to use the model for aftertreatment control applications. The next chapter (chapter 5) details the development of the CPF reduced order model that will be applied to CPF control applications.

5 CPF Reduced Order Model Development[1]

The high fidelity SCR-F/CPF model in chapter 4 has shown good capability to predict temperature and PM loading distribution and pressure drop of the CPF. For an ECU based application, the high fidelity model has to be simplified in order to run in real time for aftertreatment control applications. Hence, the high fidelity model developed in chapter 4 was reduced to improve its computational speed and reduce the computational complexity without significantly affecting the accuracy of predicting the temperature and PM mass distribution and pressure drop of the CPF.

To develop a reduced order MPF model, the following parametric study was carried out using the high fidelity model to determine the optimum model configuration for the reduced order MPF model.

- Optimum number of axial and radial zones required to predict temperature and PM mass distribution and pressure drop of the CPF for aftertreatment control applications was determined.

Further, the following model reduction assumptions were evaluated using the high fidelity SCR-F/CPF model to determine the sensitivity of these assumptions to the computational time and modeling inaccuracies.

- o Neglecting the species concentration solver and assuming uniform species concentration at each zone that is equal to the inlet concentration into the CPF (THC, NO_2 and O_2)
- o Neglecting the back diffusion of NO_2 due to the NO_2 produced by the catalyst wash coat
- o Applying average channel gas temperature assumption (Neglecting the temperature change through the substrate wall)
- o Neglecting the radiation heat transfer within the inlet channel surfaces (Radiation heat transfer is minimum below 600°C)

---

[1] Parts of the material contained in this chapter are based on references [1, 2,3] with permission of Springer.

From the parametric studies and analysis of the model reduction assumptions, a reduced order MPF model was developed. The detailed analysis of parametric study and model reduction assumptions are presented in this chapter followed by the validation of the reduced order MPF model to simulate the temperature, PM distribution and pressure drop of the CPF for aftertreatment control applications.

5.1 Model Discretization Study

A parametric study was carried out to determine the optimum required number of zones in the MPF model in the range of 4x4 to 10x10 zones for aftertreatment control applications. The filter substrate temperatures during active regeneration (450 – 600°C) are higher than the passive oxidation (250 – 400°C). The high temperatures during active regeneration result in increased temperature distribution (AR-B10-1 experiment: average temperature during active regeneration: 530°C, radial temperature distribution $\cong$ 40°C, axial temperature distribution $\cong$ 12°C) and highly non-uniform PM distribution within the filter. Hence, one of the active regeneration experiments (AR-B10-1 experiment listed in Table 3.4) was used as a reference experiment for the discretization study. Considering the nonlinear phenomenon in the CPF, the conclusions based on one reference experiment will be limited to that experiment. However, the selected reference experiment presents an average (in terms of active regeneration temperature, duration and O$_2$ concentration) active regeneration test conditions studied in this thesis.

The high fidelity SCR-F/CPF model used the model constants, PM kinetic parameters, heat transfer coefficients and filter density parameters developed in Chapter 4 for all the discretization cases. A variable step solver based on ode15s stiff solver is used to solve the temperature, PM distribution and pressure drop at each time step. The maximum time step was set to 10 seconds and minimum time step was set to 1e-8 second to achieve numerical stability of the model. The total test duration was approximately 7.33 hrs (440 minutes) for AR-B10-1 experiment. The model execution time was compared with real time using the real time factor. The real time factor is calculated as the ratio of model run time to the real time of the experiment. The real time factor of 1 indicates that the model runs as fast as real time.

Figure 5.1 shows the model discretization size versus real time factor for the AR-B10-1 experiment. From Figure 5.1, the real time factor significantly increases with increasing the discretization size. In addition, the real time factor increases linearly as a function of total number of elements (16 nodes for 4x4 model, 25 nodes for 5x5 model, 49 nodes for 7x7x model and 100 nodes for 10x10 model) as shown in Figure 5.2. The lowest real time factor is for the 4x4 zone model in which the high-fidelity SCR-F/CPF model takes 2.3 % of total real time or about 43 times faster than the real time. The 5x5 zone model takes 3.5% of total real time or about 29 times faster than the real time whereas baseline 10x10 zone model takes 12.9 % of total real time or about 8 times faster than real time. It is important to note that the SCR-F/CPF model was run on a laptop computer with the specifications of 12 GB RAM, 64bit and Intel core i7 processor. The typical ECUs used on engine applications have 32 bit and 200 MHz processors [67]. However, Matlab® is the high level programming language and it is approximately 10x slower than the C language that closely mirrors the assembly language that processors commonly use. Depcik and Assanis [68] showed that the for a sample problem presented in reference [68], the C code runs 18.1x faster than the Matlab® code. Hence, with an optimized C code, the SCR-F/CPF model with low computational requirement like the 4x4 and 5x5 zone shows high potential to run as part of a conventional ECU or a dedicated ECU that manages CPF functions exclusively.
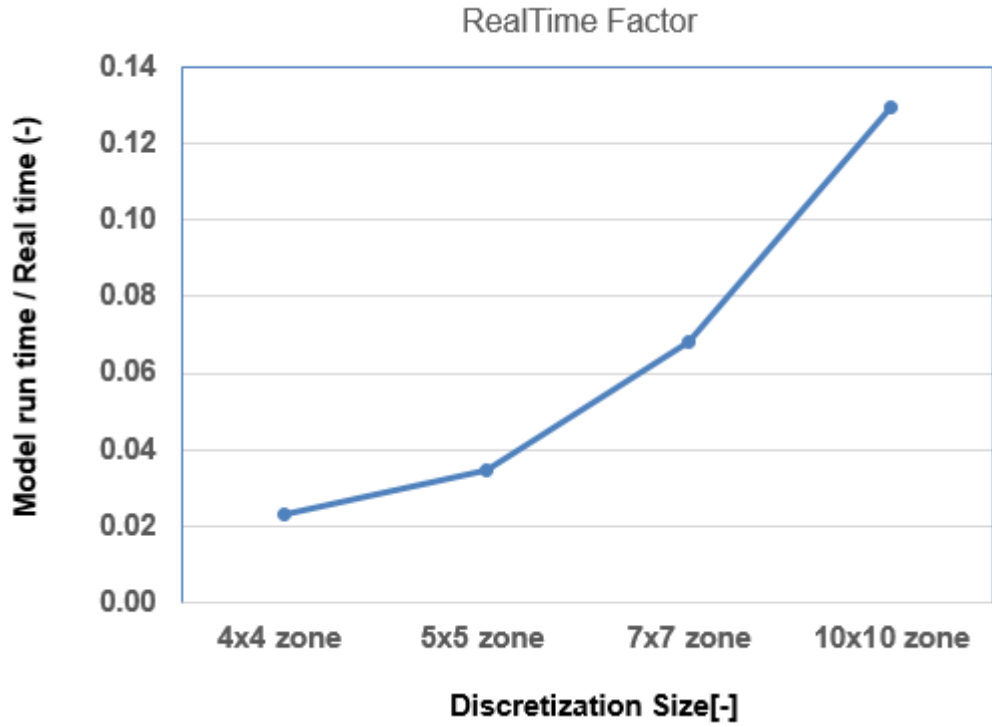
Figure 5. 1 Model discretization size versus real time factor for AR-B10-1 experiment
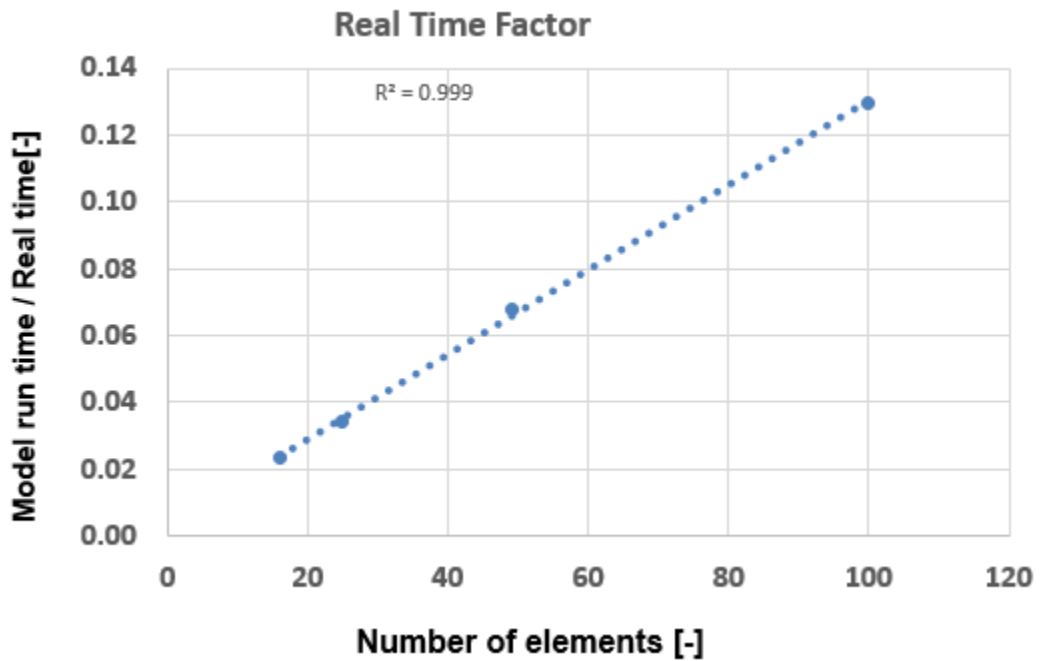
Figure 5. 2 Real time factor versus number of elements in the SCR-F/CPF model for AR-B10-1 experiment

Figures 5.3, 5.4, 5.5 and 5.6 show the comparison of PM mass retained in the experimental data and high-fidelity SCR-F/CPF model along with the PM inlet rate for 10x10, 7x7, 5x5 and 4x4 zones, respectively. From Figures 5.3 to 5.6, the 10x10 zone model showed close agreement (< 0.3 g at the end of post loading) with the experimental data. The 4x4 , 5x5 and 7x7 zone models over predict the PM loading by 2.2, 1.6 and 1.2 g respectively at the end of post loading (at 7.3 hrs).
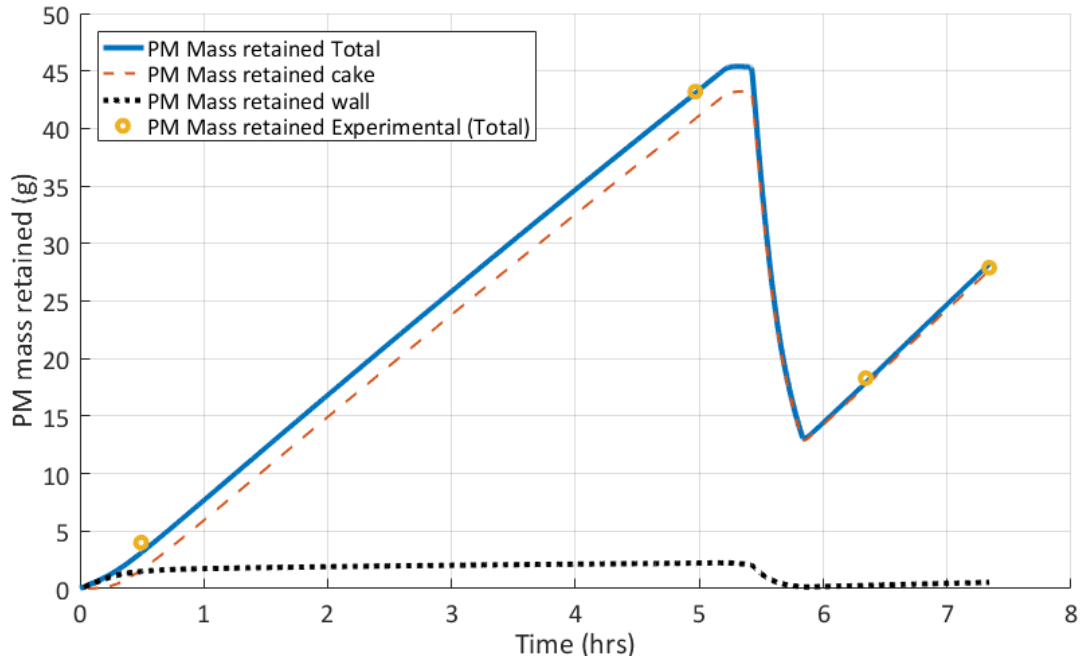
Figure 5. 3 Comparison of PM mass retained in the experimental data and high-fidelity SCR-F/CPF simulation model for 10x10 zones (AR-B10-1 experiment)
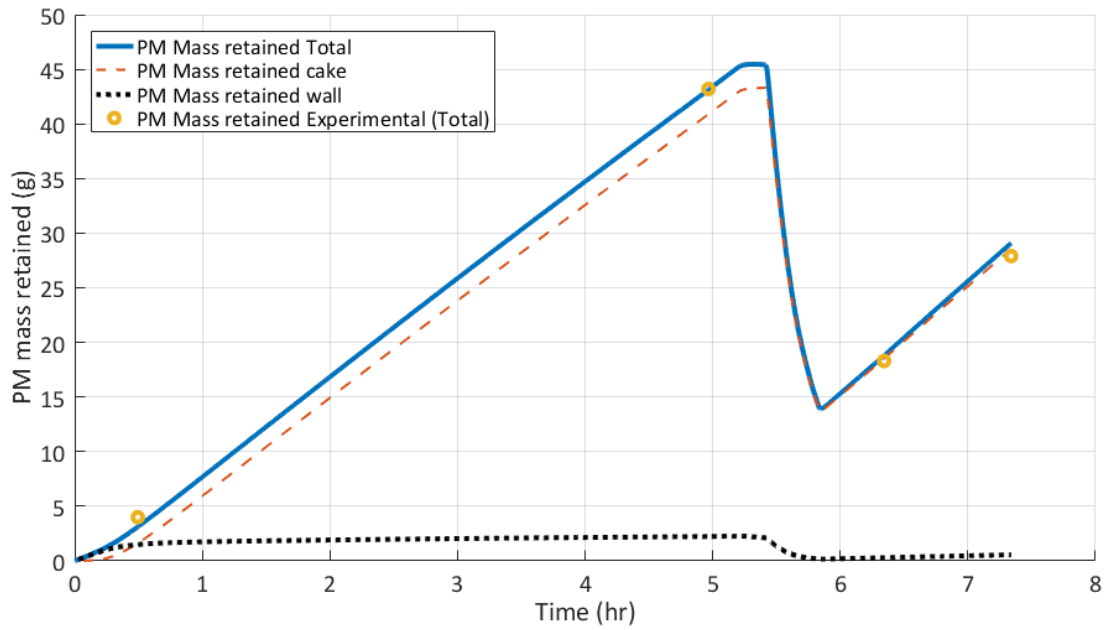
Figure 5. 4 Comparison of PM mass retained in the experimental data and high-fidelity SCR-F/CPF simulation model for 7x7 zones (AR-B10-1 experiment)
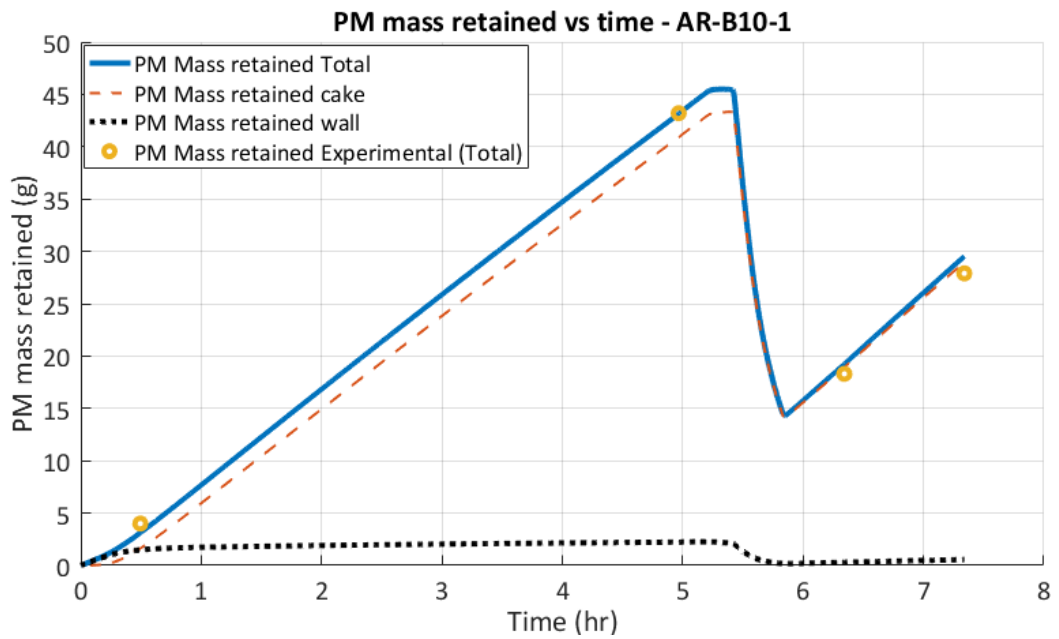
Figure 5. 5 Comparison of PM mass retained in the experimental data and high-fidelity SCR-F/CPF simulation model for 5x5 zones (AR-B10-1 experiment)
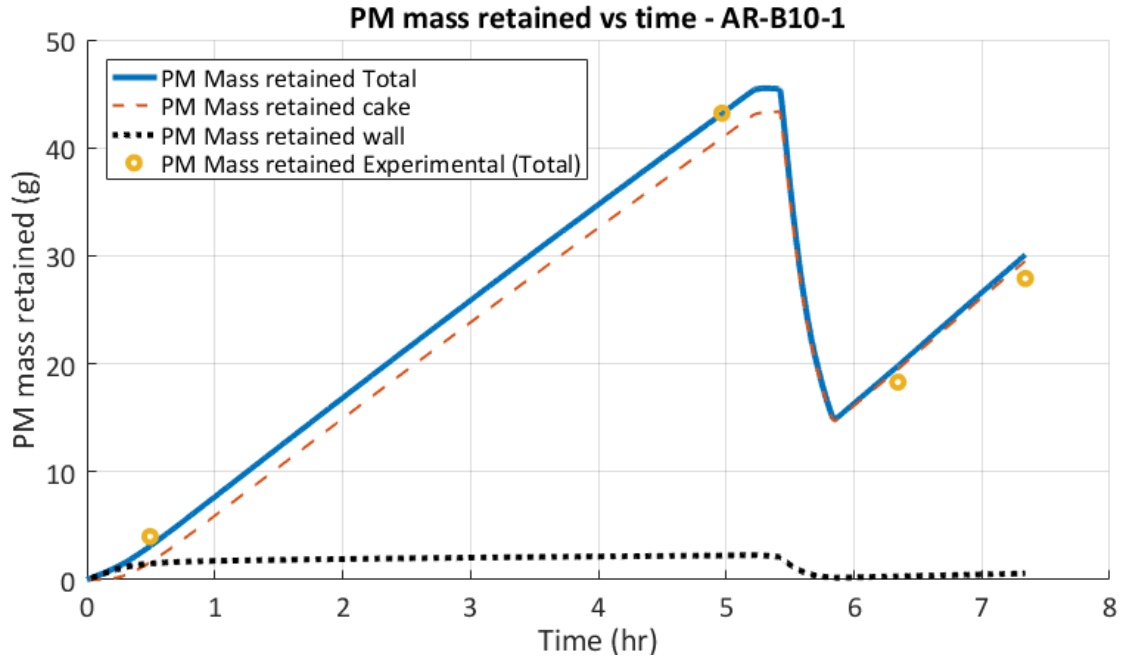
Figure 5. 6 Comparison of PM mass retained in the experimental data and high-fidelity SCR-F/CPF simulation model for 4x4 zones (AR-B10-1 experiment)

Figure 5.7 shows the experimental temperature distribution measured by 16 thermocouples for AR-B10-1 experiment at 5.63 hrs. (15 minutes after start of fuel dosing). Figures 5.8, 5.9, 5.10 and 5.11 show the comparison of simulated temperature distribution of AR-B10-1 experiment (15 minutes after fuel dosing) for 10x10, 7x7, 5x5 and 4x4 zones respectively. From Figures 5.7 to 5.11, 10x10, 7x7 and 5x5 zones model results show close agreement (RMS temperature error at 5.63 hrs < 3.5^{o}C) with the experimental data. The 4x4 model results show a RMS temperature error of 5.4^{o}C at 5.63 hrs.
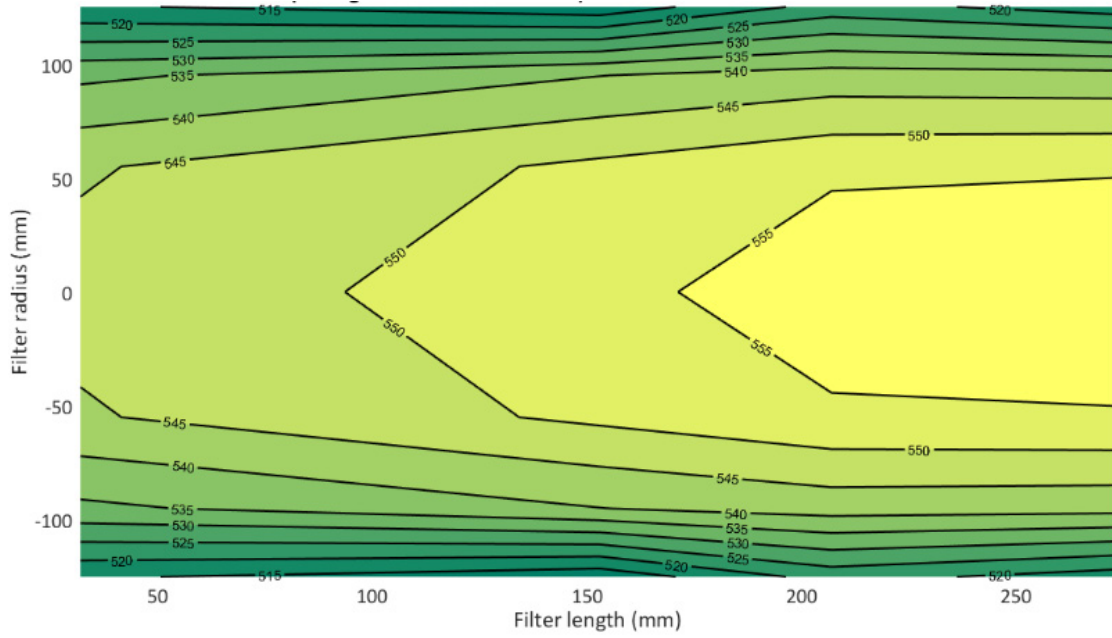
Figure 5. 7 Experimental temperature distribution in °C for AR-B10-1 experiment at 5.63 hrs. (15 minutes after start of fuel dosing)
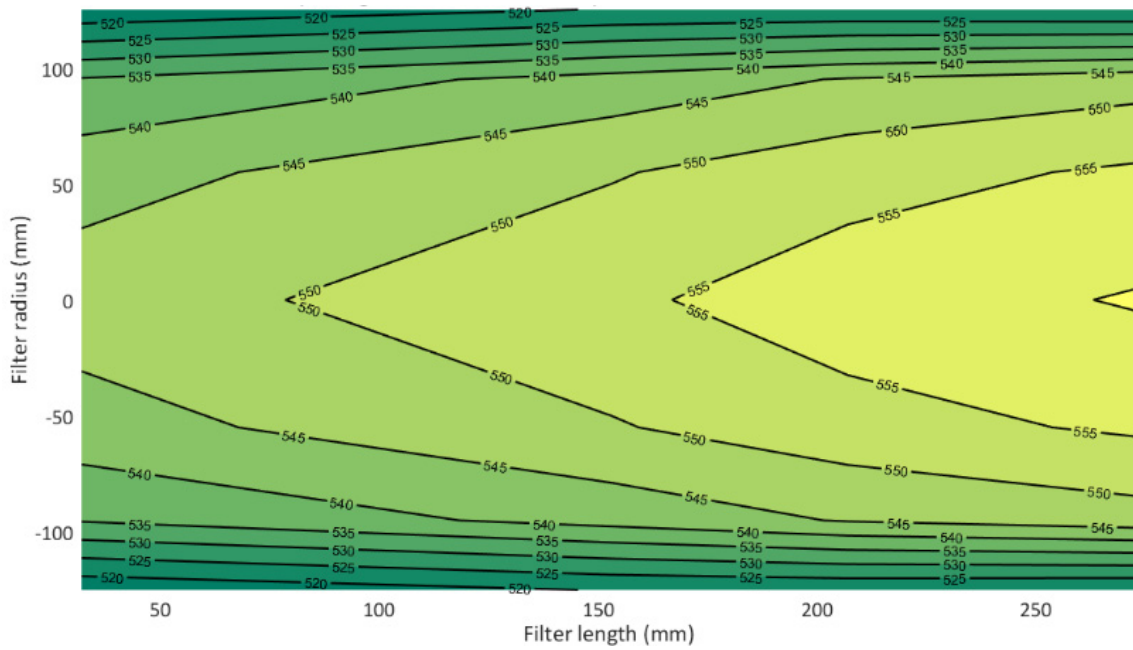
Figure 5. 8 Simulated temperature distribution in °C for AR-B10-1 experiment at 5.63 hrs. (15 minutes after start of fuel dosing) - 10x10 zones
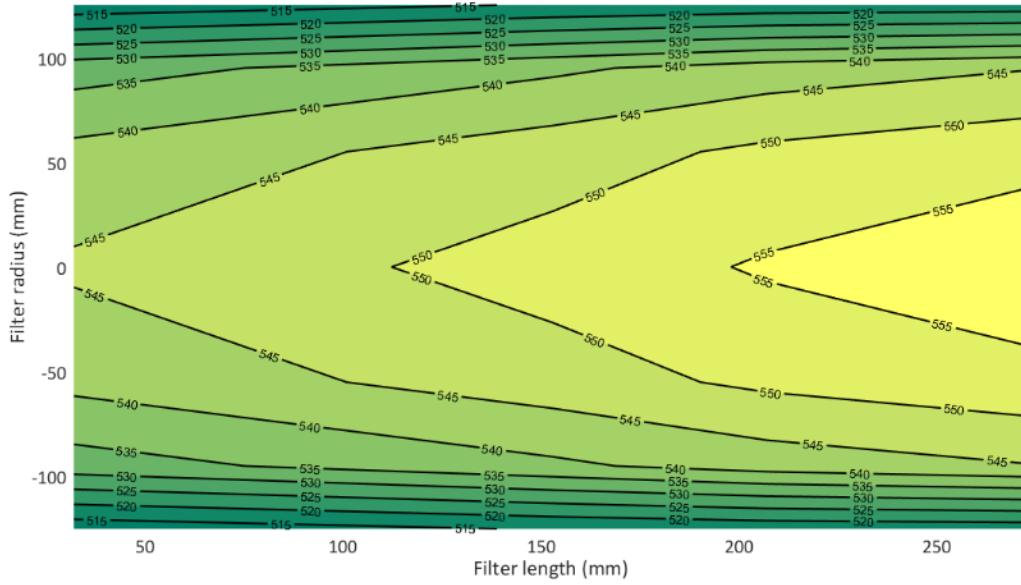
Figure 5. 9 Simulated temperature distribution in °C for AR-B10-1 experiment at 5.63 hrs. (15 minutes after start of fuel dosing) - 7x7 zones
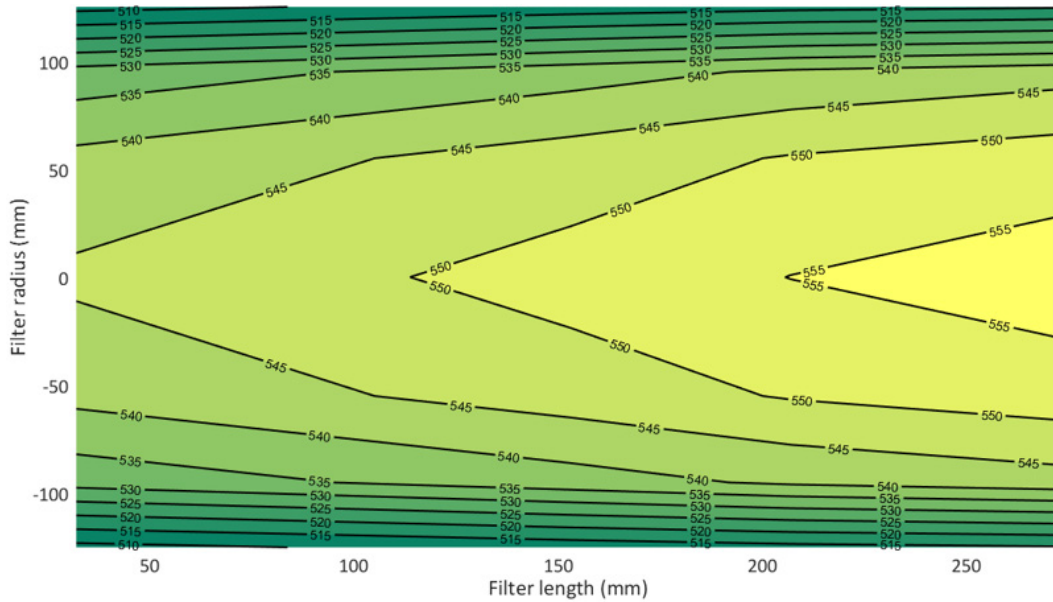
Figure 5. 10 Simulated temperature distribution in °C for AR-B10-1 experiment at 5.63 hrs. (15 minutes after start of fuel dosing) - 5x5 zones
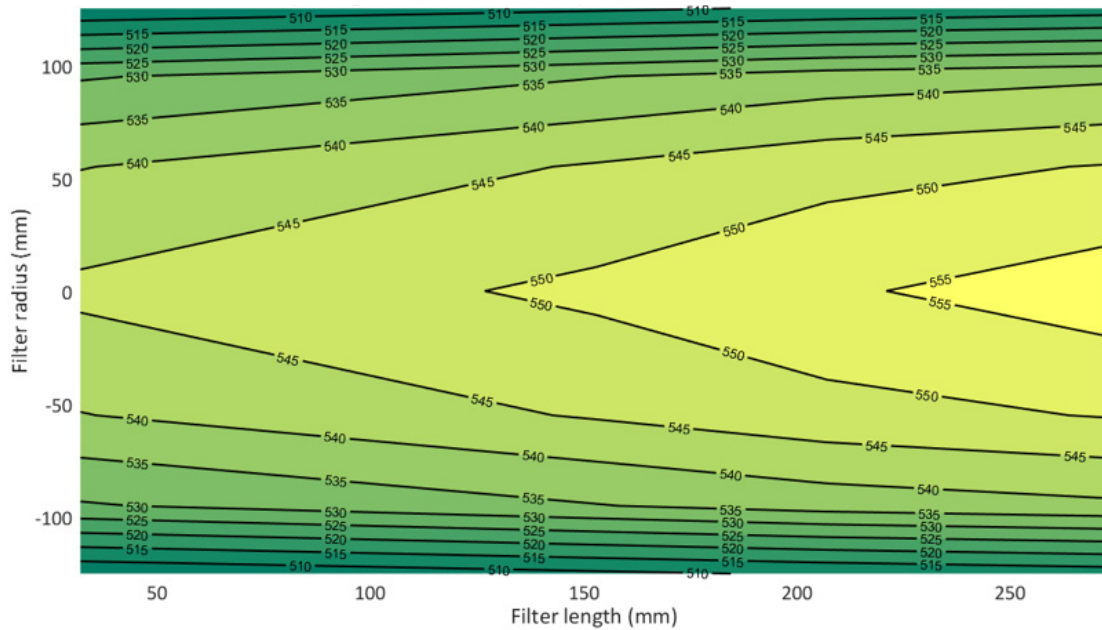
Figure 5. 11 Simulated temperature distribution in ºC for AR-B10-1 experiment at 5.63 hrs. (15 minutes after start of fuel dosing) - 4x4 zones

Figures 5.12, 5.13, 5.14 and 5.15 show the comparison of simulated PM mass distribution of AR-B10-1 experiment at the end of PM oxidation (5.82 hrs) by active regeneration for 10x10, 7x7, 5x5 and 4x4 zones respectively. From Figures 5.12 to 5.15, the PM mass distribution of the 7x7 and 5x5 zones are comparable (within $\cong$ 0.2 g/L) with the 10x10 zone model whereas the 4x4 zone model under predicts PM loading by $\cong$ 0.4 g/L at the outer radiuses of the filter (Filter radiuses > 120 mm).
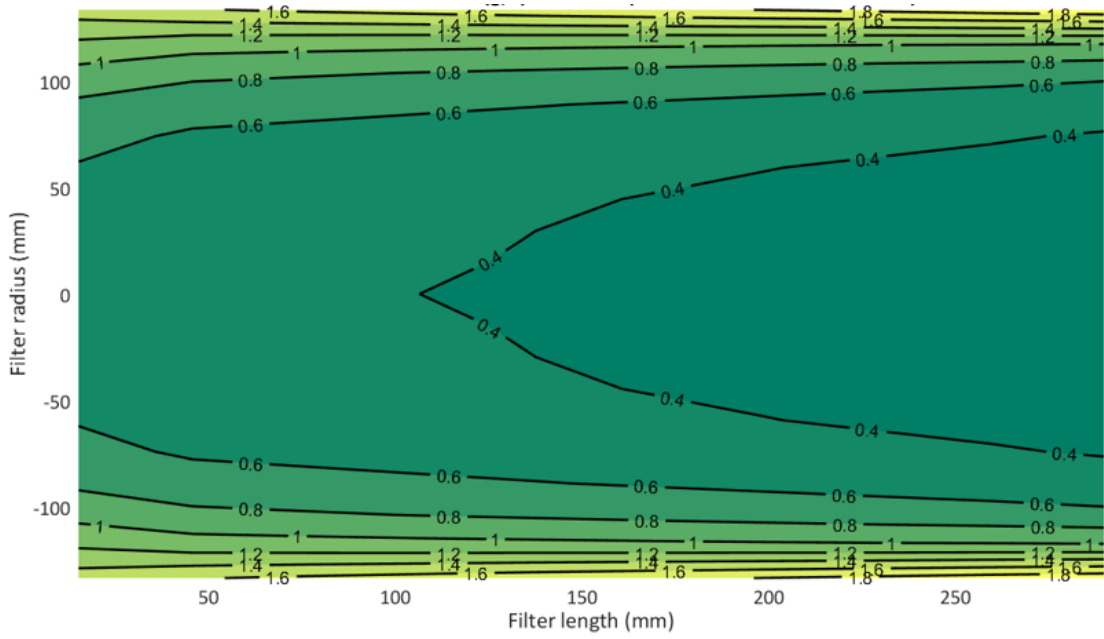
Figure 5. 12 Simulated PM mass distribution in g/L for AR-10-1 experiment at the end of PM oxidation by active regeneration (5.82 hrs) – 10x10 zones
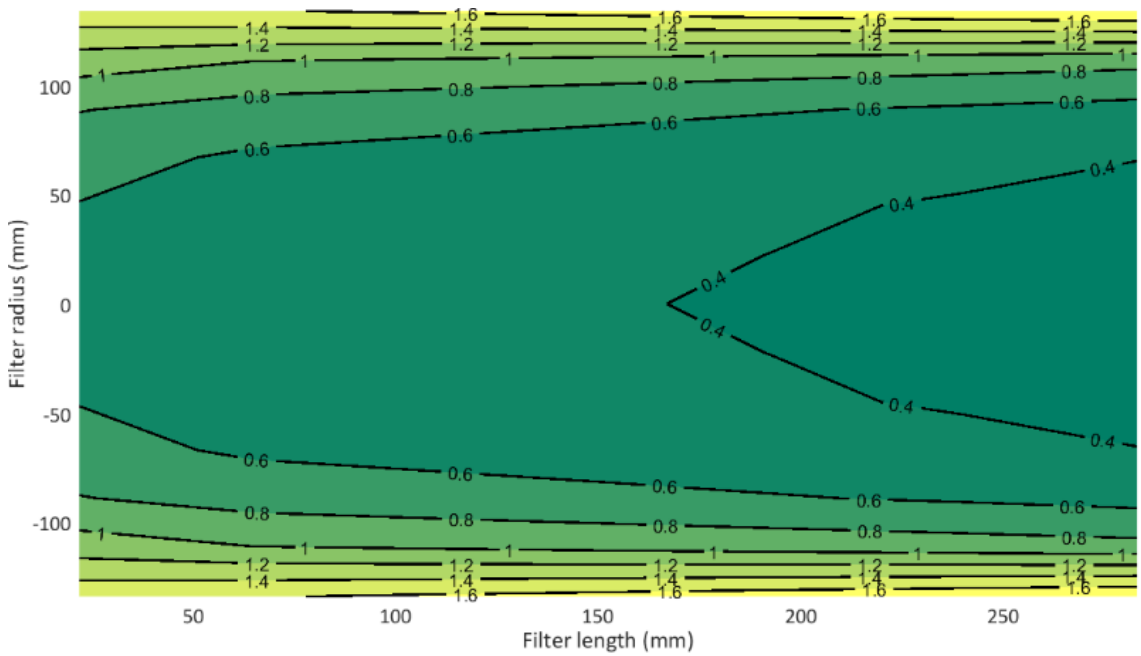
Figure 5. 13 Simulated PM mass distribution in g/L for AR-10-1 experiment at the end of PM oxidation by active regeneration (5.82 hrs) – 7x7 zones
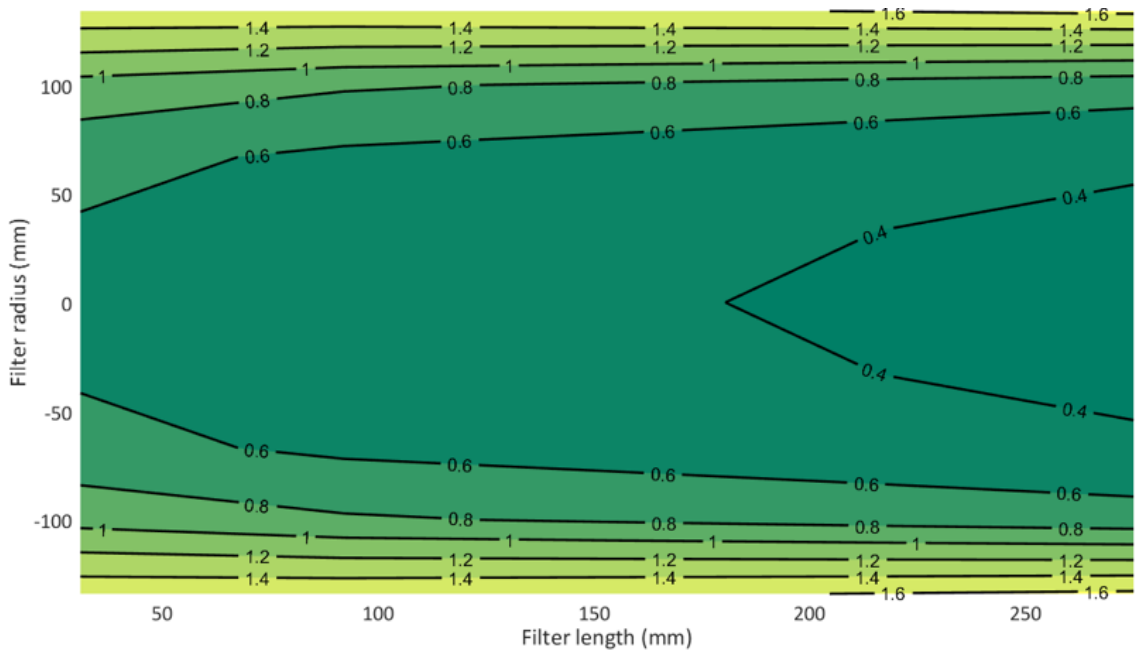
Figure 5. 14 Simulated PM mass distribution in g/L for AR-10-1 experiment at the end of PM oxidation by active regeneration (5.82 hrs) – 5x5 zones
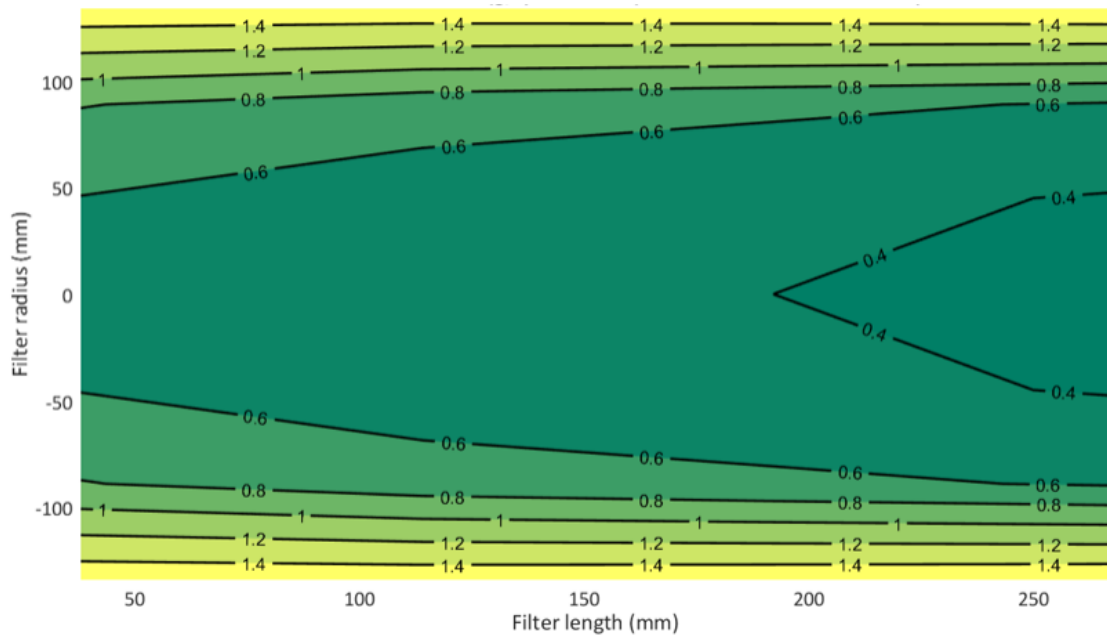
Figure 5. 15 Simulated PM mass distribution in g/L for AR-10-1 experiment at the end of PM oxidation by active regeneration (5.82 hrs) – 4x4 zones

115

Figures 5.16, 5.17, 5.18 and 5.19 show the comparison of experimental and simulated total pressure drop across the CPF and its components for the 10x10, 7x7, 5x5 and 4x4 zones respectively for the AR-B10-1 experiment. From Figures 5.16 to 5.19, 10x10 zone model show close agreement (< 0.1 kPa at the end of post loading) with the experimental data. The 4x4 model under predicts the pressure drop by 0.3 kPa at the end of post loading (at 7.3 hrs). This is mainly due to the fewer number of points in the axial momentum equation used to estimate the total channel pressure drop. In the high-fidelity model, the last node is equated to ambient pressure. Comparing Figure 5.19 with Figures 5.16 to 5.18, the channel pressure drop decreases with the increase in PM loading in the channel and this is mainly due to the fewer number of axial discretization as the increased pressure drop due to PM accumulation in the last node is neglected and set to ambient pressure. Hence, the accuracy of the pressure drop prediction reduces with the reduction in axial discretization levels as shown in Table 5.1.

Figure 5. 16 Comparison of experimental and simulated total pressure drop across CPF and its components for AR-B10-1 experiment - 10x10 zone

Figure 5. 17 Comparison of experimental and simulated total pressure drop across CPF and its components for AR-B10-1 experiment - <u>7x7 zone</u>
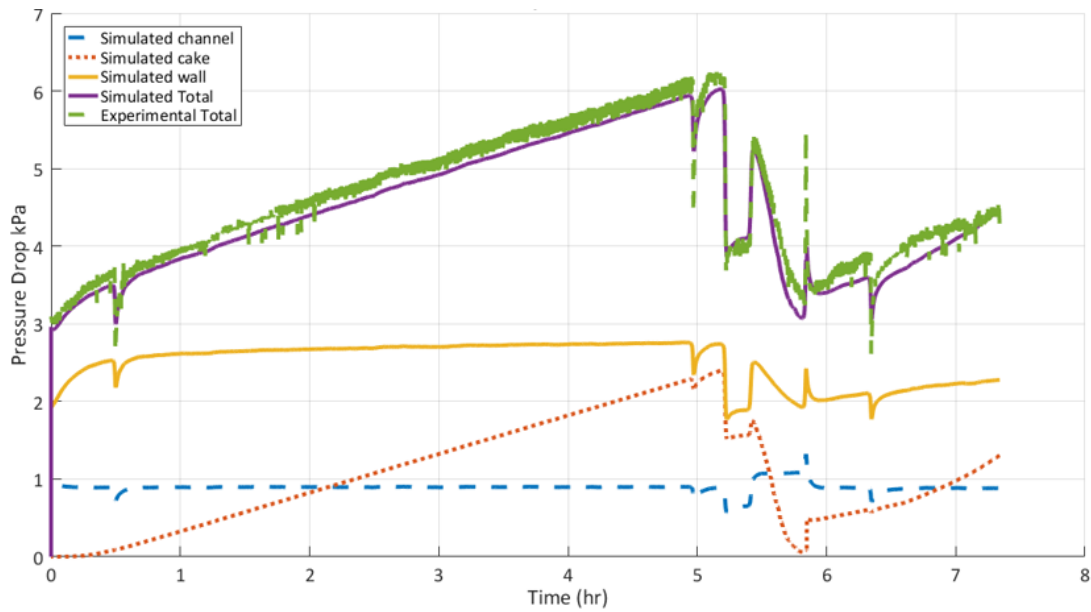
Figure 5. 18 Comparison of experimental and simulated total pressure drop across CPF and its components for AR-B10-1 experiment - <u>5x5 zone</u>

117
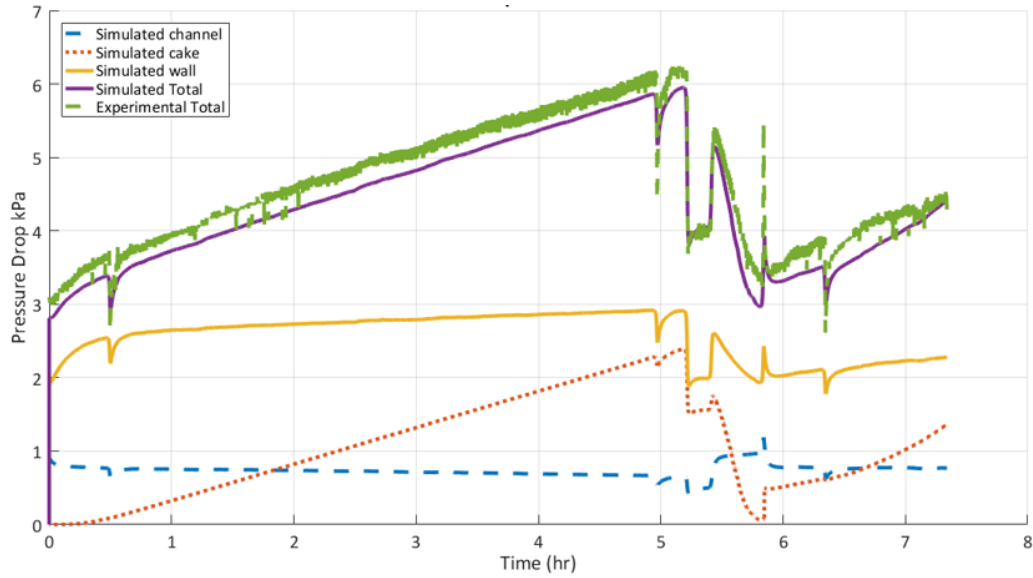
Figure 5. 19 Comparison of experimental and simulated total pressure drop across CPF and its components for AR-B10-1 experiment - <u>4x4 zone</u>

Table 5.1 summarizes the model accuracy versus computational time of the high-fidelity SCR-F/CPF model with four discretization levels. From the Table 5.1, the 5x5 zone model offers the better trade-off in terms of accuracy and computational time compared to 4x4, 7x7 and 10x10 zone models. Thus the 5x5 model was selected as the discretization size (about 4 times faster than the baseline 10x10 model) for the CPF reduced order model development and subsequent CPF estimator development presented in this thesis.

Table 5. 1 Temperature, PM loading, pressure drop and computational time trade-off for the SCR-F/CPF model

Model Discretization Level	RMS tempertaure difference @ start of PM oxidation (time: 5.6 hrs)	PM Loading difference @ end of post loading (time: 7.3 hrs)	Pressure drop difference @ end PM oxidation (time: 5.8 hrs)	Simulation time / Real time [-]
	°C	g	kPa	[-]
4x4 zone	5.4	2.2	-0.3	0.02
5x5 zone	3.5	1.6	-0.2	0.03
7x7 zone	2.6	1.2	-0.1	0.07
10x10 zone	3.1	0.3	0.0	0.13

5.2 Evaluation of Model Reduction Assumptions using High-fidelity Model

The high-fidelity model was further reduced by applying the model reduction assumptions explained in introduction to this chapter and the resultant effect on the model accuracy and computation time is also presented.

5.2.1 Effect of Varying Species Concentration on Temperature and PM Mass Distribution

The high-fidelity SCR-F/CPF model accounts for the changes in the species concentration at each zone and its effect on over all PM oxidation as explained in Chapter 4. For the purpose of reducing the computational time for aftertreatment control applications, the high-fidelity model was evaluated by assuming species concentration at each zone (wall and cake) is same as the inlet species concentration i.e. the effect of catalytic reactions in the washcoat is minimum on the cake and wall PM oxidation and could be neglected (without species solver) for the reduced order model.

Figures 5.20 and 5.21 show the comparison of simulated HC outlet concentration along with the model HC inlet concentration measured during AR-B10-1 test with and without species solver. Comparing Figures 5.21 with 5.20, HC concentration in the wall-outlet channel interface is same as that of HC inlet concentration without the species concentration solver. Hence, this increased concentration at wall-outlet channel interface will affect the temperature and PM oxidation in the substrate wall.
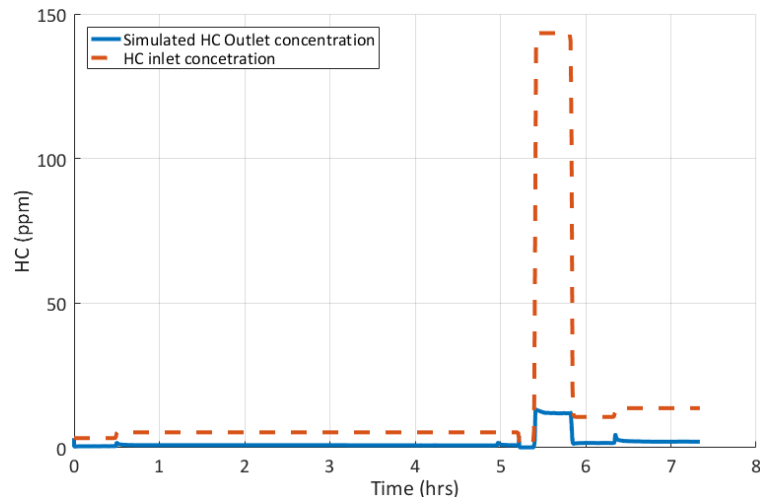
Figure 5. 20 Comparison of simulated HC outlet concentration and HC inlet concentration measured during AR-B10-1 experiment <u>with species concentration solver</u>
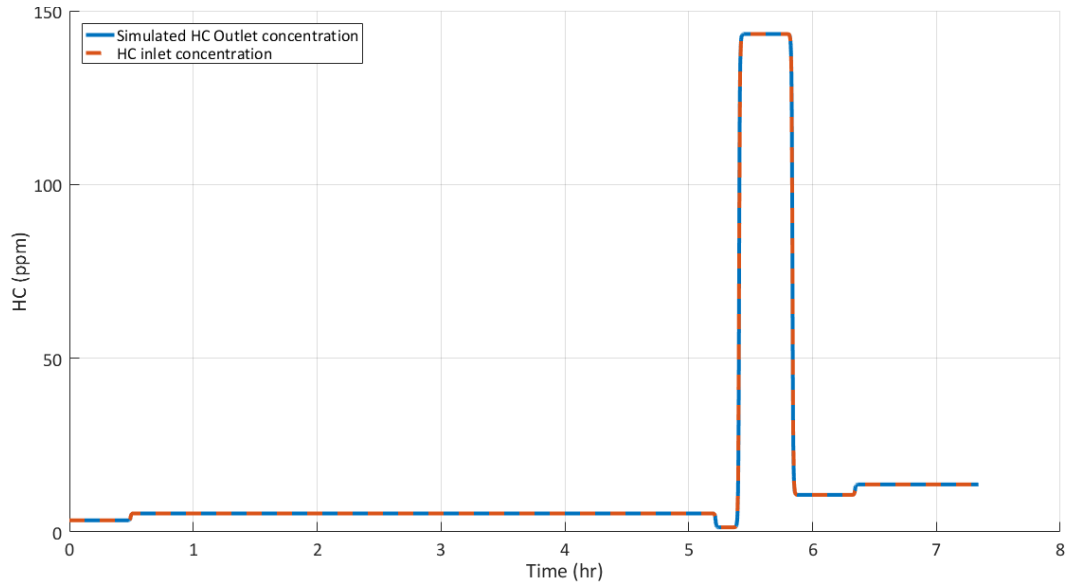
Figure 5. 21 Comparison of simulated HC outlet concentration and HC inlet concentration measured during AR-B10-1 experiment without species concentration solver

Figures 5.22 and 5.23 show the comparison of simulated O_2 outlet concentration along with the model O_2 inlet concentration measured during AR-B10-1 test with and without species solver.
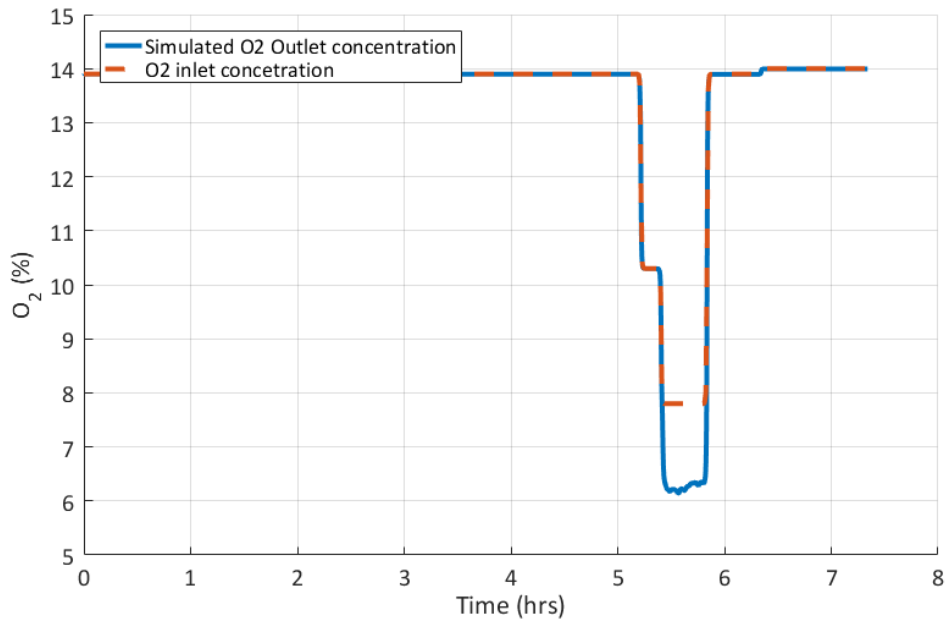
Figure 5. 22 Comparison of simulated O_2 outlet concentration and O_2 inlet concentration measured during AR-B10-1 experiment with species concentration solver
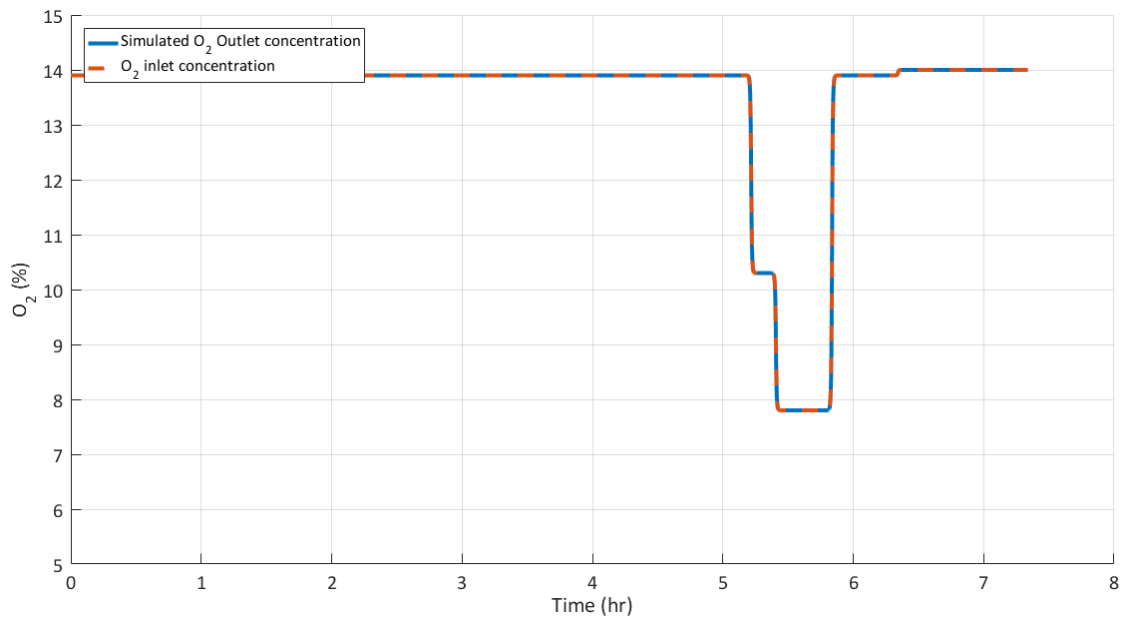
Figure 5. 23 Comparison of simulated O₂ outlet concentration and O₂ inlet concentration measured during AR-B10-1 experiment without species concentration solver

Comparing Figures 5.23 with 5.22, O_2 concentration in the wall-outlet channel interface is same as that of O_2 inlet concentration without the species concentration solver. Hence, this increased concentration at wall-outlet channel interface will affect the temperature and PM oxidation in the substrate wall.

Figures 5.24 and 5.25 show the comparison of simulated NO_2 outlet concentration along with the model NO_2 inlet concentration measured during AR-B10-1 test with and without species solver. Comparing Figure 5.25 with 5.24, NO_2 concentration in the wall-outlet channel interface is same as that of NO_2 inlet concentration without the species concentration solver. Hence, this increased concentration at wall-outlet channel interface with species solver will affect the temperature and PM oxidation in the substrate wall.
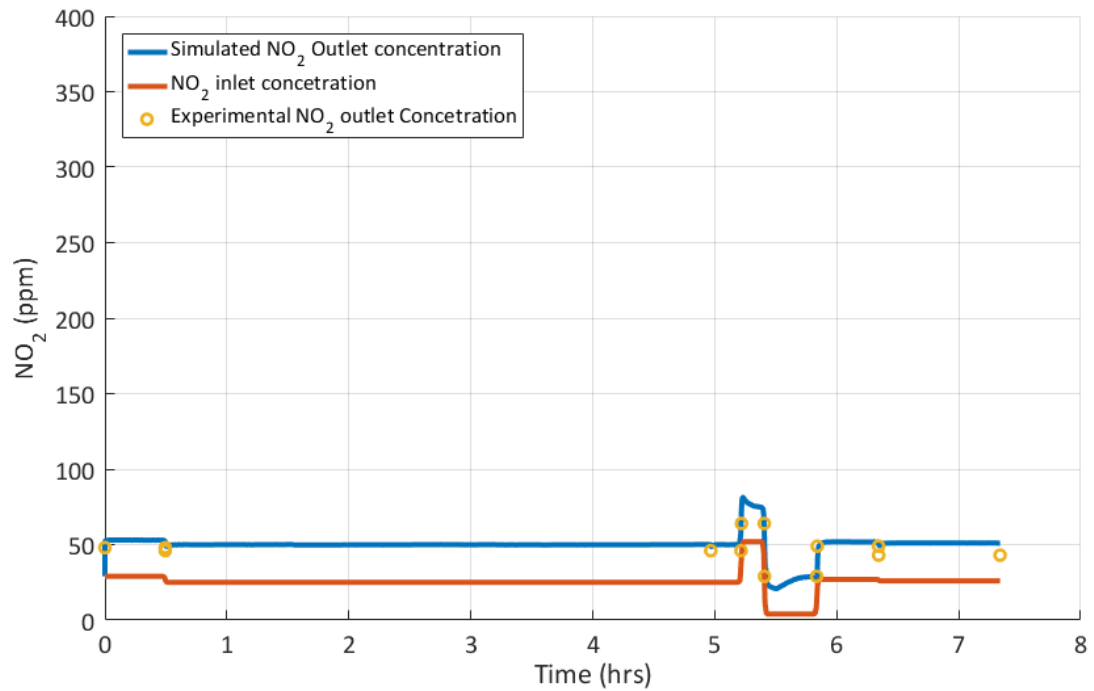
Figure 5. 24 Comparison of simulated NO₂ outlet concentration and NO₂ inlet concentration measured during AR-B10-1 experiment <u>with species concentration solver</u>
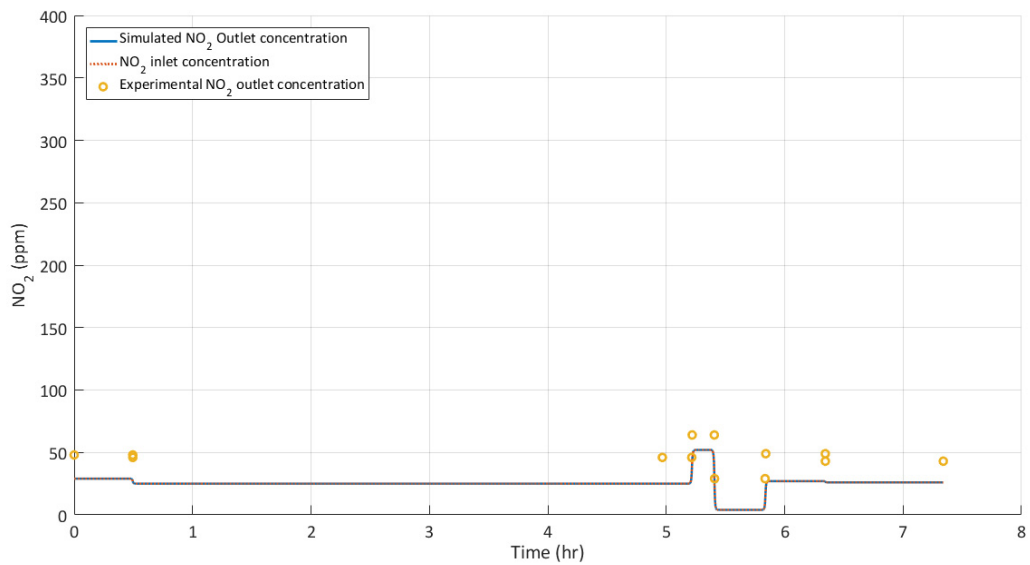
Figure 5. 25 Comparison of simulated NO₂ outlet concentration and NO₂ inlet concentration measured during AR-B10-1 experiment <u>without species concentration solver</u>

122

Figure 5.26 shows the comparison of PM mass retained in the experimental data and simulation model along with the model cumulative for PM inlet, cake and wall PM masses for AR-B10-1 experiment without species concentration solver. Comparing Figure 5.26 with Figure 5.3, the PM loading at the end of stage 4 loading is very similar (<0.1 g difference) and this assumption (neglecting this species reactions in the washcoat) has very minimum impact on the accuracy of predicting the PM mass retained.
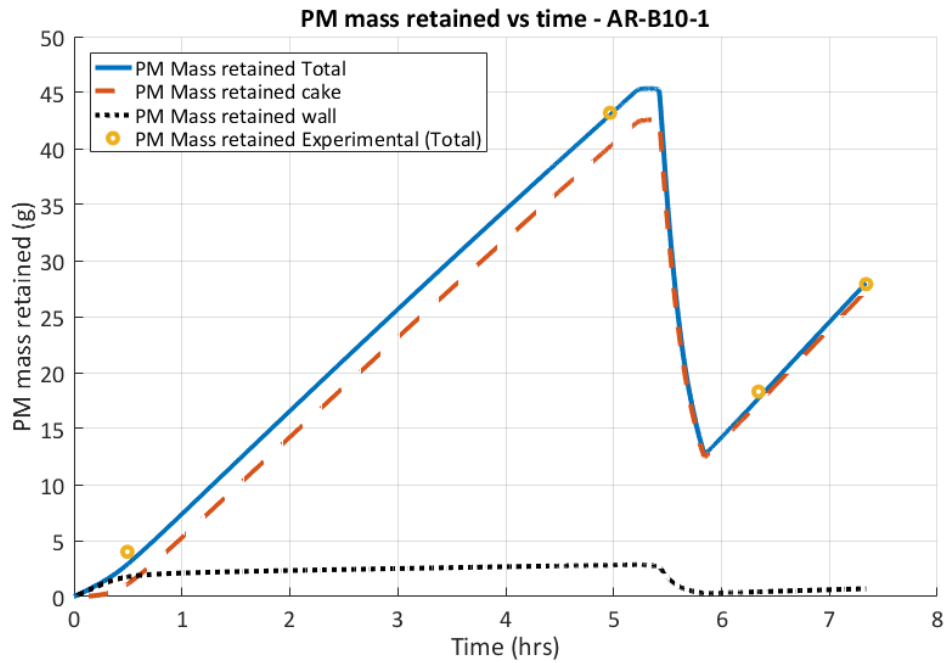
Figure 5. 26 Comparison of PM mass retained in the experimental data and simulation model along with the model cumulative for cake and wall PM masses for AR-B10-1 experiment without species concentration solver

Figure 5.27 shows the simulated temperature distribution for AR-B10-1 experiment at 5.63 hrs (15 minutes after start of fuel dosing) without species concentration solver. Comparing Figure 5.27 with Figure 5.8, the RMS temperature error at 5.63 hrs is very similar (<0.1°C difference) and this assumption (neglecting this species reactions in the washcoat) has very minimum impact on the accuracy of predicting the temperature distribution of the CPF.
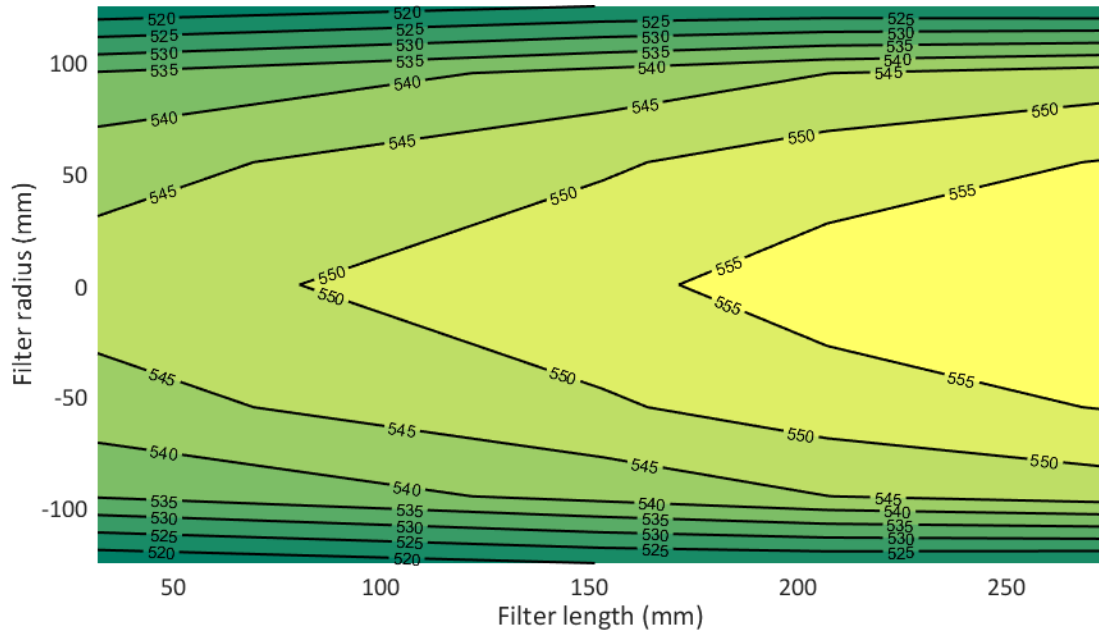
Figure 5. 27 Simulated temperature distribution in °C for AR-B10-1 experiment at 5.63 hrs (15 minutes after start of fuel dosing) without species concentration solver

Figure 5.28 shows the simulated PM mass loading distribution along the axial and radial directions at 5.82 hrs (end of PM oxidation by active regeneration) for AR-B10-1 experiment without species concentration solver. Comparing Figure 5.28 with Figure 5.12, the PM loading distribution is very similar (<0.1 g/L difference) and this assumption (neglecting this species reactions in the washcoat) has very minimum impact on the accuracy of predicting the PM mass loading distribution of the CPF.
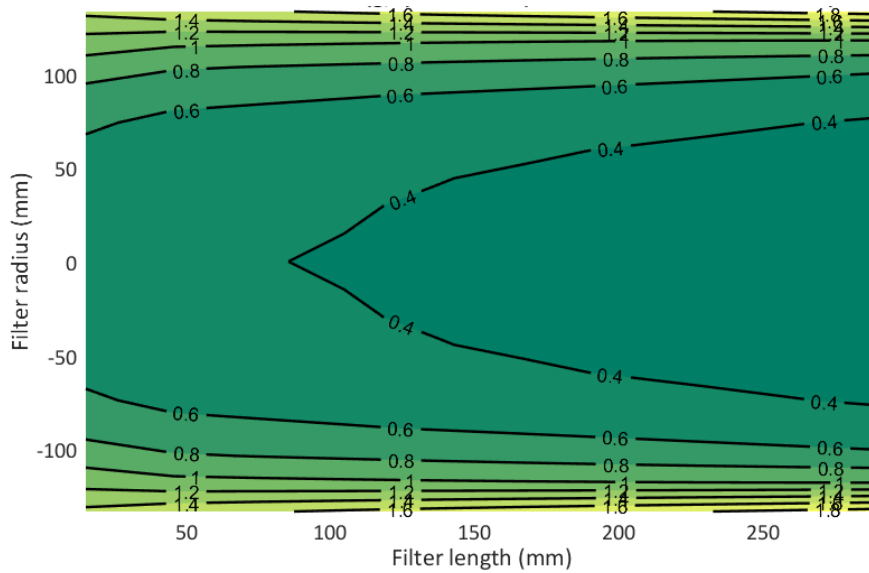
Figure 5. 28 Simulated PM mass loading distribution in g/L along the axial and radial directions at 5.82 hrs (end of PM oxidation by active regeneration) for AR-B10-1 experiment without species concentration solver
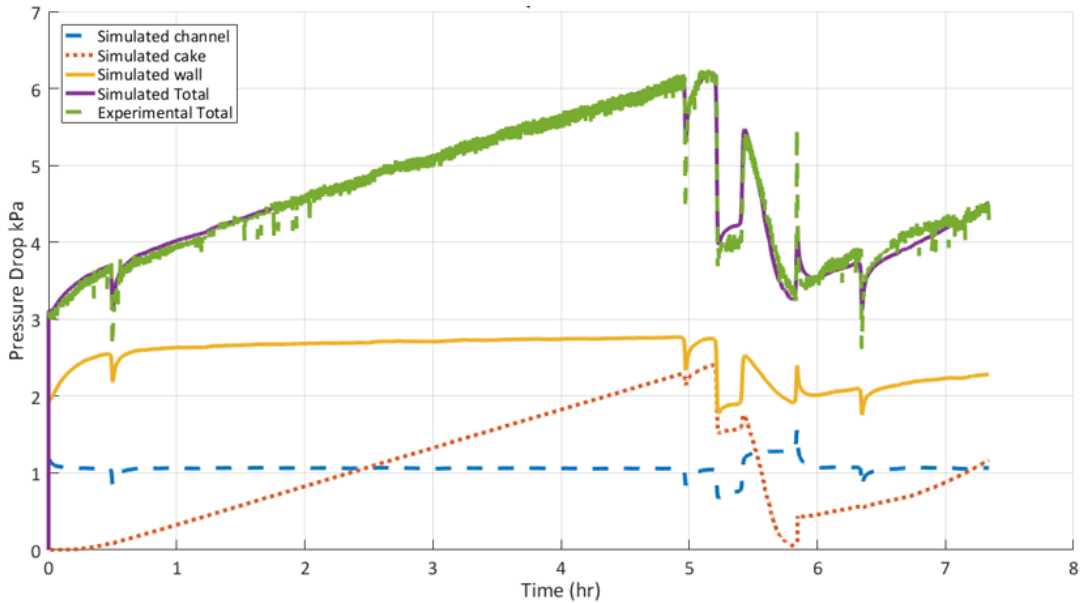
Figure 5.29 shows the comparison of experimental and simulated total pressure drop across CPF and its components for AR-B10-1 experiment without species concentration solver. Comparing Figure 5.29 with 5.16, the simulated pressure drop is very similar (<0.1 kPa difference) and this assumption (neglecting this species reactions in the washcoat) has very minimum impact on the accuracy of predicting the pressure drop of the CPF.
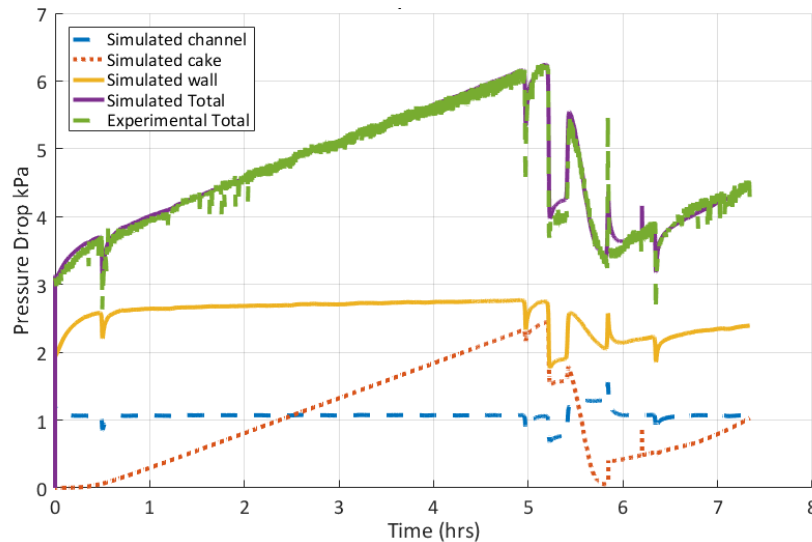
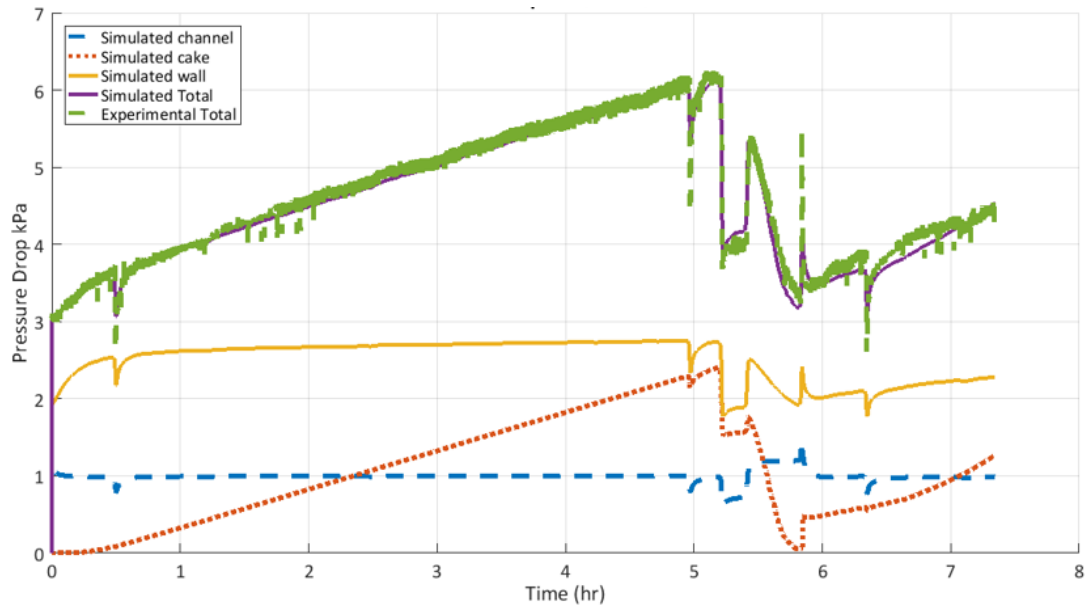*Figure 5. 29 Comparison of experimental and simulated total pressure drop across CPF and its components for AR-B10-1 experiment without species concentration solver*

125

Table 5.2 shows the temperature, PM loading, pressure drop inaccuracies and computational time trade-off with and without species concentration solver. From Table 5.2, the accuracy of the temperature, PM loading and pressure drop prediction without species solver is comparable (RMS temperature error with species solver is 2.8°C and without species solver is 2.9°C, pressure drop error is within 0.1 kPa and PM loading error is within 0.2 g) to the baseline 10x10 zone SCR-F/CPF model that runs with species solver. However, the model run time reduces significantly without species solver. The high-fidelity SCR-F/CPF model runs about 32 times faster without species solver. Hence, the catalyst wash coat reactions are neglected in the reduced order model development to reduce computation time and computational complexity.

Table 5. 2 Temperature, PM loading, pressure drop inaccuracies and computational time trade-off with and without species solver for SCR-F/CPF model

Model Discretization Level	RMS tempertaure difference @ start of PM oxidation (time:5.63 hrs)	PM Loading difference @ end of post loading (time:7.3 hrs)	Pressure drop difference @ end PM oxidation (time:5.8 hrs)	Simulation time / Real time [-]
	°C	g	kPa	[-]
10x10 zone	2.8	0.2	-0.1	0.13
10x10 zone species solver off	2.9	0.2	0.1	0.004

5.2.2 Effect of NO_2 Back Diffusion on Temperature and PM Mass Distribution

Catalyzed particulate filters are coated with Pt-based catalyst which is very effective in promoting oxidation reaction of NO. The NO molecules present in the exhaust gas flows through the inlet channels of the CPF, PM cake layer and then into the catalyst substrate wall surfaces to the outlet channels of the CPF. The Pt-based catalyst washcoat in the substrate wall oxidizes NO molecules in the gas into NO_2 molecules. Due to the concentration gradient of NO_2 between PM cake layer and the substrate wall, the NO_2 can flow back in to the PM cake layer and oxidizes PM further through NO_2 assisted cake PM oxidation. This phenomenon is called NO_2 back diffusion. Moreover, the NO_2 produced in the wash coat can also flow downstream and participate further in NO_2 assisted wall PM oxidation in the substrate wall. Haralampous et al. [69] reported that the effect of NO_2 back diffusion on PM oxidation could be up to 30% at low temperatures. Kiran et al. [22] showed that the effect is 1 to 4% for the passive oxidation experiments. The NO_2 back diffusion is most favorable in the temperature range of 300 to 400°C (passive oxidation test

conditions) [70]. Hence, in this chapter the effect of NO_2 back diffusion on cake PM oxidation for the passive oxidation experiments were studied using the high-fidelity SCR-F/CPF model. The tortuosity of the PM cake layer determines the effective diffusivities of gas species concentration in to the PM cake layer. This variable is calibrated to 1.0 in the SCR-F/CPF model to simulate the back diffusion of NO_2 into the PM cake layer. To eliminate back diffusion of NO_2 into the PM cake for this study, the tortuosity was set to close to zero (1e-8).

Figures 5.30 and 5.31 show the comparison of experimental and simulated NO_2 outlet concentration and NO_2 inlet concentration measured during PO-B10-15 experiment with (tortuosity = 1) and without NO_2 back diffusion (tortuosity = 0).
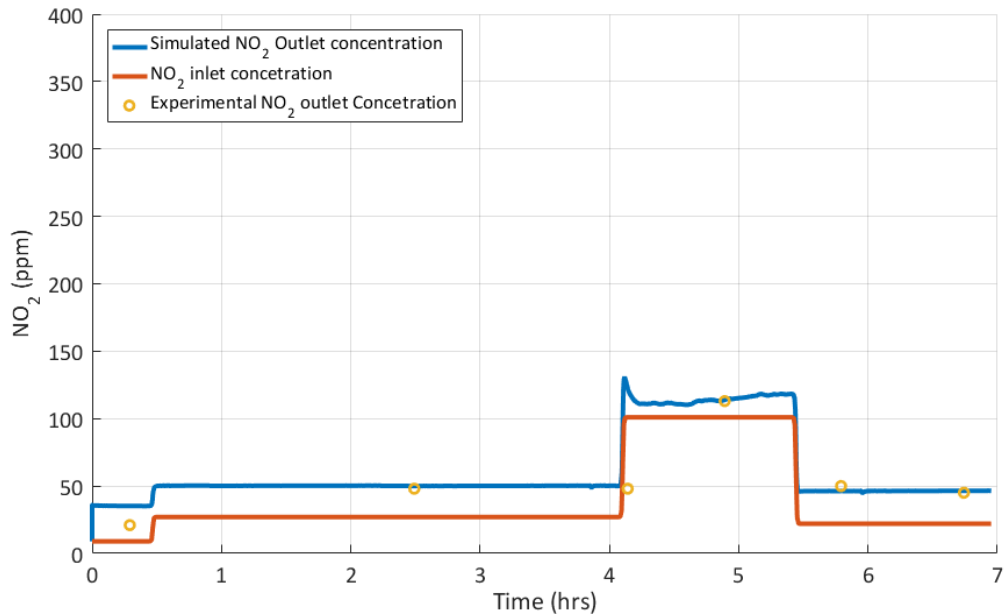
Figure 5. 30 Comparison of experimental and simulated NO_2 outlet concentrations along with the NO_2 inlet concentration measured during PO-B10-15 experiment with NO_2 back diffusion (Tortuosity of PM cake layer = 1)
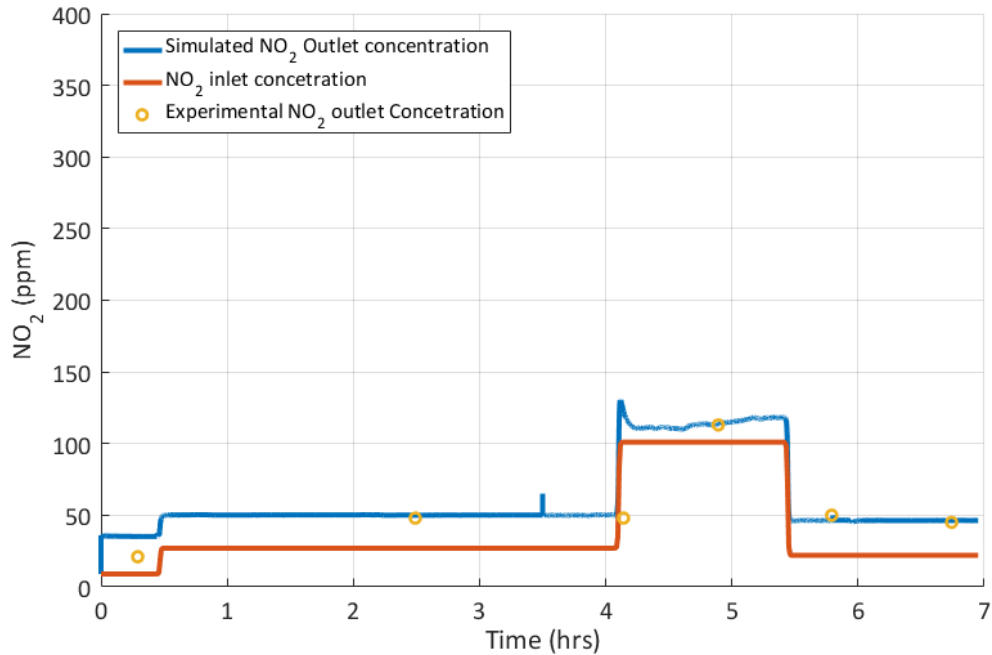
Figure 5. 31 Comparison of experimental and simulated NO₂ outlet concentration along with the NO₂ inlet concentration measured during PO-B10-15 experiment <u>without NO₂ back diffusion</u> (Tortuosity of PM cake layer = 0)

Comparison between Figures 5.31 and 5.30, the NO_2 concentration at the outlet of the CPF is similar in both cases (with and without NO_2 back diffusion).

Table 5.3 shows the effect of NO_2 back diffusion on PM oxidation for all passive oxidation experiments. From Table 5.3, the NO_2 back diffusion effect is less than 0.1 g of PM oxidized in all passive oxidation experiments. At higher temperatures of 400 to 600°C (active regeneration test conditions), NO_2 is not favored due to the chemical equilibrium limitation [70] and most of PM oxidized through thermal O_2 PM oxidation mechanism as shown in Table E.4. Hence, the NO_2 back diffusion effect is neglected in the reduced order MPF model intended for aftertreatment control applications.

Test ID	PO duration	PM oxidized with diffusion (g)	PM oxidized without diffusion (g)	Difference
PO-B10-14	101	3.3	3.4	0.0
PO-B10-15	81	18.3	18.3	0.0
PO-B10-16	43	17.3	17.2	-0.1
PO-B10-17	80	17.6	17.5	0.0
PO-B20-12	81	20.4	20.3	-0.1
PO-B20-13	42	20.4	20.3	-0.1

5.2.3 Evaluation of Average Channel Gas Temperature Assumption

The convection heat transfer between the filter substrate and the channel gas is calculated using the following equation [17]:

$$\dot{Q}_{conv\ i,j} = \dot{Q}_{wall-flow\ i,j} + \dot{Q}_{gas\ i,j} \tag{5.1}$$

$$\dot{Q}_{wall-flow\ i,j} = Q_{wall-outlet\ i,j} - Q_{inlet-wall\ i,j} \tag{5.2}$$

$$\dot{Q}_{gas\ i,j} = \dot{Q}_{outlet-conv\ i,j} - \dot{Q}_{intlet-conv\ i,j} \tag{5.3}$$

where, $\dot{Q}_{conv\ i,j}$ is the net convection heat transfer between the filter substrate and the channel gas, $\dot{Q}_{wall-flow\ i,j}$ is the net heat transfer through the wall, $\dot{Q}_{gas\ i,j}$ is the net convection heat transfer of inlet and outlet channel gas, $Q_{wall-outlet\ i,j}$ is the heat energy flowing out of the wall, $Q_{inlet-wall\ i,j}$ is the heat energy flowing into the wall, $\dot{Q}_{outlet-conv\ i,j}$ is the convection heat transfer between outlet channel gas and the filter wall and $\dot{Q}_{intlet-conv\ i,j}$ is the convection heat transfer between inlet channel gas and the filter wall.

$$Q_{inlet-wall\ i,j} = 4\ u_{wall\ i,j}\rho_{i,j}c_p(d - 2ts_{i,j})\Delta_j\frac{N_{c_i}}{2}T_{inlet\ i,j} \tag{5.4}$$

$$Q_{outlet-wall\ i,j} = 4\ u_{wall\ i,j}\rho_{i,j}c_p d\Delta_j\frac{N_{c_i}}{2}Tf_{i,j} \tag{5.5}$$

where, $u_{wall\ i,j}$ is the wall layer velocity at each zone, $\rho_{i,j}$ is the density of the gas at each zone, c_p is the specific heat of the gas, d is the channel width, $ts_{i,j}$ is the thickness of the

PM cake at each zone, Δ_j is the axial discretization length at each zone, N_{c_i} is the number of cells at each zone, $T_{inlet\ i,j}$ is the temperature of gas at the inlet channel at each zone and $Tf_{i,j}$ is the filter substrate temperature at each zone.

$$\dot{Q}_{intlet-conv\ i,j} = h_g As_{i\ i,j}\ (Tf_{i,j} - T_{inlet\ i,j}) \tag{5.6}$$

$$\dot{Q}_{outlet-conv\ i,j} = h_g As_{o\ i,j}\ (T_{outlet\ i,j} - Tf_{i,j}) \tag{5.7}$$

$$As_{i\ i,j} = 4\left(d - 2ts_{i,j}\right)\Delta_j\ \frac{N_{c_i}}{2} \tag{5.8}$$

$$As_{o\ i,j} = 4\ d\ \Delta_j\ \frac{N_{c_i}}{2} \tag{5.9}$$

where, $T_{outlet\ i,j}$ is the temperature of the gas at the outlet channel at each zone, h_g is the convective heat transfer coefficient between channel gas and wall surface, $As_{i\ i,j}$ is the surface area of the inlet channels and $As_{o\ i,j}$ is the surface area of the outlet channels.

Figures 5.32 and 5.33 show the comparison of simulated inlet and outlet channel gas temperature distribution for AR-B10-1 experiment at 5.63 hrs (15 mins after start of fuel dosing). Figure 5.34 shows the simulated substrate temperature distribution for AR-B10-1 experiment at 5.63 hrs (15 mins after start of fuel dosing). Comparing Figure 5.34 with 5.32 and 5.33, the temperature distribution looks similar at inlet channel (gas), substrate and outlet channel (gas). The maximum absolute temperature difference between inlet channel and substrate is < 3°C and RMS temperature difference is $\cong$ 1.4 °C. The maximum absolute temperature difference between outlet channel and filter is < 2°C and RMS temperature difference is $\cong$ 0.7°C.
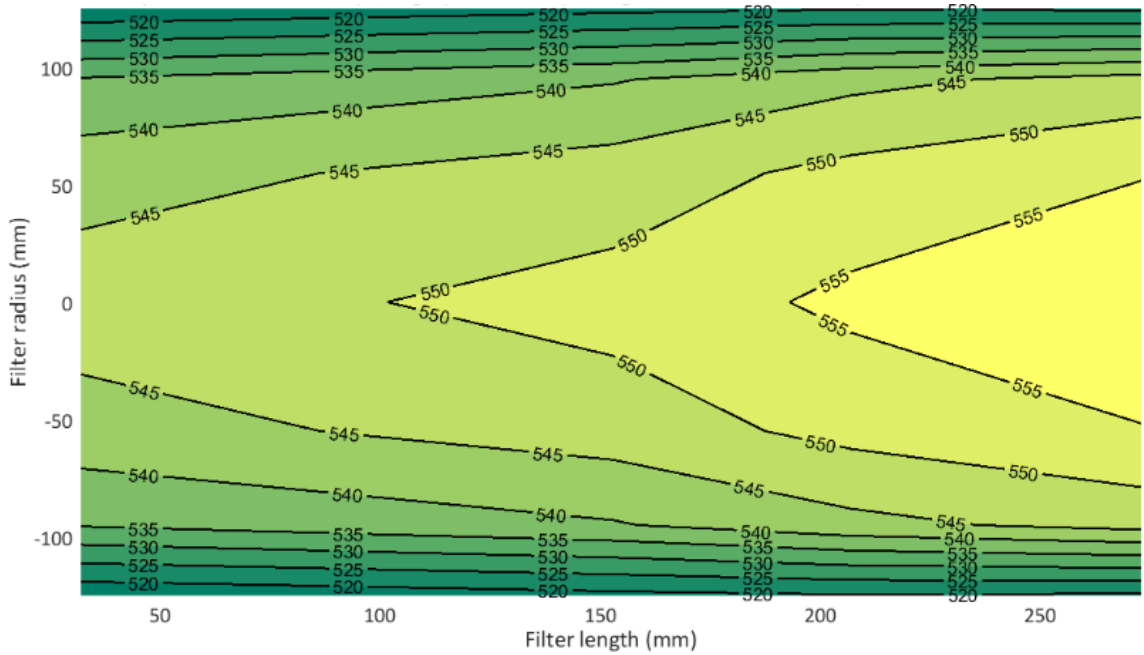
Figure 5. 32 Simulated <u>inlet gas</u> temperature distribution in °C for AR-B10-1 experiment at 5.63 hrs (15 minutes after start of fuel dosing)
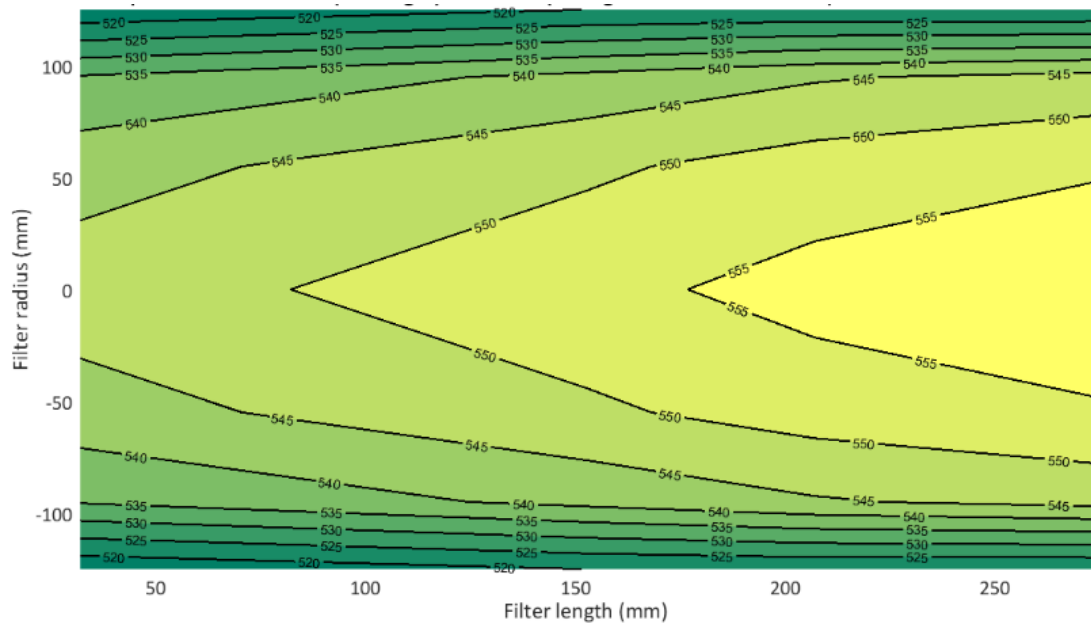
Figure 5. 33 Simulated <u>outlet gas</u> temperature distribution in °C for AR-B10-1 experiment at 5.63 hrs (15 minutes after start of fuel dosing)

131
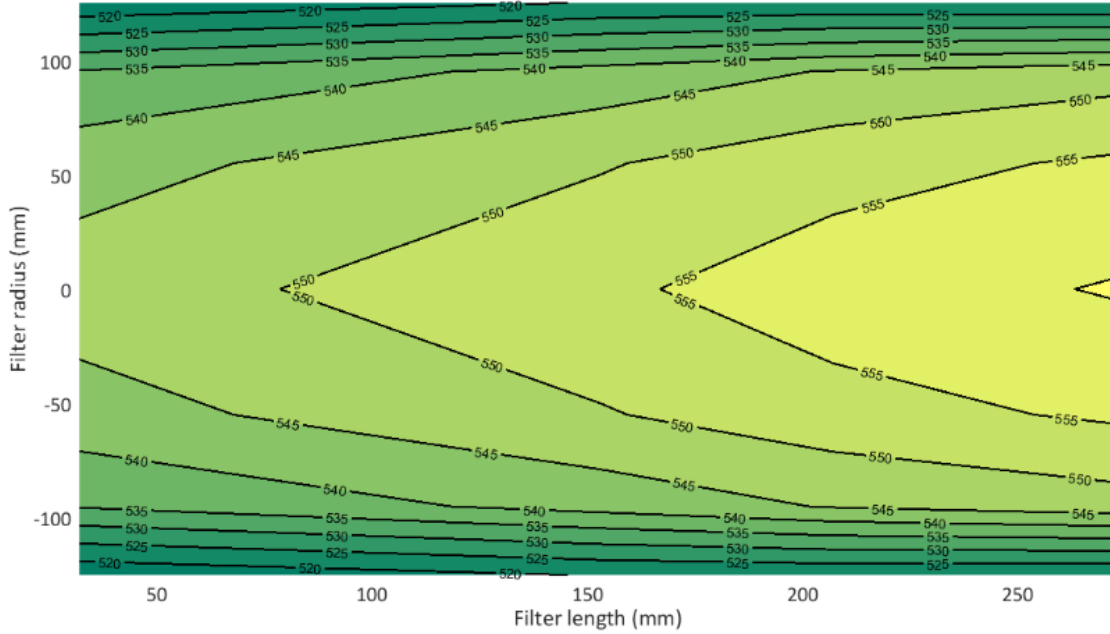
Figure 5. 34 Simulated <u>substrate</u> temperature distribution in °C for AR-B10-1 experiment at 5.63 hrs (15 minutes after start of fuel dosing)

Comparing Figures 5.32 and 5.33, the maximum absolute temperature difference between inlet and outlet channel gas is < 2°C and RMS error is within 1°C. The temperature difference between inlet and outlet channel is minimum because of the high rate of convection heat transfer between the channels and the porous substrate wall. Hence, for the purpose of the reduced order model development, the lumped model approach [13] is employed by applying average channel gas temperature for calculation of convection heat transfer between channels and the filter substrate. With the average channel temperature assumption, the temperature difference of the gas flowing through the wall can be neglected (Equations 5.4 and 5.5).

By applying average channel gas assumptions, the Equations 5.1 to 5.9 are reduced to:

The convection heat transfer between filter and channel gas is calculated using the following equation [13,53]:

$$\dot{Q}_{conv} = h_g As_{i,j} \left(T_{i,j} - Tf_{i,j} \right) \tag{5.10}$$

The combined surface area As is calculated as follows [13]

$$As_{i,j} = \frac{Nc_i}{2} \left[4\left(d - 2ts_{i,j} \right) + 4d \right] \Delta L_j \tag{5.11}$$

The inlet and outlet channels energy Equations 4.3 and 4.4 are reduced to average channel gas energy equation and it is given as [13]:

$$\rho c_p A s_{i,j} \Delta L_j \frac{dT_{i,j}}{dt} = \dot{m}_{i,j} c_p (T_{i,j-1} - T_{i,j}) - \dot{Q}_{conv} \tag{5.12}$$

5.2.4 Effect of Radiation Heat Transfer between Inlet Channel Surfaces to Overall Temperature and PM Mass Distribution

The high-fidelity SCR-F/CPF model assumes the channel gas is completely transparent to thermal radiation and the surfaces are black. The net radiation heat transfer between channel gas and filter wall is determined as [71]:

$$\dot{Q}_{rad} = -As_{i,j} \left(F_{3-1}(J_3 - J_1) + F_{3-2}(J_3 - J_2) \right) \tag{5.13}$$

$$J_1 = \sigma T_{i,j-1}^4 \tag{5.14}$$

$$J_2 = \sigma T_{i,j}^4 \tag{5.15}$$

$$J_3 = \sigma T f_{i,j}^4 \tag{5.16}$$

The effect of internal radiation is very small at lower temperatures and could be more important over 600°C and could improve the model accuracy during uncontrolled regeneration events [55]. The most of the operating conditions in the CPF are below 600°C. Hence, the radiation heat transfer between channel gas and filter wall was neglected and the effect of neglecting radiation heat transfer in terms of temperature distribution and PM mass retained prediction accuracy was studied.

Table 5.4 shows the temperature, PM loading, pressure drop inaccuracies and computational time trade-off with and without radiation heat transfer modeling.

Table 5. 4 Temperature, PM loading, pressure drop simulation inaccuracies and computational time trade-off
with and without radiation heat transfer for the SCR-F/CPF model

Model Discretization Level	RMS tempertaure error @ start of PM oxidation (time : 5.6 hrs)	PM Loading error @ end of post loading (time:7.3 hrs)	Pressure drop error @ end PM oxidation (time:5.8 hrs)	Simulation time / Real time [-]
	^{o}C	g	kPa	[-]
10x10 zone	3.1	0.3	-0.01	0.13
10x10 zone without radiation heat transfer	3.3	0.2	-0.02	0.13

From Table 5.4, the RMS temperature error increases from 3.1 to 3.3 ^{o}C by neglecting the radiation heat transfer between channel gas and substrate wall. The PM post loading error reduced from 0.3 to 0.2 g and pressure drop error increase from -0.01 to -0.02 kPa. The ratio of simulation time to real time is almost the same between both cases. As shown in Table 5.4, the simulation error by neglecting the radiation heat transfer between channel gas and the filter wall is minimum. Hence, for the purpose of the reduced order model development, the radiation heat transfer between channel gas and filter wall was neglected.

5.3 Simulation of Reduced Order MPF Model

From the parametric study and analysis presented in sections 5.1 and 5.2, a reduced order 5x5 zone MPF model was developed. The following are the key assumptions used in developing the reduced order MPF model based

- The inlet PM deposits uniformly over the entire volume of the filter substrate.
- The PM inlet rate into the each zone is assumed to be the ratio of volume of each zone to the total volume of the filter. In other words, no maldistribution of inlet PM is considered.
- Species concentrations (O_2 and NO_2) are assumed to be uniform in the inlet channel, PM cake, substrate wall and are equal to inlet concentrations.
- PM oxidation due to NO_2 back diffusion is negligible and hence not included.
- PM cake layer and substrate wall are at the same temperature. In other words, no temperature gradient across the PM cake layer and substrate wall is considered.
- Radiation heat transfer between channel gas and filter substrate is negligible and hence is not included.

- Average channel gas temperature used for the filter energy equation (lumped model approach). Hence, the temperature difference of the gas flowing through the substrate wall is neglected.
- A fully developed boundary layer exists at the inlet of the CPF.
- The exhaust gas mixture is assumed to be an ideal gas.
- The exhaust gas has the same properties as air at 1 atmosphere pressure. Properties are considered as a function of temperature.
- Molecular weight of the exhaust gas is assumed to be constant and it is equal to $28.7 \frac{kg}{kmol}$.

The reduced order MPF model was validated on one of the active regeneration experiments and the results were compared with the 10x10 high fidelity model and experimental data. The detailed simulation results of 5x5 zone reduced order MPF model for AR-B10-1 experiment is presented in this section. An explicit solver based on finite difference approach was used to solve the temperature at each time step in the reduced order model. The explicit solver time step was set to 0.01 sec to achieve numerical stability and the simulation model time step was set to 5 seconds (fixed discrete step) over the total test duration of approximately 7.33 hrs for AR-B10-1 experiment. The model calibration parameters for the reduced order MPF model are same at those in high-fidelity SCR-F/CPF model except that pre-exponential of the HC oxidation was increased from 6.0E8 to 3.0E9 $\frac{m^3}{kmol-sec}$ to improve stability of the model at lower discretization size and also to account for the reaction kinetics change in the absence of the species concentration solver and lumped channel approach. The error induced by this pre-exponential change is expected to be compensated by the state estimator feedback gains (Kalman gain) using the measured outlet temperature of the CPF which is explained in the next chapter.

Filter Outlet Temperature

Figure 5.35 shows the comparison of high-fidelity SCR-F/CPF model outlet gas temperature (high-fidelity T_{80}) with the reduced order MPF model outlet gas temperature (ROM-T_{20}) along with the CPF outlet gas temperature (Exp) measured during AR-B10-1 experiment. From Figure 5.35, the reduced order MPF model temperature prediction closely simulates with the high-fidelity SCR-F/CPF results model and the experimental

data. The maximum absolute temperature error between reduced order model and high-fidelity SCR-F/CPF model is within 5°C.
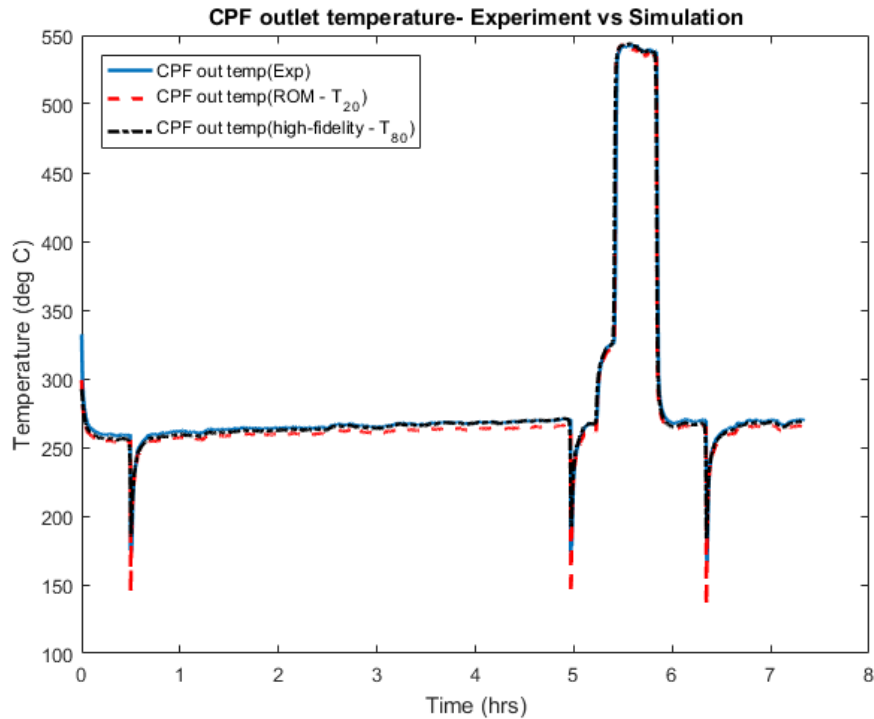
Figure 5. 35 Comparison of high-fidelity SCR-F/CPF model and reduced order MPF model CPF outlet gas temperatures along with the measured CPF outlet gas temperature for AR-B10-1 experiment

Temperature Distribution

Figures 5.36 and 5.37 show the comparison of reduced order MPF model temperature distribution data and high fidelity SCR-F/CPF model temperature distribution for the AR-B10-1 experiment at 5.63 hrs (15 min after start of fuel dosing). Comparing Figures 5.36 and 5.37, the reduced order MPF model closely simulates the results with the high-fidelity SCR-F/CPF model temperature distribution trends. The maximum absolute temperature error between the high-fidelity SCR-F/CPF model and the reduced order MPF model is within 5°C.
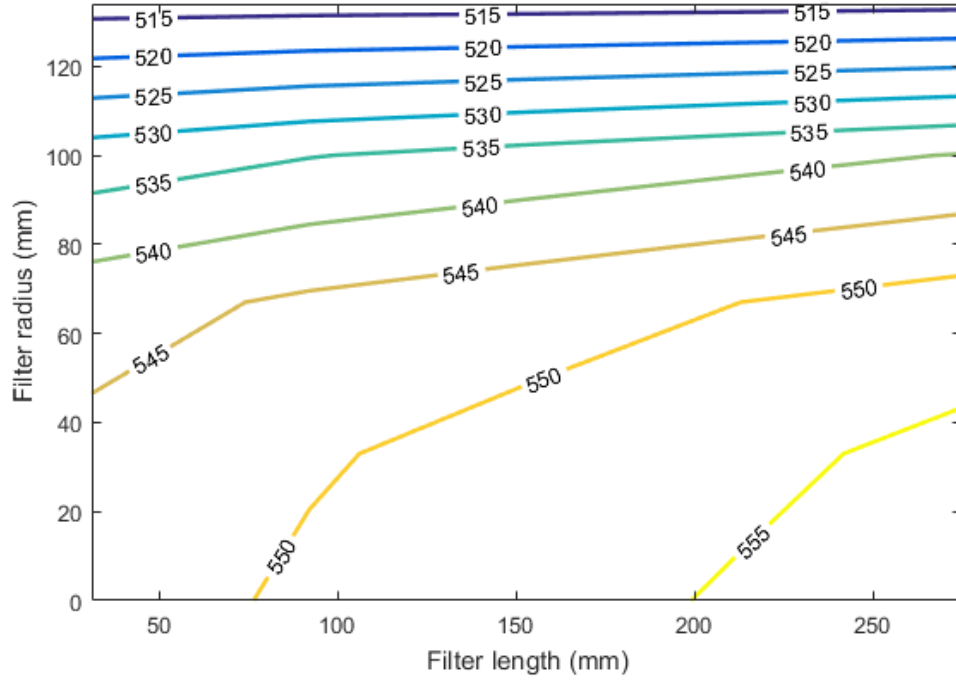
Figure 5. 36 Reduced order MPF model temperature distribution in °C for AR-B10-1 experiment at 5.63 hrs. (15 minutes after start of fuel dosing)
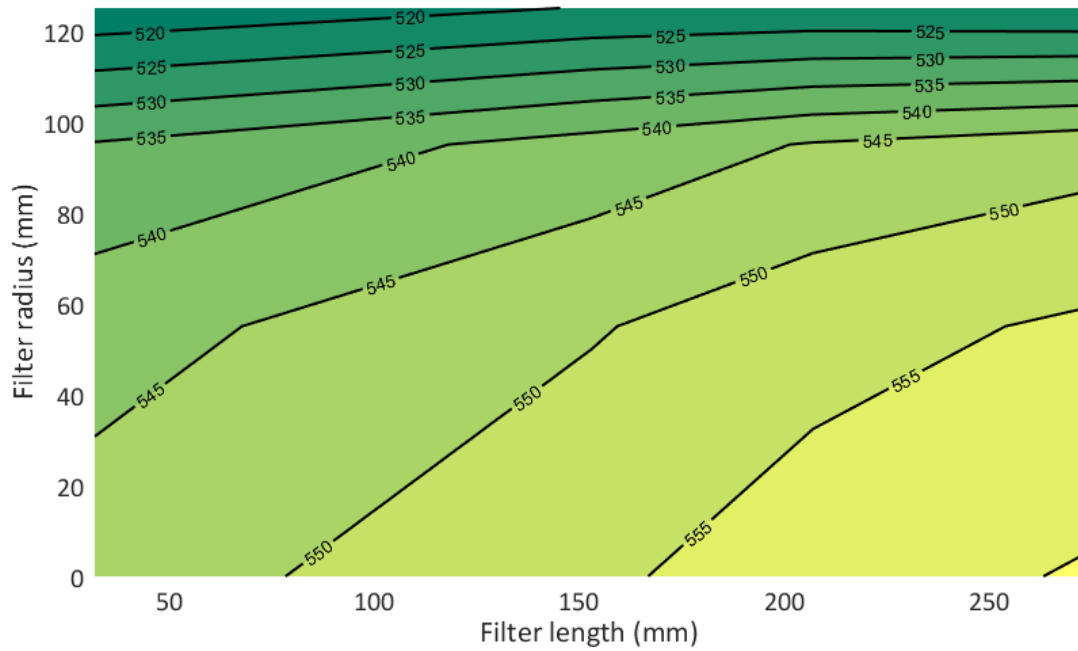
Figure 5. 37 High-fidelity SCR-F/CPF model simulated temperature distribution in °C for AR-B10-1 experiment at 5.63 hrs (15 minutes after start of fuel dosing)
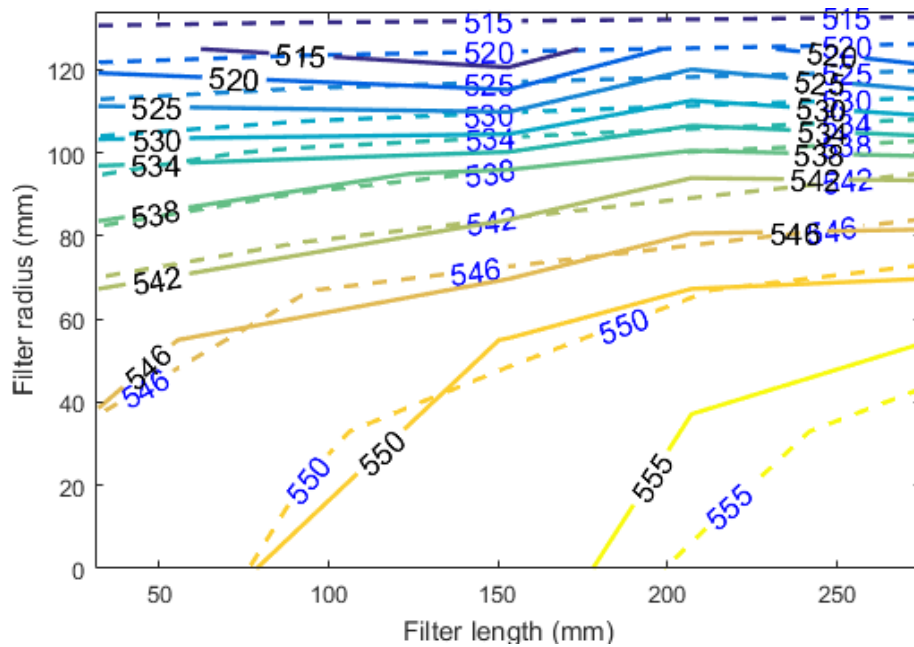
Figure 5. 38 Comparison of experimental (solid lines) and reduced order model (dotted lines) temperature distribution at 5.63 hrs (15 mins after start of fuel dosing)

Figure 5.38 shows the comparison of experimental and reduced order model temperature distribution at 5.63 hrs (15 mins after start of fuel dosing). From Figure 5.38, the reduced order model is able to closely follow the experimental temperature and the maximum absolute temperature difference between the reduced order model and the experimental data is less than 5°C.

PM Mass Retained

Figures 5.39 and 5.40 show the comparison of cumulative PM mass retained in the filter along with the cake and wall PM masses for the reduced order MPF model and the high-fidelity SCR-F/CPF model. From Figures 5.39 and 5.40, the reduced order model cumulative PM mass retained during loading, PM oxidation by active regeneration and post loading closely simulates the results of the high-fidelity SCR-F/CPF model. The maximum error in PM retained prediction is $\cong$ 0.6 g at the end of stage 4 loading compared to the high-fidelity SCR-F/CPF model.
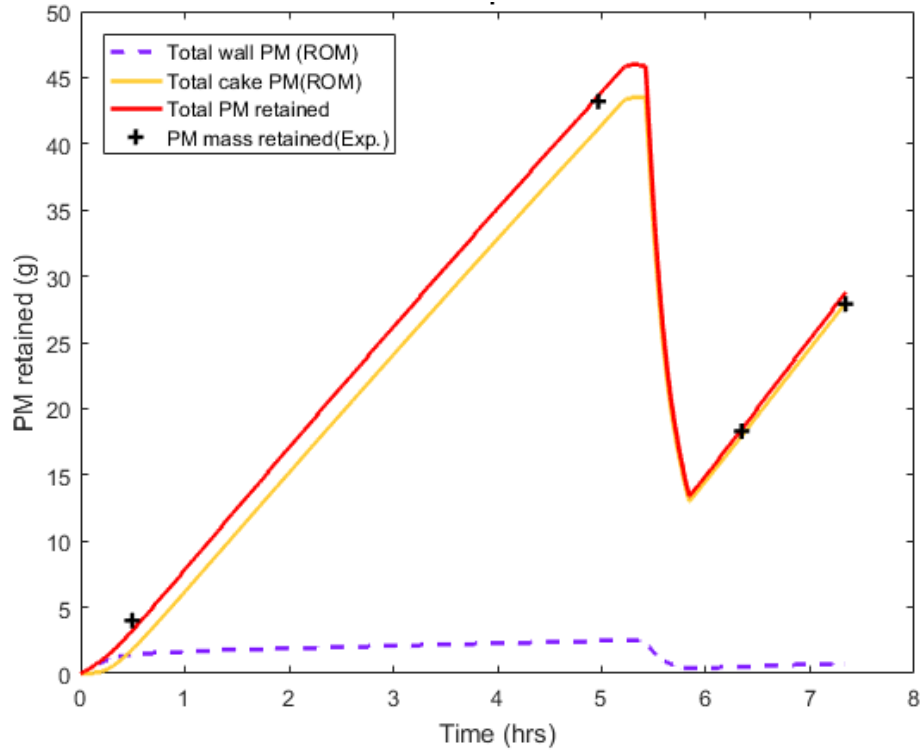
Figure 5. 39 Comparison of PM mass retained in the experimental data and reduced order model along with the cumulative cake and wall masses for AR-B10-1 experiment
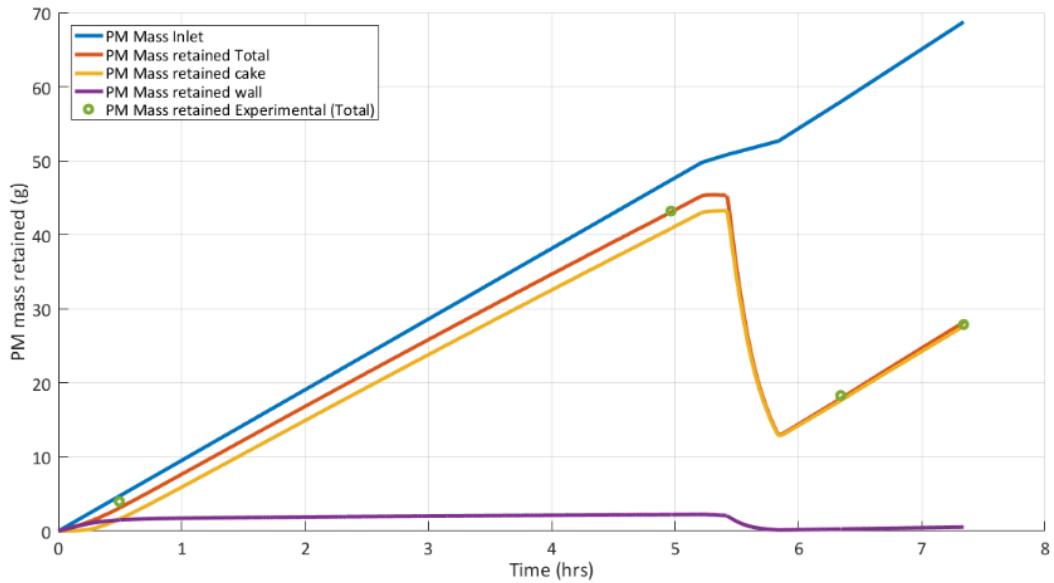
Figure 5. 40 Comparison of PM mass retained in the experimental data and high-fidelity SCR-F/CPF model along with the model cumulative for PM inlet, cake and wall PM masses for AR-B10-1 experiment

139

PM Distribution

Figures 5.41 and 5.42 show comparison of PM mass loading distribution along the axial and radial directions at the end of PM oxidation (at 5.82 hrs) by active regeneration for AR-B101 experiment simulated by the reduced order MPF model and high fidelity SCR-F/CPF model. From Figures 5.41 and 5.42, the PM loading distribution simulated by the reduced order model closely simulates the high-fidelity model. The PM loading distribution difference is less than 0.1 g/L compared to high-fidelity SCR-F/CPF model for the filter radiuses below 120 mm. The PM loading distribution simulated by the reduced order model is $\cong$ 0.2 to 0.5 g/L lower than the high-fidelity model at the outer radiuses of the filter (radiuses > 120 mm). This is mainly because of the lower discretization of the reduced order model compared to the high-fidelity SCR-F/CPF model.
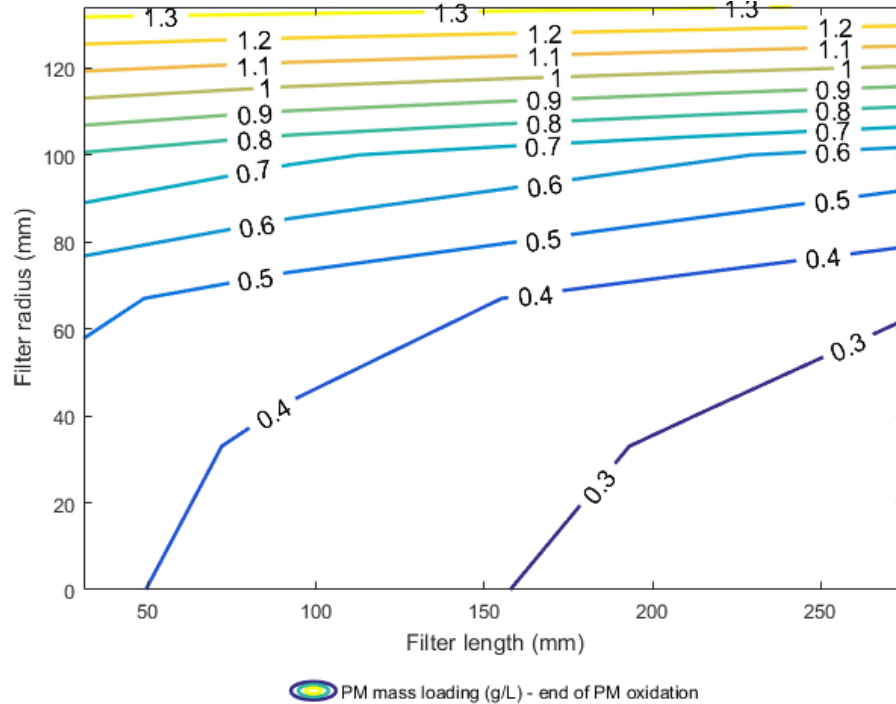
Figure 5. 41 Reduced order model PM mass loading distribution along the axial and radial directions at 5.82 hrs (end of PM oxidation by active regeneration) for AR-B10-1 experiment
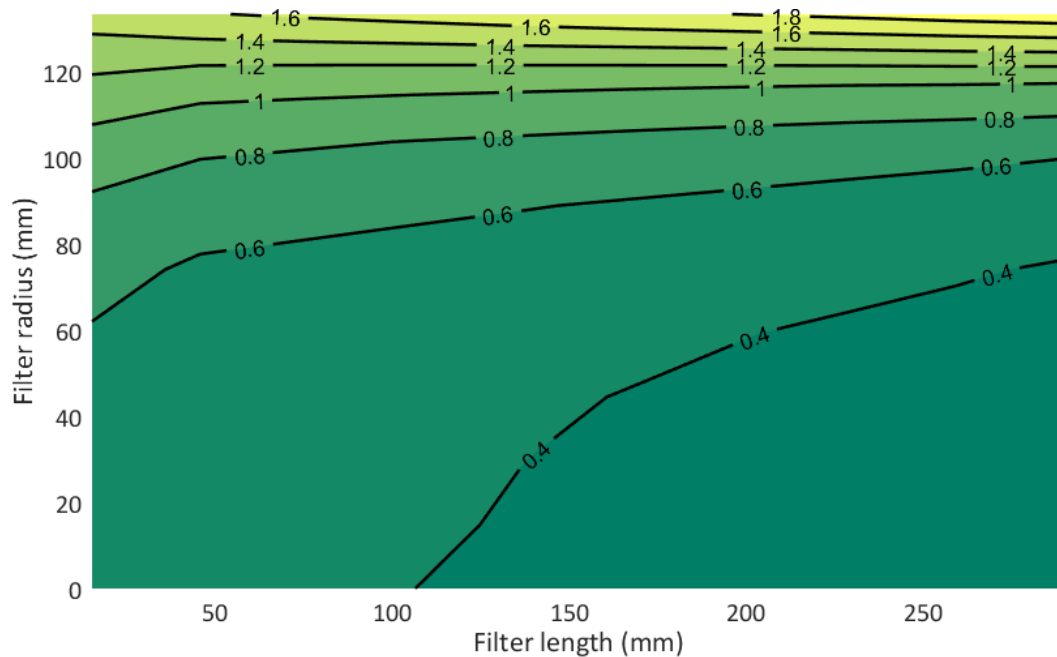
Figure 5. 42 High-fidelity SCR-F/CPF model PM mass loading distribution along the axial and radial directions at 5.82 hrs (end of PM oxidation by active regeneration) for AR-B10-1 experiment

Pressure Drop

Figures 5.43 and 5.44 show the comparison of the total pressure drop across the CPF and its components for AR-B10-1 experiment simulated by the reduced order MPF model and high-fidelity SCR-F/CPF model. From Figures 5.43 and 5.44, the pressure drop simulated by the reduced order MPF model closely simulates the high-fidelity SCR-F/CPF model trends. The maximum pressure drop simulation error with the reduced order model is $\cong$ 0.2 kPa compared to the high-fidelity SCR-F/CPF model data during the AR ramp phase of the experiment. The maximum pressure drop error with reduced order model is $\cong$ 0.4 kPa compared to the experimental data.
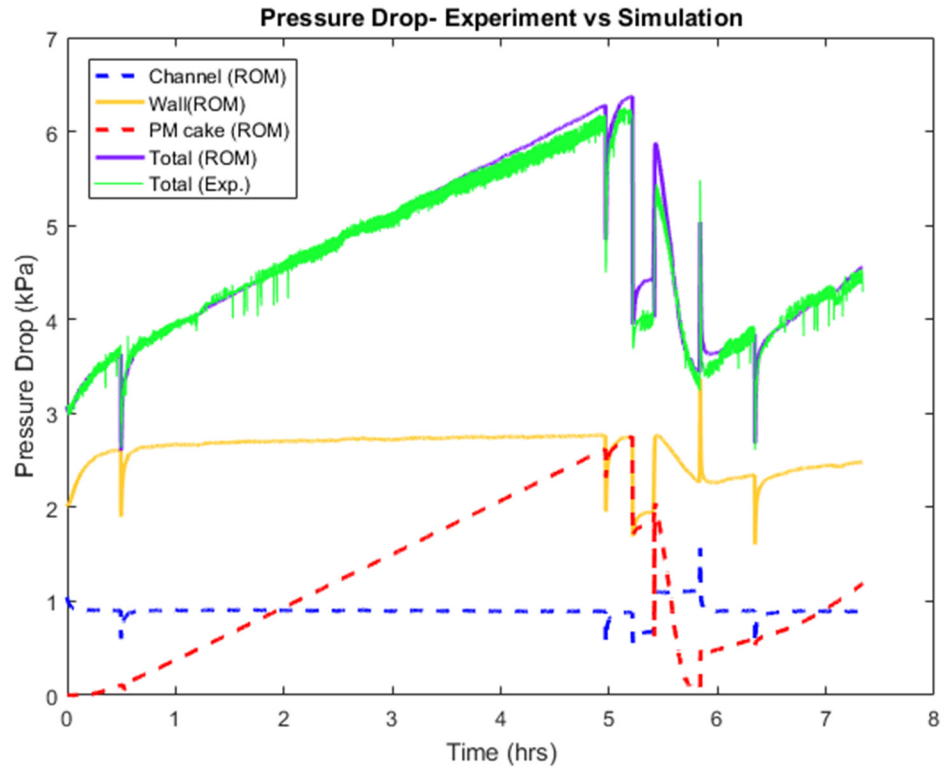
Figure 5. 43 Comparison of experimental and simulated total pressure drop across CPF and its components for AR-B10-1 experiment simulated by the reduced order MPF model
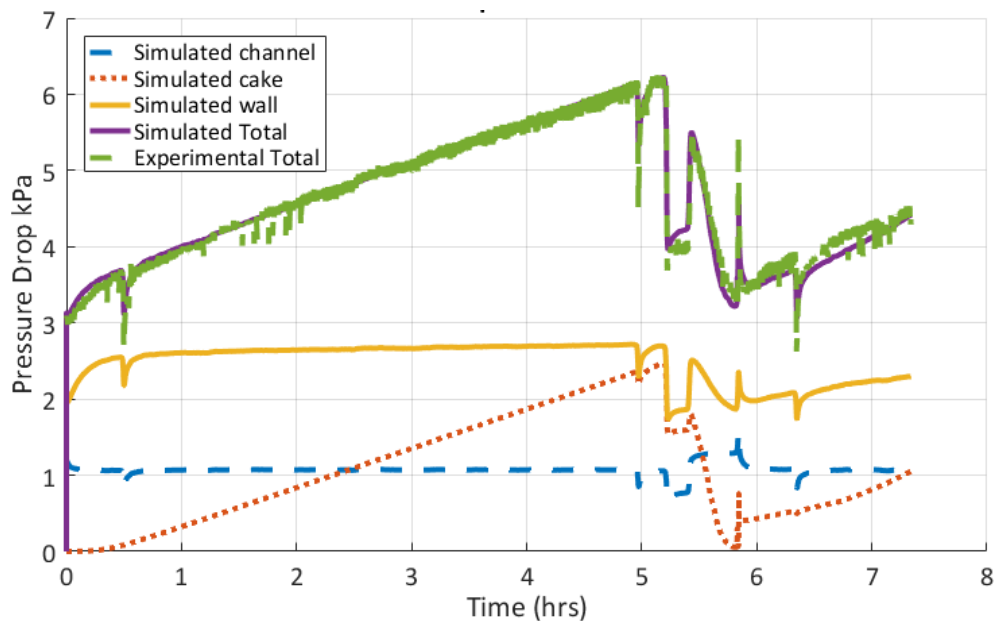
Figure 5. 44 Comparison of experimental and simulated total pressure drop across CPF and its components for AR-B10-1 experiment simulated by the high-fidelity SCR-F/CPF model

Based on the analysis of results presented in section 5.3, the reduced order MPF model with 5x5 zone discretization and simplification assumptions offers good capability to predict the temperature and PM mass distribution and pressure drop of the CPF. The absolute temperature distribution error was within 5°C, PM mass retained error within 0.6 g, PM distribution error was within 0.1 g/L (radiuses < 120 mm) and pressure drop error was within 0.2 kPa compared to the high-fidelity SCR-F/CPF model. This 5x5 zone reduced order model was used to develop a real time CPF state estimator to estimate the unknown states of the CPF such as temperature and PM distribution and pressure drop of the CPF. The development and validation of CPF state estimator is explained in the next chapter.

6 CPF State Estimator Development[1]

This chapter describes the development of the state estimator for the CPF to predict unknown states of the CPF such as temperature and PM loading distribution and pressure drop of the CPF. In a linear system with Gaussian noise, the Kalman filter is optimal [72]. In a system that is nonlinear, an extended Kalman filter can be used, but the unscented Kalman filter and particle filter may give better results at the price of additional computational effort. For ECU based applications, the linear and extended Kalman filters provide better trade-off in terms of computational effort compared to unscented Kalman filter and particle filters. Hence, the CPF state estimator developed in this thesis uses an extended Kalman filter (EKF) for the estimation of the temperature and PM loading distribution and a linear Kalman filter (LKF) for the estimation of pressure drop across the CPF.

The reduced order 5x5 zone MPF model presented in Chapter 5 was used for the development of the CPF state estimator. The CPF state estimator uses the DOC outlet temperature, NO_2 and HC concentrations from the DOC state estimator as the input conditions (DOC outlet temperature, NO_2 and HC concentrations) to the CPF state estimator. Hence, a DOC state estimator developed by Harsha Surenahalli [48] was integrated with the CPF state estimator developed in this thesis. The implementation details of EKF and LKF and the simulation of DOC-CPF state estimator on the active regeneration experiment (AR-B10-1) is presented in this chapter. Figure 6.1 shows the schematic of the DOC-CPF state estimators with all the inputs needed.

---

[1] Parts of the material contained in this chapter are based on references [1, 2,3] with permission of Springer.
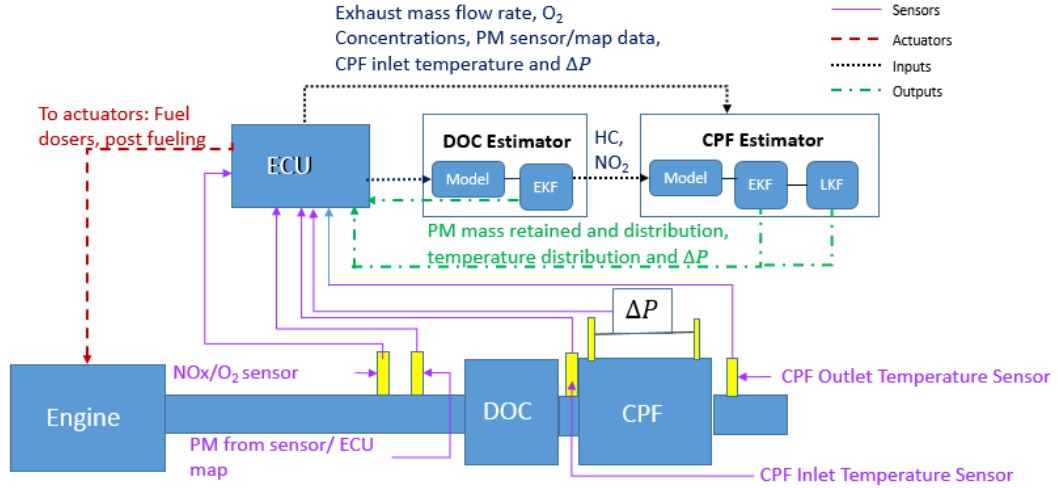
Figure 6. 1 Schematic of a CPF estimator showing the all the inputs needed

6.1 Development of Kalman Filter Based CPF State Estimator

The main function of the Kalman filter is to predict the state and error covariance for the next time step based on system model and then compensate for the difference between measurement and prediction and compute the new estimate of the state. If the system model is non-linear, then the Kalman filter linearizes the system model with the current mean and covariance [72]. This type of Kalman filter is called extended Kalman filter. In this thesis, a non-linear system model is applied (Equation 6.1) for the estimation of temperature distribution and the linear model is applied for the pressure drop estimation (Equation 6.2). The system model equation for temperature distribution in a discrete form is given as:

$$\left[Temp\_filter_{i,j}\right]_k = \left[Temp\_filter_{i,j}\right]_{k-1} +$$

$$\frac{\dot{Q}_{cond.axial\,i,j} + \dot{Q}_{cond.radial\,i,j} + \dot{Q}_{conv\,i,j} + \dot{Q}_{reac,PM\,i,j} + \dot{Q}_{reac,HC\,i,j}}{(\rho_s c_s V s_{i,j} + \rho_f c_f V f_{i,j})} \Delta t \qquad (6.1)$$

Similarly, the system model equation for the pressure drop estimation is given as

$$\Delta P_{Total} = \Delta P_{channel\,MPF\,model} + \Delta P_{wall\,MPF\,model} + \Delta P_{est.cake} \qquad (6.2)$$

Extended Kalman Filter (EKF) for Temperature and PM distribution Estimation

The scope of this estimator is to predict the unknown states of the CPF temperature distribution. The estimator output equations calculate the PM mass distribution and

pressure drop using the temperature states. The brief description of the extended Kalman filter based state space model formulation is presented here.

The state space representation of a simple discrete nonlinear model with states x_k, inputs u_k and noises w_k and v_k can be represented as [72],

$$x_k = f_{k-1}(x_{k-1}, u_{k-1}, w_{k-1})$$ (6.3)

$$y_k = h_k(x_k, v_k)$$ (6.4)

The function f is used to predict the state estimate and the function h is used to compute the predicted measurement. w_k and v_k are the process and observation noises. In general, noise values are estimated statistically and noise is assumed to be in normal distribution and this means average is always zero. In Kalman filter, w_k and v_k are assumed to be zero mean multivariate Gaussian noises with covariance Q_k and R_k respectively [72]. The modeling of process noise (w_k) is difficult and needed to be determined from the basic knowledge and experience of the system. Similarly, the measurement noise covariance (R_k) is estimated from the knowledge of predicted observation errors. If both covariance matrices are difficult to obtain in analytically, they can be determined by trial and error [73]. In this thesis, the process noise (w_k) was neglected and the covariance matrix (R_k) was constructed using the covariance of 0.1 for the observation noise (v_k) based on earlier references [48]. The implementation of extended Kalman filter algorithm involves the following steps [72]:

1) Compute the F_k and L_k matrices:

$$F_k = \left. \frac{\partial f_{k-1}}{\partial x} \right|_{x_{k-1}, u_{k-1}}$$ (6.5)

$$L_k = \left. \frac{\partial f_{k-1}}{\partial w} \right|_{x_{k-1}, u_{k-1}}$$ (6.6)

2) Predict the state and error variance:

$$x_k^- = f_{k-1}(x_{k-1}^+, u_{k-1}, 0)$$ (6.7)

$$P_k^- = F_{k-1}P_{k-1}^+ F_{k-1}^T + L_{k-1}Q_{k-1}L_{k-1}^T$$ (6.8)

3) Compute the matrices of H_k and M_k:

$$H_k = \left.\frac{\partial h_k}{\partial x}\right|_{x_k^-} \tag{6.9}$$

$$M_k = \left.\frac{\partial h_k}{\partial v}\right|_{x_k^-} \tag{6.10}$$

4) Compute the optimal Kalman gain:

$$K_k = P_k^- H_k^T (H_k P_k^- H_k^T + M_k R_k^- M_k^T)^{-1} \tag{6.11}$$

5) Compute the estimate and error covariance:

$$x_k^+ = x_k^- + K_k(y_k - h_k(x_k^-, 0)) \tag{6.12}$$

$$P_k^+ = (I - K_k H_k)P_k^-(I - K_k H_k)^T + K_k R_k K_k^T \tag{6.13}$$

Steps 1 to 5 are followed at each time step and the optimal gain matrix and state estimates are calculated. The temperature states for the discretized 5x5 zone reduced order MPF model are defined as:

$$x_k = \begin{Bmatrix} T_{2,k} \\ T_{3,k} \\ T_{4,k} \\ T_{5,k} \\ T_{7,k} \\ \vdots \\ T_{25,k} \end{Bmatrix} \tag{6.14}$$

Figure 6.2 shows the schematic of the CPF temperature states for the 5x5 zone CPF state estimator. The input temperatures for the CPF state estimator are T_1, T_6, T_{11}, T_{16} and T_{21} and they are calculated from the DOC outlet temperature $T_{in,4}$ using the thermal boundary layer Equation A.2. The measurement Equation (6.4) uses the $T_{out,20}$ as the feedback signal for performing the measurement update of the state estimate in Equation 6.12. The function f for each temperature state is determined from the discretized system model Equation 6.1 at various locations of the axial and radial temperature states (T_1 to T_{25}).
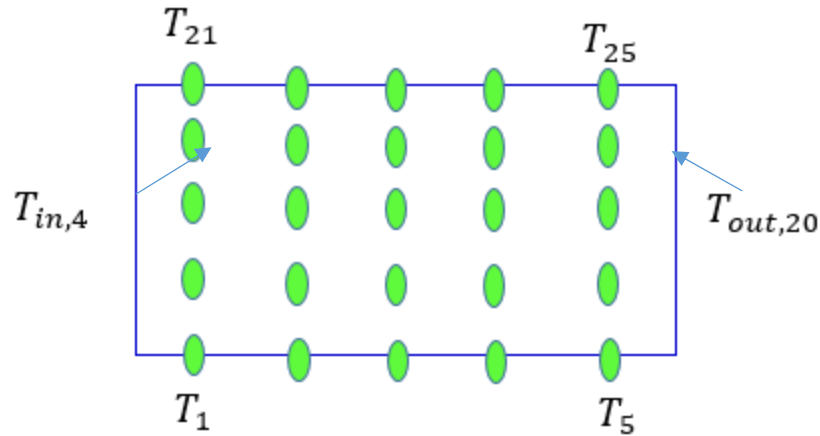
Figure 6. 2 Schematic of temperature states of the CPF estimator

Linear Kalman Filter for Pressure Drop Estimation

The temperature and PM mass distribution can be accurately estimated using the temperature state estimates. However, at fixed flow and temperature conditions, the pressure drop across the filter is governed by:

- PM flow rate (PM concentration and volumetric flow rate)
- Thickness of the PM cake layer (PM mass retained)
- PM within the pores of the substrate wall (filtration efficiency)
- PM cake oxidation rate (Temperature, NO_2 and O_2 concentration)
- PM wall oxidation rate (Temperature, NO_2 and O_2 concentration)
- Permeability of wall (clean wall, packing density, partial oxidation of PM in the wall, slip flow etc.)
- Permeability of cake (initial, damage values, damage recovery, slip flow etc.).

From the above parameters affecting pressure drop, it is evident that the temperature estimates and subsequent PM oxidation alone are not good enough to accurately predict the pressure drop estimates. Hence, the linear Kalman filter is necessary that could use the measured total pressure drop from the ECU sensor to predict unknown components of the pressure drop measurement such as cake pressure drop.

The state space representation of a simple linear model with state x_k, inputs u_k and noises w_k and v_k can be represented as [72],

$$x_k = Ax_{k-1} + w_{k-1} \tag{6.15}$$

$$z_k = H_k x_{k-1} + v_k \tag{6.16}$$

The implementation algorithm for the linear Kalman filter is given as:

1) Predict the state and error variance:

$$x_k^- = Ax_{k-1}^+ \tag{6.17}$$
$$P_k^- = AP_{k-1}^+ A^T + Q_{k-1} \tag{6.18}$$

2) Compute optimal Kalman gain:

$$K_k = P_k^- H_k^T (H_k P_k^- H_k^T + R_k^-)^{-1} \tag{6.19}$$

3) Compute the estimate and error covariance:

$$x_k^+ = x_k^- + K_k(z_k - H_k x_k^-) \tag{6.20}$$
$$P_k^+ = P_k^- - K_k H_k P_k^- \tag{6.21}$$

The state x_k is total pressure drop and the output z_k is the cake pressure drop. The other components of pressure drop such as wall pressure drop and total channel pressure drop are determined from the model equations developed in Chapter 4.

The process noise (w_k) is assumed to be equal to zero and the covariance for the measurement (R_k) was calculated assuming standard deviation of 0.5 kPa for the measurement noise (v_k).

From the above extended Kalman filter implementation algorithm, a Kalman filter based CPF state estimator was developed. The CPF state estimator uses the following inputs:

1) Instantaneous exhaust mass flow rate ($\dot{m}$)
2) CPF inlet concentrations (PM, NO_2, O_2 and C_3H_6)
3) CPF inlet temperature ($T_{in,4}$)
4) Ambient pressure and temperature

The CPF state estimator uses the above inputs to estimate the temperature states at axial and radial locations of the filter. The temperature state estimates are used in the output Equations 4.7 to 4.15 to estimate the temperature and PM distribution and pressure drop

of the filter. Further, linear Kalman filter within the CPF state estimator uses the measured ΔP sensor signal values to estimate the unknown states of the pressure drop such as cake pressure drop using Equation 4.22. The CPF estimator temperature ($T_{in,4}$) and the CPF inlet concentrations (NO_2, O_2 and C_3H_6) are determined from the DOC state estimator developed by Harsha Surenahalli [48]. The next section explains the integration details of DOC state estimator with the CPF state estimator.

6.2 Integration of DOC and CPF Estimators

The main purpose of the DOC state estimator is to estimate the DOC outlet temperature and concentrations such as NO_2 and C_3H_6 from the engine out concentrations. Figure 6.3 shows the Simulink schematic of the DOC state estimator [74]. This DOC estimator uses the inputs from engine sensors and engine maps to estimate DOC states such as DOC outlet temperature and concentrations (NO_2 and C_3H_6).
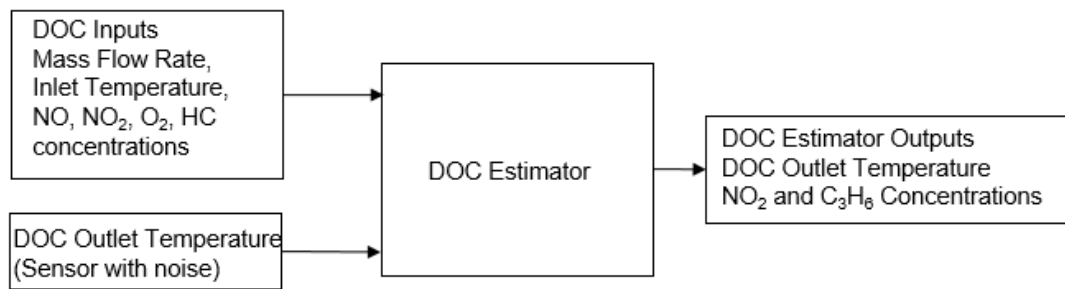
Figure 6. 3 Schematic of the DOC state estimator – adapted from reference [74]

The DOC outlet temperature and concentrations (NO_2 and C_3H_6) along with the other engine sensor/map inputs such as ΔP, PM inlet and O_2 concentrations and CPF outlet temperature are used as the input conditions for the CPF state estimator. The schematic of the CPF state estimator integrated with the DOC estimator along with other inputs is shown in Figure 6.4.

150
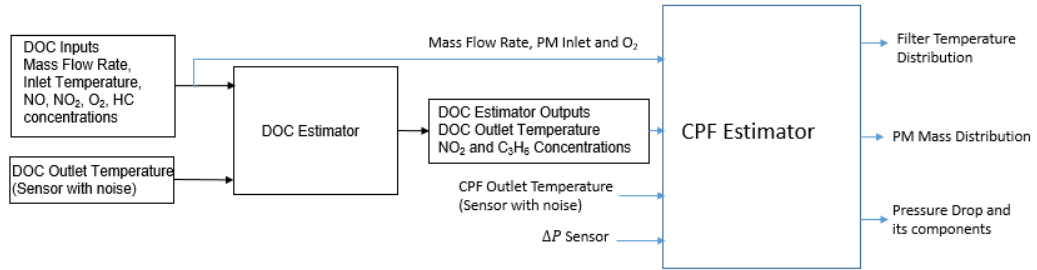
Figure 6. 4 Schematic of DOC-CPF state estimator

6.3 Simulation of DOC-CPF State Estimator

The DOC-CPF state estimator was simulated on one of the active regeneration experiments (AR-B10-1) and the results were compared with the 10x10 high fidelity model and experimental data. The detailed simulation results are presented in this section. The DOC-CPF state estimator used the reduced order model explained in Chapter 5, to predict the temperature states of the current time. Further, the temperature estimates are improved by the extend Kalman filter algorithm explained in section 6.2. The inputs to the DOC-CPF estimators were sampled at 1Hz. The discrete time step solver with 1 second time step was used to run the DOC-CPF state estimator. With the fixed step discrete solver and the model time step of 1 second, the real time factor for the DOC-CPF state estimator is 0.152 (15.2 % of real time or $\cong$ 6.5 times faster than the real time) using the Laptop computer with the specifications of 12 GB RAM, 64 bit and Intel core i7 processor.

DOC State Estimator Results

The active regeneration experiment (AR-B10-1) was used for the simulation of the DOC-CPF state estimator. The active regeneration run (AR-B10-1) was selected as the representative case for the simulation of the DOC state estimator because during active regeneration, the DOC inlet hydrocarbon concentrations are high ($\cong$ 3700 ppm of C_3H_6) and the hydrocarbons at the inlet of the DOC increases the DOC outlet temperature ($\cong$ 75°C higher than the DOC inlet temperature). Hence, an accurate estimate of DOC outlet temperature, hydrocarbon and NO_2 concentrations are necessary for the estimation of temperature and PM mass distribution in the CPF state estimator.

The reaction parameters in the DOC estimator was calibrated to simulate the AR-B10-1 experimental data. The calibrated model reaction kinetics for the DOC state estimator is

shown in Table 6.1. The DOC estimator internal time step was set to 0.0025 second to improve the numerical stability of the DOC reduced order model during active regeneration with the higher temperature gradients.

Table 6. 1 Reaction kinetics used in the DOC state estimator

Reaction	Activation Energy (E_i) $kJ/gmol$	Pre-Exponential (A_i) $gmol/m^3.s$
NO	54.39	2.6E04
CO	55.00	1.0E07
HC	43.50	1.2E05

DOC Outlet/CPF Inlet Temperature

Figure 6.5 shows the DOC inlet temperature measured along with the comparison of estimated DOC outlet temperature and measured DOC outlet temperature. From Figure 6.5, the DOC estimator is able to simulate the DOC outlet measured temperature using the optimal Kalman gain determined from the extended Kalman filter algorithm. The temperature increase during active regeneration phase of the experiment is $\cong 74^oC$.
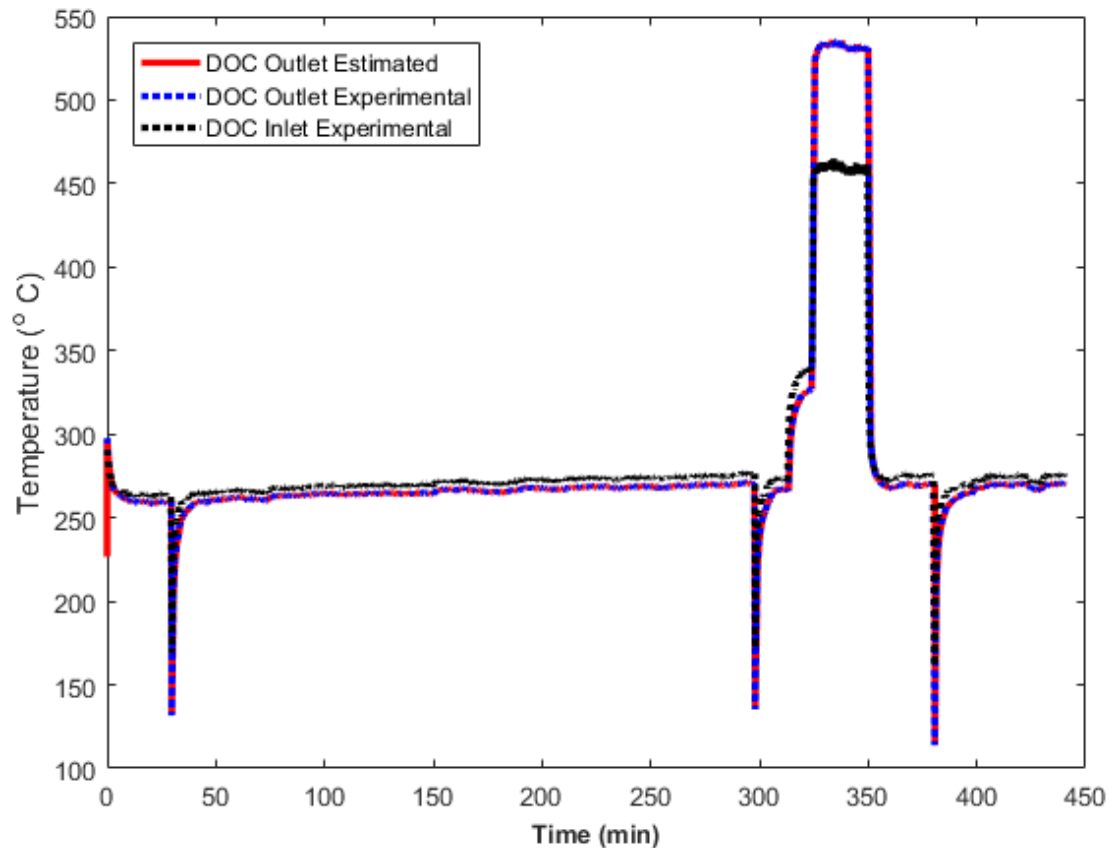
Figure 6. 5 DOC inlet temperature and a comparison between the estimated and measured DOC outlet temperature for   AR-B10-1 experiment

NO$_2$ DOC Outlet Concentration

Figure 6.6 shows the DOC inlet NO$_2$ concentration measured along with the comparison of estimated DOC outlet temperature and measured DOC outlet NO$_2$ concentrations. From Figure 6.6, the DOC estimator outlet concentration error is within 3 ppm during stage 1, 2 loading 3, 4 post loading and within 15 ppm during active regeneration compared to the measured NO$_2$ outlet concentration. The original DOC estimator work by Harsha Surenahalli showed a typical error of less than 20 ppm for a surrogate FTP run [48]. The error levels of 20 ppm is may be partly due to the measurement uncertainty associated with the emissions measurement system, test procedure and the reduced fidelity with DOC estimator models because of the various model reduction assumptions employed. The DOC inlet concentration during AR ramp up phase was not available, hence the DOC

inlet NO_2 concentration was assumed as 30% (based on typical DOC performance at the inlet temperature of $\cong$ 350°C) of the total NOx concentration.
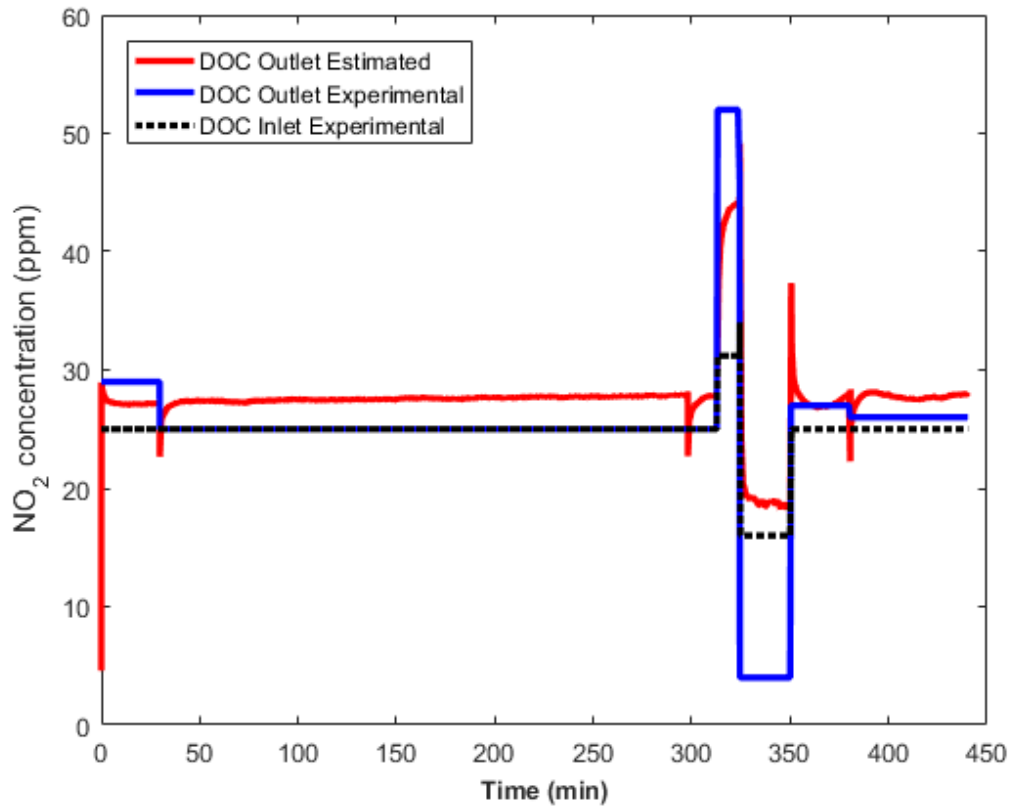
Figure 6. 6 DOC inlet NO_2 concentration and a comparison between the estimated and measured DOC outlet NO_2 concentration for AR-B10-1 experiment

HC DOC Outlet Concentration

Figure 6.7 shows the estimated DOC inlet C_3H_6 concentration along with the comparison of estimated DOC outlet temperature and measured DOC outlet C_3H_6 concentrations. The DOC inlet hydrocarbon concentrations were calculated from the dosing flow rate and exhaust flow rate as explained in reference [51]. From Figure 6.7, the DOC estimator outlet C_3H_6 concentration error is within 35 ppm compared to the measured outlet concentration. The DOC inlet C_3H_6 concentration during active regeneration was $\cong$ 3760 ppm and is oxidized to 143 ppm at the outlet of the DOC.
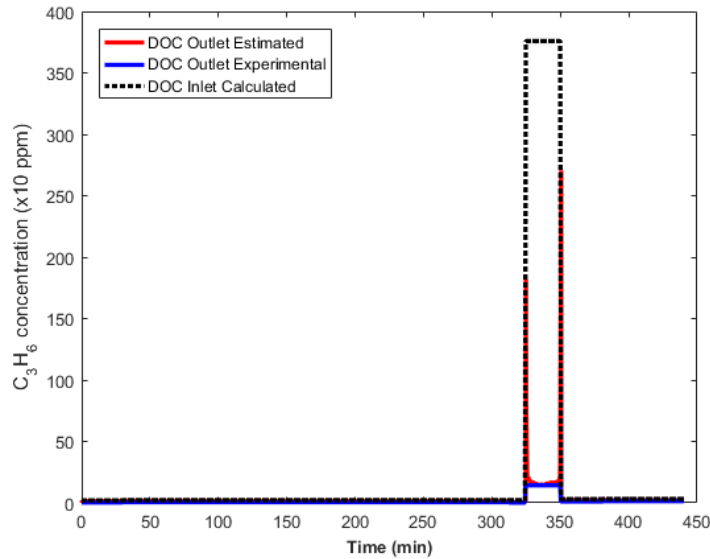
Figure 6. 7 DOC inlet C₃H₆ concentration and a comparison between the estimated and measured DOC
outlet C₃H₆ concentration for AR-B10-1 experiment

CPF State Estimator Results

The active regeneration experimental (AR-B10-1) data was used for the validation of DOC-CPF state estimator. The active regeneration run (AR-B10-1) was selected as the representative case for the validation of the CPF state estimator because the filter substrate temperatures during active regeneration experiments are in the range of 450 - 600°C which is higher than the passive oxidation experiments (250 to 400°C). The active regeneration experiments are short in duration (6 to 39 minutes) because of the high PM oxidation rates. The MPF model validation is presented for one sample active regeneration experiment (AR-B10-1) because it provides a good assessment of the designed CPF estimator. This is because of the need to consider the higher filter substrate temperature and short PM oxidation duration and its effect on the heat transfer, temperature and filter PM loading distribution within the filter and the pressure drop characteristics of the CPF. The results are presented in the following section.

The CPF estimator used the NO_2 outlet concentration from the DOC estimator and O_2 concentration measured at the inlet to the DOC. The outlet O_2 concentration is lower during active regeneration due to the HC oxidation in DOC. This resulted in changes in the CPF PM kinetic parameters. Hence, CPF PM kinetic parameters (pre-exponential for NO_2 and

155

O$_2$-thermal assisted PM oxidation) were re-calibrated. The calibrated CPF estimator PM kinetic parameters are shown in Table 6.2.

Table 6. 2 Reaction kinetics used in the DOC-CPF state estimator

PM Oxidation	Symbol	Description	Recalibrated Pre-Exponential (A$_i$) m/K-s	SCR-F/CPF Model Pre-Exponential (A$_i$) m/K-s
NO$_2$-assisted	A$_{NO2\ cake}$ temp. solver	Pre-exponential for NO$_2$-assisted PM oxidation used in the temperature model	0.0026 (combined cake and wall)	0.006 (cake) and 0.0187(wall)
	A$_{NO2\ cake}$	Pre-exponential for NO$_2$-assisted PM oxidation used in the filtration and pressure drop models	0.0031	0.006
	A$_{NO2\ wall}$	Pre-exponential for NO$_2$-assisted PM oxidation used in filtration and pressure drop model	0.011	0.0187
Thermal (O$_2$)	A$_{O2\ cake}$ temp. solver	Pre-exponential for thermal (O$_2$) PM oxidation used in the temperature model	0.6098 (combined cake and wall)	0.71 (cake) and 1.27 (wall)
	A$_{O2\ cake}$	Pre-exponential for thermal (O$_2$) PM oxidation used in the filtration and pressure drop models	0.5112	0.71
	A$_{O2\ wall}$	Pre-exponential for thermal (O$_2$) PM oxidation used in filtration and pressure drop model	0.9138	1.27

CPF Outlet Temperature

Figure 6.8 shows the comparison of high-fidelity SCR-F/CPF model outlet gas temperature (high-fidelity T_{80}) with the DOC-CPF state estimator outlet gas temperature (ROM-T_{20}) along with the CPF experimental outlet gas temperature measured during the AR-B10-1 experiment. From Figure 6.8, the DOC-CPF state estimator temperature prediction closely simulates the high-fidelity SCR-F/CPF model data and the experimental data using the optimal Kalman gain and measured sensor data as shown in Equation 6.12. The CPF estimator simulated the sensor feedback assumed to be close to T_{20} location (sensor tip at 33 mm from the surface of the pipe) as shown in Figure 6.2.
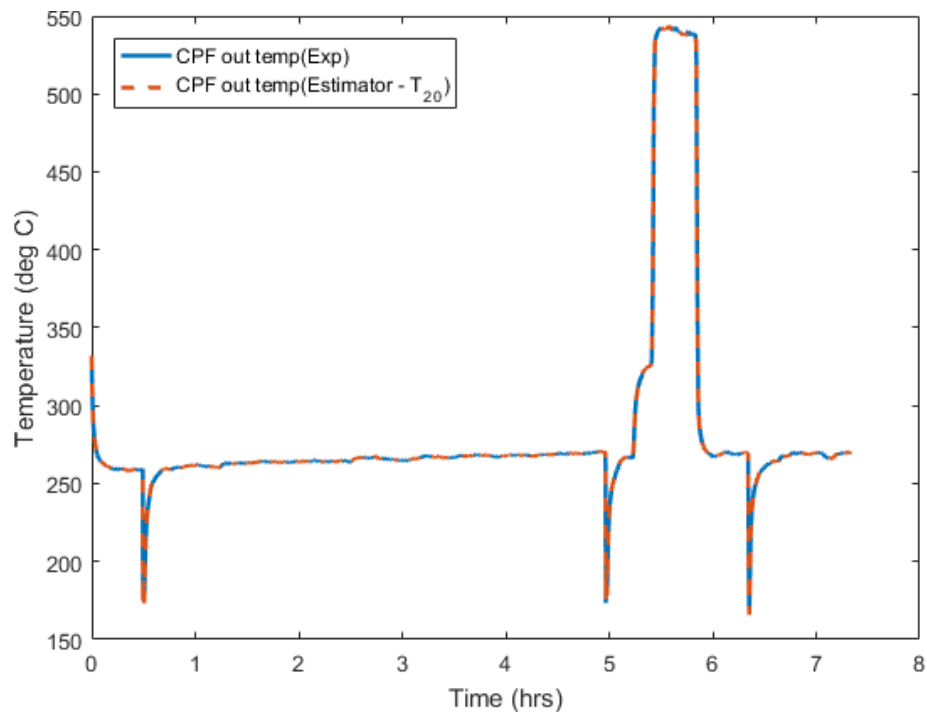
Figure 6. 8 Comparison of DOC-CPF estimator outlet gas temperatures along with the measured CPF outlet gas temperature for AR-B10-1 experiment

CPF Temperature Distribution

Figures 6.9 and 6.10 show the comparison of DOC-CPF estimator temperature distribution data and from the high fidelity SCR-F/CPF model temperature distribution for AR-B10-1 experiment at 5.63 hrs (15 mins after start of fuel dosing). Comparing Figures 6.9 and 6.10, the DOC-CPF estimator temperature distribution data simulates the high-fidelity

SCR-F/CPF model temperature distribution trends with the maximum absolute temperature error between the high-fidelity SCR-F/CPF model and the DOC-CPF estimator being within 5°C below filter radiuses of 120 mm and is within 7°C at outer radiuses of the filter (filter radiuses > 120 mm).
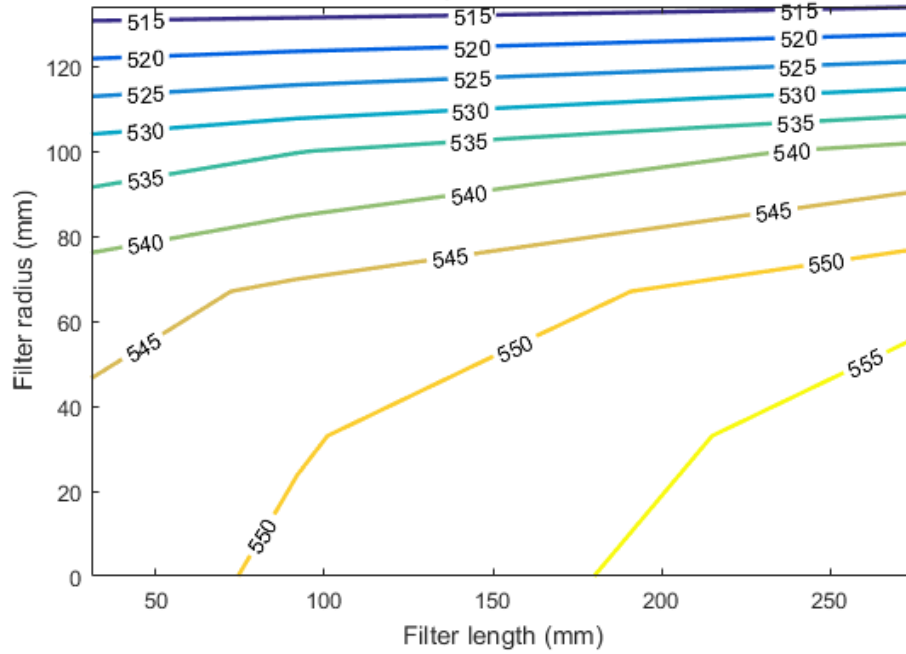
Figure 6. 9 DOC-CPF estimator temperature distribution in °C for AR-B10-1 experiment at 5.63 hrs. (15 minutes after start of fuel dosing)
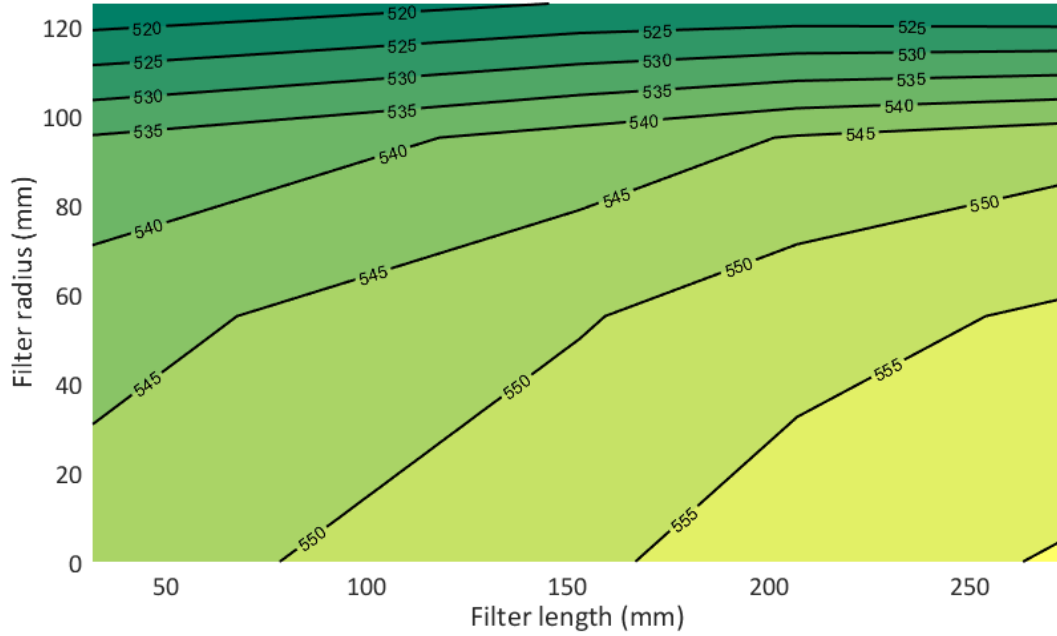
Figure 6. 10 High-fidelity SCR-F/CPF model simulated temperature distribution in ºC for AR-B10-1 experiment at 5.63 hrs (15 minutes after start of fuel dosing)
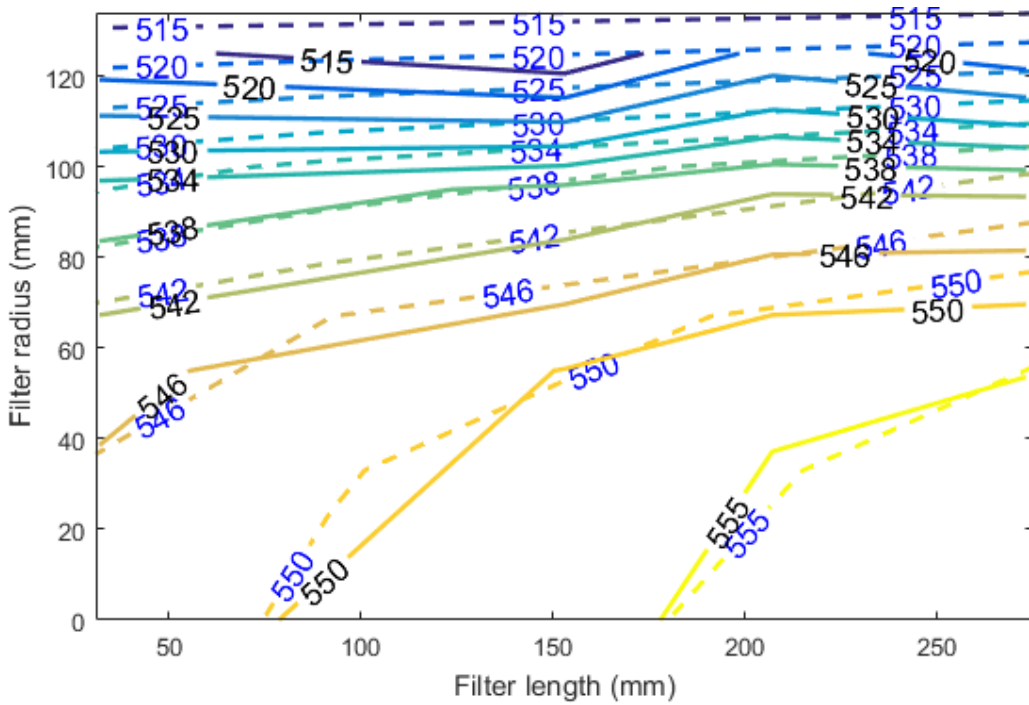
Figure 6. 11 Comparison of experimental (solid lines) and DOC-CPF estimator temperature distribution in ºC at 5.63 hrs (15 mins after start of fuel dosing)

Figure 6.11 shows the comparison of experimental and DOC-CPF temperature distribution at 5.63 hrs (15 mins after start of fuel dosing). From Figure 6.11, the DOC-CPF state estimator is able to closely follow the experimental temperature distribution and the maximum absolute temperature difference between the reduced order model and experimental data is less than 5°C at radiuses less than 120 mm. The RMS temperature error is $\cong$ 2.7°C. Comparing Figure 6.11 with Figure 5.38, the DOC-CPF estimator is able to minimize the error in the reduced order model (open loop) by taking the feedback of the CPF outlet sensor value and optimal Kalman gain from the extend Kalman filter. The estimator corrections are evident while comparing the dashed yellow lines (temperature contour of 555°C pointed by green arrow) between Figures 5.38 and 6.11.

PM Mass Retained

Figures 6.12 and 6.13 show the comparison of cumulative PM mass retained in the filter along with the cake and wall PM masses for the DOC-CPF state estimator and the high-fidelity SCR-F/CPF model. In Figures 6.12 and 6.13, the DOC-CPF state estimator PM mass retained plot closely simulates the high-fidelity SCR-F/CPF model and the experimental data. The maximum difference in PM loading prediction of the DOC-CPF state estimator is 1.1 g at the end of stage 2 loading and less than 0.2 and 0.7 g at the end of stage 3 and 4 loading respectively compared to the experimental data.
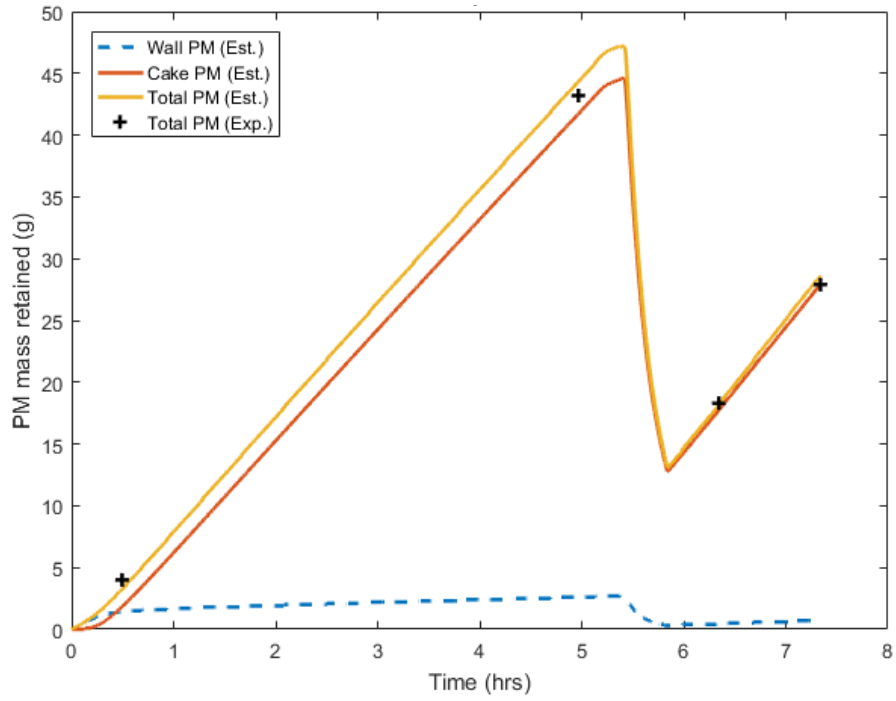
Figure 6. 12 Comparison of PM mass retained in the experimental data and DOC-CPF state estimator data along with the cumulative PM inlet and oxidation masses for AR-B10-1 experiment
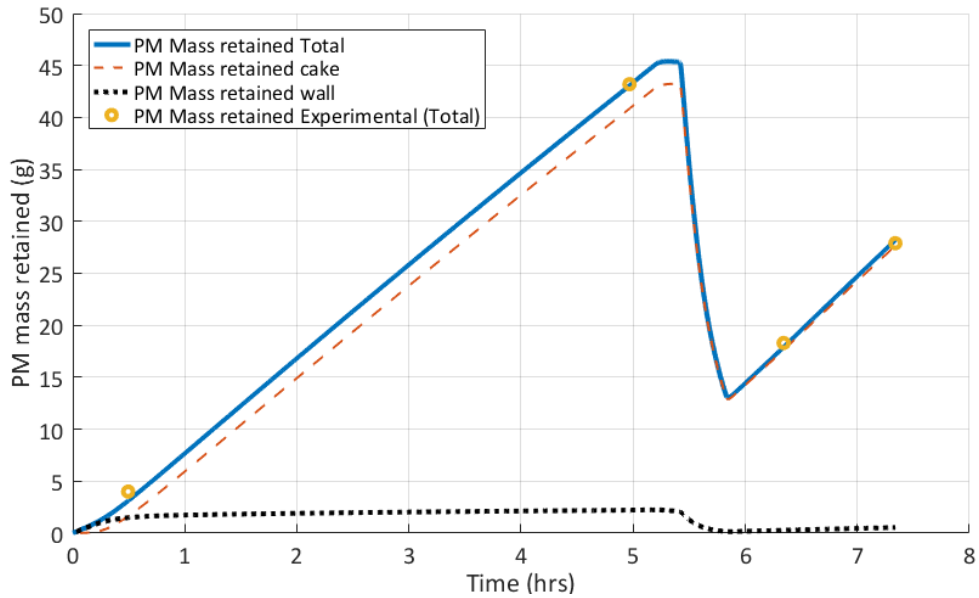
Figure 6. 13 Comparison of PM mass retained in the experimental data and high-fidelity SCR-F/CPF model along with the model cumulative for PM inlet, cake and wall PM masses for AR-B10-1 experiment

161

PM Distribution

Figures 6.14 and 6.15 show the comparison of PM mass loading distribution in the axial and radial directions at the end of PM oxidation (at 5.82 hrs) by active regeneration for AR-B101 experiment simulated by the DOC-CPF estimator and the high fidelity SCR-F/CPF model. From Figures 6.14 and 6.15, the PM loading distribution simulated by the DOC-CPF state estimator closely simulates the data from the high-fidelity model. The PM loading distribution difference is less than 0.1 g/L compared to high-fidelity SCR-F/CPF model for filter radiuses less than 120 mm. The PM loading distribution simulated by the DOC-CPF state estimator is $\cong$ 0.2 to 0.5 g/L lower than the high-fidelity model at outer radiuses of the filter (radiuses > 120 mm). This is mainly because of the lower discretization of the DOC-CPF estimator compared to the high-fidelity SCR-F/CPF model.
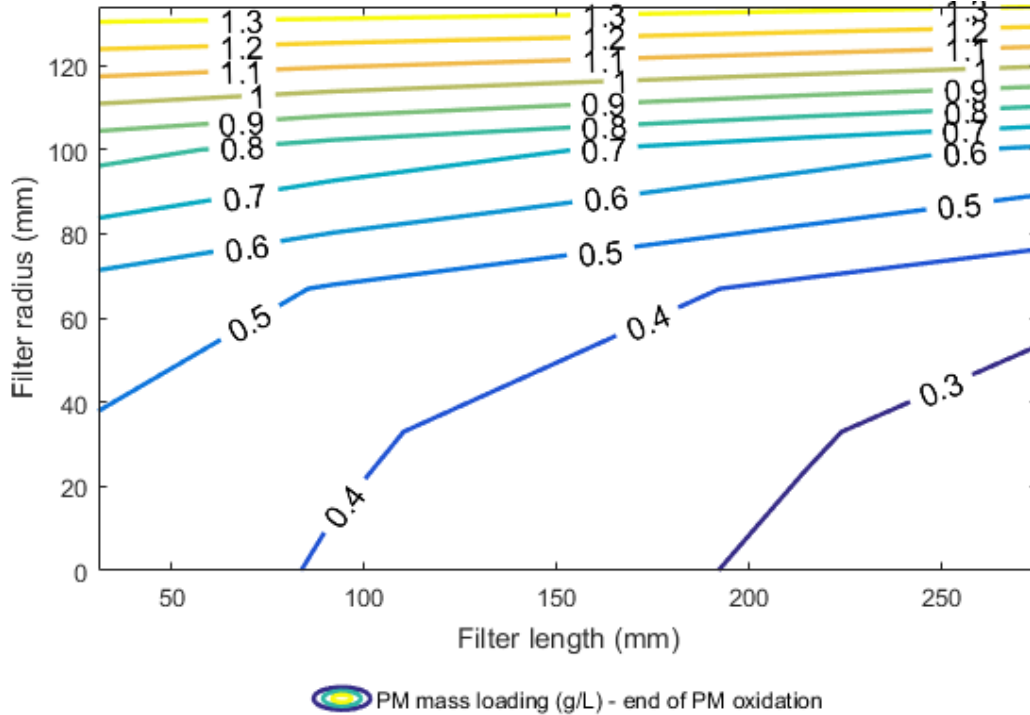
Figure 6. 14 DOC-CPF state estimator PM mass loading distribution in g/L along the axial and radial directions at 5.82 hrs (end of PM oxidation by active regeneration) for AR-B10-1 experiment

162
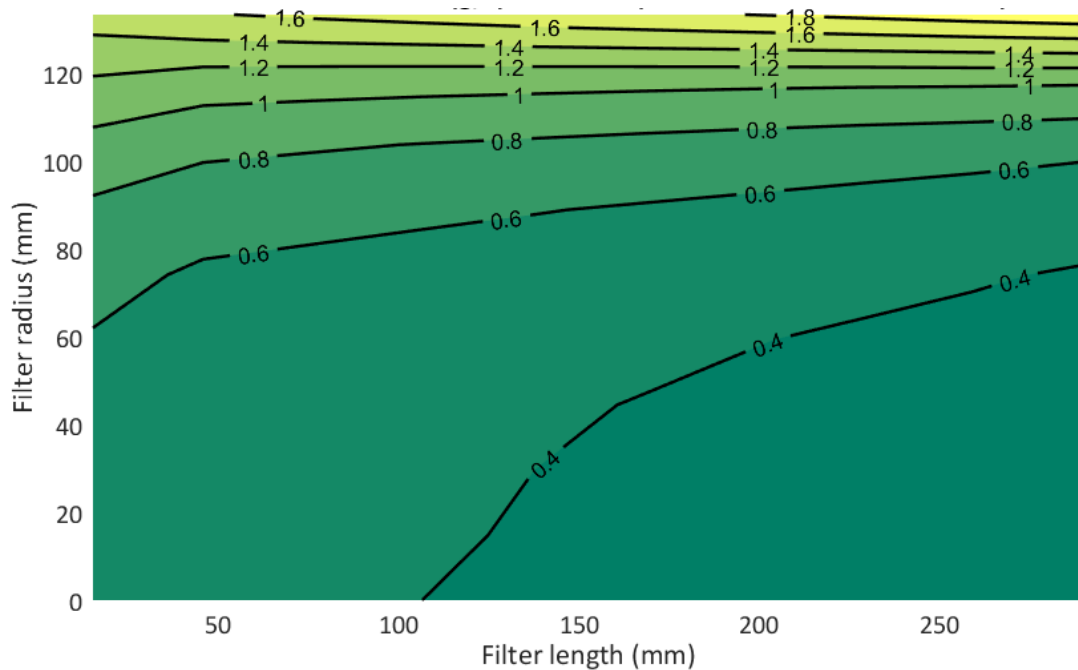
Figure 6. 15 High-fidelity SCR-F/CPF model PM mass loading distribution in g/L along the axial and radial directions at 5.82 hrs (end of PM oxidation by active regeneration) for AR-B10-1 experiment

Pressure Drop

Figures 6.16 and 6.17 show the comparison of the total pressure drop across the CPF and its components for AR-B10-1 experiment simulated by the DOC-CPF estimator and the high-fidelity SCR-F/CPF model. From Figures 6.16 and 6.17, the pressure drop simulated by the DOC-CPF estimator simulates the high-fidelity SCR-F/CPF model trends with the maximum pressure drop simulation error with the DOC-CPF state estimator of $\cong$ 0.5 kPa compared to the high-fidelity SCR-F/CPF model data during the AR ramp phase of the experiment. The maximum pressure drop error with DOC-CPF estimator is $\cong$ 0.5 kPa during the AR ramp up phase and the start of active regeneration compared to the experimental data.
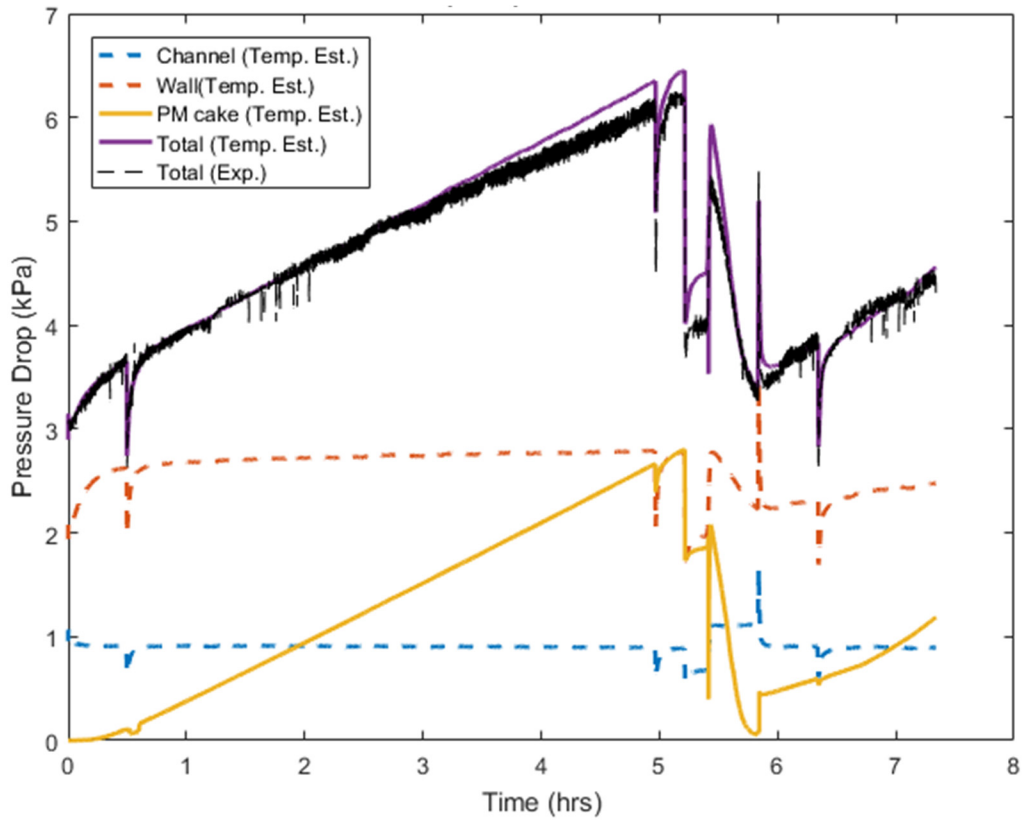
Figure 6. 16 Comparison of experimental and DOC-CPF state estimator total pressure drop across CPF and its components for AR-B10-1 experiment using extended Kalman filter for temperature
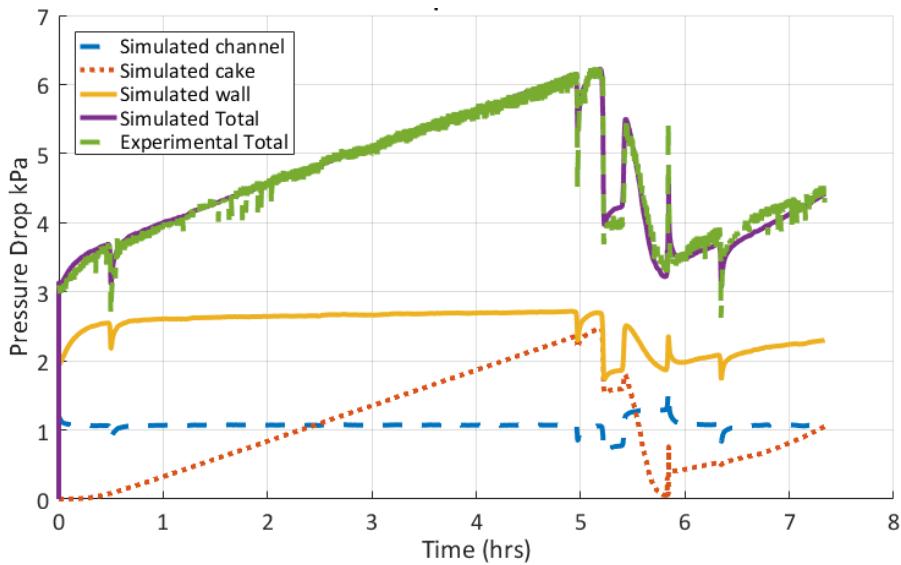
Figure 6. 17 Comparison of experimental and simulated total pressure drop across CPF and its components for AR-B10-1 experiment simulated by the high-fidelity SCR-F/CPF model

164
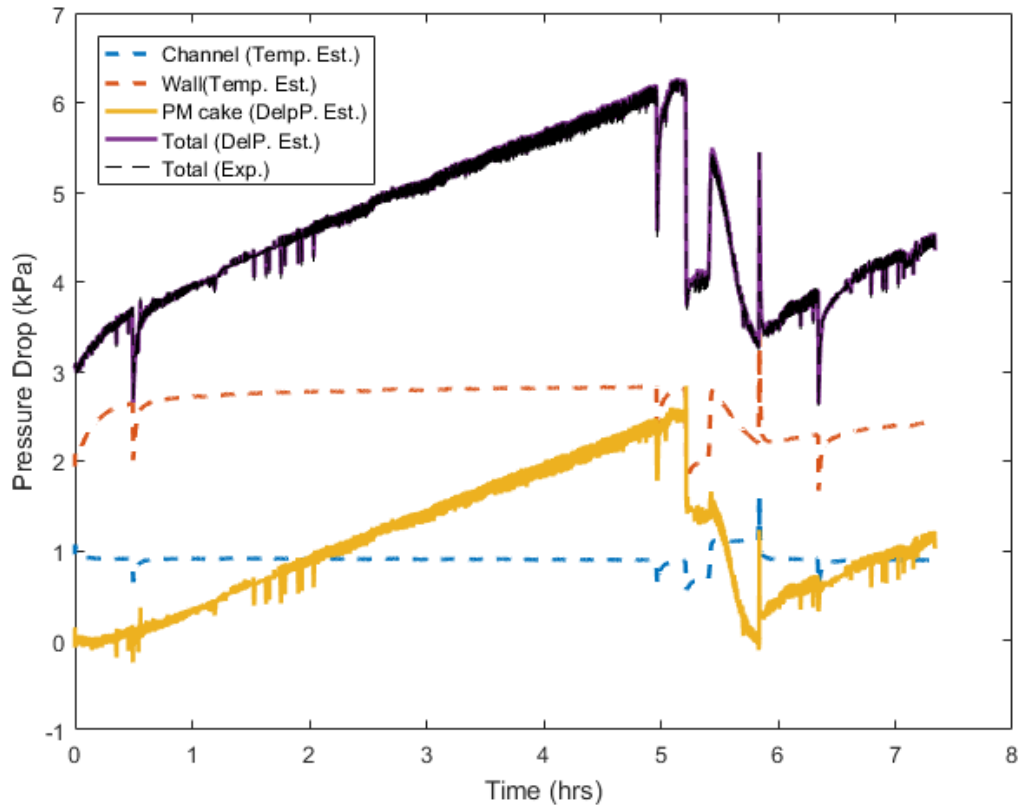
Figure 6. 18 Comparison of experimental and DOC-CPF state estimator total pressure drop across CPF and its components for AR-B10-1 experiment using linear Kalman filter for pressure drop

Figure 6.18 shows the comparison of the experimental and estimated pressure drop value and its components for the AR-B10-1 experiment using the linear Kalman filter for pressure drop. From Figure 6.18, the estimated total pressure drop closely simulates with the measured pressure using the optimal Kalman gain and feedback ΔP pressure sensor values as shown in Equation 6.20. Using the estimated total pressure drop values from the linear Kalman estimator and Equation 6.2, the cake pressure drop was estimated. Figure 6.19 shows the estimated cake pressure drop for various cake PM loading during the AR-B10-1 experiment. From Figure 6.19, three distinct regions of CPF operating can be determined. During loading, the cake pressure drop increases proportional to the loading of the filter shown as a linear line increasing as a function of filter PM loading. During PM oxidation by active regeneration, the cake pressure drop reduces as the PM cake oxidizes through thermal (O_2) and NO_2 assisted PM oxidation reactions. The pressure drop during PM cake oxidation at a given cake PM loading is lower than the pressure drop during loading due to the increased permeability of PM cake layer during

PM oxidation. The wall pressure drop also reduces significantly during PM oxidation and approaches the clean wall pressure drop because of oxidation of PM within the substrate wall as shown in Figure 6.18. During post loading, the pressure cake drop increases proportional to the PM cake loading, however the cake pressure drop values at a given PM cake mass are lower than the cake pressure drop values during loading. This is mainly because of presence of the damaged PM cake layer due to the earlier PM oxidation event. By comparing cake pressure drop estimates along with the wall and channel pressure drop estimates suitable control actions can be taken in the event of failure of sensors, components or excess PM loading of the CPF. For example, in the event of cracked substrate wall, the overall pressure drop measured by the ΔP pressure sensor will be lower causing negative estimated cake pressure estimates which is an indication of failure of a component and can be determined from the pressure drop estimator. Without a pressure drop estimator, it will be difficult to diagnose the problem, because the measured pressure drop will still be within the in-range (non-zero, within upper and lower bounds of the typical operation) checks of the ECU.
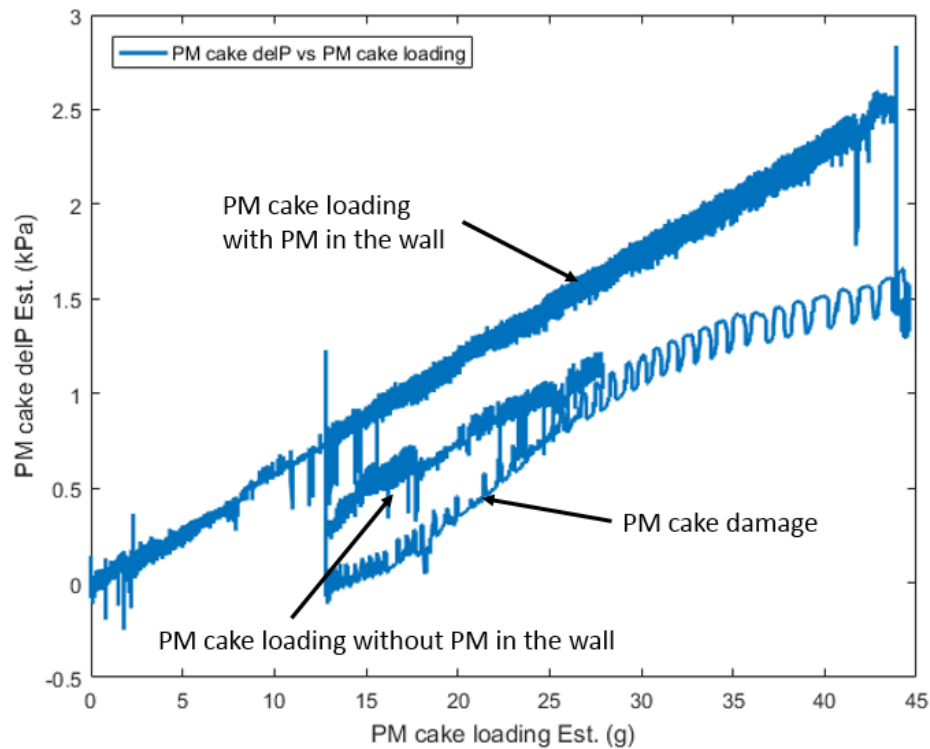
Figure 6. 19 Comparison of PM cake loading and PM cake ΔP estimated using linear Kalman estimator during AR-B10-1 experiment

166

From the above analysis, it is evident that the DOC-CPF state estimator presented in this research shows the capability to predict temperature and PM loading distribution and pressure drop of the CPF at various operating conditions. The DOC-CPF state estimator used the engine outlet temperature and NOx, HC and O_2 concentrations from the ECU sensors or maps to estimate the temperature distribution and PM mass retained and distribution and pressure drop components of the CPF. With the extended Kalman filter for temperature estimation and linear Kalman filter for pressure drop estimation, the outlet gas temperature and ΔP across the CPF were closely simulated with the measured sensor signals. The RMS error in temperature distribution estimated by the DOC-CPF state estimator is within 5°C and absolute PM mass retained was within 0.7 g of the experimental data at the end of stage 4 loading. The total pressure drop estimated by the reduced order model used in the extended Kalman filter estimator was within 0.5 kPa and was compensated with optimal Kalman gain to predict unknown states of the pressure drop components such as cake pressure drop. The overall summary of results and conclusions from this thesis are presented in the next chapter.

7 Summary and Conclusions[1]

7.1 Summary

A new multi-zone SCR-F/CPF model was developed to simulate the substrate temperature distribution, PM mass retained and distribution and pressure drop of the CPF. The newly developed SCR-F/CPF model accounted for the variation in inlet temperature of the exhaust gas using fully developed thermal boundary layer equations and PM filtration and oxidation within the substrate wall and PM cake using the classical filtration theory developed by Johnson and Konstandopoulos [15]. The PM oxidation included NO_2 assisted and thermal (O_2) PM oxidation mechanisms. The back diffusion of NO_2 into the PM cake layer is also included using the species concentration solver developed by Venkata Chundru. The SCR-F/CPF model also accounted for the oxidation of hydrocarbons within the filter and includes heat transfer within and external to the filter and the thermal resistances of the insulation and outer can. The pressure drop model used in the SCR-F/CPF model accounted for the PM filtration in the wall and cake, variable wall and cake permeability accounting for the changes in the mean free path length of the gas and permeability evolution of PM cake during PM oxidation and post loading using the newly developed cake permeability model [3]. The outputs of the high fidelity CPF model are temperature distribution within the filter substrate, inlet and outlet channels, total PM mass retained including masses in the cake and wall, PM loading distribution within the filter, species concentration at the filter outlet (NO, NO_2, CO, CO_2, O_2, HC, and PM concentration) and pressure drop across the filter.

---

[1] Parts of the material contained in this chapter are based on references [1, 2,3] with permission of Springer.

A new cake permeability model [3] was developed to account for the damage in the PM cake during PM oxidation. Based on the experimental data analysis, it was found that the permeability of the PM cake layer increases during PM oxidation (passive oxidation and active regeneration experiments). The increase in permeability during PM oxidation was attributed to the damage in the PM cake (holes, cracks etc.) and leads to near zero pressure drop during PM oxidation. This increased permeability of the PM cake layer during PM oxidation was simulated using the newly developed cake permeability as a function of PM oxidation rate during PM oxidation. During post loading, the holes and cracks formed in the PM cake are filled with incoming PM. This damage recovery process reduces the permeability of PM cake during post loading (passive oxidation and active regeneration) and was simulated using the new cake permeability model as a function of PM mass retained in the cake.

The experimental data collected by Shiel [49] and Pidgeon [51] on a 2007 inline 6-cylinder ISL 8.9L diesel engine rated at 272 kW with DOC and CPF aftertreatment systems were used as basis for developing the models. The experiments were performed with three fuels – ULSD, B10 and B20 blends. The SCR-F/CPF model was calibrated at eighteen different operating conditions (six passive oxidation and twelve active regeneration experiments). The detailed calibration procedure for calibration of PM kinetics and pressure drop model parameters was developed. The experimental thermocouple data in the CPF channels recorded during eighteen experimental runs were used for the development of the thermal boundary layer model and calibration of heat transfer within and external to the filter.

A reduced order multi-zone particulate filter model (MPF) was developed to reduce the computational time and the complexity of the high-fidelity SCR-F/CPF model for use in a ECU based application and specially for the CPF state estimator. A parametric study was carried out to determine the optimum number of zones for the reduced order MPF model and it was found that the 5x5 zone model was sufficient for the accuracy and the computational speed. Further model reduction assumptions were evaluated to improve the computational speed without affecting the accuracy of the model prediction significantly. The elimination of the species solver, effect of NO_2 back diffusion equations, radiation heat transfer within the channels and assuming average channel gas

temperatures instead of separate inlet and outlet channel gas temperatures increased the computational speed by about 32 times without significantly affecting the accuracy.

A CPF state estimator was developed to predict unknown states of the CPF such as temperature distribution, PM mass retained and distribution and pressure drop components of the CPF. An extended Kalman filter based state estimator was developed to predict unknown temperature states and a linear Kalman filter based estimator was developed to predict unknown components of the pressure drop such as the cake pressure drop. The DOC state estimator developed by Harsha Surenahalli [48] was integrated with the CPF state estimator to provide inlet conditions (DOC outlet temperature, NO_2 and HC concentrations) to the CPF. The integrated DOC-CPF model was recalibrated and validated on a active regeneration test condition. The DOC-CPF state estimator was shown to have the capability to predict temperature distribution, PM mass retained and distribution and the pressure drop components of the CPF.

7.2 High Fidelity SCR-F/CPF Model Conclusions

Based on the simulation results using the high fidelity SCR-F/CPF model, the following specific conclusions can be made:

1. The SCR-F/CPF model is able to simulate the axial and radial temperature distribution and PM mass retained and distribution and pressure drop of the CPF for the passive oxidation and active regeneration experiments.

2. Temperature within the substrate varies axially and radially. The radial temperature distribution is significant and it is up to $\cong 32^{\circ}C$ during PM oxidation by passive oxidation and $\cong 40^{\circ}C$ duing PM oxidation by active regeneration. The axial temperature variation is $\cong 12^{\circ}C$ for the active regeneration experiments and $\cong 2^{\circ}C$ for the passive oxidation experiments.

3. The radial temperature distribution initiates well before the inlet of the CPF and affects the temperature distribution for the entire length of the CPF. This radial temperature distribution can be characterized using thermal boundary layer equations. For the CPF studied, 50% of the overall temperature gradient is in the 20% of the filter section closest to the outer radius of the filter.

4. The accurate temperature distribution at the inlet of the CPF is essential for accurate simulation of the temperature distribution within the CPF. Hence, strategic placement (number of sensors and locations) of CPF inlet temperature sensors along with a model is necessary to capture accurate inlet temperature distribution profiles.

5. The simulated PM distribution is uniform (2.0 ± 0.03 g/L) during loading and becomes non-uniform at the end of PM oxidation. The active regeneration of the filter leads to non-uniform PM distribution (minimum PM loading is 0.4 g/L and maximum PM loading is 1.8 g/L at the end of PM oxidation by active regeneration) compared to the passive oxidation test conditions (minimum PM loading is 1.1 g/L and maximum PM loading is 1.6 g/L at the end of PM oxidation by passive oxidation). The high-fidelity model is able to predict non-uniformities in the PM loading distribution.

6. Permeability of the PM cake layer changes during PM oxidation. It is almost constant at the beginning of the PM oxidation and increases rapidly during PM oxidation. The PM cake permeability increases about 5 to 7 times during PM oxidation for the passive oxidation and active regeneration experiments. The increase in permeability is attributed to the damage in the PM cake layer (cracks and holes) and was simulated using the newly developed cake permeability model.

7. The increase in permeability of the PM cake during PM oxidation by passive oxidation experiments are steeper than the active regeneration experiments ($\beta_{kNO2} = 6.0$ versus $\beta_{kO2} = 3.6$) indicating higher damage in the PM cake due to lower oxidation rates with the NO_2 assisted PM oxidation than thermal (O_2) PM oxidation.

8. The increased permeability of the PM cake layer during PM oxidation leads to lower pressure drop of the PM cake for the passive oxidation and active regeneration experiments.

9. The wall pressure drop reduces during passive oxidation and active regeneration due to the oxidation on PM within the substrate wall. The

oxidation of PM within the wall substrate increases the permeability of the substrate wall and reduces the pressure drop. During PM oxidation by active regeneration, most of the PM in the wall is oxidized and the wall pressure drop approaches the clean wall pressure drop.

10. The pressure drop model along with the newly developed cake permeability model has shown the capability to predict pressure drop across the filter during loading, PM oxidation by passive oxidation and active regeneration and post loading. The RMS error in the pressure drop estimate was less the 0.2 kPa for all eighteen experiments.

7.3 Reduced order MPF Model Conclusions

Based on the simulation results using the reduced order MPF model, the following specific conclusions can be made:

1. The reduced order MPF model is able to simulate temperature distribution and PM mass retained and distribution and pressure drop of the CPF.

2. From the discretization study, 5x5 zone SCR-F/CPF model was found to be 4 times faster than the baseline 10x10 model with RMS temperature of $3.5^{\circ}C$, absolute PM loading difference of 1.6 g at the end of stage 4 loading and absolute pressure drop difference of 0.2 kPa at the end of stage 4 loading, compared to the experimental data.

3. From the model reduction assumptions evaluation, by neglecting the reactions in the catalysts washcoat (without species solver), the SCR-F/CPF model runs 32 times faster than the baseline model with species solver without affecting the prediction accuracy (RMS temperature difference is $2.8^{\circ}C$ with species solver and $2.9^{\circ}C$ without species solver compared to experimental data).

4. The effect of NO_2 back diffusion on PM oxidation is minimum (< 0.1 g of PM oxidized). Hence, the NO_2 back diffusion effect is neglected in the reduced order model.

5. The absolute temperature difference between inlet channel gas and outlet channel gas is less than 2°C and RMS temperature difference during PM oxidation is within 1°C. Hence, for the purpose of the reduced order model development, the lumped model approach employed by applying average channel gas temperature for calculation of convection heat transfer between channels and the filter substrate is sufficient.

6. Simulation error by neglecting the radiation heat transfer between channel gas and the filter wall is minimum. The RMS temperature difference increases from 3.1 to 3.3°C and the PM post loading error reduces from 0.3 to 0.2 g and pressure drop error increases from -0.01 to -0.02 kPa and model run time is almost same for both cases. Hence, for the purpose of the reduced order model development, radiation heat transfer between channel gas and filter wall was neglected.

7.4 DOC-CPF State Estimator Conclusions

Based on the simulation results using the DOC-CPF state estimator, the following specific conclusions can be made:

1. The DOC-CPF state estimator is able to simulate temperature distribution and PM mass retained and distribution and pressure drop of the CPF during PM loading, oxidation and post loading. The PM loading error is within 0.7 g at the end of stage 4 loading, the RMS temperature error during PM oxidation is 2.7°C, pressure drop error is 0.5 kPa using the temperature estimator and the pressure drop estimates closely (< 0.1 kPa) simulate the experimental data with the linear pressure drop estimator.

2. The DOC state estimator was integrated with the CPF estimator to provide DOC outlet temperature and concentrations (NO_2 and THC) inputs to the CPF state estimator. The DOC outlet NO_2 concentration is within 15 ppm and HC concentration is within 35 ppm of C_3H_6 compared to the experimental data.

7.5 Future Work

Based on the simulation results of the high-fidelity SCR-F/CPF model, reduced order MPF model and DOC-CPF state estimator, the following are the recommendations for the future work:

1. The newly developed cake permeability models can be validated on the real world duty cycles and transient operating conditions. During transient validation of the model, the PM oxidation rates varies continuously.Hence, the damage variable may have to be determined based on the real-time PM oxidation rates. The corresponding real-time mass offset values have to be calculated and applied to simulate PM cake permeability during continuously varying PM oxidation and PM loading of the damaged PM cake.

2. This thesis work focused on the validation of SCR-F/CPF model for the CPF application. The temperature distribution, PM loading and pressure drop model developed in this thesis along with the newly developed cake permeability model can also be validated on the on-going SCR-F research work at MTU to validate the SCR-F/CPF model along with SCR reactions for the SCR-F type applications.

3. The DOC-CPF estimator developed in this work could be implemented on an engine ECU to simulate temperature and PM mass distribution and pressure drop of the CPF. An ECU implementation of the DOC-CPF estimator needs to account for the part to part variation caused by the measurement devices such a temperature sensors, PM sensor and uncertainty associated with the map based inputs. For the accurate determination of PM loading and temperature distribution, the PM sensor input is very critical. However, the PM sensor is not available yet for the particulate filter applications. Use of the DOC-CPF estimator using the map based PM input rather than the actual PM sensor measurement, may lead to large estimation errors because of the uncertainty in the PM measurements because of the PM differences between engines parts (part to part variation), environmental conditions (temperature, altitude and humidity), engine health i.e. aging of the critical performance and emissions affecting parts such as injectors, power cylinder wear, cylinder head, valves etc.

4. DOC-CPF estimator could be further extended by adding species concentration solver to provide estimates of CPF outlet NO_2 concentration for a DOC-CPF-SCR architecture.

5. Cake pressure drop estimates from the CPF state estimator show potential to use as a pressure drop diagnostics tool for monitoring cake PM loading and other pressure drop components in an ECU. This could be further explored by studying the model response for the various failure scenarios of the CPF.

6. The model developed in this thesis accounted for the temperature distribution at the inlet of the CPF. However, the inlet pipe geometries affect the velocity and flow distribution at the inlet of the CPF. The flow distribution affects the PM distribution within the CPF. Hence, the PM distribution within the CPF could be further improved by adding inlet flow distribution models to include non-uniform distribution of flow caused by inlet pipe geometry.

References

1. Mahadevan, B.S., Johnson, J.H., and Shahbakhti, M., Development of a catalyzed diesel particulate filter multi-zone model for simulation of axial and radial substrate temperature and particulate matter distribution, Journal of Emiss. Control Sci. Technol., Vol. 1, pp 183-202, 2015, doi:10.1007/s40825-015-0015-x, 2015.

2. Mahadevan, B.S., Johnson, J.H., and Shahbakhti, M., Experimental and Simulation Analysis of Temperature and Particulate Matter Distribution for a Catalyzed Diesel Particulate Filter, Journal of Emiss. Control. Sci. Technol.,Vol.1, pp 255-283, 2015, doi: 10.1007/s40825-015-0022-y, 2015.

3. Mahadevan, B.S., Johnson, J.H., and Shahbakhti, M., Predicting pressure drop, temperature and particulate matter distribution of a catalyzed diesel particulate filter using a multi-zone model including cake permeability, Journal of Emiss. Control Sci. Technol., doi: 10.1007/s40825-017-0062-6, 2017.

4. https://www.dieselnet.com/standards/us/hd.php. Accessed: 10 Dec 2014.

5. Rose, K., Hamje, H., Jansen, L., Fittavolini, C., Almena, M.D.C., Katsaounis, D., Samaras, C., Geivanidis, S., and Samaras, Z., "Impact of FAME Content on the Regeneration Frequency of Diesel Particulate Filters (CPFs)," SAE Int. J. Fuels Lubr. 7(2):2014, doi:10.4271/2014-01-1605, 2014.

6. Robert Bosch GmbH, "Diesel-Engine Management", John Wiley & Sons, 4th edition, ISBN 0-470-02689-8, 2005.

7. Rose, D.,and Boger, T., "Different Approaches to Soot Estimation as Key Requirement for CPF Applications", SAE Technical Paper No.2009-01-1262 , 2009.

8. Raghavan, K.G., An experimental investigation into the effect of NO_2 and temperature on the passive oxidation and active regeneration of particulate matter in a diesel particulate filter, Master's Thesis, Michigan Technological University, 2015.

9. Kladopoulou,E.A., Yang, S.L., Johnson, J.H., Parker, C.G., Konstandopoulos, A.G., A study describing the performance of diesel particulate filters during loading and regeneration – a lumped parameter model for controls applications, SAE Tech Paper No. 2003-01-0842, 2003.

10. Nagar, N., He,X., Iyengar, V., Acharya, N., Kalinoski, A., Kotrba, A., Gardner, T., and Yetkin, A., Real time implementation of doc-cpf models on a production-intent ecu for controls and diagnostics of a pm emission control system, SAE Paper No 2009-01-2904, 2009.

11. Mulone, V., Cozzolini, A., Abeyratne, P., Littera, D., Thiagarajan, M., Besch, M.C., and Gautam, M., Soot modeling for advanced control of diesel engine aftertreatment, ASME ICEF2010-35160, 2010, doi:10.115/ICEF2010-35160, 2010.

12. Mulone, V., Cozzolini, A., Abeyratne, P., Besch,M., Littera, D., Gautam, M., Exhaust:CPF model for real-time applications, SAE Technical Paper No. 2011-24-0183, 2011.

13. Depcik, C., Langness, C., and Mattson, J., Development of a simplified diesel particulate filter model intended for an engine control unit, SAE Technical Paper No. 2014-01-1559, 2014.

14. Depcik, C., Combining the classical and lumped diesel particulate filter models, SAE Int. J. Engines 8(3):2015, doi:10.4271/2015-01-1049, 2015.

15. Konstandopoulos, A., and Johnson, J., Wall-Flow Diesel Particulate Filters – Their Pressure Drop and Collection Efficiency, SAE Technical Paper 890405, 1989.

16. Konstandopoulos, A.G., Kostoglou, M., and Housiada, P., Spatial non-uniformities in diesel particulate trap regeneration, SAE Technical Paper No. 2001-01-0908, 2001.

17. Miyairi, T., Miwa, S., Abe, F., Xu, Z., and Nakasuji, Y., Numerical study on forced regeneration of wall-flow diesel particulate filters, SAE Technical Paper No. 2001-01-0912, 2001.

18. Yi, Y., Simulating the soot loading in wall-flow CPF using a three-dimensional macroscopic model, SAE Technical Paper No. 2006-01-0264, 2006.

19. Ranalli, M., Hossfeld, Christoph., Kaiser, Rolf., Schmidt, Stefan., and Elfinger, Gerhard., Soot loading distribution as a key factor for a reliable DPF system: an innovative development methodology, SAE Technical Paper No 2002-01-2158, 2002.

20. Kostoglou, M., Housiada, P., and Konstandopoulos, A.G., Multi-channel simulation of regeneration in honeycomb monolithic diesel particulate filters, Chem. Eng. Sci. 58(14), 3273-3283 (2003). doi:10.1016/S0009-2509(03)00178-7, 2003.

21. Koltsakis, G., Haralampous, O., Depcik, C., and Ragonoe, J.C., Catalyzed diesel particulate filter modeling, Reviews in Chemical Engineering, 29(1):1-61,2013,doi:10.1515/revce-2012-008,2013.

22. Premchand, K.C., Surenahalli, H., and Johnson, J., Particulate matter and nitrogen oxides kinetics based on engine experimental data for a catalyzed diesel particulate filter, SAE Technical Paper No. 2014-01-1553, 2014.

23. Premchand, K.C., Development of a 1-D catalyzed diesel particulate filter for simulation of the performance and the oxidation of particulate matter and nitrogen oxides using passive oxidation and active regeneration engine experimental data, PhD Dissertation, Michigan Technological University, 2013.

24. Premchand, K.C., Raghavan, K.G., and Johnson, J.H., A modeling study of the exhaust flow rate and temperature effects on the particulate matter thermal oxidation during the active regeneration of a diesel particulate filter, SAE Technical Paper No. 2015-01-1044, 2015.

25. Pinturaud, D., Charlet, A., Cailllol, C., Higelin, P., Girot, P., and Briot, A., Experimental study of DPF loading and incomplete regeneration, SAE Technical Paper No. 2007-24-0094, 2007.

26. Bensaid, S., Marchisio, D.L., Russo, N., and Fino, D., Experimental investigation of soot deposition in diesel particulate filters, Catl. Today 147, 147S, 295S-300S (2009), doi: 10.1016/j.cattod.2009.07.039, 2009.

27. Foley, R., Experimental investigation into particulate matter distribution in catalyzed particulate filters using a 3D Terahertz wave scanner, MS Thesis, Michigan Technological University, 2013.

28. Foley, R., Naber, J., Johnson, J., and Rogoski, L., Development of the methodology for quantifying the 3D PM distribution in catalyzed particulate filters using a 3D Terahertz wave scanner, SAE Technical Paper No. 2014-01-1573,2014.

29. Foley, R., Johnson, J.H., Naber, J., and Rogoski, L., Experimental Measurements of Particulate Matter Distribution in a Catalyzed Particulate Filter, Journal of Emiss. Control Sci. Technol. Doi:10.1007/s40825-014-0005-4, 2015.

30. Haralampous, O.A., Kandylas, I.P., Koltasakis, G.C., and Samaras, Z.C., Diesel particulate filter pressure drop. Part 1: modeling and experimental validation, Int.J.Engine Res., Vol. 5 (2), 149-162, 2004.

31. Haralampous, O.A., Kandylas, I.P., Koltasakis, G.C., and Samaras, Z.C., Diesel particulate filter pressure drop. Part 2: on-board calculation of soot loading, Int.J.Engine Res., Vol. 5(2), 163-173, 2004.

32. Pulkrabek, W.W., and Ibele, W.E., The effect of temperature on the permeability of the porous material, Int. J. Heat and Mass Transfer, Vol. 30, No 6, pp 1103-1109, 1987.

33. Versaevel, P., Colas, H., Rigaudeau, C., Noirot, R., Koltsakis, G.C., and Stamatelos, A.M., Some empirical observations on diesel particulate filter modeling and comparison between simulation and experiments, SAE Paper No. 2000-01-0477, 2000.

34. Konstandopoulos, A.G., Kostoglou, M., Vlachos, N., and Kladopoulo, E., Advances in chemical engineering, Vol. 33, pp 213-275, 2007.

35. Daido, S., and Takagi, N., Visualization of the PM deposition and Oxidation behavior inside the DPF wall, SAE Technical Paper No. 2009-01-1473, 2009.

36. Choi, S., and Lee, K., Detailed investigation of soot deposition and oxidation charecterstics in a diesel particulate filter using optical visualization, SAE Technical Paper No. 2013-01-0528, 2013.

37. Shadman, F., Kinetics of soot combustion during regeneration of surface filters, Comb. Sci. and Technol., Vol. 63, pp 183-191, 1989.

38. Kostoglou, M., Konstandopoulos, A.G., Effect of soot layer microstructure on diesel particulate filter regeneration, AIChE Journal, 51 (9), pp. 2534-2546 (2005), 2005.

39. Picandet, V., Khelidj, A., and Bastial, G., Effect of axial compressive damage on gas permeability of ordinary and high-performance concrete, Cement and Concrete Research 31 (2201) 1525-1532, 2001.

40. Stengel, R.F., Optimal control and estimation, Dover Publications, ISBN 0-486-68200-5, 1994.

41. Chauvin, J., Moulin, P., Corde, Gilles., Peit, N., and Rouchon, P., "Kalman filtering for real-time individual cylinder air fuel ratio observer on a diesel engine test bench," American Control Conference, 2006.

42. Tschanz, F., Amstutz, A., Onder, C., and Gizzella, L., "Feedback control of particulate matter and nitrogen oxide emissions in diesel engines," Control Engineering Practice 21 (2013) 1809-1820,http://dx.doi.org/10.1016/j.conengprac.2012.09.014, 2012.

43. Hsieh, M., Wang, J., Design and experimental validation of an extended Kalman filter-based NOx concentration estimator in selective catalytic reduction system applications, Control Engineering Practice 19 (2011) 346-353, 2011.

44. Guardiola, C., Pla, B., Rodrigue, B., and Eriksson, L., A computationally efficient kalman filter based estimator for updating look-up tables applied to NOx estimation in diesel engines, Control Engineering Practice, 21 (2013) 1455-1468, http://dx.doi.org/10.1016/j.conengprac. 2013.06.015, 2013.

45. Surenahalli, H.S., Parker, G., and Johnson, J., Extended Kalman filter estimator for NH3 strorage, NO, NO2 and NH3 estimation in a SCR, SAE Technical Paper 2013-01-1581, 2013.

46. Surenahalli, H.S., Parker, G.G., Johnson, J.H., and Devarakonda, M.N., A Kalman filter estimator for a diesel oxidation catalyst during active regeneration of a CPF, American Control Conference, 2012.

47. Surenahalli, H.S., Parker, G.G., and Johnson, J.H., Extended Kalman Filter to Estimate NO, NO2, Hydrocarbon and Temperatures in a DOC during Active Regeneration and Under Steady State Conditions, SAE Technical Paper No. 2015-01-1059, 2015.

48. Surenahalli, H.S., Dynamic model based state estimation in a heavy duty diesel aftertreatment system for onboard diagnostics and controls, PhD Dissertation, Michigan Technological University, 2013.

49. Shiel,K.L., Study of the effect of biodiesel fuel on passive oxidation in a catalyzed filter, Master's Thesis, Michigan Technological University, 2012.

50. Shiel,K.L., Naber, J., Johnson, J.H., and Hutton, C.R., Catalyzed particulate filter passive oxidation study with ULSD and biodiesel blended fuel, SAE Technical Paper No. 2012-01-0837,2012, 2012.

51. Pidgeon, J., An experimental investigation into the effect of biodiesel blends on particulate matter oxidation in a catalyzed particulate filter during active regeneration," Master's Thesis, Michigan Technological University, 2013.

52. Pidgeon, J., Naber, D N.,, and Johnson, J.H., An engine experimental investigation into the effects of biodiesel blends on particulate matter oxidation in a catalyzed particulate filter during active regeneration," SAE Technical Paper No. 2013-01-0521, SAE Congress 2013, 2013.

53. Cengel, Y.A., Heat and mass transfer – a practical approach, McGraw-Hill Publication,Third Edition, ch. 8, sec. 8.3, pp 455-456, ISBN-13: 978-0-07-063453-4, 2007.

54. Konstandopoulos,A.G., Kostoglou,M., Skaperdas, E., Papaioannou,E., Zarvalis, D., and Kladopoulou, E., Fundamental studies of diesel particulate filters: transient loading, regeneration and aging, SAE Technical Paper No. 2000-01-1016, 2000.

55. Koltsakis,G.C., Haralampous,O.A., Margaritis,N.A., Samras,Z.C., Vogt, C.-D., Ohara, E., Watanabe, Y., and Mizutani, T., 3-dimensional modeling of the regeneration in SiC particulate filters, SAE Technical Paper No. 2005-01-0953, 2005.

56. Johnson, J.H.,Naber, J.N.,Parker,G.,Yang,S., Stevens, A., and Pihl, J., Experimental studies for CPF and SCR model, control system, and OBD development for engine using diesel and biodiesel fuels, DOE Report Number : DOE-2013-MTU-01-FINAL dated July 29, 2013.

57. Johnson, J.H., Parker, G., Chundru, V.R., and Mahadevan, B.S., SCR-F model (v1.5) new temperature model and calibration results (Cummins 2007 ISL data), Diesel Engine Aftertreatment Consortium Report, Michigan Technological University, August 14, 2016.

58. Depcik, C., and Assanis, D., Simulating area conservation and the gas-wall interface for one-dimensional based diesel particulate filter models, Journal of Engineering for Gas Turbines and Power, November 2008, Vol.130/062807-1, 2008.

59. Bissett, E.J., Kostoglou, M., and Konstandopoulos, A.G., Frictional and heat transfer characteristics of flow in square porous tubes of wall-flow monoliths, Journal of Chemical Engineering Science, 84(2012), 255-265, 2012.

60. Kostoglou, M., Bissett, E.J., and Konstandopoulos, A.G., Improved Transfer Coefficients for Wall-Flow Monolithic Catalytic Reactors: Energy and Momentum Transport, Ind. Eng. Chem. Res., 51, 13062-13072, 2012.

61. Konstandopoulos, A., Kostoglou, M., Skaperdas, E., Papaioannou, E., Zarvalis, D., and Kladopoulou, E., Fundamental studies of diesel particulate filters: Transient loading, regeneration and aging, SAE Technical Paper 2000-01-1016, 2000, doi:10.4271/2000-01-1016, 2000.

62. Cengel, Y.A., Heat and mass transfer – a practical approach, McGraw-Hill Publication,Third Edition, ch. 5, sec. 5.5, pp 311-334, ISBN-13: 978-0-07-063453-4, 2007.

63. Anderson Jr, John.D., Computational fluid dynamics – the basics with applications, McGraw-Hill Publication, ch.4, sec. 4.4, pp 145-153, ISBN 0-07-113210-4, 1995.

64. Nelder, J. A., and Mead, R., A simplex method for function minimization, Comput. J., 7(4), pp. 308–313, 1965.

65. Martyr, A.J., and Plint, M.A., Engine testing – the design, building, modifications and use of powertrain test facilities, Butterworth-Heinemann Publications, ch. 6, sec. 1, pp 113-118, ISBN-13: 978-0-08-096949-7, 2012.

66. Sappok, A., Wang, Y., Wang, R., Kamp, C., Theoretical and experimental analysis of ash accumulation and mobility in ceramic exhaust particulate filters and potential for improved ash management, SAE Int.J.Fuel Lubr. Volume 7, Issue 2, June 2014, doi:10.4271/20444-01-1941.

67. Delphi.com, Delphi DCM medium duty diesel engine controller series, http://delphi.com/shared/pdf/ppd/cv/pwrtm/dcm-medium-duty-diesel-engine-controller-series.pdf, accessed on Sep, 2014.

68. Depcik, C., and Assanis, D., Graphical user interfaces in an engineering educational environment, computer applications in engineering education, 13(1):48-59, 2005, doi: 10.1002/cae.20029.

69. Haralampous, O.A., and Koltsakis, G.C., Back-diffusion modeling of NO2 in catalyzed diesel particulate filters, Ind.Eng.Chem.Res., 43,875-883, 2004.

70. Haralampous, O.A., Kotlsakis, G.C., Samaras, Z.C., Vogt, C.-D., Ohara. E., Watanabe, Y., and Mizutani, T., Reaction and diffusion phenomena in catalyzed diesel particulate filters, SAE Technical Paper No. 2004-01-0696, 2004.

71. Cengel, Y.A., Heat and mass transfer – a practical approach, McGraw-Hill Publication,Third Edition, ch. 13, sec. 13.4, pp 727-739, ISBN-13: 978-0-07-063453-4, 2007.

72. Simon, D., "Optimal State Estimation: Kalman, H Infinity and Non-linear approaches, John Wiley and Sons, ch. 13, sec. 13.2, pp 400-409, ISBN-13 978-0-471-70858-2, 2006.

73. Kim, P., Kalman filters for beginners with MATLAB examples, CreateSpace, ch. 11, sec. 11.2, pp 86-88, ISBN-13:1463648350, 2011.

74. Surenahalli, H.S., Quick start guide for DOC EKF estimator version 4.0, Michigan Technological University, February 17, 2013.

Appendix A Thermal Boundary Layer Equations[1]

A.1 Experimental Data Analysis

As shown in Figure 3.6, the temperature factor for all eighteen runs are same. Hence, AR-B10-1 experiment was used as the reference experiment for calculation of the thermal boundary layer coefficients. The temperatures measured by thermocouples C1-C4 were used for calculation of temperature factor.

Table A 1 CPF inlet temperatures measured by C1-4 thermocouples and temperature factor

Radial distance in mm	Temperature ID	Temperature @ 0.30 hrs in °C	Temperature @ 5.8 hrs in °C	Diameter ratio	Temperature Factor @ Stage 1 - loading 0.3 hrs	Temperature Factor @ Active Regneration - 5.8 hrs
0	C1 (measured)	268.6	542.7	0.00	1.70	1.76
55	C2 (measured)	268.9	539.8	0.41	1.72	1.63
95	C3 (measured)	263.2	529.3	0.71	1.17	1.16
122	C4 (measured)	255.6	513.1	0.91	0.42	0.44
133	Ts (extrapolated)	251.3	503.2	1.00	0.00	0.00

T_m (calculated)	261.5	525.6
T_m/T_s	1.041	1.045
Avg T_m/T_s	1.043	

Surface temperature (Ts) in the Table A 1 was extrapolated from C1-C4 thermocouple measurements as shown in Figures A 1 and A 2.

---

[1] Parts of the material contained in this chapter are based on references [1, 2, 3] with permission of Springer.
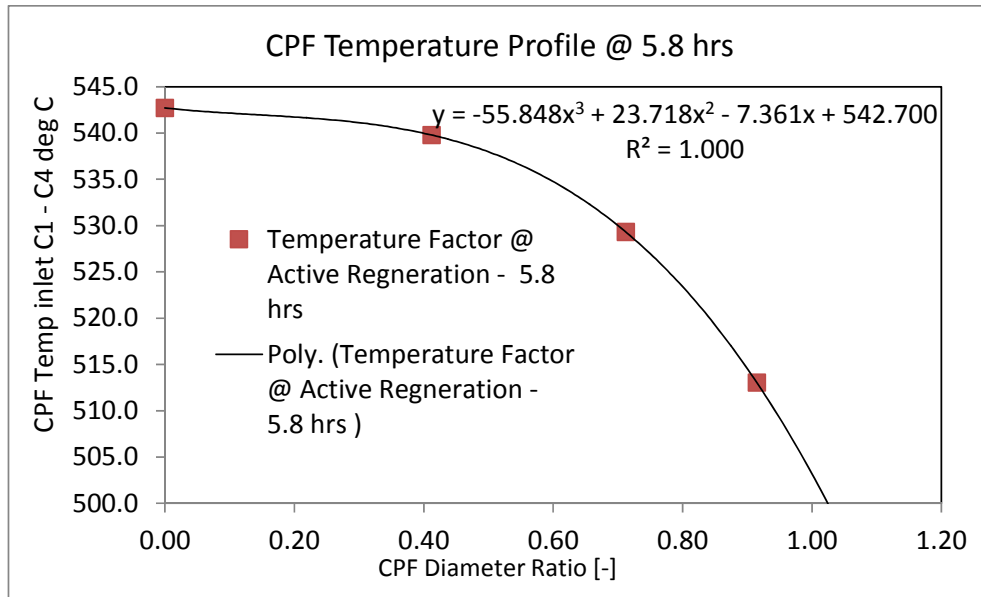
184

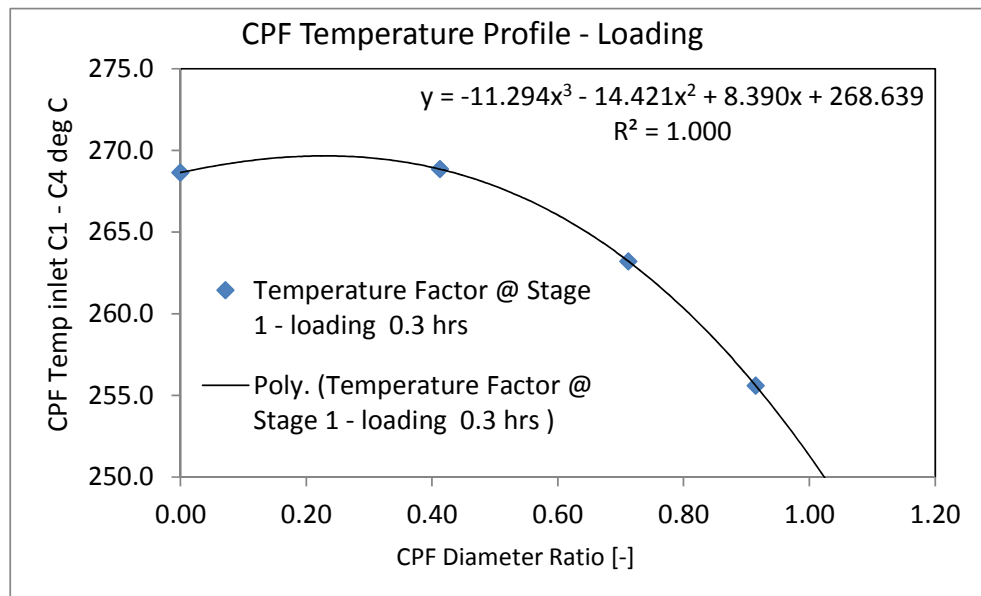*Figure A 1 CPF inlet temperature profile at 5.8 hrs*

Figure A 2 CPF inlet temperature profile at stage 1 loading 0.3 hrs

The temperature factors [53] were calculated using equation A.1. The sample calculation at R1 = 0 mm is shown below

$$\text{Temperature factor} = \frac{T_s - T_r}{T_s - T_m} \qquad (A.1)$$

where T_m = Mean exhaust gas tempertuare

T_s = Wall inner surface temperature

T_r = Temperature at a given radial location

Temperature factor @ R1, 0 mm @ 5.8 hrs = $\frac{503.2-542.7}{503.2-525.6}$ = 1.76

Figure A 3 shows the plots of temperature factors for stage 1 loading @ 0.3 hrs (a sample point at low temperature region of the test) and active regeneration @ 5.8 hrs (a sample point at high temperature region) test conditions. From Figure A 3, it is evident that the temperature varies significantly between 0.3 (262°C) and 5.8 hrs (523°C), the temperature factor profile looks similar for both conditions, confirming that the one factor can be applied for the entire duration of the test. The following equation represents temperature factors of both test conditions with R2 value of 1.00.

Temperature Factor @ x = -2.493x3 + 1.0585x2 - 0.3285x + 1.7631   (A.2)
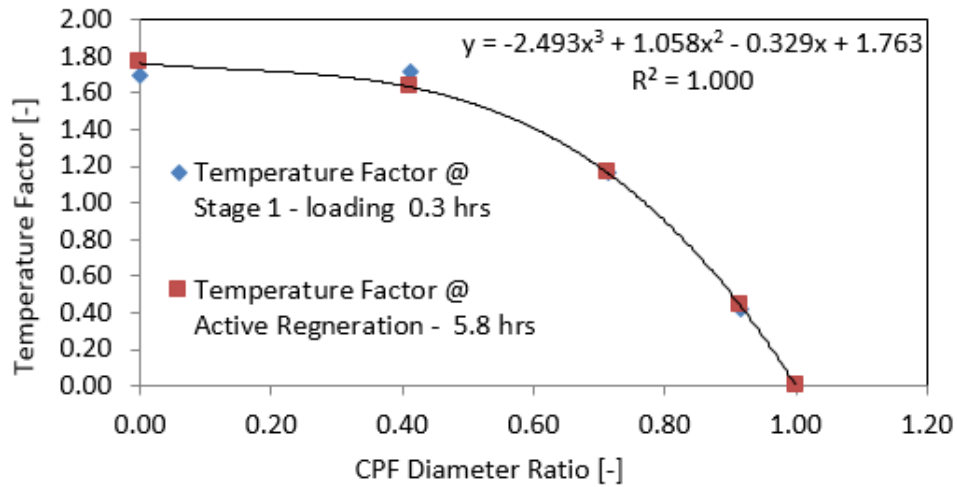
Where x is the CPF diameter ratio.

Figure A 3 Temperature factor

Using Equation A.1 and knowing the temperature at any radial location at the CPF inlet, the temperatures at the other radial locations can be determined as shown below

$$\frac{T_s-T}{T_s-T_m} = F1 = Temperature\ Factor \tag{A.3}$$

186

$$\frac{T_m}{T_s} = F2 = mean\ to\ surface\ temperature\ ratio \tag{A.4}$$

Combining Equations (D.3) and (D.4) yields

$$\frac{T_s - T}{T_s - F2.T_s} = F1 \tag{A.5}$$

$$F1(T_s - F2.T_s) + T - T_s = 0 \tag{A.6}$$

Example calculation: To find temperature Ts, assume we have a temperature measurement T = 539.8°C at x = 0.41.From equation (C.2), F1 = 1.63 for x = 0.41. Then substituting F2 = 1.043 (from Table C 1), F1 = 1.63 and T = 539.8°C in equation (A.6), the Ts can be calculated as follows

$$1.63\ (T_s - 1.043 * T_s) + 539.8 - T_s = 0$$

and Ts = 504.4°C.Similarly, temperatures at other locations can be determined using equation (A.3).

A.2 Thermally Fully Developed Flow Analysis

The thermal boundary layer starts when the fluid enters the pipe whose surface temperature (T_s) is different than the fluid temperature (T_r) as shown in Fig. A 4.

Thermal boundary layer

T_s

T_r

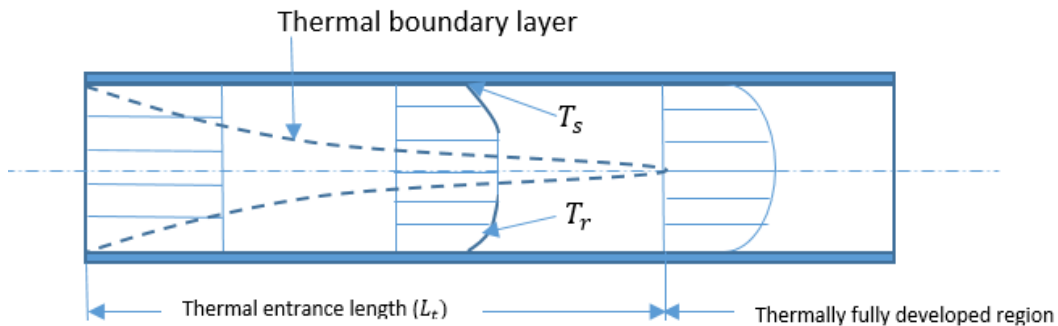Thermal entrance length (L_t)

Thermally fully developed region

Figure A 4 Development of the thermal boundary layer

The region of flow over which the thermal boundary layer develops and reaches the tube center is called the thermal entrance region [71], and the length of this region is called thermal entry length (L_t). The flow is thermally fully developed in the region beyond the

thermal entry length. The thermally fully developed condition is different from the hydraulically developed flow condition as shown by equations A.7 and A.8.

Hydrodynamically fully developed: $\frac{\partial u(r,x)}{\partial x} = 0 \rightarrow u = u(r)$ (A.7)

Thermally fully developed: $\frac{\partial}{\partial x}\left[\frac{T_s(x)-T(r,x)}{T_s(x)-T_m(x)}\right] = 0$ (A.8)

In case of thermally fully developed flow, the temperature profile can be different at different cross sections of the tube in the fully developed region of the flow. However, the dimensionless temperature profile is remained unchanged in the thermally fully developed region when the temperature or heat flux of the tube surface is remained constant.

$$\left[\frac{T_s(x)-T(r,x)}{T_s(x)-T_m(x)}\right] = C$$ (A.9)

The relative growth of the velocity and thermal boundary layer can be expressed using the Prandtl number Pr. For fluids with Pr $\ll$ 1, the thermal boundary layer out grows velocity boundary layer. Hence, the thermal boundary layer is shorter than the velocity boundary layer.

For laminar flow, the hydrodynamic and thermal entry lengths are given approximately as [71]

$L_{h,laminar} \approx 0.05\, Re\, D$ (A.10)

$L_{t,laminar} \approx 0.05\, Re\, Pr\, D$ (A.11)

The entry length is shorter for the turbulent flows because of the random fluctuations in the flow overshadows the effect of molecular diffusion. Therefore, the velocity and thermal entrance lengths are similar and they are independent of the Prandtl number. For turbulent flows, the hydrodynamic and thermal entry lengths are approximately taken as [71]

$L_{h,turbulent} \approx L_{h,turbulent} \approx 10D$ (A.12)

The sensitivity analysis of thermal entrance lengths (L_t) for an exhaust flow of 7.9 $\frac{kg}{min}$ (AR-B10-1 experiment) at different diameters of exhaust pipe and CPF channel diameter at different PM cake layer thicknesses are shown in Table A 2.

Location	Diameter		PM cake thickness		Temp.	Total Flow	Re	Pr	L_h laminar	L_t laminar	L_h turbulent	L_t turbulent
	in	mtr	μm	mtr	°C	kg/sec	(-)	(-)	mtr	mtr	mtr	mtr
Exhaust Pipe	6.0	0.152	NA	NA	530	0.13	3.0E+04	0.70	NA	NA	1.5	1.5
Exhaust Pipe	8.0	0.203	NA	NA	530	0.13	2.3E+04	0.70	NA	NA	2.0	2.0
Exhaust Pipe	10.5	0.267	NA	NA	530	0.13	1.7E+04	0.70	NA	NA	2.7	2.7
CPF Channel	0.0591	0.0015	0	0.00E+00	530	0.13	277	0.70	0.021	0.015	NA	NA
CPF Channel	0.0591	0.0015	15	1.50E-05	530	0.13	289	0.70	0.021	0.015	NA	NA
CPF Channel	0.0591	0.0015	30	3.00E-05	530	0.13	301	0.70	0.022	0.015	NA	NA

From the analysis in Table A.2, the flow is hydrodynamically and thermally fully developed at 21 mm from the inlet of the CPF. The thermocouple measurements used in this thesis for the inlet temperature distribution analysis is about 32 mm from the inlet of the CPF (C1 to C4 in Fig. 3.3) indicating fully developed flow. The hydrodynamic and thermal entrance lengths are longer (1.5 to 2.7 mtrs) for the exhaust pipe in the upstream sections of DOC and downstream piping between DOC and CPF. The flow development is further affected by the discontinuities between DOC and CPF sections. Hence, the pipe geometry, flow paths, flow discontinuities, temperature sensor size and location have to be considered while developing inlet temperature distribution profile for the CPF.

Appendix B SCR-F/CPF Model Development Equations[1]

The total volume of each zone (V), empty volume (Ve) and filter volume (Vf) are [13]

$$V_{i,j} = \pi(r_i{}^2 - r_{i-1}{}^2)\Delta L_j \tag{B.1}$$

$$V_{e_{i,j}} = N_{c_i} d^2 \Delta L_j \tag{B.2}$$

$$V_{f_{i,j}} = V_{i,j} - V_{e_{i,j}} \tag{B.3}$$

The inlet PM is assumed to be deposited uniformly over the entire volume of filter, hence mass of PM deposited in each zone is calculated as

$$ms_{i,j} = \frac{ms_t V_{i,j}}{V_t} \tag{B.4}$$

The average thickness of PM cake in each zone is calculated using total PM mass, PM density and channel geometry as follows [21],

$$ts_{i,j} = \frac{1}{2}\left| d - \sqrt{d^2 - \frac{ms_{i,j}}{\frac{Nc_t}{2}\Delta L_{i,j}\rho_s}} \right| \tag{B.5}$$

The empty volume while accounting for PM is calculated as follows (Ves),

$$V_{es_{i,j}} = \frac{Nc_i}{2}\lfloor(d - 2ts_{i,j})^2 + d^2\rfloor\Delta L_j \tag{B.6}$$

Finally, the PM cake volume is calculated as

$$Vs_{i,j} = V_{i,j} - Vf_{i,j} - V_{es_{i,j}} \tag{B.7}$$

The detailed calculations and assumptions in discretization are explained in reference [13].

---

[1] Parts of the material contained in this chapter are based on references [1, 2,3] with permission of Springer.

Filter Temperature Equations

The energy balance in the filter is affected by a) heat conduction along the length of the filter (axial conduction), b) heat conduction along radial direction of the filter (radial conduction), c) convection between filter and channel gas, d) energy released during oxidation of PM cake, and e) heat transfer due to radiation exchange between channel surfaces.

The energy flow through wall is neglected as there will be no distinction between inlet and outlet channels [13]. Hence the energy balance equation for the filter is:

$$(\rho_s c_s V s_{i,j} + \rho_f c_f V f_{i,j})\frac{dTf_{i,j}}{dt} = \dot{Q}_{cond.axial} + \dot{Q}_{cond.radial} + \dot{Q}_{conv} + \dot{Q}_{reac,PM} + \dot{Q}_{reac,HC} + \dot{Q}_{rad} \tag{B.8}$$

where, T_f is the filter substrate temperature.

The axial and radial conduction along the length of the filter is calculated using resistance node methodology [13,55]:

$$\dot{Q}_{cond.axial} = \lambda_{i,j} A f_{i,j}\left[\frac{Tf_{i,j+1} - Tf_{i,j}}{\frac{1}{2}(\Delta L_{j+1} + \Delta L_j)} + \frac{Tf_{i,j-1} - Tf_{i,j}}{\frac{1}{2}(\Delta L_{j-1} + \Delta L_j)}\right] \tag{B.9}$$

$$\dot{Q}_{cond.radial} = \lambda_{i,j} A r_{i,j}\left[\frac{Tf_{i+1,j} - Tf_{i,j}}{In(rc_{i+1}/rc_i)} + \frac{Tf_{i,j-1} - Tf_{i,j}}{In(rc_i/rc_{i-1})}\right] \tag{B.10}$$

$$A f_{i,j} = \frac{Vf_{i,j} + Vs_{i,j}}{\Delta L_j} \tag{B.11}$$

$$A_{r_{i,j}} = 2\pi\Delta L_j \tag{B.12}$$

$$\lambda_{i,j} = \frac{\lambda_f Vf_{i,j} + \lambda_s Vs_{i,j}}{Vf_{i,j} + Vs_{i,j}} \tag{B.13}$$

The convection heat transfer between filter and channel gas is calculated using the equation 4.2

The energy released during exothermic reactions is given by [13, 21]

$$\dot{Q}_{reac,th} = -\frac{ms_{i,j}}{\rho_s}\dot{S}c_{(th)}\Delta H_{reac,th} \tag{B.14}$$

$$\dot{Q}_{reac,NO_2} = -\frac{ms_{i,j}}{\rho_s}\dot{S}c_{(NO_2)}\Delta H_{reac\ NO_2} \tag{B.15}$$

$$\dot{Q}_{reac,PM} = \dot{Q}_{reac,th} + \dot{Q}_{reac,NO_2} \qquad (B.16)$$

$$\dot{Q}_{reac,HC} = -\Delta H_{hc} RR_{HC} dw_s \Delta_j \qquad (B.17)$$

where $\dot{Sc}_{(th)}$ is the PM mass lost due to thermal (O_2) oxidation of PM, $\dot{Sc}_{(NO_2)}$ is the PM mass oxidized due to NO_2 assisted combustion and RR_{HC} is the reaction rate of hydrocarbon, w_s is the thickness of the substrate and Δ_j is the axial discretization length.

The gas energy balance equation for the channel gas entering and leaving the zone is calculated using the equations 4.3 and 4.4.

The mass flow rate to the each zone is given by

$$\dot{m}_{i,j} = \dot{m}_{total} \frac{Ves_{i,j}}{\sum_i Ves_{i,j}} \qquad (B.18)$$

Radiation between the channel surfaces:

In the MPF model, each zone is treated as an enclosure as shown in Fig. A 1. The surface 3 is the substrate wall with PM cake (black body radiation) and surface 1 and 2 are the inlet and outlet of this enclosure (the gas interface between the zones) which are assumed to be black for simplicity of the analysis and moreover radiation escaping the surface 1 and 2 will be absorbed in to the adjacent black surface).
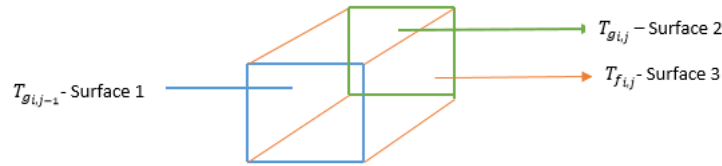
Figure B 1 Schematic of a enclosure (zone) for the radiation heat transfer model

Assuming channel gas is completely transparent to thermal radiation and the surfaces are black, the net radiation heat transfer between channel gas and filter wall can be determined as [71]:

$$\dot{Q}_{rad} = -As_{i,j} \left(F_{3-1}(J_3 - J_1) + F_{3-2}(J_3 - J_2) \right) \qquad (B.19)$$

$$J_1 = \sigma T_{i,j-1}^4 \qquad (B.20)$$

192

$$J_2 = \sigma T_{i,j}^4 \tag{B.21}$$

$$J_3 = \sigma T f_{i,j}^4 \tag{B.22}$$

The effect of internal radiation is very small at lower temperatures and could be more important over 600°C and could improve the model accuracy during uncontrolled regeneration events [55].

PM Oxidation

The PM oxidation equations include PM oxidation by thermal (O_2) and NO_2 assisted reactions. The chemical reaction expression for thermal (O_2) oxidation is [13]

$$C_{(s)} + a_{o_2}O_2 \rightarrow 2(a_{o_2} - 0.5)CO_2 + 2(1 - a_{o_2})CO \tag{B.23}$$
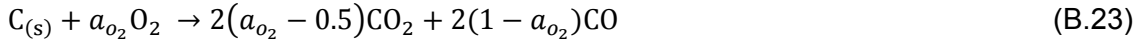
Similarly, the reaction equation for NO_2 assisted oxidation is given by [21]

$$C(s) + \propto_{NO2} NO_2 \rightarrow \propto_{NO2} NO + (2 - \propto_{NO2}) CO + (\propto_{NO2} - 1) CO2 \tag{B.24}$$
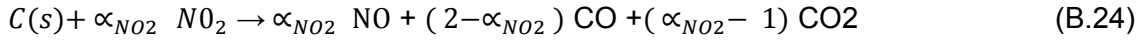
The oxidation of PM mass on the surface due to thermal and NO_2 assisted oxidation is equal to

$$\dot{S}_{c_{(th)}} = -(S_p \rho Y_{i,j,o_2} k_{o_2}) \frac{W_{c_{(s)}}}{a_{o_2} W_{o_2}} \tag{B.25}$$

$$\dot{S}_{c_{(NO_2)}} = -(S_p \rho Y_{i,j,NO_2} k_{NO_2}) \frac{W_{c_{(s)}}}{a_{NO_2} W_{NO_2}} \tag{B.26}$$

The Arrehenius reaction rate for thermal and NO_2 assisted reaction is equal to:

$$k_{o_2} = A_{o_2} T f_{i,j} exp\left[-E_{o_2}/(R_u T f_{i,j})\right] \tag{B.27}$$

$$k_{NO_2} = A_{NO_2} T f_{i,j} exp\left[-E_{NO_2}/(R_u T f_{i,j})\right] \tag{B.28}$$

Velocity Equations

From Depcik et al [13], the average inlet channel velocity can be determined as:

$$u_I|_{z=0} = \frac{\dot{m}_{total}}{\rho \frac{Nc_t}{2}(d - 2.\overline{ts})^2} \tag{B.29}$$

Using the Equation (B 29), the radial zone velocity (mass flow is axially same for each zone) is calculated as:

$$u_{I_i}|_{z=0} = \frac{\dot{m}_{i,J}}{\rho_{i,j}\frac{Nc_i}{2}(d-2.\overline{ts_i})^2} \tag{B.30}$$

where $\overline{ts_i}$ is the average PM cake thickness in each radial zone and $\frac{Nc_i}{2}$ is the number of inlet channels in each radial zone.

From Depcik et al [13], average velocity through the PM cake (u_s) and wall layers (u_w) is:

$$u_s = \frac{\dot{m}_{total}}{4\rho\frac{Nc_t}{2}(d-2.\overline{ts})\,L_t} \tag{B.31}$$

$$u_w = \frac{u_s(d-2.\overline{ts})}{d} \tag{B.32}$$

Writing the (B.31) and (B.32) equations for each radial zone is,

$$u_{s_i} = \frac{\dot{m}_{i,J}}{4\rho_{i,j}\frac{Nc_i}{2}(d-2.\overline{ts_i})\,L_t} \tag{B.33}$$

$$u_{w_i} = \frac{u_{s_i}(d-2.\overline{ts_i})}{d} \tag{B.34}$$

From Depcik et al [13], average velocity through the inlet channel (u_I) and outlet channel (u_{II}) is:

$$u_I|_j = u_I|_{j-1} - \frac{4u_s}{d-2.\overline{ts}}\,\Delta L_{j-1} \tag{B.35}$$

$$u_{II}|_j = u_{II}|_{j-1} + \frac{4u_w}{d}\,\Delta L_{j-1} \tag{B.36}$$

Writing the (B.35) and (B.36) equations for each radial zone,

$$u_I|_{i,j} = u_I|_{i,j-1} - \frac{4u_{s_i}}{d-2.\overline{ts_i}}\,\Delta L_{j-1} \tag{B.37}$$

$$u_{II}|_{i,j} = u_{II}|_{i,j-1} + \frac{4u_{w_i}}{d}\,\Delta L_{j-1} \tag{B.38}$$

The detailed formulation of Equations (B.30, 31, 32, 33 and 34) are found in reference [13].

Filter Temperature Boundary Conditions

At the inlet of MPF model (for nodes i = 1 to imax and j = 1), the temperature profile is calculated using the thermal boundary layer Equation (12) and the CPF inlet temperature at a given location. At the center of the filter (for i =1, j = 1 to jmax) due to the symmetry, the boundary condition equals to [13]

$$\frac{dTf}{dr}\bigg|_{r=0} = 0 \qquad\qquad (B.39)$$

At the exterior of the CPF (i = imax, j = 2 to jmax),

$$(\rho_s c_s Vs_{i,j} + \rho_f c_f V_{f_{i,j}} + \rho_{ins} c_{p,ins} V_{ins} + \rho_{can} c_{p,can} V_{can}) \frac{dTf_{i,j}}{dt} = \dot{Q}_{cond.axial} + \dot{Q}_{cond.radial} +$$

$$\dot{Q}_{conv} + \dot{Q}_{reac,PM} + \dot{Q}_{reac,HC} + \dot{Q}_{wall-flow} + \dot{Q}_{rad} \qquad\qquad (B.40)$$
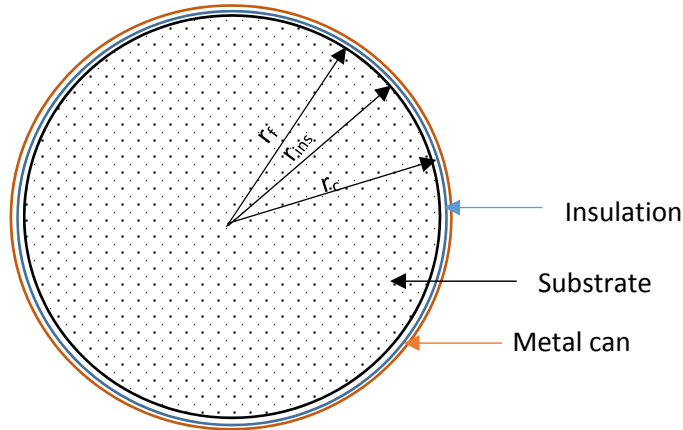
Figure B 2 Thermal resistance due to insulation and metal can

The radial conduction heat transfer is given as:

$$\dot{Q}_{cond.radial} =$$

$$\lambda_{i,j} Ar_{i,j} \frac{Tf_{i-1,j} - Tf_{i,j}}{\ln\left(\frac{rc_i}{rc_{i-1}}\right)} +$$

$$h_{amb} k_{ins} k_{metal} A_{amb} \frac{(T_{amb} - Tf_{i,j})}{k_{ins} k_{can} + \ln\left(\frac{r_{ins}}{r_f}\right)_{i,j} r_{c\,i,j} k_{can} h_{amb} + \ln\left(\frac{r_c}{r_{ins}}\right)_{i,j} r_{c\,i,j} k_{ins} h_{amb}} +$$

$$\varepsilon_r \sigma A_{amb} (Tf_{amb}^4 - Tf_{i,j}^4) \qquad\qquad (B.41)$$

The surface area of the CPF is calculated as follows

$$A_{amb} = \pi D \Delta L_j \qquad (B.42)$$

The equation B.41 accounts for the thermal resistance of the insulation and metal can as well along with the radiation heat transfer to the ambient air as shown in Figure B 1.

Appendix C Filtration and Pressure Drop Model Equations[1]

C.1 Filtration Model Equations

In filtration sub-model, the substrate wall is divided in to n_{max} (n_{max} = 4) number of slabs. Each slab consists of several spherical wall collectors [15, 61]. The diameter of unit collector increases as the PM accumulates in to the collector. The initial diameter of the unit collector is given as

$$dc_{0,w} = \frac{3}{2}\left(\frac{1-\varepsilon_{0,s}}{\varepsilon_{0,s}}\right) d_{pore,wall} \qquad \text{C.1}$$

The number of pores in each zone of the substrate wall is given as [14]

$$Np_{i,j} = \frac{Veo_{i,j}}{\frac{4\pi}{3}\left(\frac{d_{pore,wall}}{2}\right)^3} \qquad \text{C.2}$$

The empty volume of the substrate wall is given as

$$Veo_{i,j} = \varepsilon_{0,s} V_{f\,i,j} \qquad \text{C.3}$$

The number of pores in each slab at each zone is calculated as

$$\left[Np_{i,j}\right]_n = \frac{Np_{i,j}}{4} \qquad \text{C.4}$$

where, n is 1, 2, 3 and 4.

Wall collector efficiency at each slab is calculated as

$$\eta_{wall_{i,j}\,slab\,n} = \left[\eta_{D_{i,j}} + \eta_{R_{i,j}} - \eta_{D_{i,j}}\eta_{R_{i,j}}\right]_{wall,slab\,n} \qquad \text{C.5}$$

The filtration efficiency of a unit collector in the PM cake layer is calculated as

$$\eta_{cake_{i,j}} = \left[\eta_{D_{i,j}} + \eta_{R_{i,j}} - \eta_{D_{i,j}}\eta_{R_{i,j}}\right]_{cake} \qquad \text{C.6}$$

---

[1] Parts of the material contained in this chapter are based on references [1, 2,3] with permission of Springer.

Partition coefficient is used to determine transition from deep bed filtration regime to cake filtration regime and it is calculated as

$$\Phi = \frac{dc^2_{wall,slab1_{i,j}} - dc^2_{0,wall\ slab\ 1}}{(\Psi b)^2 - dc^2_{0,wall\ 1}}$$

C.7

where, $dc_{wall\ slab\ 1}$ is the unit collector diameter in the first slab of the substrate wall at a given axial and radial direction, Ψ is the percolation factor and b is the unit cell diameter and it is calculated as

$$\frac{dc^3_{0,s_{i,}}}{b^3} = 1 - \varepsilon_{0,s}$$

C.8

The detailed formulation of equations (C.5) to (C.7) is explained in references [23].

C.2 Pressure Drop Model Equations

In pressure drop sub model, the pressure drop at each radial section is calculated by starting out with exit pressure $P_2|_{x=L} = P_{Baro}$ and then traversing through all possible streamlines (dashed lines) shown in Figure C 1.
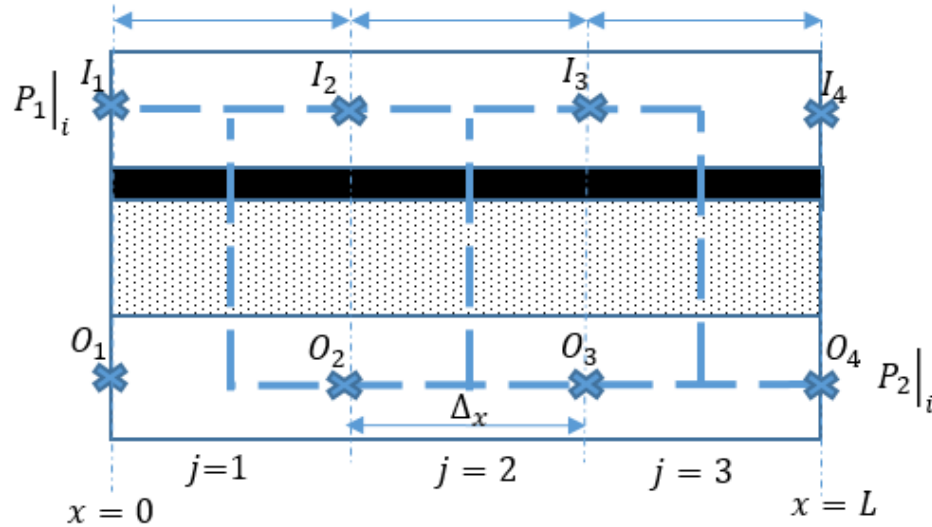
Figure C 1 Schematic of the streamlines (shown a dashed lines) used for calculating the pressure drop across CPF for 3x1 zone model (4 axial and 1 radial discretization).

The absolute pressure of radial section (i) is calculated by following the streamlines ($s1, s2$ and $s3$) shown below

$$P_1|_{i,s1} = O_4 \rightarrow \Delta P_{wall_{i,j}} \rightarrow \Delta P_{cake_{i,j}} \rightarrow I_3 \rightarrow I_2 \rightarrow I_1 \qquad \text{C.9}$$

$$P_1|_{i,s2} = O_4 \rightarrow O_3 \rightarrow \Delta P_{wall_{i,j}} \rightarrow \Delta P_{cake_{i,j}} \rightarrow I_2 \rightarrow I_1 \qquad \text{C.10}$$

$$P_1|_{i,s3} = O_4 \rightarrow O_3 \rightarrow O_2 \rightarrow \Delta P_{wall_{i,j}} \rightarrow \Delta P_{cake_{i,j}} \rightarrow I_1 \qquad \text{C.11}$$

The pressure drop in the outlet channel stream lines (O_4, O_3, O_2 and O_1) are calculated using the following equation

$$P_2|_{i,j} = P_2|_{i,j+1} + \rho v_2^2|_{i,j+1} - \rho v_2^2|_{i,j} + F\Delta x \frac{\mu v_2}{a^2}|_{i,j} \qquad \text{C.12}$$

The pressure drop in the inlet channel stream lines (I_4, I_3, I_2 and I_1) are calculated using the following equation

$$P_1|_{i,j} = P_1|_{i,j+1} + \rho v_1^2|_{i,j+1} - \rho v_1^2|_{i,j} + F\Delta x \frac{\mu v_1}{a^2}\left(\frac{a*}{a}\right)^2|_{i,j} \qquad \text{C.13}$$

The wall pressure drop at each zone is calculated using the following equation

$$\Delta P_{wall_{i,j}} = \mu_{i,j} v_{w_{i,j}} \frac{w_s}{k_{wall_{i,j}}} \qquad \text{C.14}$$

The cake pressure drop at each zone is calculated using the following equation

$$\Delta P_{cake_{i,j}} = \mu_{i,j} v_{s_{i,j}} \frac{w_{p_{i,j}}}{k_{cake_{i,j}}} \qquad \text{C.15}$$

The pressure drop across each radial section is calculated as

$$\Delta P_{CPF,i,s1} = [P_1|_{x=0} - P_2|_{x=L}]_{i,s1} \qquad \text{C.16}$$

$$\Delta P_{CPF,i,s2} = [P_1|_{x=0} - P_2|_{x=L}]_{i,s2} \qquad \text{C.17}$$

$$\Delta P_{CPF,i,s3} = [P_1|_{x=0} - P_2|_{x=L}]_{i,s3}$$

The overall pressure drop of the CPF is calculated using the following equation

$$\Delta P_{CPF} = \frac{\sum_{s1}^{smax}\left[\sum_{i=1}^{i=imax} VF_i \Delta P_{CPF,i}\right]}{3} \qquad \text{C.18}$$

Appendix D Post Loading Permeability[1]

During post loading of PM in the CPF, the cracks and holes formed in the PM cake during PM oxidation is filled by the incoming PM. This damage recovery process of the PM cake reduces the permeability. Figure D 1 shows the relative change in permeability during post loading for the passive oxidation experiments. For this analysis, all the passive oxidation experiment runs listed in Table 3.3 were used except PO-B10-14 because of very low PM oxidation rates causing gain in PM mass retained during PM oxidation. The post loading permeability ratios for the PO-B10-14 experiment were in the range of 1 to 1.10.
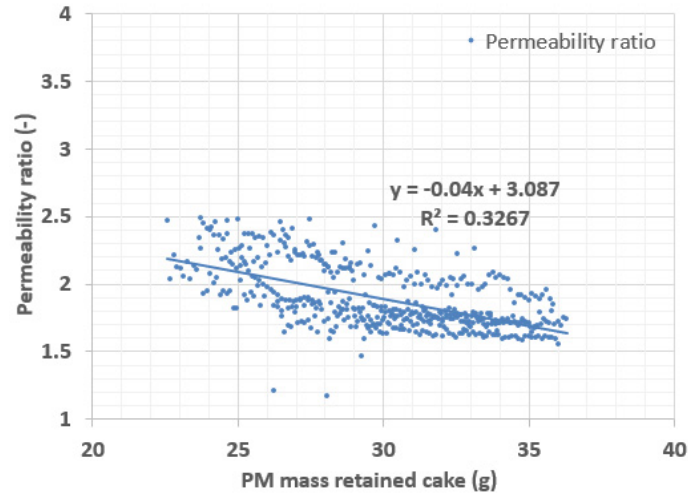
Figure D. 1 Relative change in permeability ratio during the post loading for the passive oxidation experiments

From the data presented in Figure D 1, the PM cake permeability during post loading is calculated as

$$k_{d_{i,j}} = k_{p_{i,j}} \left(C_{10} \sum_{i=1,j=1}^{i=imax,j=jmax} mc_{i,j} + C_{11} \right)$$

D.1

where, $k_{d_{i,j}}$ is the PM cake layer permeability accounting for the damage in the PM cake during PM oxidation (passive oxidation and active regeneration),

---

[1] Parts of the material contained in this chapter are based on references [1, 2, 3] with permission of Springer.

$k_{p_{i,j}}$ is the PM cake layer permeability accounting for the changes in mean free path length of the gas at each zone, C_{10} is the slope of the post loading cake permeability equation, C_{11} is the constant for the post loading cake permeability equation and $mc_{i,j}$ is the mass of cake PM in each zone.

Figure D 2 shows the change in permeability during the post loading for the active regeneration experiments. In Fig. D 2, it can be seen that the permeability ratio changes are non-monotonic and non-linear indicating that the PM cake appears to exhibit a kind of "deep bed" filtration during the damage recovery with PM being primarily in the cracks at lower PM cake masses at the beginning of the post loading. For the SCR-F/CPF model, it was determined to use Eqn. D.1 for the passive oxidation and active regeneration experiments to calculate PM cake layer permeability during post loading. The post loading cake permeability calibration coefficients C_{10} and C_{11} were determined independently for passive oxidation and active regeneration experiments to minimize the overall pressure drop simulation error of all eighteen experiments during post loading.
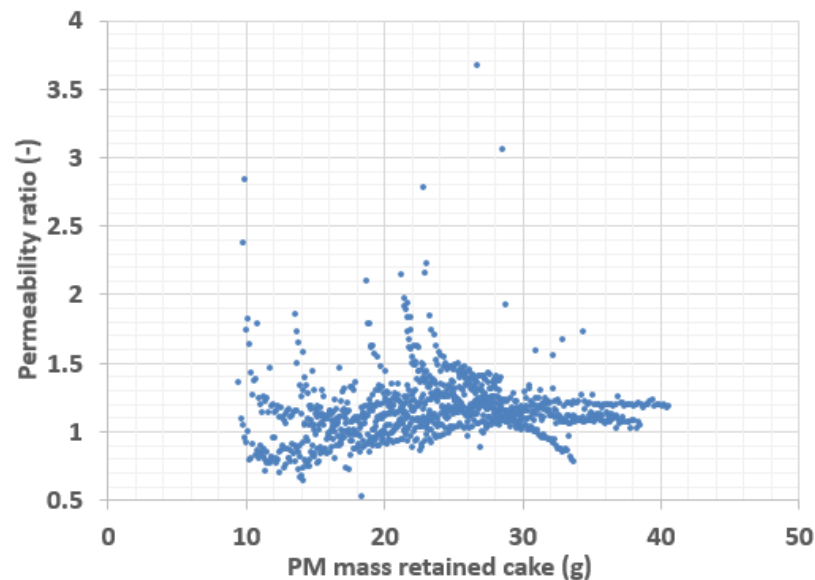
Figure D. 2 Relative change in permeability ratio during the post loading for the active regeneration experiments

Appendix E High Fidelity MPF Model Summary[1]

Table E. 1 Comparison of experimental and model average CPF outlet gas temperature 5 mins. before end of PO/AR phase

No	Expt.name	Average Filter Oulet Gas Temperature (ºC)		
		DNCPF [5 mins. before end of PO/AR)		
		Expt.	Model	Diff
1	PO-B10-14	250	251	1
2	PO-B10-15	354	356	2
3	PO-B10-16	411	414	4
4	PO-B10-17	354	356	2
5	PO-B20-12	349	351	3
6	PO-B20-13	406	410	4
7	AR-ULSD-1	577	580	4
8	AR-ULSD-2	598	612	14
9	AR-ULSD-4	538	544	5
10	AR-ULSD-5	536	541	4
11	AR-ULSD-6	551	555	4
12	AR-B10-1	538	545	7
13	AR-B10-2	538	543	6
14	AR-B10-4	571	574	4
15	AR-B20-1	480	482	2
16	AR-B20-2	514	517	3
17	AR-B20-5	541	546	4
18	AR-B20-6	552	556	4
RMS error			5	

Table E. 2 Comparison of experimental and model total filtration efficiency during stage 2 loading

No	Expt.name	Filtration Efficiency		
		Stage 2		
		Expt.	Model	Diff
1	PO-B10-14	97.0	97.1	0.1
2	PO-B10-15	96.6	97.1	0.5
3	PO-B10-16	96.6	97.1	0.5
4	PO-B10-17	96.6	97.1	0.5
5	PO-B20-12	96.6	97.1	0.5
6	PO-B20-13	97.0	97.1	0.1
7	AR-ULSD-1	97.2	97.2	0.0
8	AR-ULSD-2	97.9	97.1	-0.8
9	AR-ULSD-4	96.8	97.2	0.4
10	AR-ULSD-5	95.4	97.1	1.7
11	AR-ULSD-6	97.2	97.1	-0.1
12	AR-B10-1	97.5	97.1	-0.4
13	AR-B10-2	97.5	97.1	-0.4
14	AR-B10-4	96.5	97.2	0.7
15	AR-B20-1	97.3	97.1	-0.2
16	AR-B20-2	98.2	97.1	-1.1
17	AR-B20-5	97.1	97.1	0.0
18	AR-B20-6	93.5	97.1	3.6
RMS error			1.0	

---

[1] Parts of the material contained in this chapter are based on references [1, 2,3] with permission of Springer.

Table E. 3 Comparison of experimental and model PM mass retained at the end of stage 1, stage 2, stage 3 and stage 4 loading

No	Expt.name	PM retained [g]											
		Stage-1			Stage-2			Stage-3			Stage-4		
		Expt.	Model	Diff	Expt.	Model	Diff	Expt.	Model	Diff	Expt.	Model	Diff
1	PO-B10-14	4.3	2.7	-1.6	36.4	34.8	-1.6	42.8	41.4	-1.4	50.8	49.9	-0.9
2	PO-B10-15	4.6	3.0	-1.6	35.9	34.0	-1.9	27.0	26.7	-0.3	36.9	36.3	-0.6
3	PO-B10-16	4.3	2.7	-1.6	36.5	34.9	-1.6	26.0	28.5	2.5	35.1	37.5	2.4
4	PO-B10-17	4.6	3.0	-1.6	37.0	35.9	-1.1	29.8	28.7	-1.1	39.4	37.2	-2.2
5	PO-B20-12	3.6	2.3	-1.3	39.1	38.7	-0.4	28.9	30.1	1.2	37.1	37.6	0.5
6	PO-B20-13	4.0	2.5	-1.5	38.5	37.7	-0.8	27.2	27.7	0.5	36.1	36.0	-0.1
7	AR-ULSD-1	6.0	4.7	-1.3	44.3	41.4	-2.9	25.2	22.3	-2.9	38.4	35.8	-2.6
8	AR-ULSD-2	5.6	4.4	-1.2	44.0	41.9	-2.1	15.7	18.4	2.7	27.7	31.4	3.7
9	AR-ULSD-4	4.4	3.7	-0.7	43.5	42.8	-0.7	25.9	25.5	-0.4	35.9	34.6	-1.3
10	AR-ULSD-5	5.4	4.1	-1.3	41.1	40.3	-0.8	25.2	27.4	2.2	37.1	38.7	1.6
11	AR-ULSD-6	5.6	3.6	-2.0	41.9	39.5	-2.4	23.3	21.5	-1.8	35.8	33.2	-2.6
12	AR-B10-1	4.0	3.1	-0.9	43.2	42.9	-0.3	18.8	17.8	-1.0	27.9	28.1	0.2
13	AR-B10-2	3.7	2.9	-0.8	40.7	38.4	-2.3	18.2	18.8	0.6	27.4	29.4	2.0
14	AR-B10-4	4.0	3.4	-0.6	40.9	40.5	-0.4	18.8	17.6	-1.2	29.1	30.2	1.1
15	AR-B20-1	3.0	2.1	-0.9	37.5	35.5	-2.0	25.2	22.0	-3.2	33.0	31.2	-1.8
16	AR-B20-2	3.7	2.2	-1.5	37.9	36.7	-1.2	15.4	12.8	-2.6	23.0	21.7	-1.3
17	AR-B20-5	3.5	2.2	-1.3	36.9	35.8	-1.1	10.0	10.3	0.3	18.4	19.6	1.2
18	AR-B20-6	3.6	2.9	-0.7	39.9	40.4	0.5	14.1	13.1	-1.0	23.1	23.6	0.5
RMS error		1.3			1.5			1.8			1.8		

Table E. 4 Fractional PM mass oxidized during passive oxidation and active regeneration phases of all experiments

No	Expt.name	Temprature	NO$_2$-assisted	Thermal (O$_2$)
		(°C)	(-)	(-)
1	PO-B10-14	253	1.00	0.00
2	PO-B10-15	355	0.99	0.01
3	PO-B10-16	408	0.94	0.06
4	PO-B10-17	356	0.99	0.01
5	PO-B20-12	350	0.98	0.02
6	PO-B20-13	403	0.92	0.08
7	AR-ULSD-1	554	0.05	0.95
8	AR-ULSD-2	581	0.05	0.95
9	AR-ULSD-4	526	0.08	0.92
10	AR-ULSD-5	524	0.07	0.93
11	AR-ULSD-6	532	0.05	0.95
12	AR-B10-1	530	0.11	0.89
13	AR-B10-2	528	0.14	0.86
14	AR-B10-4	554	0.08	0.92
15	AR-B20-1	476	0.34	0.66
16	AR-B20-2	503	0.14	0.86
17	AR-B20-5	528	0.12	0.88
18	AR-B20-6	531	0.13	0.87

Table E. 5 Comparison of experimental and model pressure drop during end of stage 2 loading, PO/AR phase and stage 4 loading phase of the experiment

No	Expt.name	Pressure Drop (kPa)								
		End of Stage-2 Loading (5 mins, before end of stage 1)			End-of-PO/AR (5 mins before end of PO/AR)			End-of-post-loading (5 mins before end of stage 4)		
		Expt.	Model	Diff	Expt.	Model	Diff	Expt.	Model	Diff
1	PO-B10-14	5.8	5.7	-0.1	2.4	2.5	0.1	6.5	6.6	0.1
2	PO-B10-15	5.9	5.7	-0.2	2.3	2.5	0.2	4.5	4.6	0.0
3	PO-B10-16	5.8	5.6	-0.2	6.1	6.2	0.1	4.4	4.6	0.2
4	PO-B10-17	5.9	5.8	-0.1	2.6	2.6	0.0	4.0	3.9	0.0
5	PO-B20-12	5.9	5.9	0.0	2.5	2.5	0.0	4.5	4.6	0.1
6	PO-B20-13	5.9	5.8	-0.1	5.9	5.5	-0.4	4.3	4.5	0.1
7	AR-ULSD-1	6.0	5.9	0.0	4.2	3.8	-0.4	5.1	5.1	-0.1
8	AR-ULSD-2	6.0	5.8	-0.1	5.8	5.5	-0.3	4.5	4.5	0.0
9	AR-ULSD-4	6.0	5.9	-0.1	3.5	3.4	-0.1	3.8	3.8	0.1
10	AR-ULSD-5	5.9	5.9	-0.1	3.7	3.3	-0.3	4.9	5.0	0.1
11	AR-ULSD-6	6.1	6.0	-0.2	3.8	3.3	-0.5	4.7	4.5	-0.3
12	AR-B10-1	6.1	6.1	0.0	3.5	3.3	-0.2	4.4	4.3	0.0
13	AR-B10-2	5.9	5.8	-0.1	3.6	3.6	0.0	4.4	4.4	0.0
14	AR-B10-4	6.0	5.8	-0.2	4.2	4.1	-0.1	4.6	4.5	-0.1
15	AR-B20-1	5.3	5.8	0.5	3.3	2.9	-0.4	4.8	4.5	-0.2
16	AR-B20-2	6.0	5.8	-0.2	3.2	3.1	-0.1	4.3	3.9	-0.3
17	AR-B20-5	5.8	5.7	-0.1	3.2	3.3	0.1	4.1	3.8	-0.3
18	AR-B20-6	6.0	6.0	0.0	3.8	3.7	0.0	4.4	4.0	-0.3
RMS error		0.2			0.2			0.2		

Table E. 6 Comparison of experimental and model NO$_2$ concentration values

No	Expt.name	Stage 2 Loading				PO/AR				Stage 4 Loading			
		UPCPF	DNCPF			UPCPF	DNCPF			UPCPF	DNCPF		
		Expt.	Expt.	Model	Diff	Expt.	Expt.	Model	Diff	Expt.	Expt.	Model	Diff
1	PO-B10-14	25	44.0	49.5	5.5	112.0	142.0	179.1	37.1	28.0	48.0	53.5	5.5
2	PO-B10-15	27	48.0	50.1	2.1	101.0	113.0	111.4	-1.6	22.0	45.0	46.5	1.5
3	PO-B10-16	23	42.0	47.5	5.5	61.0	84.0	65.3	-18.7	23.0	48.0	47.8	-0.2
4	PO-B10-17	22	46.0	45.7	-0.3	90.0	109.0	104.3	-4.7	9.0	25.0	39.6	14.6
5	PO-B20-12	25	43.0	49.7	6.7	90.0	112.0	108.2	-3.8	28.0	46.0	53.3	7.3
6	PO-B20-13	17	36.0	42.6	6.6	64.0	92.0	68.8	-23.2	24.0	49.0	48.8	-0.2
7	AR-ULSD-1	20	36.0	45.2	9.2	4.0	11.0	11.3	0.3	17.0	41.0	42.4	1.4
8	AR-ULSD-2	31	48.0	57.4	9.4	7.0	19.0	4.6	-14.4	26.0	50.0	56.8	6.8
9	AR-ULSD-4	27	48.0	54.8	6.8	8.0	23.0	21.2	-1.8	29.0	54.0	64.4	10.4
10	AR-ULSD-5	29	49.0	54.3	5.3	6.0	30.0	24.4	-5.6	31.0	56.0	52.2	-3.8
11	AR-ULSD-6	26	45.0	51.0	6.0	4.0	32.0	24.1	-7.9	25.0	50.0	50.8	0.8
12	AR-B10-1	25	46.0	49.7	3.7	4.0	29.0	25.9	-3.1	27.0	49.0	51.0	2.0
13	AR-B10-2	25	42.0	50.1	8.1	7.0	16.0	23.3	7.3	26.0	50.0	50.0	0.0
14	AR-B10-4	26	45.0	40.8	-4.2	3.0	10.0	10.7	0.7	26.0	52.0	35.1	-16.9
15	AR-B20-1	30	43.0	53.8	10.8	10.0	47.0	34.7	-12.3	33.0	59.0	57.3	-1.7
16	AR-B20-2	25	48.0	49.7	1.7	4.0	36.0	33.6	-2.4	30.0	55.0	52.1	-2.9
17	AR-B20-5	25	44.0	50.6	6.6	7.0	32.0	30.7	-1.3	27.0	54.0	51.0	-3.0
18	AR-B20-6	23	42.0	47.2	5.2	10.0	17.0	20.6	3.6	24.0	45.0	47.6	2.6
RMS error			6.3				12.6				6.6		

Appendix F Temperature Distribution and Pressure Drop Plots
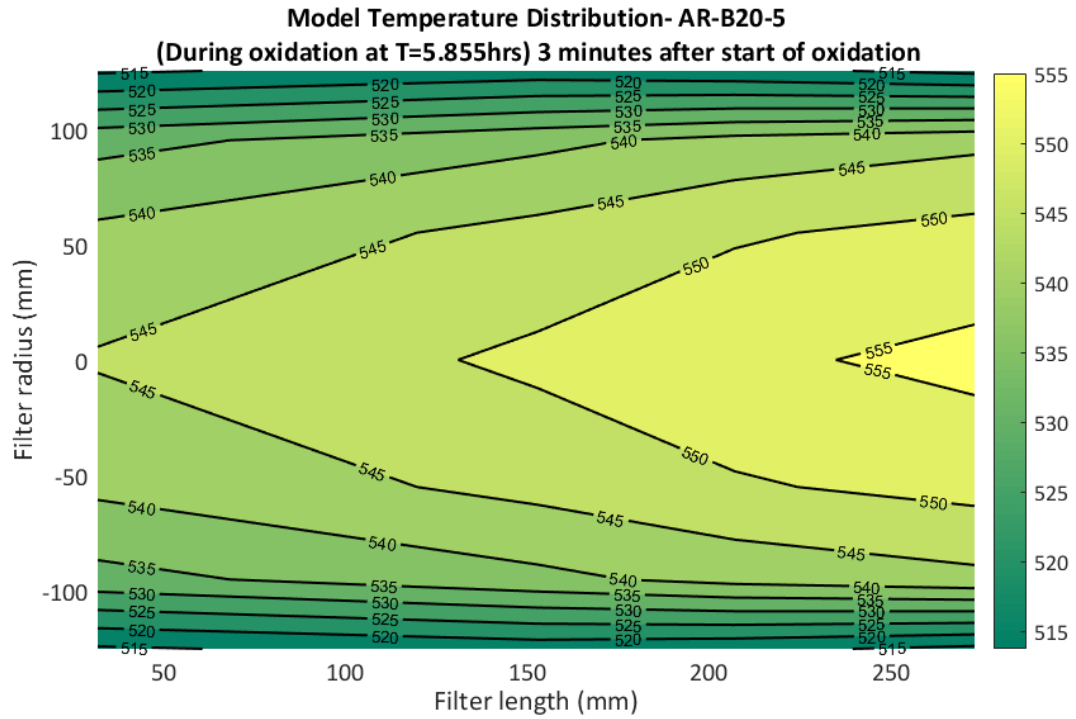
F.1 Temperature Distribution Plots
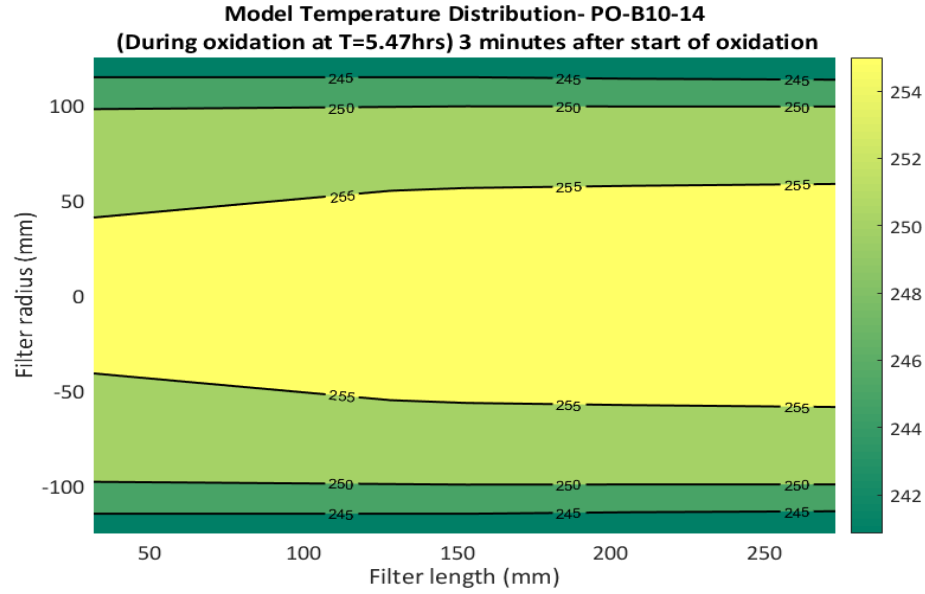
Figure F. 1 High-fidelity SCR-F/CPF model simulated temperature distribution for PO-B10-14 experiment at 5.47 hrs (3 minutes after start of oxidtion)
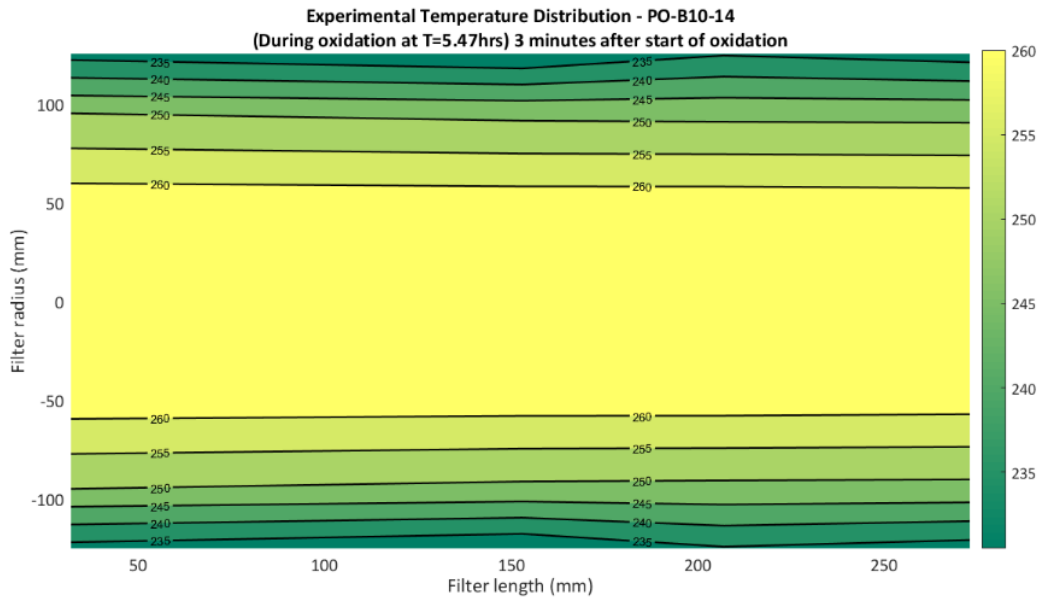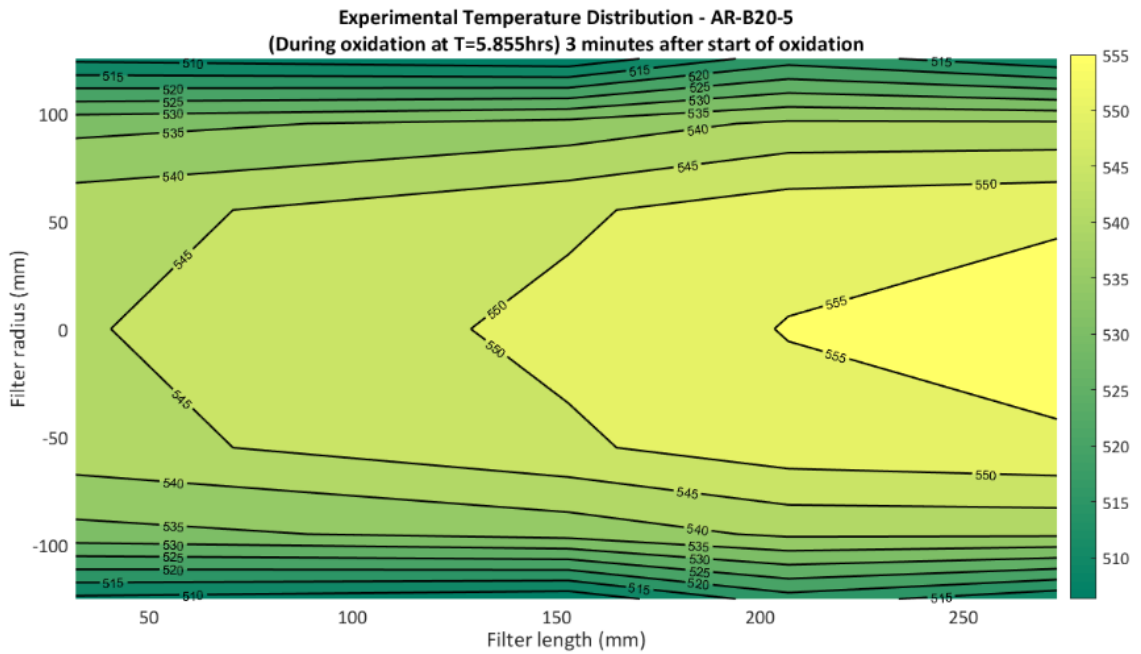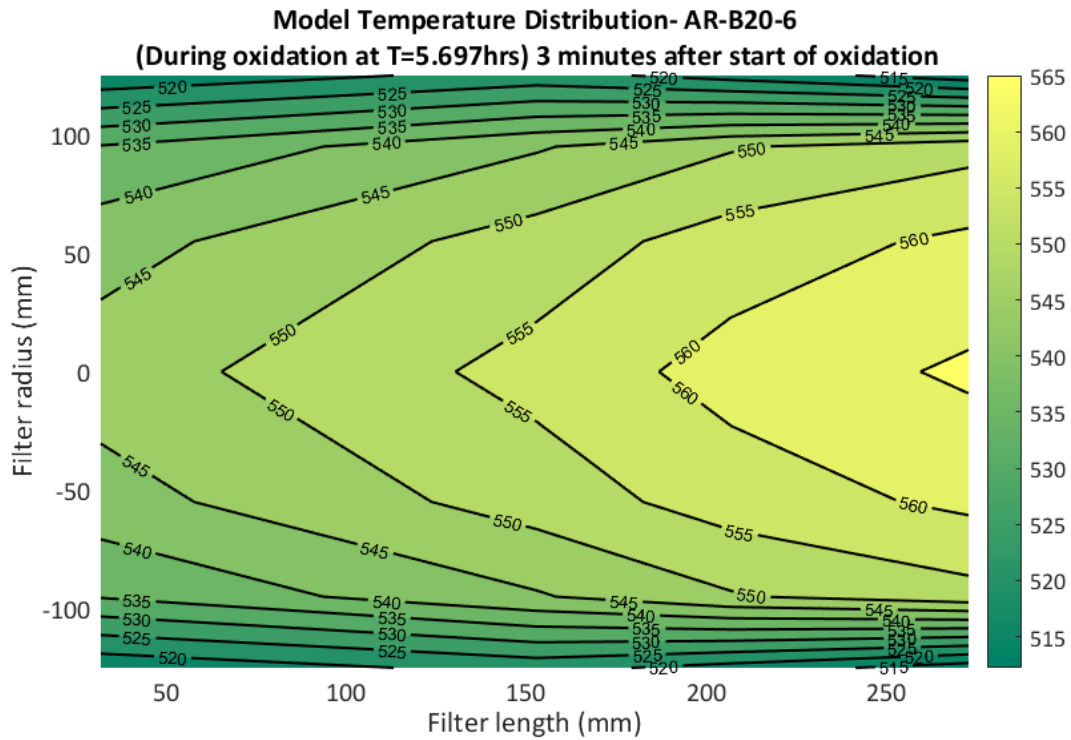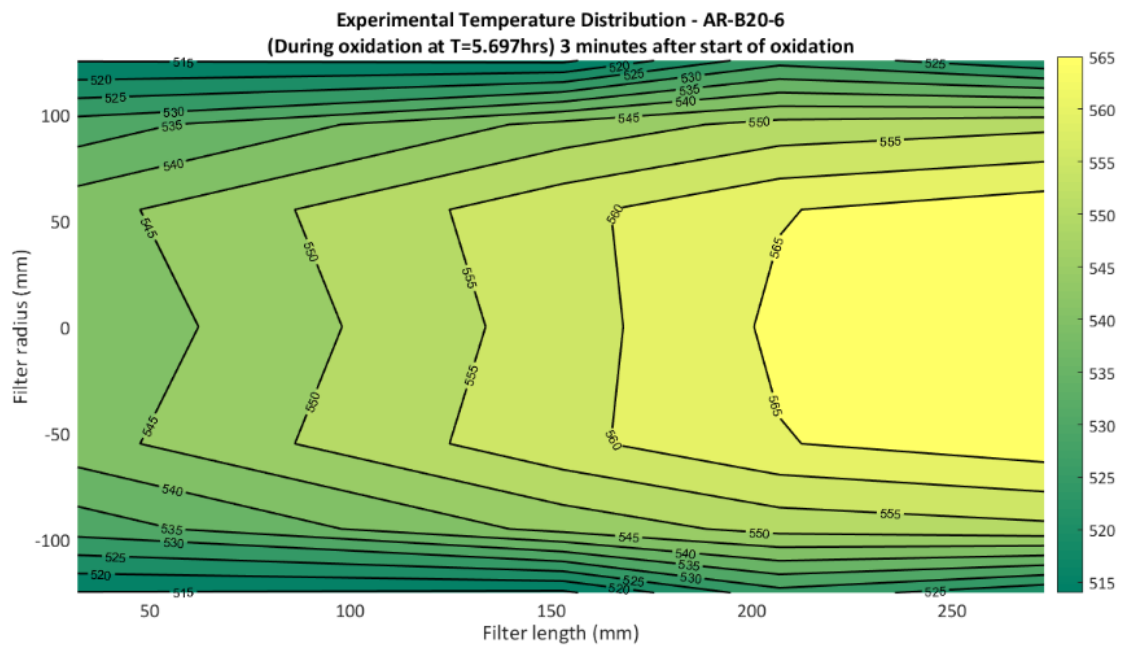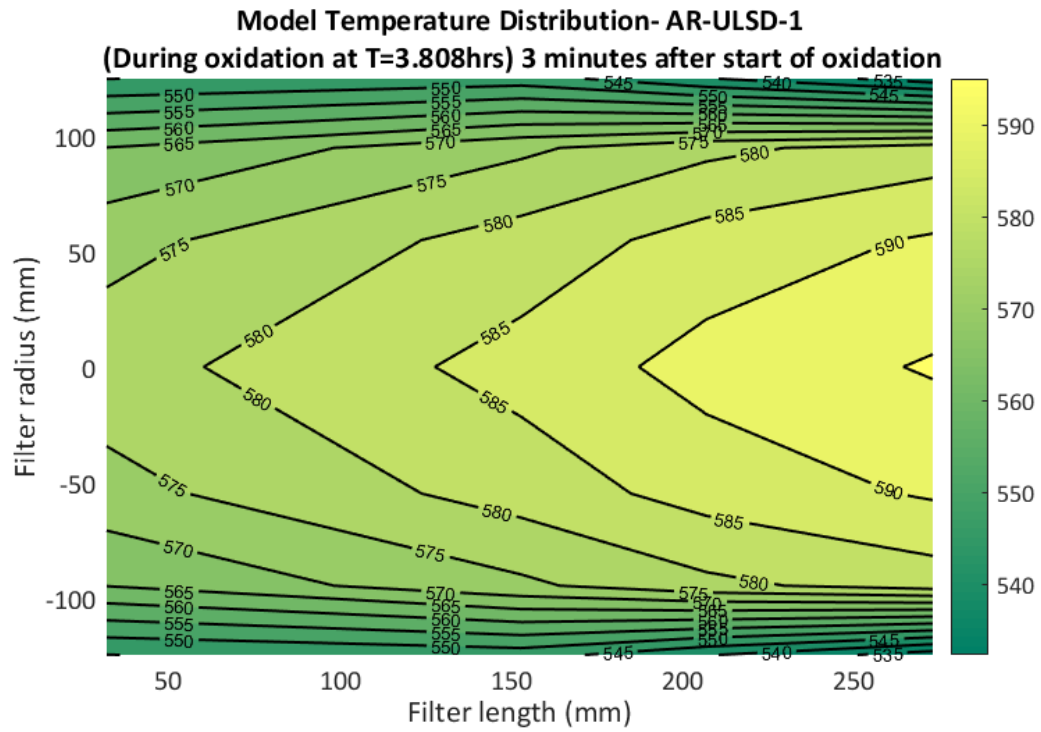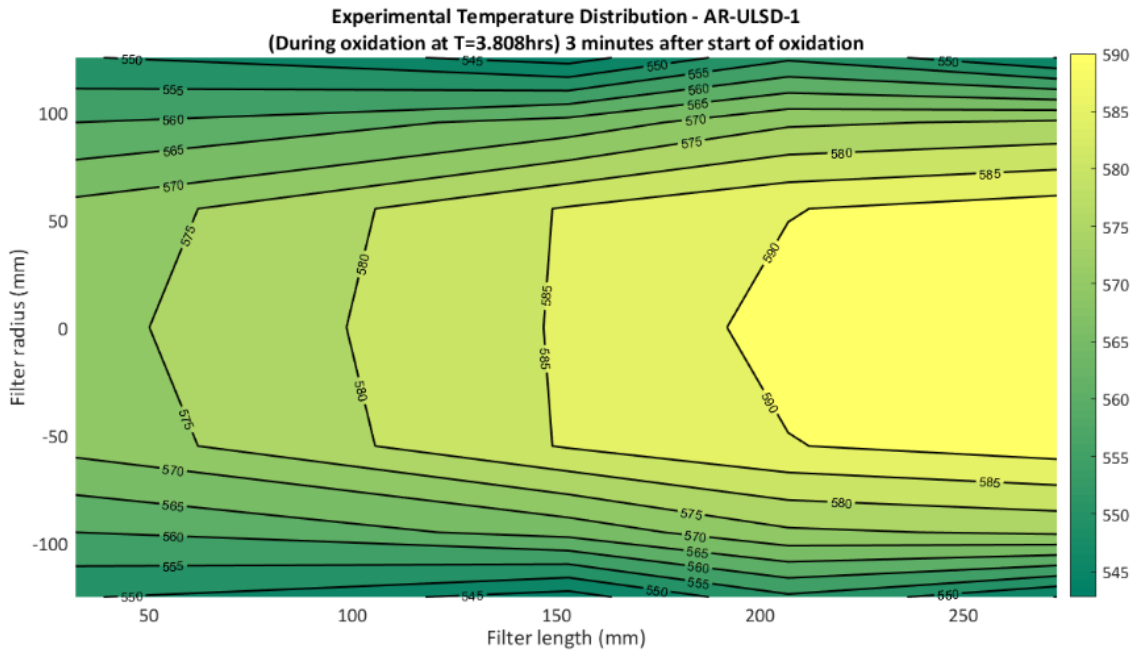

Figure F. 2 Experimental temperature distribution for PO-B10-14 experiment at 5.47 hrs (3 minutes after start of oxidation)
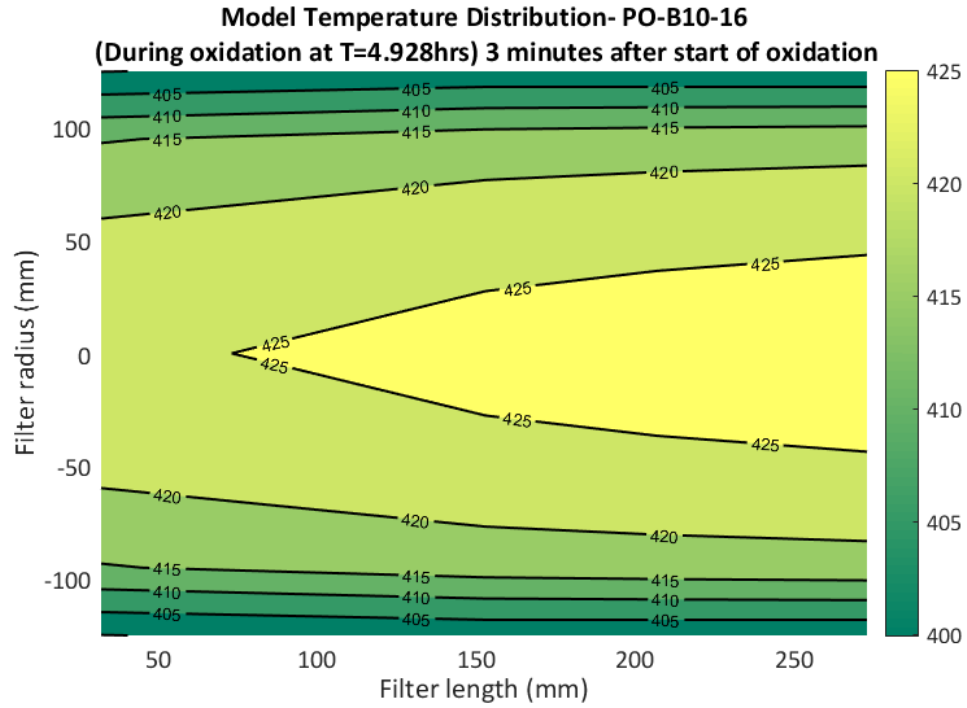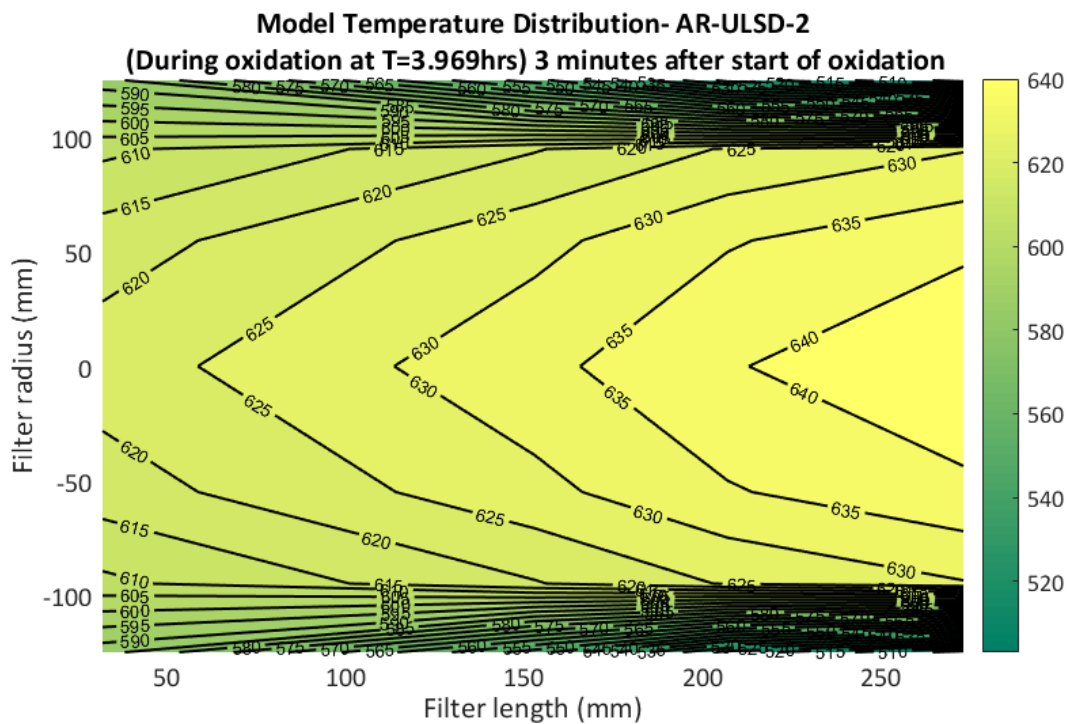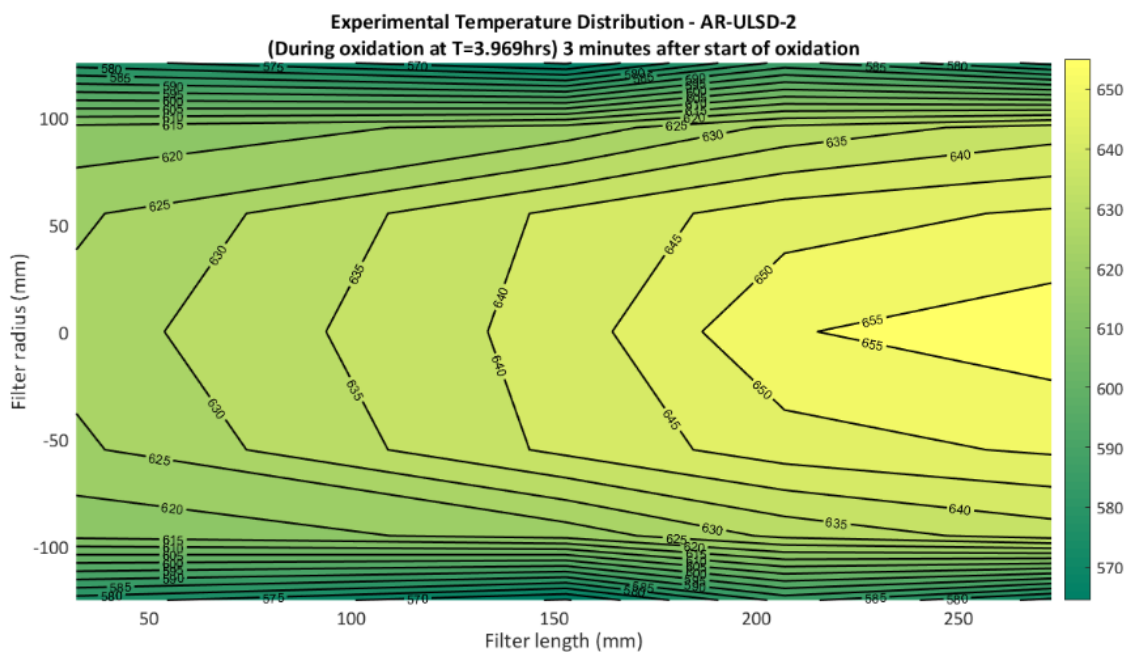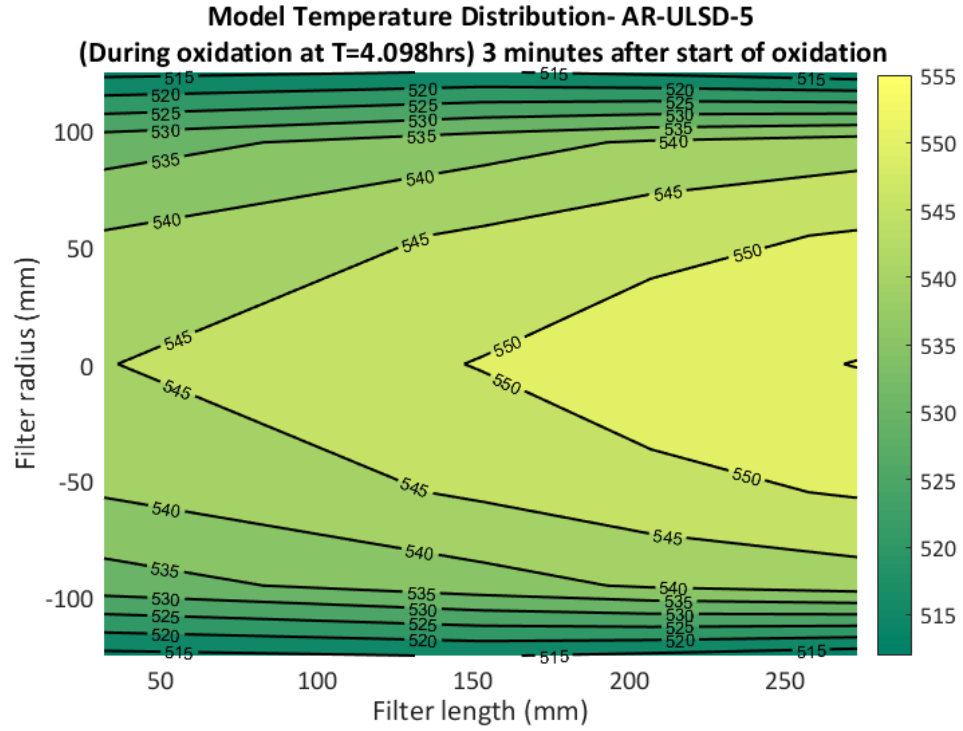
Figure F. 3 High-fidelity SCR-F/CPF model simulated temperature distribution for PO-B10-16 experiment at 4.93 hrs (3 minutes after start of oxidation)
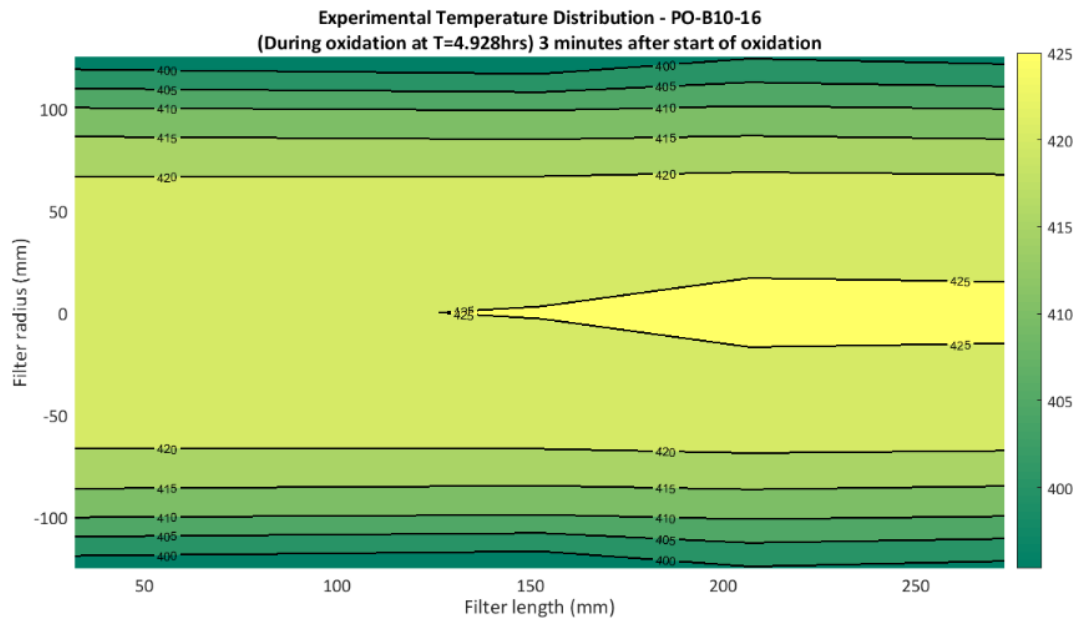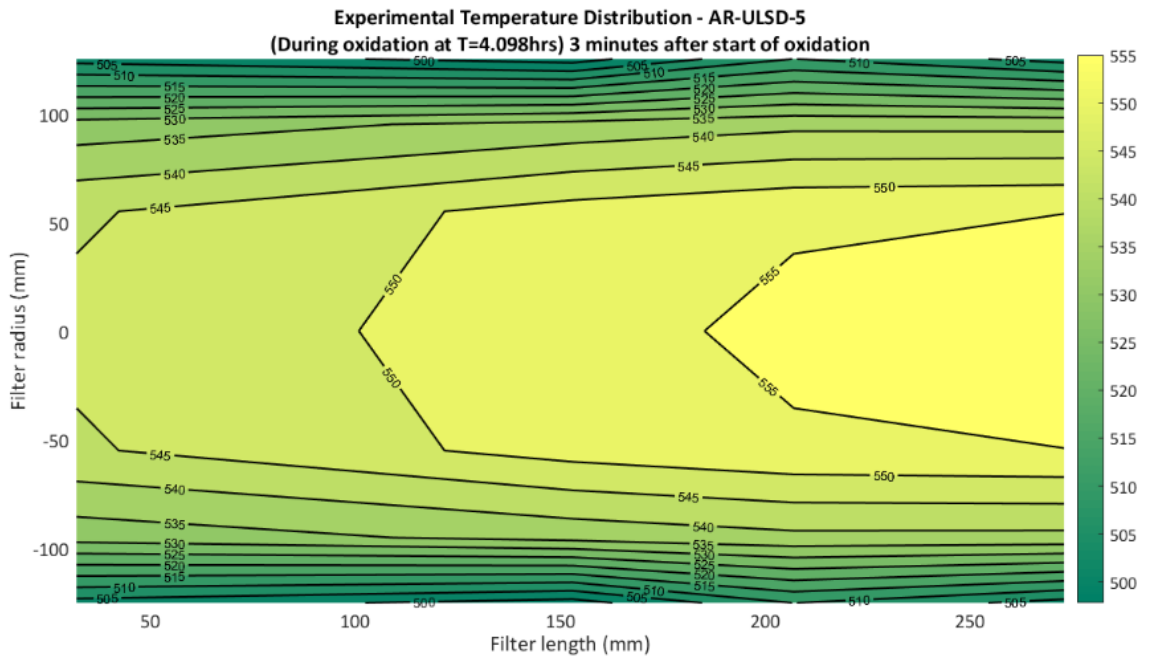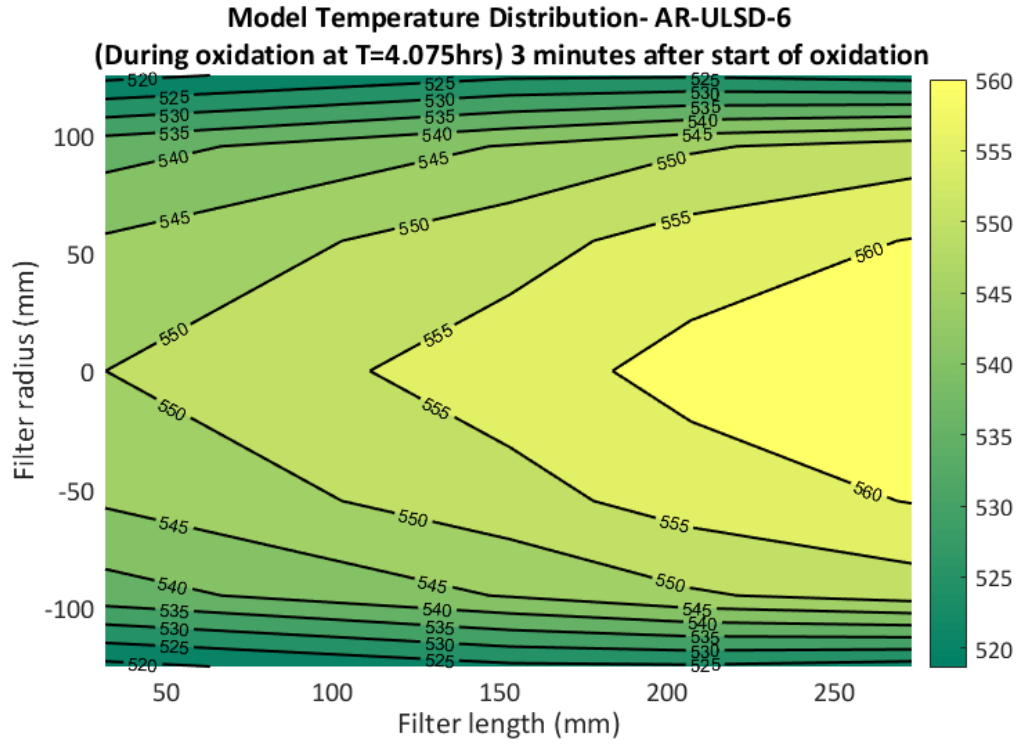

Figure F. 4 Experimental temperature distribution for PO-B10-16 experiment at 4.93 hrs (3 minutes after start of oxidation)

207
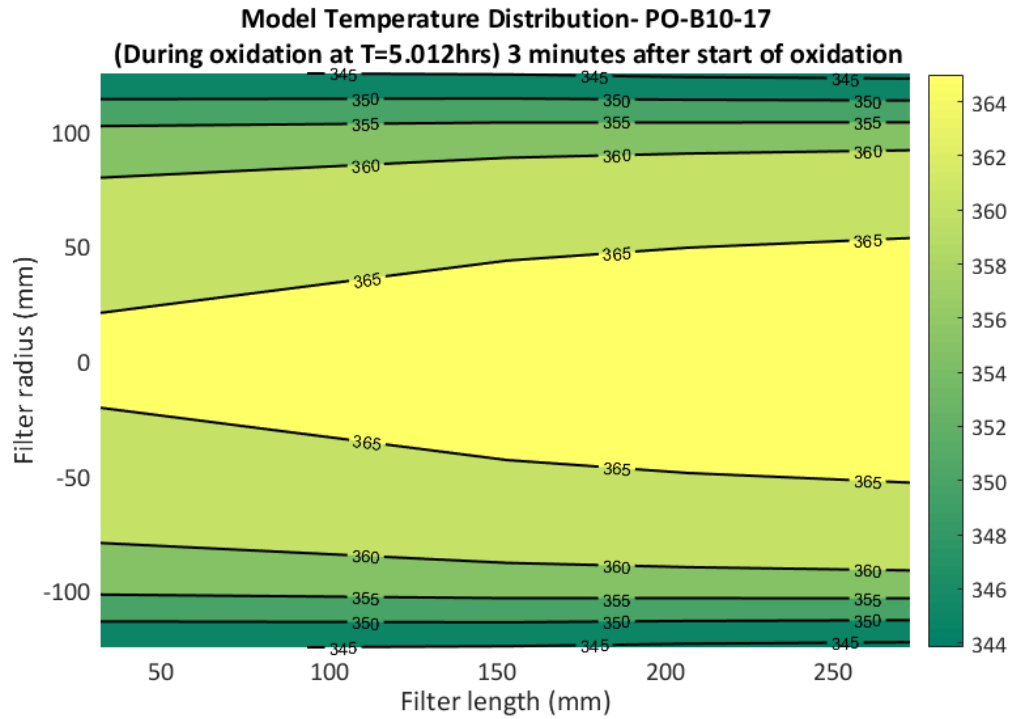
Figure F. 5 High-fidelity SCR-F/CPF model simulated temperature distribution for PO-B10-17 experiment at 5.01 hrs (3 minutes after start of oxidation)
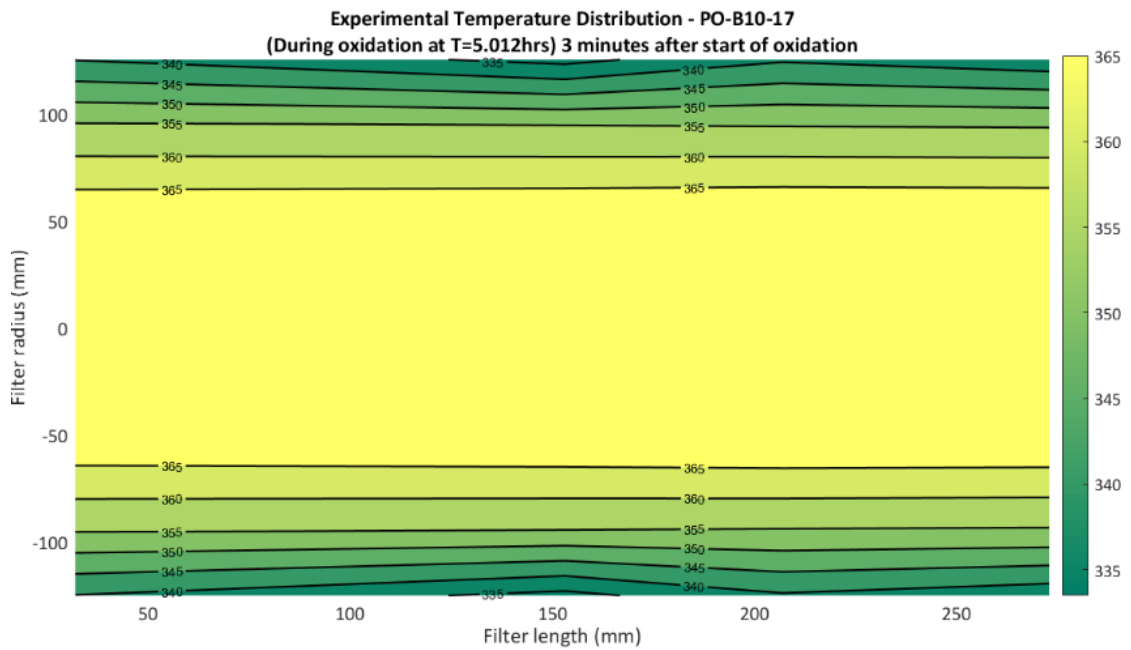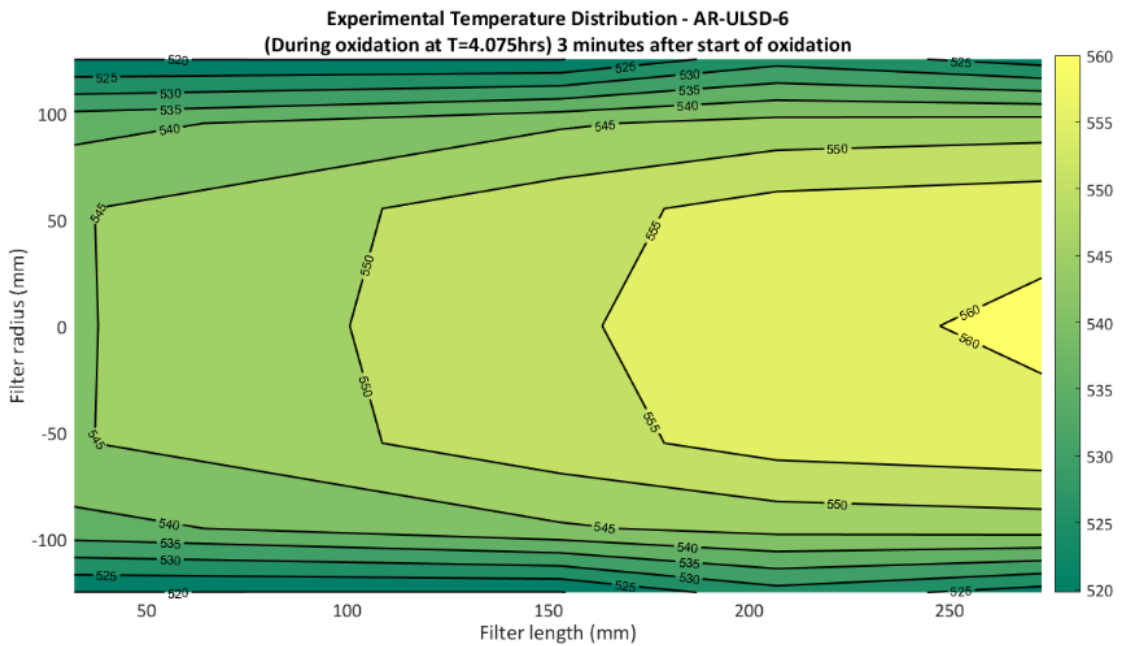

Figure F. 6 Experimental temperature distribution for PO-B10-17 experiment at 5.01 hrs (3 minutes after start of oxidation)

208
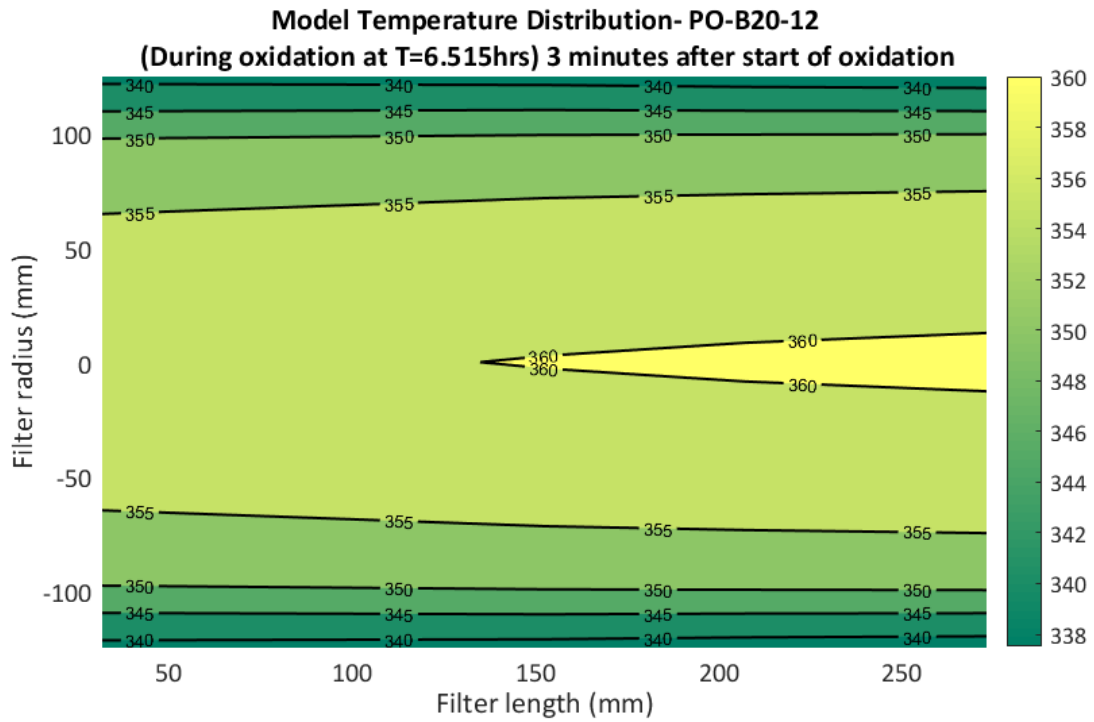
Figure F. 7 High-fidelity SCR-F/CPF model simulated temperature distribution for PO-B20-12 experiment at 6.52 hrs (3 minutes after start of oxidation)
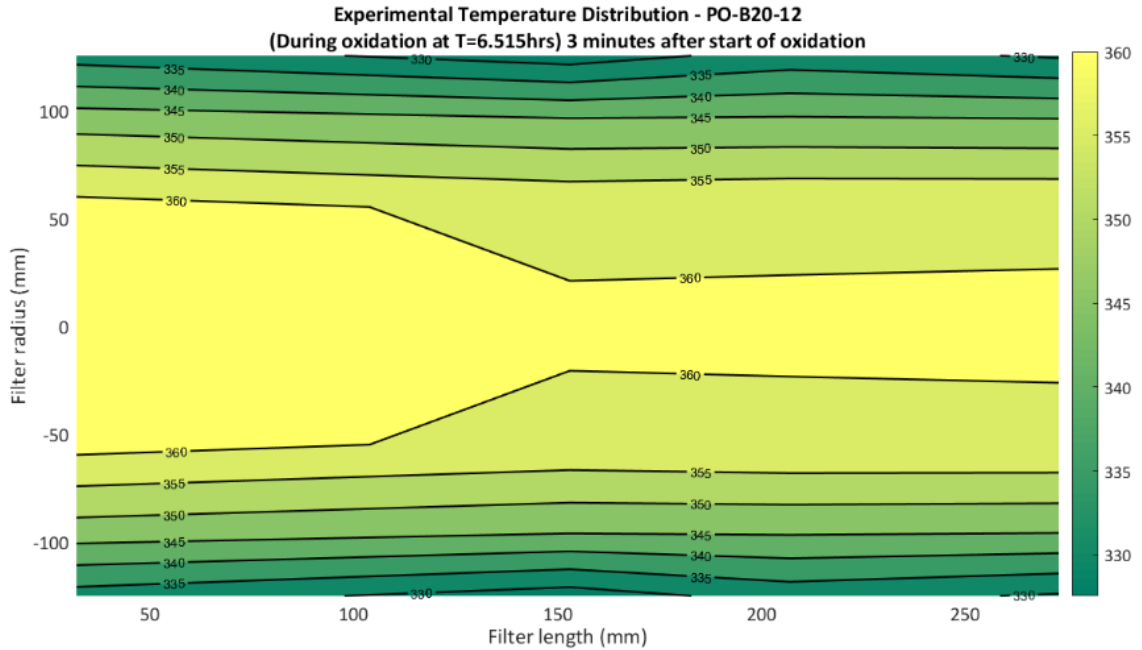
Figure F. 8 Experimental temperature distribution for PO-B20-12 experiment at 6.52 hrs (3 minutes after start of oxidation)
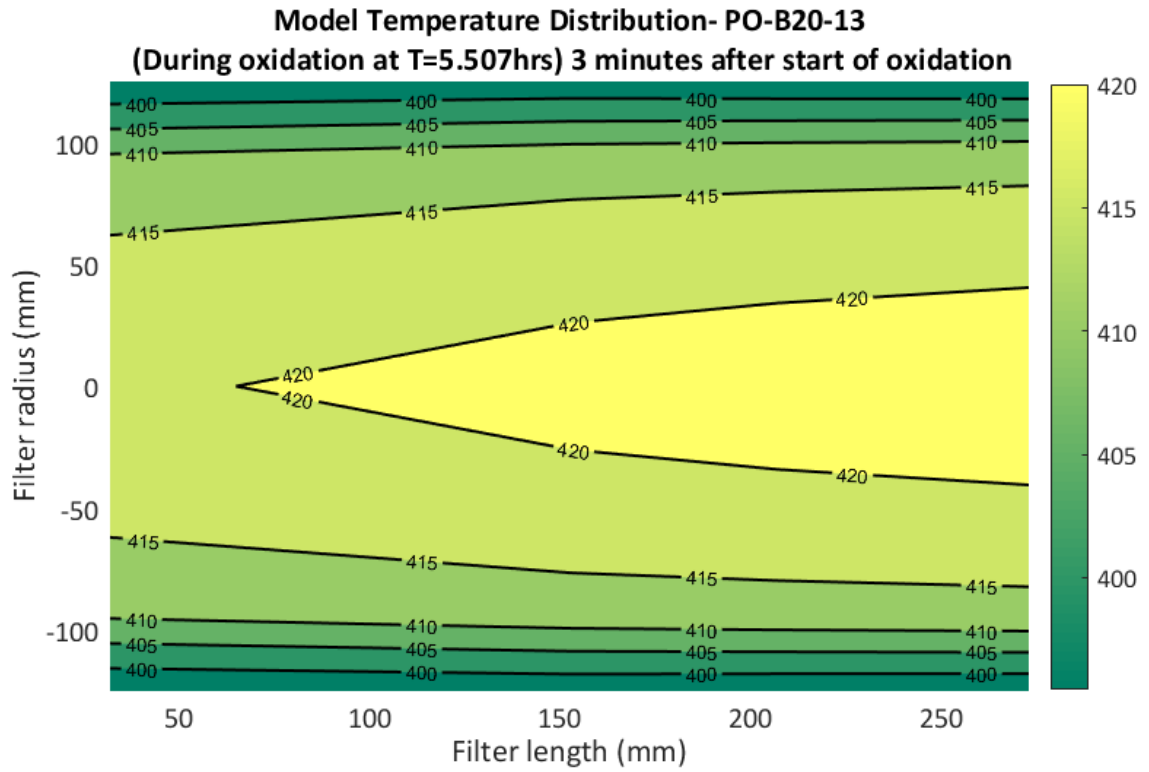
Figure F. 9 High-fidelity SCR-F/CPF model simulated temperature distribution for PO-B20-13 experiment at 5.51 hrs (3 minutes after start of oxidation)
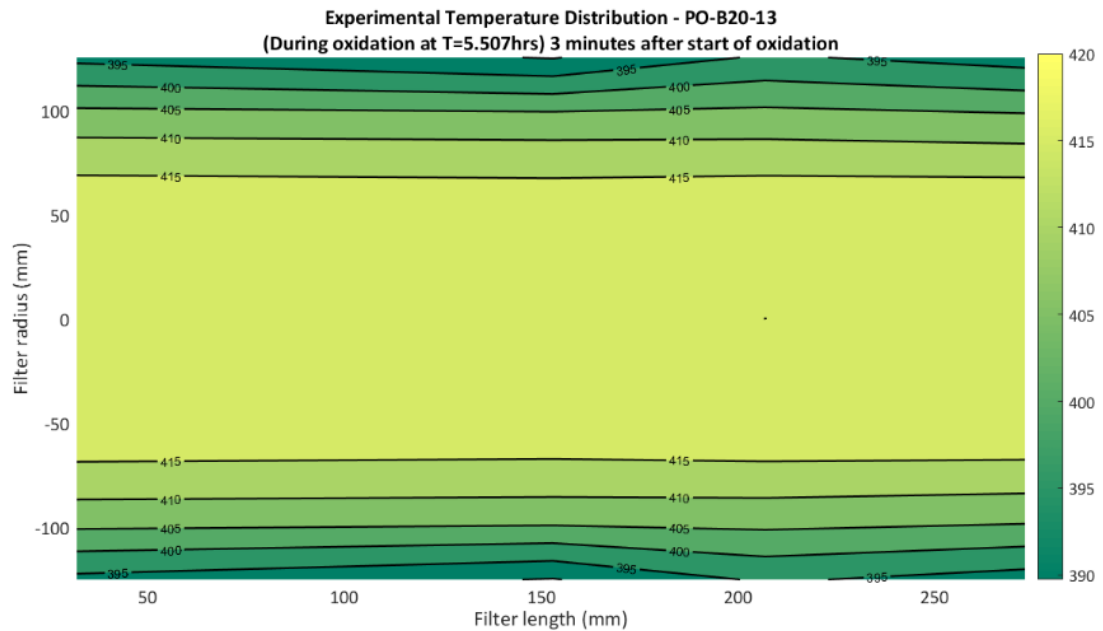
Figure F. 10 Experimental temperature distribution for PO-B20-13 experiment at 5.51 hrs (3 minutes after start of oxidation)
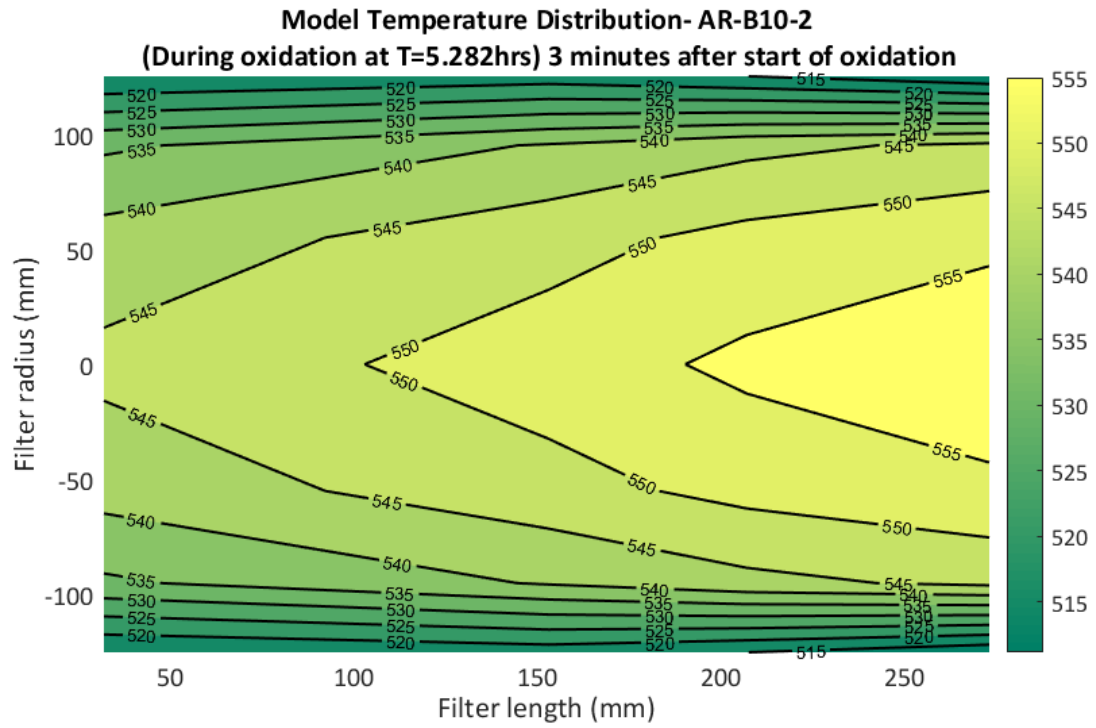
Figure F. 11 High-fidelity SCR-F/CPF model simulated temperature distribution for AR-B10-2 experiment at 5.28 hrs (3 minutes after start of oxidation)
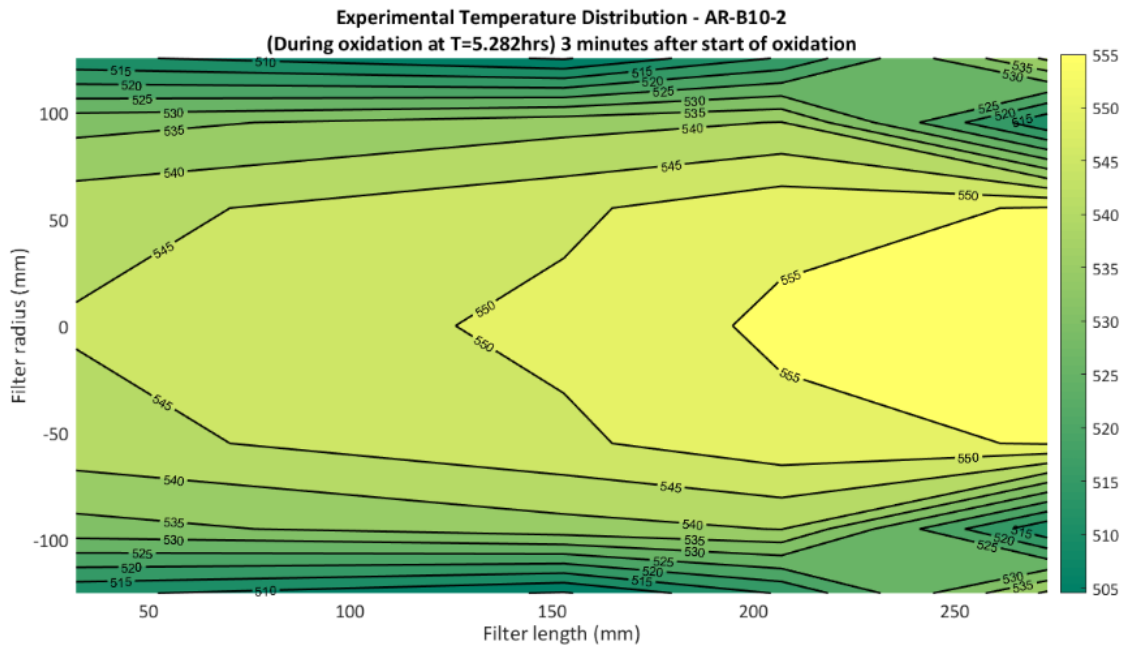
Figure F. 12 Experimental temperature distribution for AR-B10-2 experiment at 5.28 hrs (3 minutes after start of oxidation)
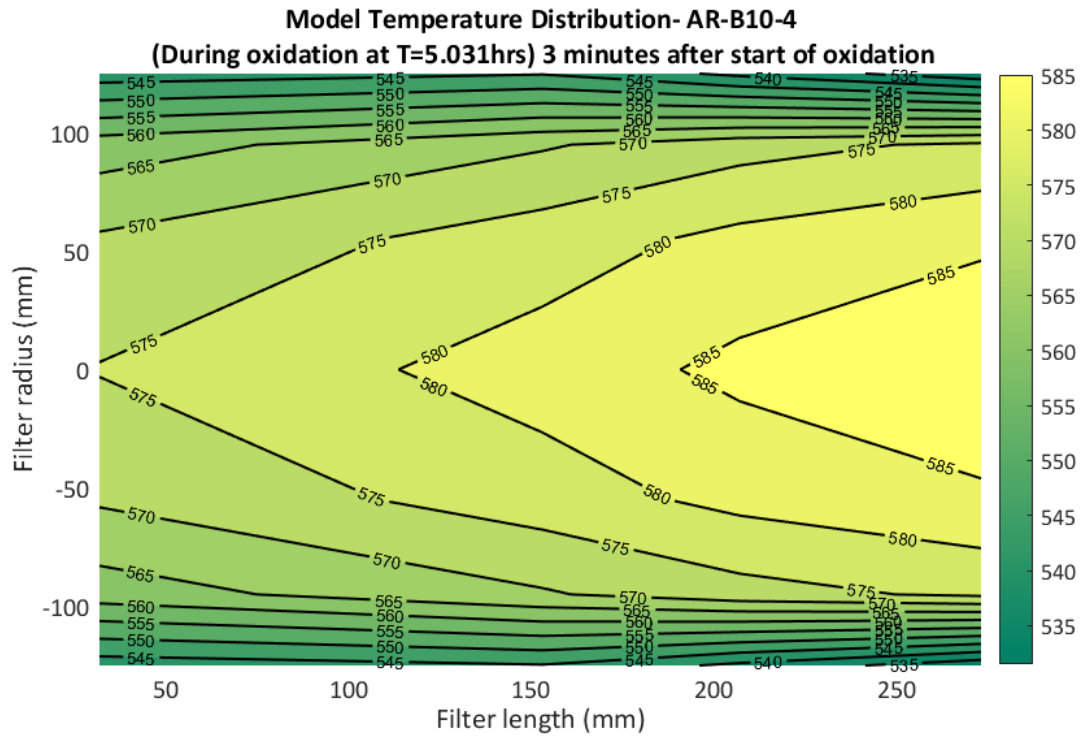
Figure F. 13 High-fidelity SCR-F/CPF model simulated temperature distribution for AR-B10-4 experiment at 5.03 hrs (3 minutes after start of oxidation)
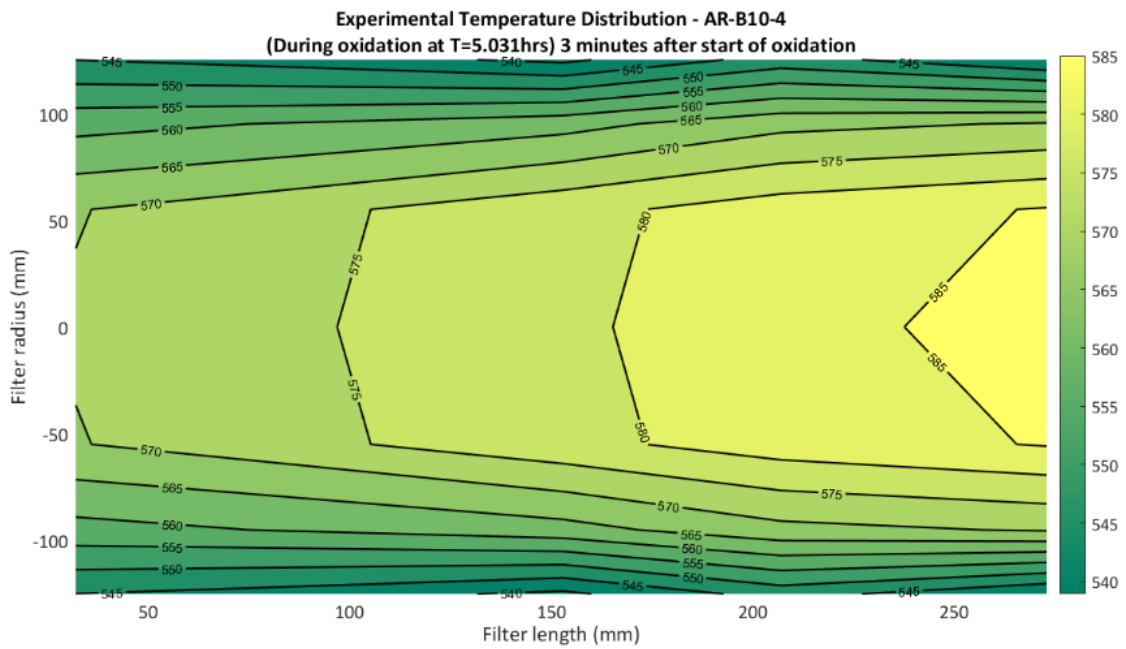
Figure F. 14 Experimental temperature distribution for AR-B10-4 experiment at 5.03 hrs (3 minutes after start of oxidation)

212
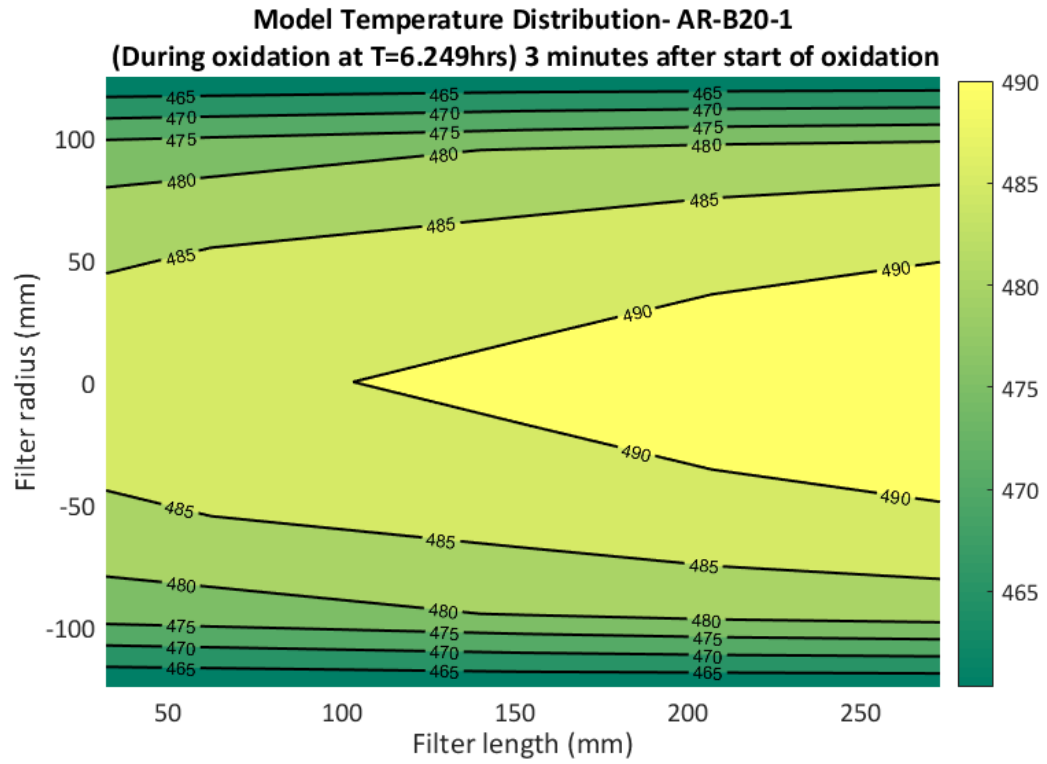
Figure F. 15 High-fidelity SCR-F/CPF model simulated temperature distribution for AR-B20-1 experiment at 6.25 hrs (3 minutes after start of oxidation)
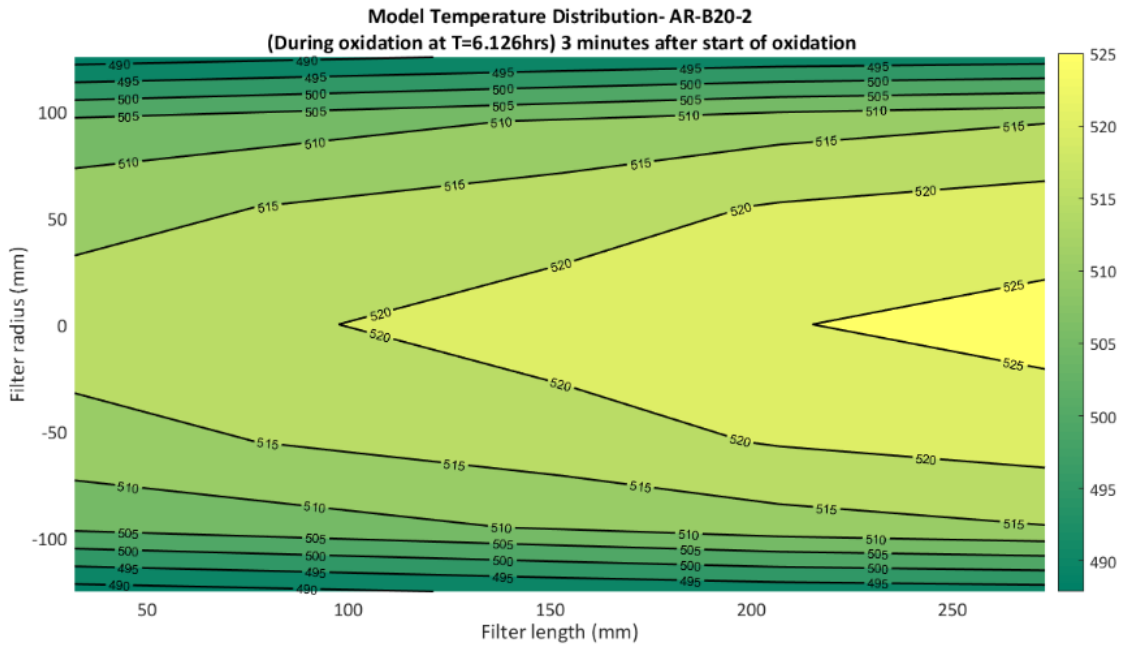
Figure F. 16 High-fidelity SCR-F/CPF model simulated temperature distribution for AR-B20-2 experiment at 6.13 hrs (3 minutes after start of oxidation)

213

Figure F. 17 High-fidelity SCR-F/CPF model simulated temperature distribution for AR-B20-5 experiment at 5.86 hrs (3 minutes after start of oxidation)

Figure F. 18 Experimental temperature distribution for AR-B20-5 experiment at 5.86 hrs (3 minutes after start of oxidation)

214

Figure F. 19 High-fidelity SCR-F/CPF model simulated temperature distribution for AR-B20-6 experiment at 5.70 hrs (3 minutes after start of oxidation)

Figure F. 20 Experimental temperature distribution for AR-B20-6 experiment at 5.70 hrs (3 minutes after start of oxidation)

Figure F. 21 High-fidelity SCR-F/CPF model simulated temperature distribution for PO-B20-13 experiment at 5.51 hrs (3 minutes after start of oxidation)

Figure F. 22 Experimental temperature distribution for PO-B20-13 experiment at 5.51 hrs (3 minutes after start of oxidation)

216

Figure F. 23 High-fidelity SCR-F/CPF model simulated temperature distribution for PO-B20-13 experiment at 5.51 hrs (3 minutes after start of oxidation)

Figure F. 24 Experimental temperature distribution for PO-B20-13 experiment at 5.51 hrs (3 minutes after start of oxidation)

Figure F. 25 High-fidelity SCR-F/CPF model simulated temperature distribution for AR-ULSD-5 experiment at 4.10 hrs (3 minutes after start of oxidation)

Figure F. 26 Experimental temperature distribution for AR-ULSD-5 experiment at 4.10 hrs (3 minutes after start of oxidation)

Figure F. 27 High-fidelity SCR-F/CPF model simulated temperature distribution for AR-ULSD-6 experiment at 4.08 hrs (3 minutes after start of oxidation)

Figure F. 28 Experimental temperature distribution for AR-ULSD-6 experiment at 4.08 hrs (3 minutes after start of oxidation)
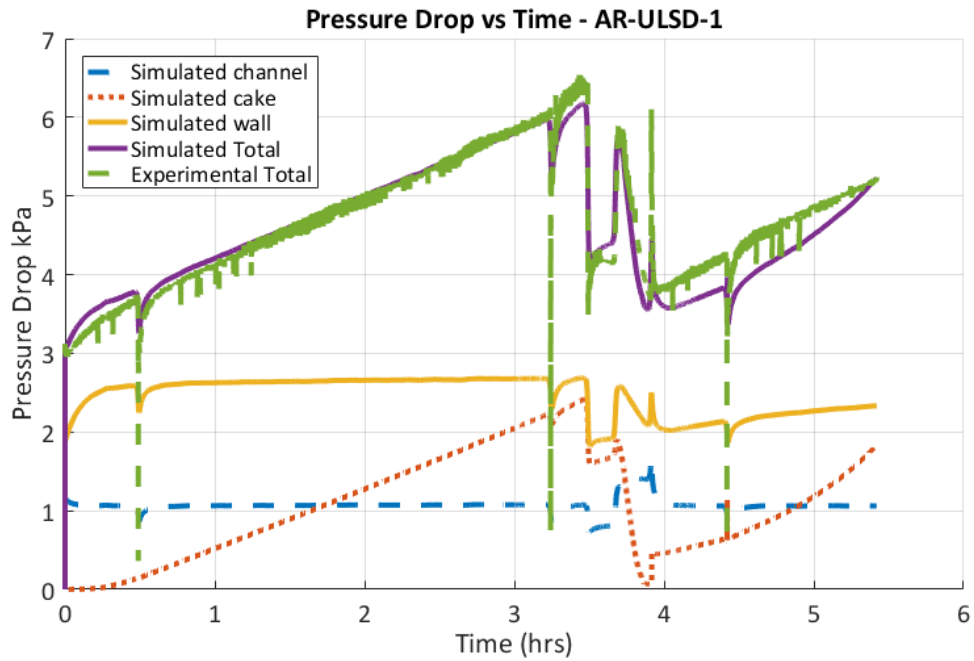
219

F.2 Pressure Drop Plots
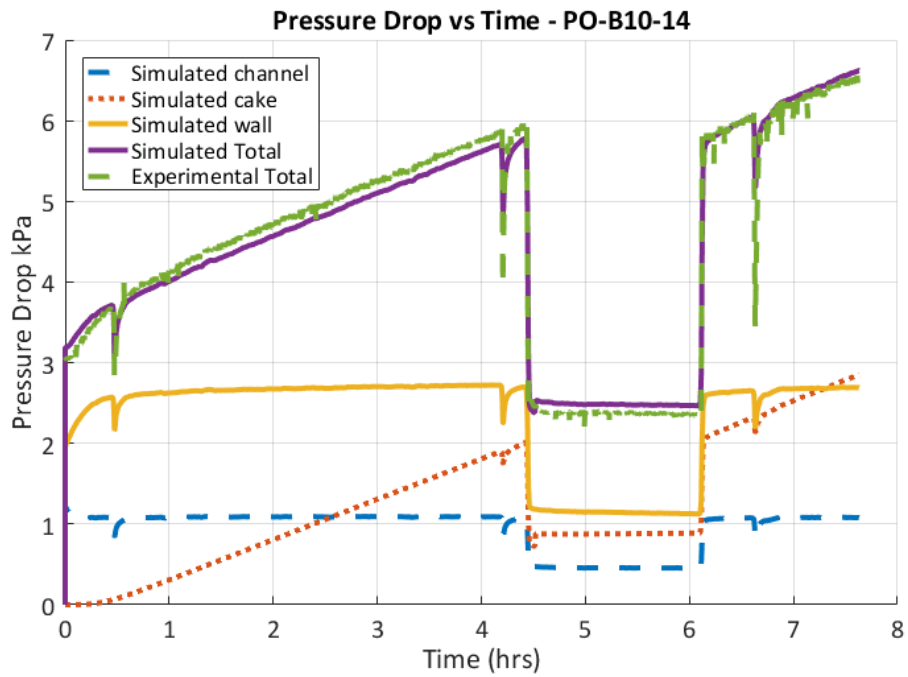
Figure F. 29 Comparison of experimental and simulated total pressure drop across CPF and its components for PO-B10-14 experiment
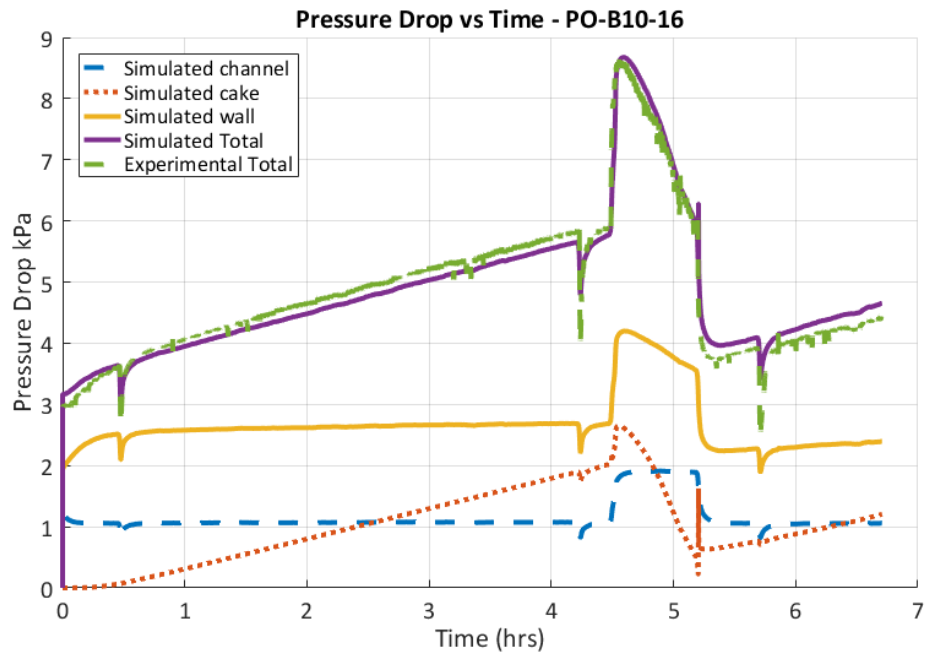
Figure F. 30 Comparison of experimental and simulated total pressure drop across CPF and its components for PO-B10-16 experiment
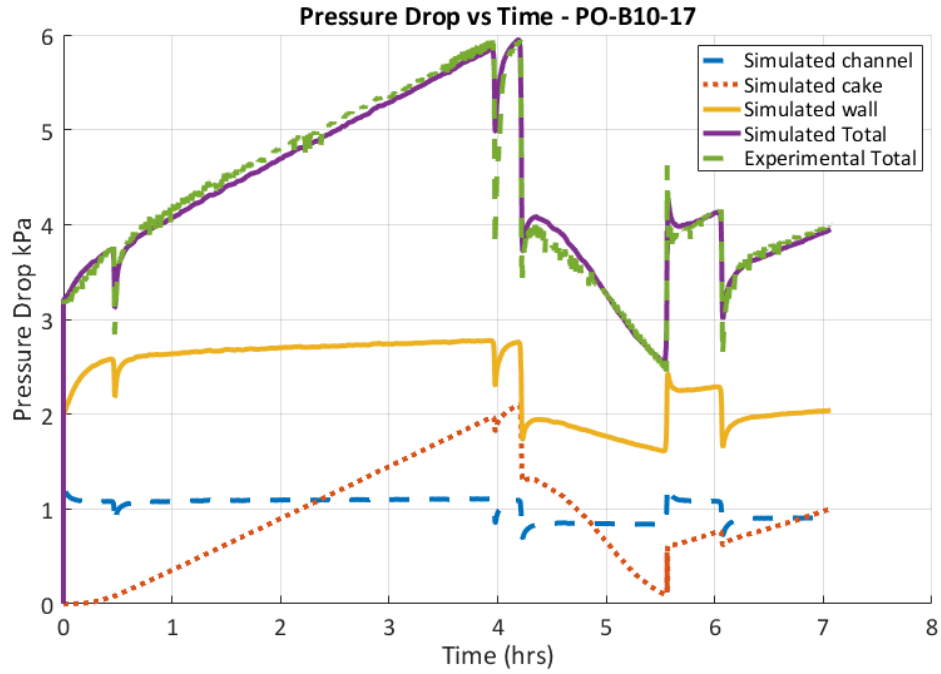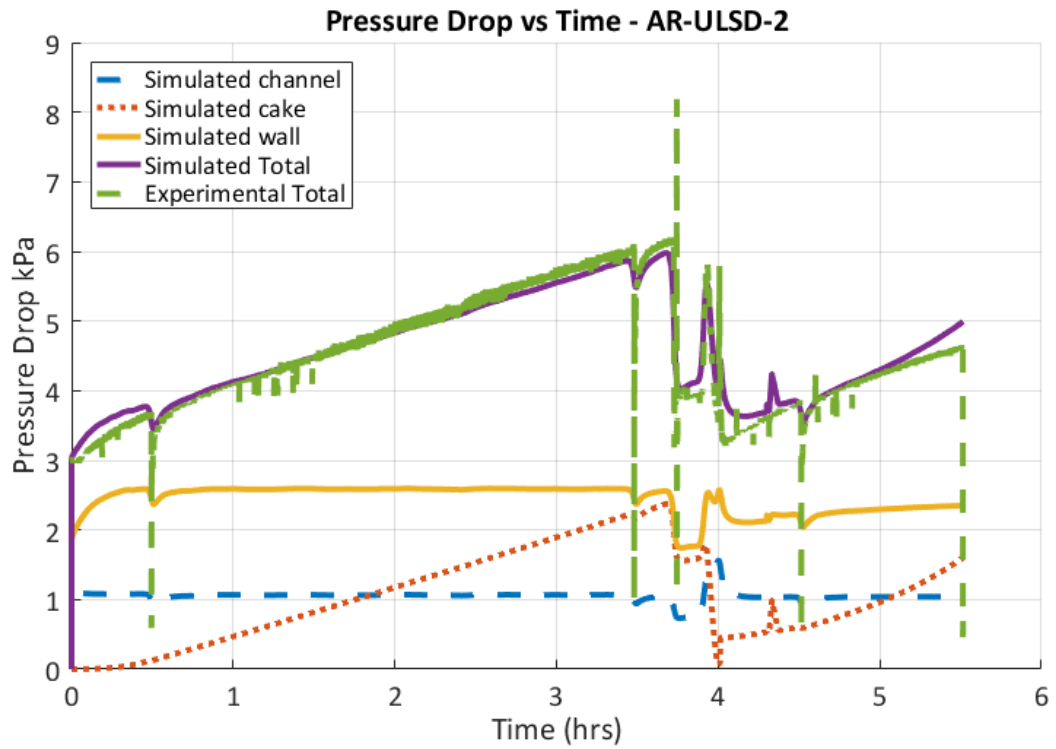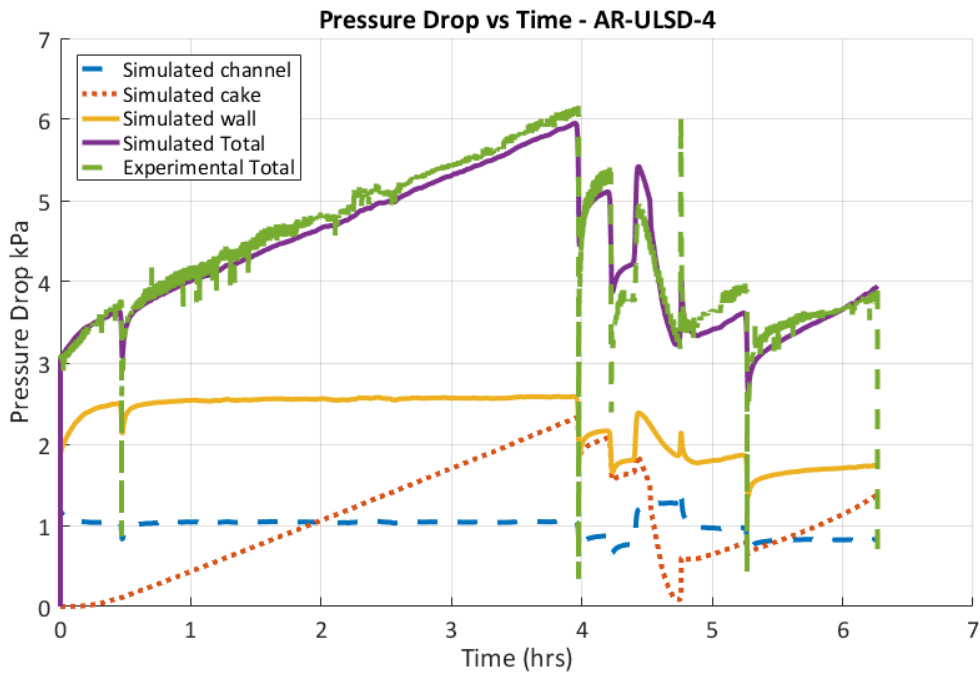
Figure F. 31 Comparison of experimental and simulated total pressure drop across CPF and its components for PO-B10-17 experiment
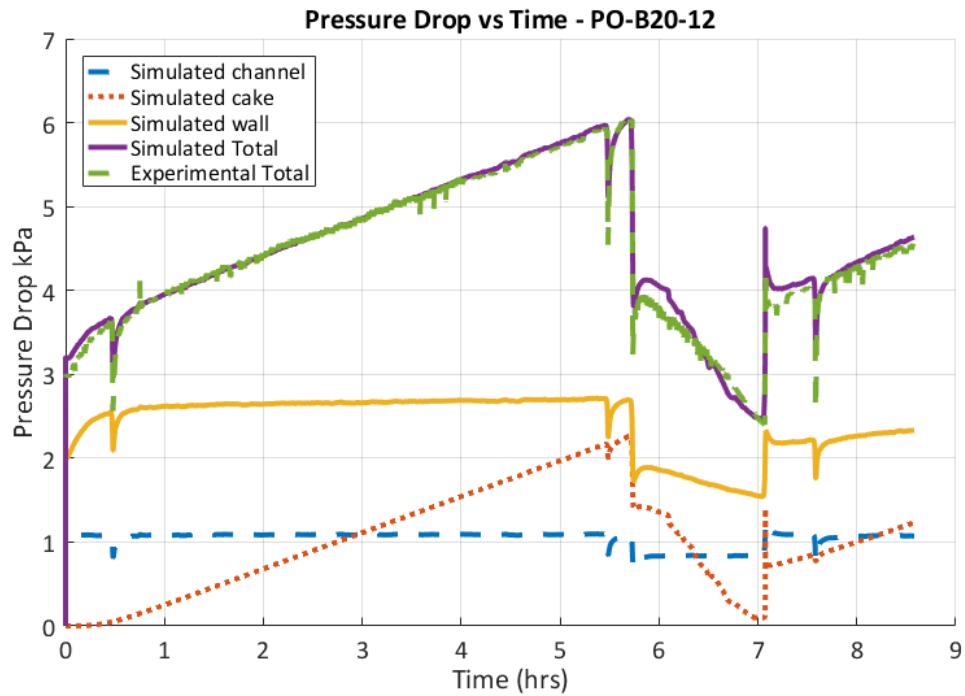
Figure F. 32 Comparison of experimental and simulated total pressure drop across CPF and its components for PO-B20-12 experiment
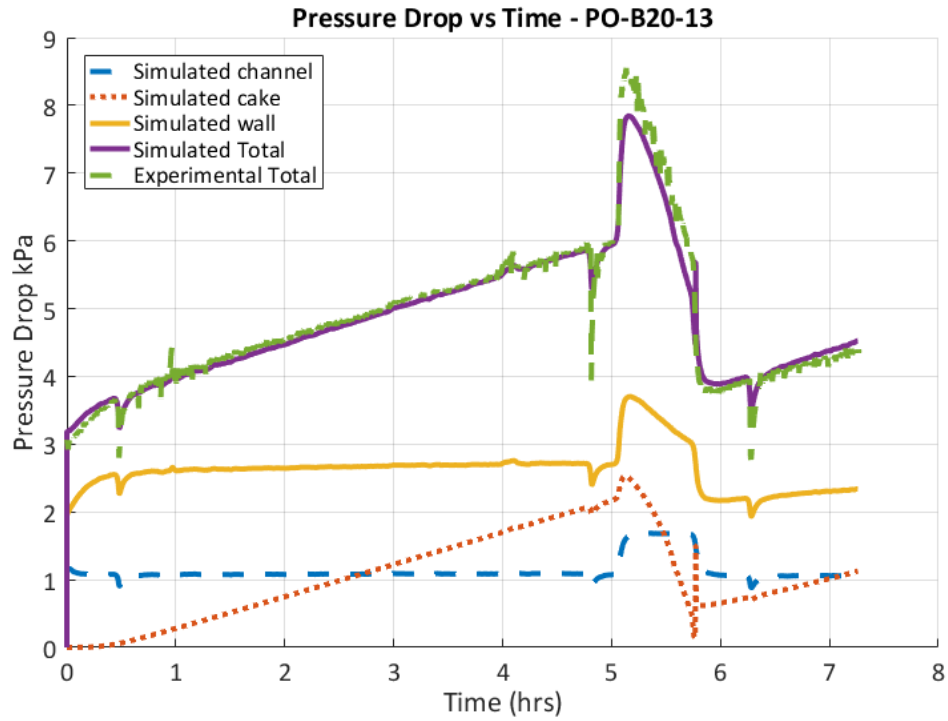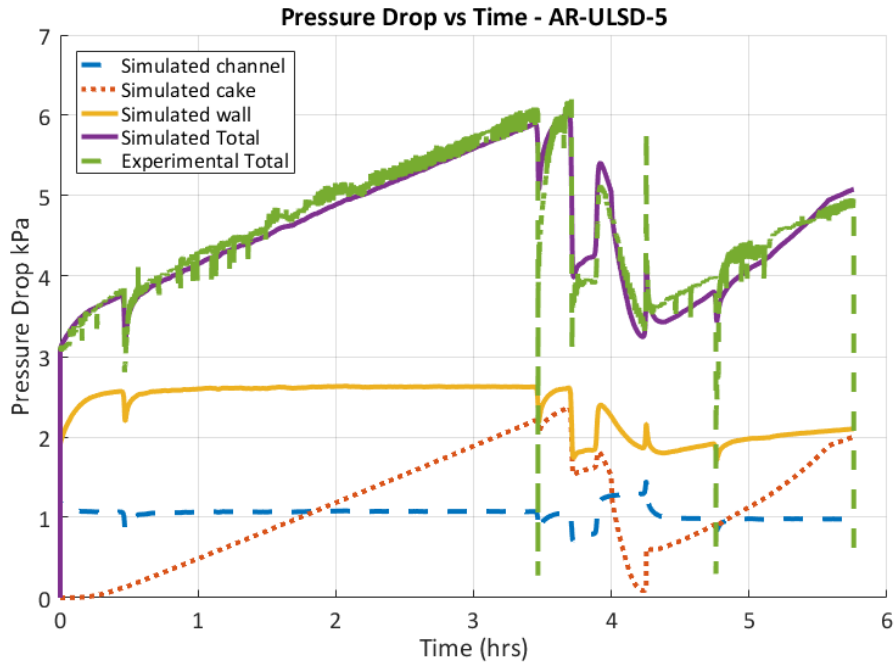
Figure F. 33 Comparison of experimental and simulated total pressure drop across CPF and its components for PO-B20-13 experiment
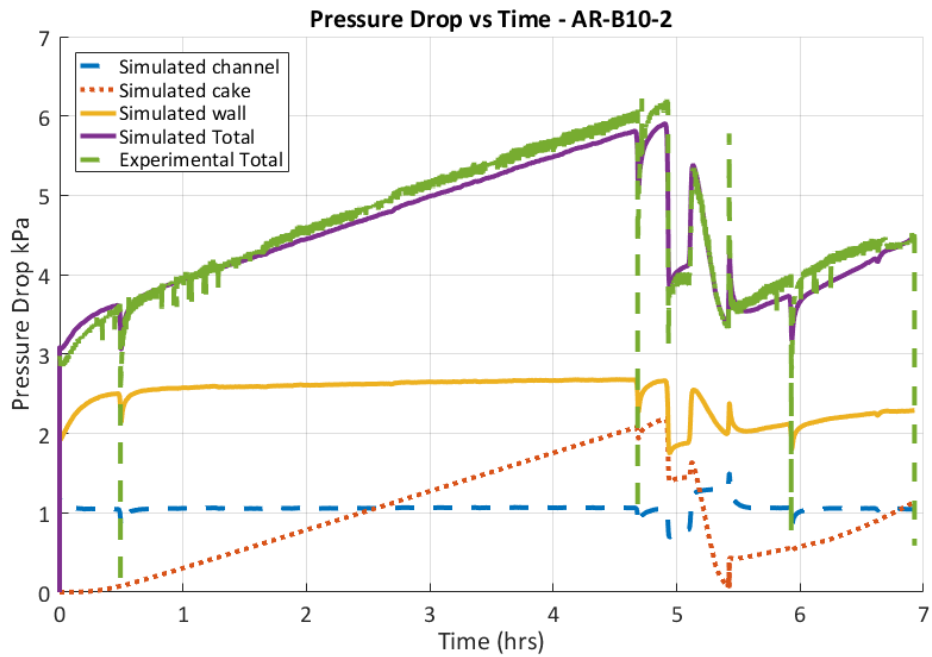
Figure F. 34 Comparison of experimental and simulated total pressure drop across CPF and its components for AR-B10-2 experiment
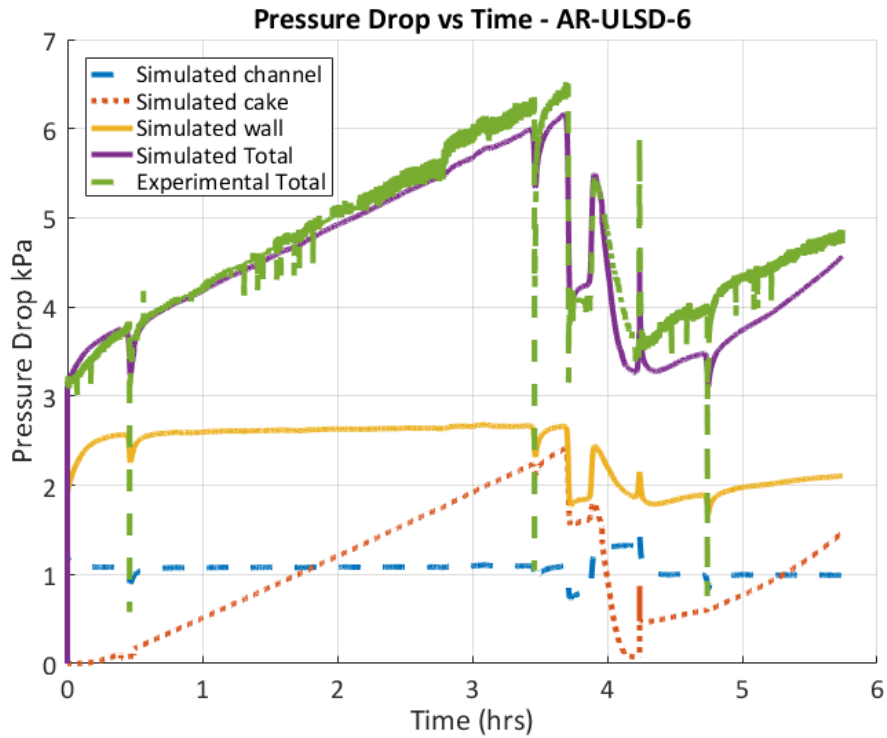
222
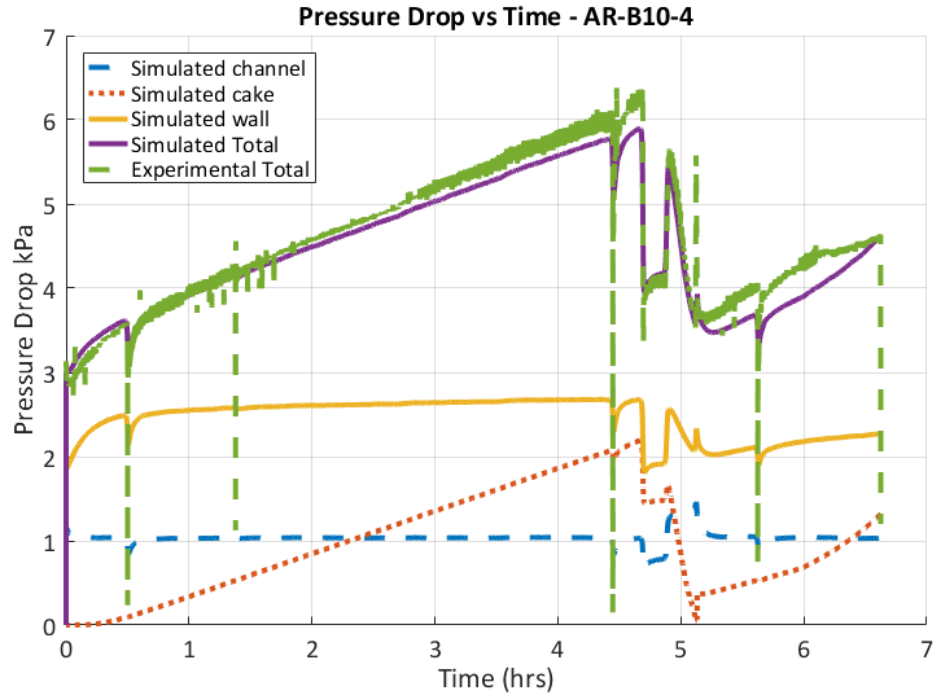
Figure F. 35 Comparison of experimental and simulated total pressure drop across CPF and its components for AR-B10-4 experiment
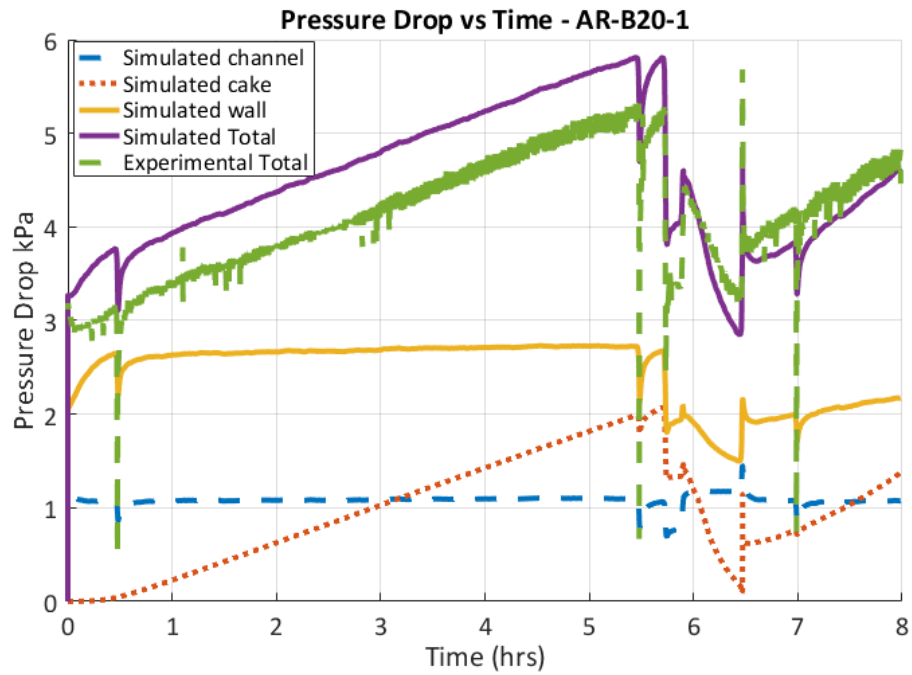
Figure F. 36 Comparison of experimental and simulated total pressure drop across CPF and its components for AR-B20-1 experiment

223
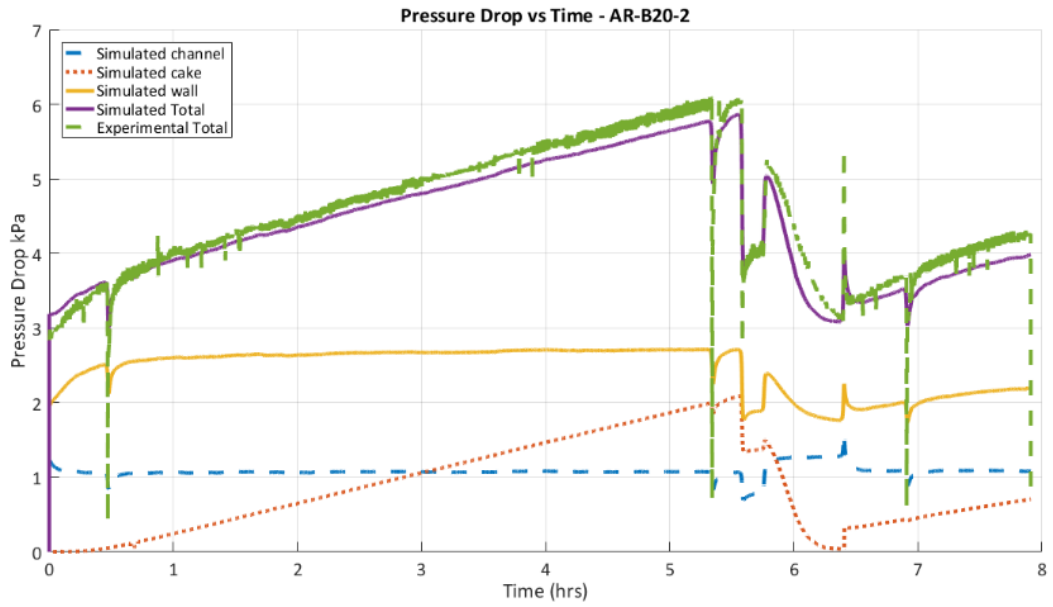
Figure F. 37 Comparison of experimental and simulated total pressure drop across CPF and its components for AR-B20-2 experiment
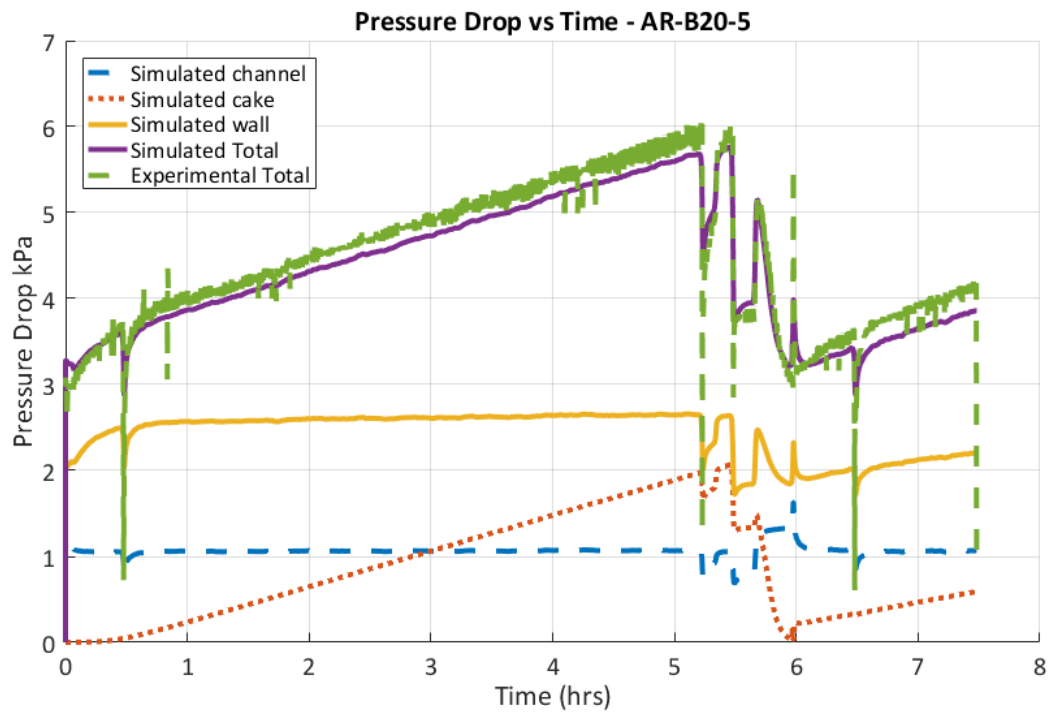
Figure F. 38 Comparison of experimental and simulated total pressure drop across CPF and its components for AR-B20-5 experiment

224
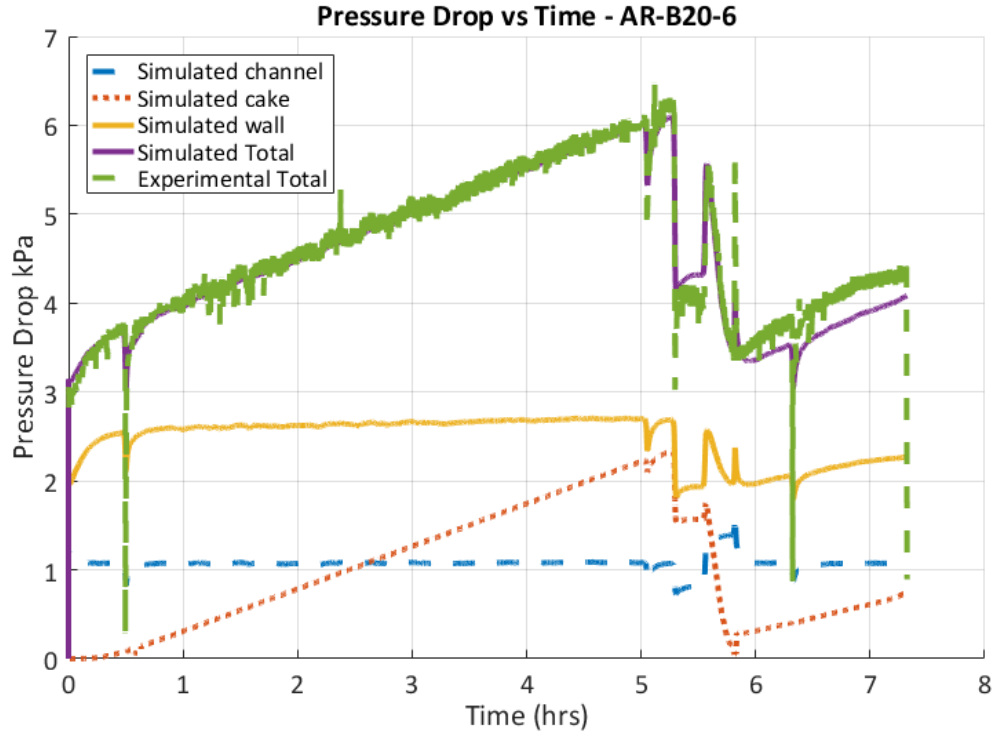
Figure F. 39 Comparison of experimental and simulated total pressure drop across CPF and its components for AR-B20-6 experiment

Figure F. 40 Comparison of experimental and simulated total pressure drop across CPF and its components for AR-ULSD-1 experiment

225

Figure F. 41 Comparison of experimental and simulated total pressure drop across CPF and its components for AR-ULSD-2 experiment

Figure F. 42 Comparison of experimental and simulated total pressure drop across CPF and its components for AR-ULSD-4 experiment

226

Figure F. 43 Comparison of experimental and simulated total pressure drop across CPF and its components for AR-ULSD-5 experiment

Figure F. 44 Comparison of experimental and simulated total pressure drop across CPF and its components for AR-ULSD-6 experiment

227

Appendix G Model Improvements over Prior Works and Flow Distribution Effect

G.1 Model Improvements over Prior Works

The model improvements in temperature and PM mass distribution and pressure drop simulation in comparison with prior works are presented in this section for a sample experiment of AR-B10-1 experiment.

Temperature Distribution

Figure G 1 shows the simulated temperature distribution for AR-B10-1 experiment at 5.63 hrs (15 minutes after start of fuel dosing) with constant inlet temperature distribution assumption used in references [13, 23]. Comparing Figure G 1 with experimental temperature distribution in Figure 4.32, the model over predicts temperature by $\cong$ 35 ºC.
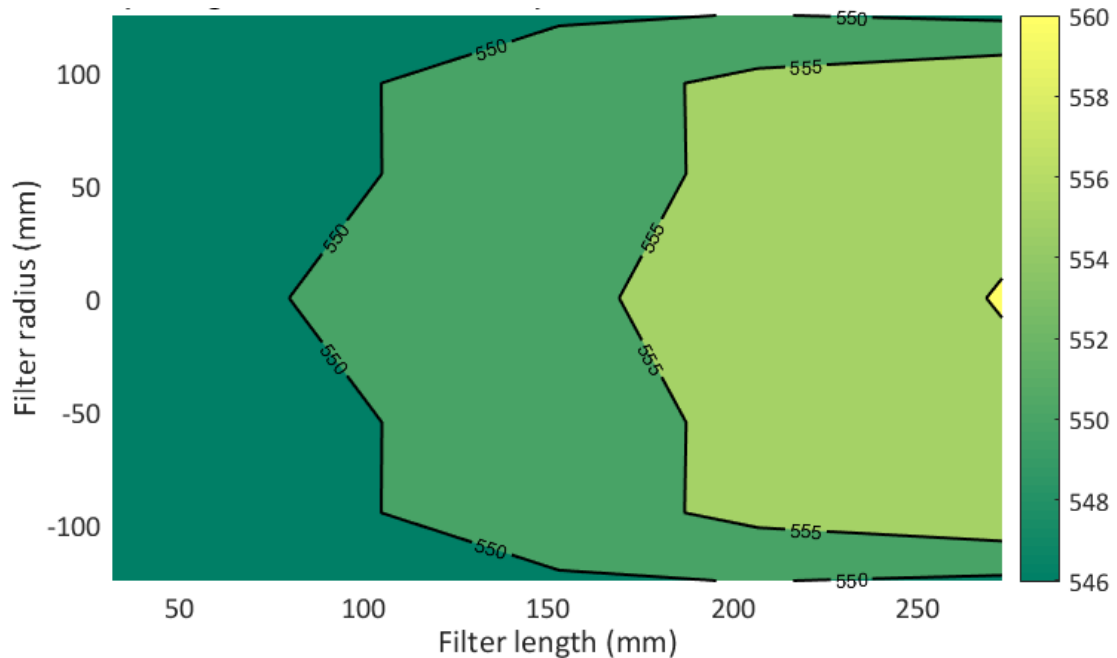
Figure G 1 Simulated temperature distribution in ºC for AR-B10-1 experiment at 5.63 hrs (15 minutes after start of fuel dosing) with constant inlet temperature distribution assumption in references [13, 23] (without fully developed boundary layer equations for temperature distribution)

PM Distribution

Figure G 2 shows the simulated PM mass loading distribution along axial and radial direction at the end of PM oxidation (at 5.82 hrs) by active regeneration for AR-B10-1 experiment with constant inlet temperature assumption. Comparing the simulated PM loading distribution in Figure G 2 with the Figure 4.37, the model under predicts the PM distribution by $\cong$ 0.8 g/L with constant inlet temperature assumption. This is mainly because of the higher CPF temperatures at the outer radiuses of the filter with constant inlet temperature assumption compared to the experimental temperature distribution because of lack consideration of thermal boundary layer development in the flow. The new model developed in this thesis accounts for the boundary layer development in the flow and uses the full developed boundary layer equations explained in Appendix A to develop temperature profile inlet to the CPF.
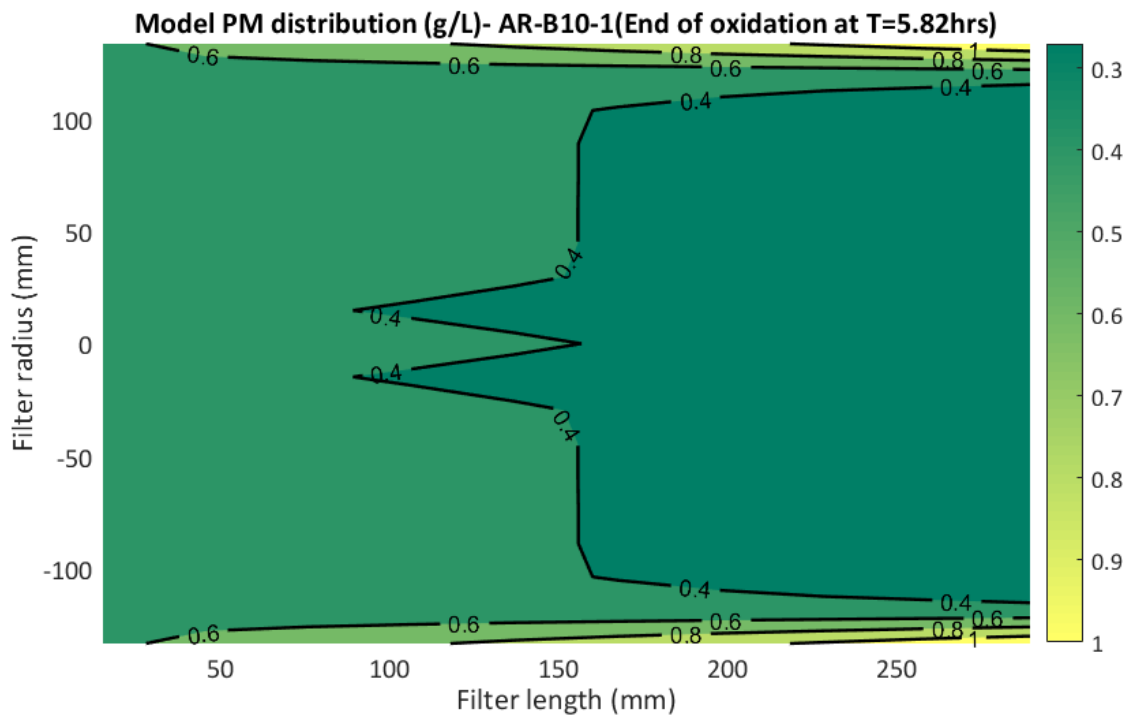
Figure G 2 Simulated PM mass loading distribution in g/L along the axial and radial directions at 5.82 hrs (end of PM oxidation by active regeneration) for AR-B10-1 experiment <u>*with constant inlet temperature assumption*</u> *in references [13, 72, 23] (without fully developed boundary layer equations for temperature distribution)*

Pressure Drop

Figure G 3 shows the comparison of experimental and simulated total pressure drop across CPF and its components during AR-B10-1 experiment without slip flow correction for wall and cake permeability as in references [13, 14, 23].
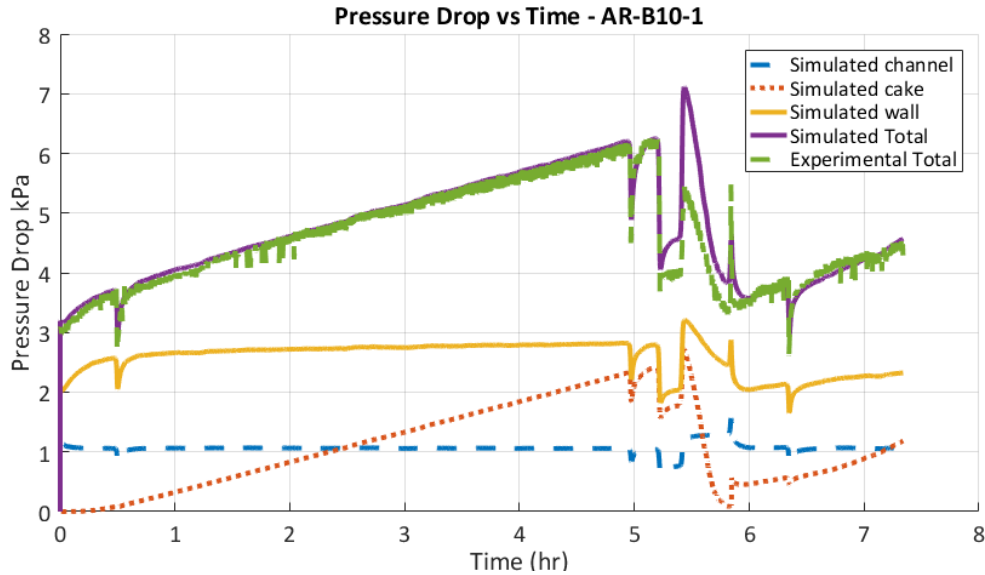

Figure G 3 Comparison of experimental and simulated total pressure drop across CPF and its components for AR-B10-1 experiment without slip flow correction for wall and cake permeability as in references [13, 14, 23]

From Figure G 3, the model over predicts the pressure drop by $\cong 0.6$ kPa during AR ramp (5.22 to 5.38 hrs). Similarly, the model over predicts the pressure drop by $\cong 1.7$ kPa at the start of PM oxidation by active regeneration (5.4 hrs). This is mainly because of the absence of the slip flow effect in the model. During high temperature flow, the permeability of the substrate wall and PM cake increases causing reduced pressure drop. The new SCR-F/CPF model accounts for the permeability increase in the substrate wall and PM cake layer due to the slip flow. Comparing Figure G 3 with Figure 4.39, the model error reduced to < 0.3 kPa during AR ramp phase (5.3 hrs) and < 0.1 kPa at the start of PM oxidation (5.4 hrs) with slip flow correction for wall and cake permeability.

The permeability increase for the PM cake layer is modeled using Versaevel correction [33] as shown in Eqn. 4.19. The substrate wall permeability is modeled using Pulkrabek correction [32] as shown in Eqn. 4.18. The Stokes-Cunningham correction [54] is widely used in the literatures for the slip flow correction in the substrate wall. For the experimental

data presented in this thesis, the Stokes-Cunningham correction is small compared to the permeability correction proposed by Pulkrabek as shown in Fig. G 4. By optimizing the constant C4 in Pulkrabek Eqn. 4.18, pressure drop estimates are closer to the experimental data. Hence, Pulkrabek correction factor is used in this thesis for the wall permeability correction. The magnitude of correction observed in the temperature range of 550 to 800K in this work is comparable ($\cong 20\%$) with corrections reported by Pulkrabek as shown in Figure 2.7.
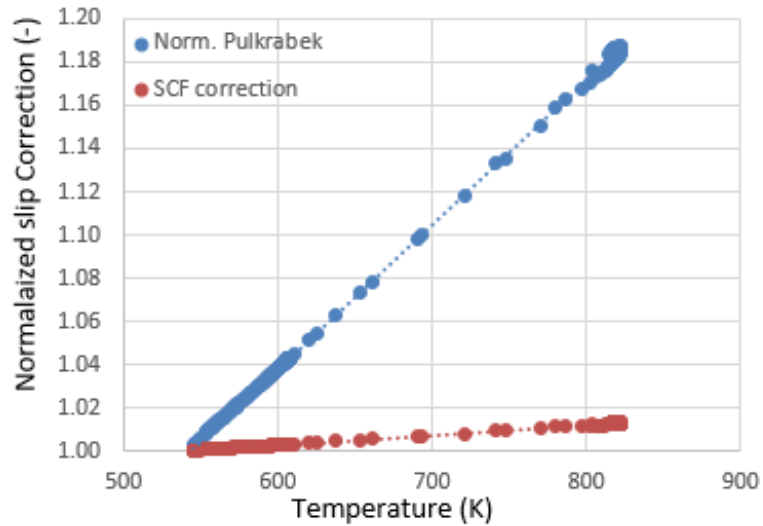
Figure G 4 Comparison of normalized wall permeability correction between Pulkrabek formulation and Stokes-Cunningham formulation
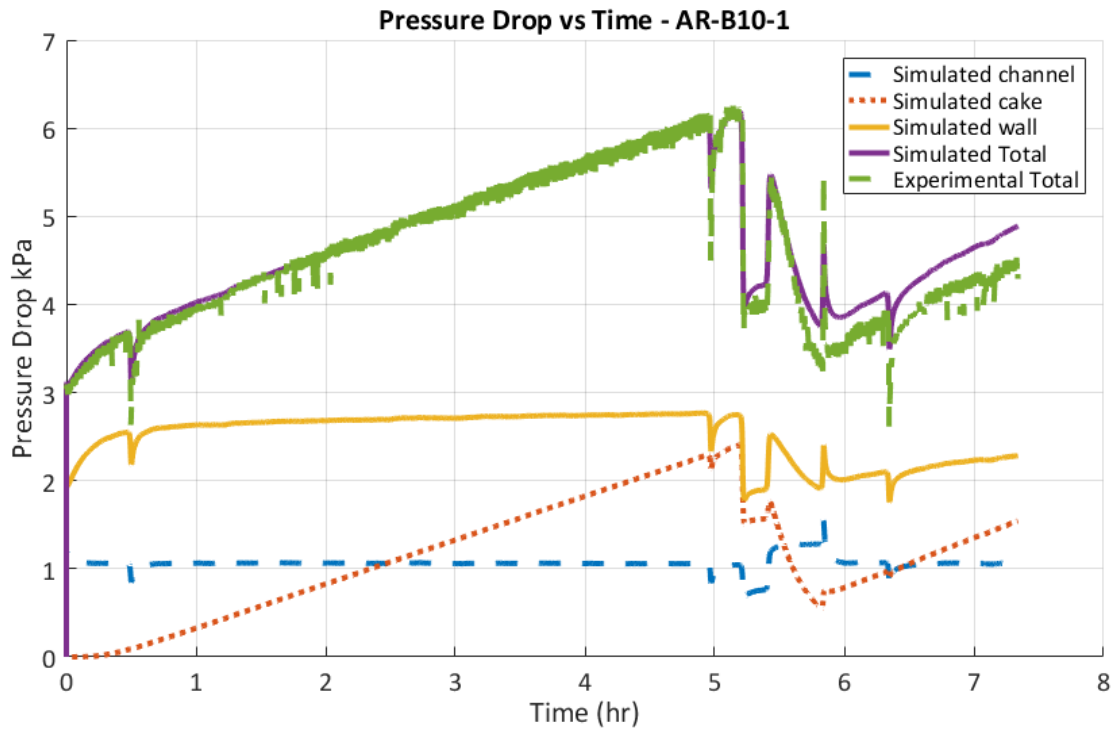
Figure G 4 shows the comparison of experimental and simulated total pressure drop across CPF and its components during AR-B10-1 experiment without new cake permeability model during PM oxidation (5.38 to 5.82 hrs) and post loading (>5.82 hrs) as in references [13, 14, 23]. Comparing Figure G 4 with Figure 4.39, the model over predicts pressure drop at the end of PM oxidation by $\cong 0.5$ kPa. This is mainly because of the potential PM cake layer damage during PM oxidation causing increased flow through the cracks and holes which results in reduced pressure drop through the PM cake layer. The models in the references [13, 14, 23] neglected this effect or used flow correction factors to compensate this effect. The newly developed cake permeability model in this thesis accounts for the permeability increase due to the PM cake damage and able to closely simulate the experimental pressure drop (within 0.1 kPa) as shown in Figure 4.39. During

post loading (>5.82 hrs), the simulated total pressure drop is higher than the measured total pressure drop in Figure G 4 by $\cong$ 0.4 kPa at the end of post loading. This is mainly because of the damaged PM cake layer from the earlier PM oxidation event. With new PM cake permeability model, the increased permeability during post loading process is accounted using the post loading permeability Eqn. D.1 shown in Appendix D. The pressure drop error with the new cake permeability is model is <0.1 kPa at the end of post loading.

Figure G 5 Comparison of experimental and simulated total pressure drop across CPF and its components for AR-B10-1 experiment without new cake permeability model during PM oxidation and post loading as in references [13, 14, 23]

G.2 Flow Distribution Effect

The PM distribution is also affected by the flow distribution at the inlet of the CPF. Ranalli et al. [19] show that at lower flow rates, the flow distribution tends to become homogeneous as the PM loading increases. However, at higher flow rates, the PM distribution is non-homogeneous because of the inlet pipe geometry (shape, size, layout

etc.). The inlet pipe geometries affect the velocity and flow distribution within the pipe. The flow distribution could affect PM loading as well as pressure drop distribution within the CPF. Hence, the flow distribution effect on PM distribution has to be accounted as indicated in future work (Chapter 7.5) of this thesis. The model presented in this thesis assumes the uniform flow distribution at the inlet of the CPF. The simulated pressure drop distribution for radial sections 1 to 5 (diameter of 0 to 133 mm) during AR-B10-1 experiments are shown in Figure G 6 and for radial sections 6 to 10 (diameter of 133 to 267) are shown in Figure G 7. Figure G 8 shows the comparison of the radial sections 1 (at the center of the filter) and 10 (at outer radius of the filter). From Figures G 6, G 7 and G8, the pressure drop curves during stage 1 and stage 2 loading (< 4.9 hrs) are comparable between the radial sections. The pressure drop at the outer radiuses of the CPF increases during PM oxidation. The pressure drop at the outer radius of the filter increases by 0.8 kPa compared to the center of the filter at the end post loading. This increase in pressure drop at the outer radius is because of the increased PM loading at the outer radiuses of the filter compared to the center of the filter caused by the lower substrate temperatures.
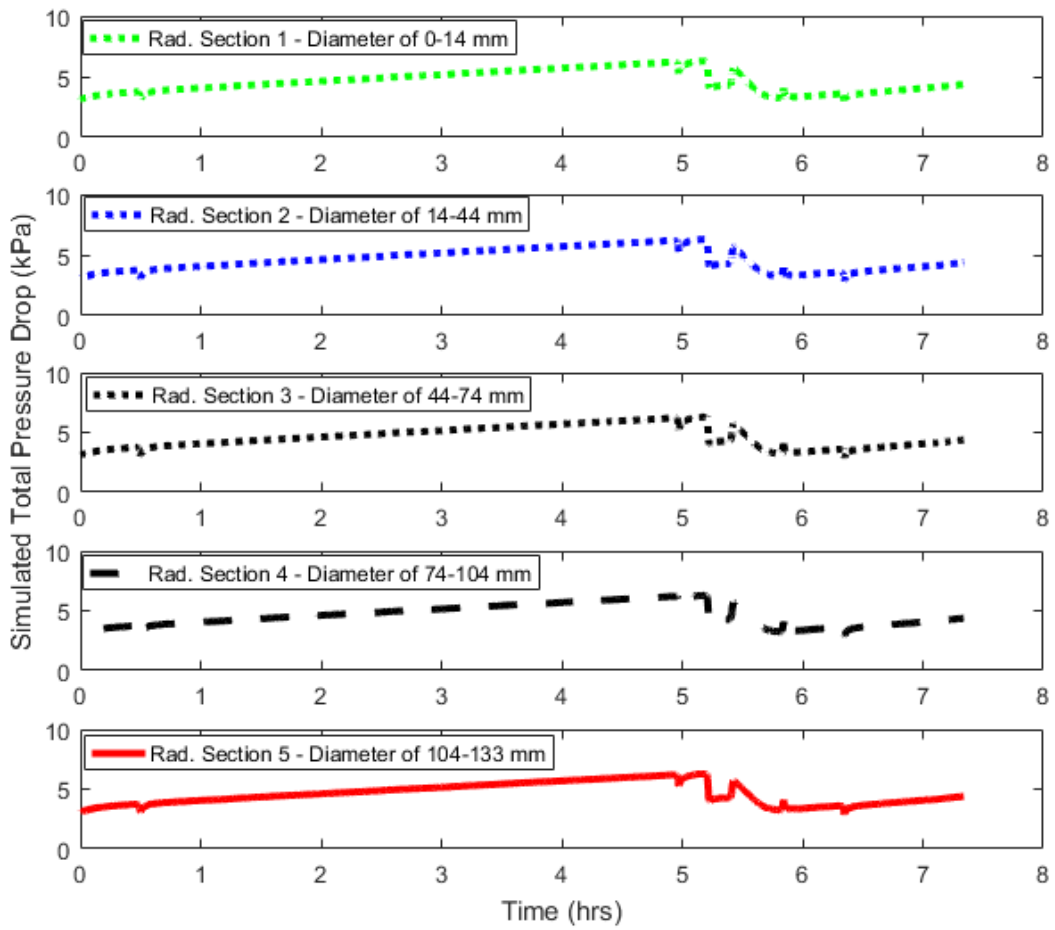
Figure G 6 Simulated total pressure drop distribution in kPa for AR-B10-1 experiment with constant inlet flow distribution assumption along radial sections 1 to 5

234
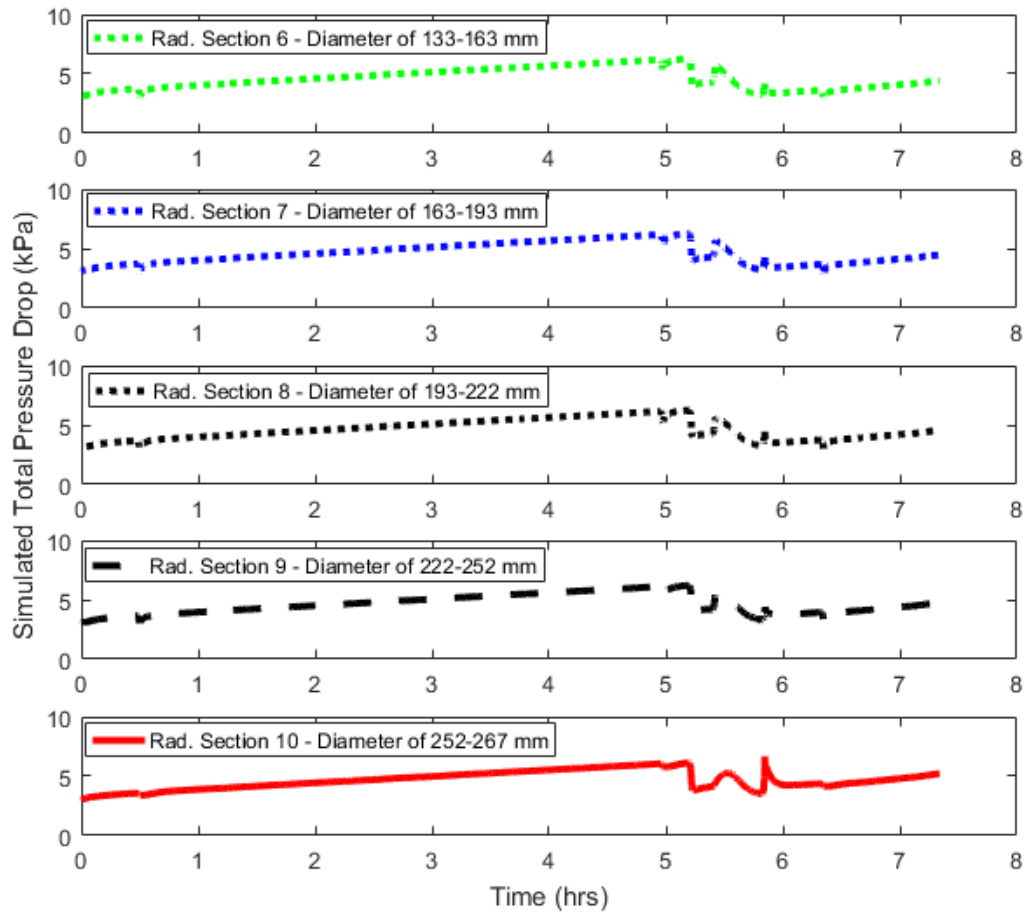
Figure G 7 Simulated total pressure drop distribution in kPa for AR-B10-1 experiment with constant inlet flow distribution assumption along radial sections 6 to 10
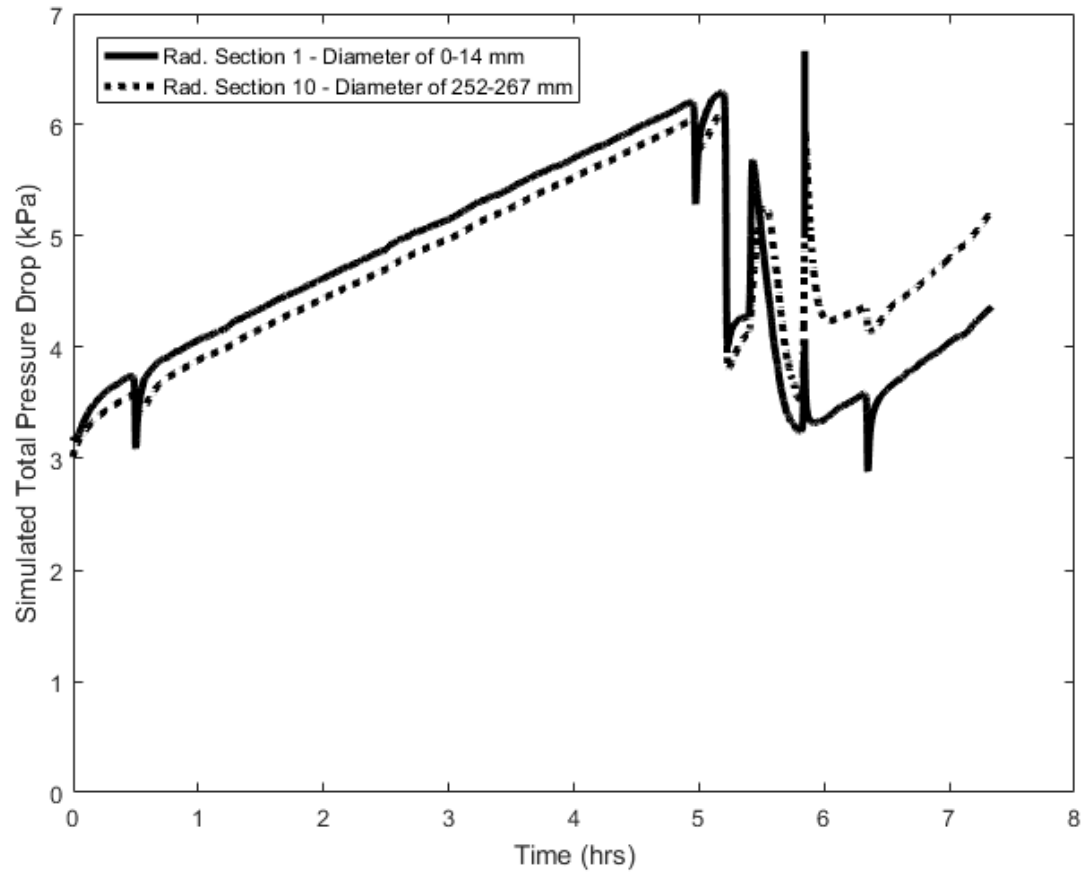
Figure G 8 Comparison of simulated total pressure drop distribution in kPa for AR-B10-1 experiment <u>for radial sections 1 and 10</u> with constant inlet flow distribution assumption

Appendix H Measurement Accuracy Summary

Table H1 shows the measurement accuracy details of the experimental data used in this work.

Table H 1 Measurement accuracy details of the experimental data [51, 49, 27, 8]

Sl. No	Sensor	Make	Measurement Error
1	Temperature sensors used for temperature distribution data (DOC, CPF and Engine Exhaust)	Watlow, K Type Thermocouple P/N: AX1078701, PT 227664-001 (DOC), AX1078801 (CPF), ACGF00Q060U40000 (Engine Exhaust)	Accuracy: $\pm$ 2.2°C
2	Pressure sensors used for the pressure drop measurement across laminar flow element (LFE), CPF, DOC : ΔP LFE, ΔP CPF	Sensotec Range: ΔP LFE : 0 to 0.5 psid ΔP DOC : 0 to 2 psid ΔP CPF(PO) : 0 to 10 psid	Accuracy: $\pm$ 0.25% FS Linearity: $\pm$ 0.15% FS Hysteresis: $\pm$ 0.10% FS Repeatability: $\pm$ 0.05% FS
3	Emissions concentration – THC (FID), CO (IRD), CO_2 (IRD), O_2 (Paramagnetic), NO and NOx (CLD)).	Pierburg Emissions Bench (AMA 4000)	Repeatability $\leq$ 0.5 % of measured value + 2x Detection limit Noise $\leq$ 1 % of measured value + 2x Detection limit Detection Limits: THC 30 ppb C_3, CO 125 ppb, CO_2 15 ppm, O_2 15 ppm, NO and NO_2 35 ppb

4	CPF PM mass retained	Ohaus Ranger Model 35LM	Readability $\pm$ 0.1g Repeatability $\pm$ 0.3 g Certified Readability $\pm$ 1g
5	Air flow measurement	Meriam Instruments	Accuracy: 0.72 to 0.86% of reading Repeatability: 0.1%
6	PM Concentration	Sampling: Anderson Instruments Inc Filter: Pall Corporation (WA) Weighing: Mettler Toledo UMT2 microbalance	Sampling: 47 mm glass fiber PM sampling filter Weighing Balance: Readability 0.1μg Repeatability 0.25μg Linearity $\pm$ 1μg

Appendix I PhD Publications

I.1 Peer Reviewed Published Journal Papers

1. Mahadevan, B.S., Johnson, J.H., and Shahbakhti, M., Development of a catalyzed diesel particulate filter multi-zone model for simulation of axial and radial substrate temperature and particulate matter distribution, Journal of Emiss. Control Sci. Technol., Vol. 1, pp 183-202, 2015, doi:10.1007/s40825-015-0015-x, 2015.

2. Mahadevan, B.S., Johnson, J.H., and Shahbakhti, M., Experimental and Simulation Analysis of Temperature and Particulate Matter Distribution for a Catalyzed Diesel Particulate Filter, Journal of Emiss. Control. Sci. Technol.,Vol.1, pp 255-283, 2015, doi: 10.1007/s40825-015-0022-y, 2015.

3. Mahadevan, B.S., Johnson, J.H., and Shahbakti, M., Predicting pressure drop, temperature and particulate matter distribution of a catalyzed diesel particulate filter using a multi-zone model including cake permeability, Journal of Emiss. Control Sci. Technol., Accepted for publication on 1st Feb 2017, doi: 10.1007/s40825-017-0062-6, 2017.

Appendix J Program and Data File Summary

J.1 Chapter 1

File Name	File Description
\Chapter1_Introduction\Excel_Tables	Chapter 1 Figure 1.1

J.3 Chapter 3

File Name	File Description
\CPF_Temp_Analysis\thermal_bl_cpf_function_call.m	Chapter 3 Figure 3.9

J.4 Chapter 4

File Name	File Description
SCR-F Model v1.5.2_PO_B10_15_Thesis_Results\ results_publish.m	Chapter 4 Figures 4.16 to 4.28 simulation results for AR-B0-1 experiment
SCR-F Model v1.5.2_AR_B10_1_Thesis_Results\ results_publish.m	Chapter 4 Figures 4.29 to 4.39 simulation results for AR-B0-1 experiment

J.5 Chapter 5

File Name	File Description
SCR-F Model\CPF_Estimator_ROM\ CPF_estimator_plots_5secs_ROM.m	Chapter 5 Figures 5.35, 5.36, 5.38 to 5.41, 5.43 and 5.44 simulation results for reduced order MPF model for AR-B0-1 experiment

J.6 Chapter 6

File Name	File Description
SCR-F Model\CPF_Estimator_AR-B10-1\ Plot_Results_doc_estimator_14_Oct_2016	Chapter 6 Figures 6.5 to 6.7 simulation results for DOC estimator results for AR-B0-1 experiment
SCR-F Model\CPF_Estimator_AR-B10-1\ CPF_estimator_plots_1secs_Estr.m	Chapter 6 Figures 6.8, 6.9, 6.11 to 6.14, 6.16, 6.18 and 6.19 simulation results for DOC-CPF estimator results for AR-B0-1 experiment

J.7 Appendix A

File Name	File Description
\Publications\Thermal_boundary_Layer\ Sample_calc_volume_15Sep2014.xls	Table A 1, Figures A 1 to A 3

J.7 Appendix D

File Name	File Description
\Publications\Pressure_drop_Analysis\ Cake_permeability_Model_Analysis\ Cake_permeability_estimates_6Jan2016_PO.xls	Figure D.1
\Publications\Pressure_drop_Analysis\ Cake_permeability_Model_Analysis\ Cake_permeability_estimates_23Jan2016- AR_worampup.xls	Figure D.2

J.7 Appendix E

File Name	File Description
result_extract_no_o_summary.m	Table E. 4 Fractional PM mass oxidized during passive oxidation and active regeneration phases of all experiments
result_extract_summary_allruns.m	Table E.1 to E.3, Table E.5 to Table E.6
Summary_Tables_Oct8_2016.xls	Excel summary for Tables in Appendix E
no2_o2_frac_summary.xls	Matlab output file from 'result_extract_no_o_summary.m' script
fl_summary_sim_exp.xls	Matlab output file from 'result_extract_summary_allruns.m' script

J.7 Appendix F

File Name	File Description
SCR-F Model\All_runs\runname\ results_publish.m	Chapter F Figures F.1 to F.44 simulation results for all experiments

J.8 Appendix G

File Name	File Description
SCR-F Model\Thesis_Appendix\ results_publish.m	Chapter G Figures G.1 to G.3 and G.4 to G.8

Appendix K Letters of Permission

K.1 Letter of Permission for Chapter 1

Figure 1.1 EPA emissions standard summary from dieselnet, Permission not required as this is data in public domain and emissions standards are developed by EPA (employees of the federal government).

K.2 Letter of Permission for Chapter 2

Figures 2.1, 2.2, 2.3, 2.4, 2.5, 2.6, 2.8 and 2.9.

Michigan Tech   Boopathi Singalandapuram Mahadevan <bsingala@mtu.edu>

Permission to use copyrighted SAE material for my PhD dissertation
4 messages

Boopathi Singalandapuram Mahadevan <bsingala@mtu.edu>   Thu, Sep 22, 2016 at 7:36 PM
To: copyright@sae.org

Hello,

I am a current PhD student at Michigan Tech University (MTU) located in Houghton, MI. I would like to request permission from SAE to re-use the following material for my PhD dissertation.

SAE Paper No. 2001-01-0908	Figure 15
SAE Paper No. 2001-01-0912	Figures 3a and 3b
SAE Paper No. 2006-01-0264	Figure 10
SAE Paper No. 2002-01-2158	Figures 6 and 7
SAE Paper No. 2009-01-1473	Figure 12
SAE Paper No. 2013-01-0528	Figure 6

The dissertation is tentatively titled "Development of a Multi-zone Catalyzed Particulate Model and Kalman Filter Estimator for Simulation and Control of Particulate Matter Distribution of a CPF for Engine ECU applications".

The dissertation will be distributed electronically throughout various individuals/departments at MTU and MTU Aftertreatment consortium partners and will be printed upon completion with an expected publication date of Dec, 2016.

Kindly let me know if any other information is needed.

Thank you

Boopathi Singalandapuram Mahadevan

Dear Boopathi,

Thank you for your request.

Reproduction use of SAE Figures as stated within your email, is hereby granted upon receipt of copyright fee(s), and subject to the following terms and conditions:

-Permission is granted for non-exclusive English language rights, and for the specific use as indicated in your email;

-Permission is required for new requests, or for further use of the material;

-The SAE material must be clearly identified and include the following statement "Reprinted with Permission from SAE International";

-We also request that you include a complete reference to the SAE document in the reference section for each figure used;

-The permission does not cover any third-party copyrighted work which may appear in the material requested;

-Licensor's use of this material, in whole or in part, is entirely its responsibility, and SAE International does not warrant or is not responsible for any use of the material.

Best,

Nikole Aston

IP Compliance Specialist

SAE INTERNATIONAL

400 Commonwealth Drive

Warrendale, PA 15096 USA

o: +1.724.772.4095

e: nikole.aston@sae.org

Boopathi Singalandapuram Mahadevan <bsingala@mtu.edu>   Fri, Sep 23, 2016 at 7:52 PM
To: copyright <copyright@sae.org>

Dear Nikole Aston,

Thank you for the note. The note indicates the copy right fees for the use of material and could not find any payment information in the note. Kindly provide further details on the copyright fees please as I am requesting permission to use the material in my PhD dissertation.

Thanks and regards

Boopathi S.M
[Quoted text hidden]

copyright <copyright@sae.org>   Mon, Sep 26, 2016 at 1:46 PM
To: Boopathi Singalandapuram Mahadevan <bsingala@mtu.edu>

Dear Boopathi,

Please disregard fee language. There is no fee associated with your permission request. Image use, per your email request, is approved.

Thank you.

_____

Nikole Aston

IP Compliance Specialist

SAE INTERNATIONAL

Figure 2.7

INTRODUCTION

1. The publisher for this copyrighted material is Elsevier. By clicking "accept" in connection with completing this licensing transaction, you agree that the following terms and conditions apply to this transaction (along with the Billing and Payment terms and conditions established by Copyright Clearance Center, Inc. ("CCC"), at the time that you opened your Rightslink account and that are available at any time at http://myaccount.copyright.com).

GENERAL TERMS

2. Elsevier hereby grants you permission to reproduce the aforementioned material subject to the terms and conditions indicated.

3. Acknowledgement: If any part of the material to be used (for example, figures) has appeared in our publication with credit or acknowledgement to another source, permission must also be sought from that source. If such permission is not obtained then that material may not be included in your publication/copies. Suitable acknowledgement to the source must be made, either as a footnote or in a reference list at the end of your publication, as follows:

"Reprinted from Publication title, Vol /edition number, Author(s), Title of article / title of chapter, Pages No., Copyright (Year), with permission from Elsevier [OR APPLICABLE SOCIETY COPYRIGHT OWNER]." Also Lancet special credit - "Reprinted from The Lancet, Vol. number, Author(s), Title of article, Pages No., Copyright (Year), with permission from Elsevier."

4. Reproduction of this material is confined to the purpose and/or media for which permission is hereby given.

5. Altering/Modifying Material: Not Permitted. However figures and illustrations may be altered/adapted minimally to serve your work. Any other abbreviations, additions, deletions and/or any other alterations shall be made only with prior written authorization of Elsevier Ltd. (Please contact Elsevier at permissions@elsevier.com)

6. If the permission fee for the requested use of our material is waived in this instance, please be advised that your future requests for Elsevier materials may attract a fee.

7. Reservation of Rights: Publisher reserves all rights not specifically granted in the combination of (i) the license details provided by you and accepted in the course of this licensing transaction, (ii) these terms and conditions and (iii) CCC's Billing and Payment terms and conditions.

8. License Contingent Upon Payment: While you may exercise the rights licensed immediately upon issuance of the license at the end of the licensing process for the transaction, provided that you have disclosed complete and accurate details of your proposed use, no license is finally effective unless and until full payment is received from you (either by publisher or by CCC) as provided in CCC's Billing and Payment terms and conditions. If full payment is not received on a timely basis, then any license preliminarily granted shall be deemed automatically revoked and shall be void as if never granted. Further, in the event that you breach any of these terms and conditions or any of CCC's Billing and Payment terms and conditions, the license is automatically revoked and shall be void as if never granted. Use of materials as described in a revoked license, as well as any use of the materials beyond the scope of an unrevoked license, may constitute copyright infringement and publisher reserves the right to take any and all action to protect its copyright in the materials.

9. Warranties: Publisher makes no representations or warranties with respect to the licensed material.

10. Indemnity: You hereby indemnify and agree to hold harmless publisher and CCC, and their respective officers, directors, employees and agents, from and against any and all claims arising out of your use of the licensed material other than as specifically authorized pursuant to this license.

11. No Transfer of License: This license is personal to you and may not be sublicensed, assigned, or transferred by you to any other person without publisher's written permission.
12. No Amendment Except in Writing: This license may not be amended except in a writing signed by both parties (or, in the case of publisher, by CCC on publisher's behalf).
13. Objection to Contrary Terms: Publisher hereby objects to any terms contained in any purchase order, acknowledgment, check endorsement or other writing prepared by you, which terms are inconsistent with these terms and conditions or CCC's Billing and Payment terms and conditions. These terms and conditions, together with CCC's Billing and Payment terms and conditions (which are incorporated herein), comprise the entire agreement between you and publisher (and CCC) concerning this licensing transaction. In the event of any conflict between your obligations established by these terms and conditions and those established by CCC's Billing and Payment terms and conditions, these terms and conditions shall control.
14. Revocation: Elsevier or Copyright Clearance Center may deny the permissions described in this License at their sole discretion, for any reason or no reason, with a full refund payable to you. Notice of such denial will be made using the contact information provided by you. Failure to receive such notice will not alter or invalidate the denial. In no event will Elsevier or Copyright Clearance Center be responsible or liable for any costs, expenses or damage incurred by you as a result of a denial of your permission request, other than a refund of the amount(s) paid by you to Elsevier and/or Copyright Clearance Center for denied permissions.

LIMITED LICENSE

The following terms and conditions apply only to specific license types:
15. **Translation**: This permission is granted for non-exclusive world **English** rights only unless your license was granted for translation rights. If you licensed translation rights you may only translate this content into the languages you requested. A professional translator must perform all translations and reproduce the content word for word preserving the integrity of the article.
16. **Posting licensed content on any Website**: The following terms and conditions apply as follows: Licensing material from an Elsevier journal: All content posted to the web site must maintain the copyright information line on the bottom of each image; A hyper-text must be included to the Homepage of the journal from which you are licensing at http://www.sciencedirect.com/science/journal/xxxxx or the Elsevier homepage for books at http://www.elsevier.com; Central Storage: This license does not include permission for a scanned version of the material to be stored in a central repository such as that provided by Heron/XanEdu.
Licensing material from an Elsevier book: A hyper-text link must be included to the Elsevier homepage at http://www.elsevier.com . All content posted to the web site must maintain the copyright information line on the bottom of each image.

Posting licensed content on Electronic reserve: In addition to the above the following clauses are applicable: The web site must be password-protected and made available only to bona fide students registered on a relevant course. This permission is granted for 1 year only. You may obtain a new license for future website posting.
17. **For journal authors**: the following clauses are applicable in addition to the above:
Preprints:
A preprint is an author's own write-up of research results and analysis, it has not been peer-reviewed, nor has it had any other value added to it by a publisher (such as formatting, copyright, technical enhancement etc.).
Authors can share their preprints anywhere at any time. Preprints should not be added to or enhanced in any way in order to appear more like, or to substitute for, the final versions of articles however authors can update their preprints on arXiv or RePEc with their Accepted Author Manuscript (see below).
If accepted for publication, we encourage authors to link from the preprint to their formal

publication via its DOI. Millions of researchers have access to the formal publications on ScienceDirect, and so links will help users to find, access, cite and use the best available version. Please note that Cell Press, The Lancet and some society-owned have different preprint policies. Information on these policies is available on the journal homepage.

Accepted Author Manuscripts: An accepted author manuscript is the manuscript of an article that has been accepted for publication and which typically includes author-incorporated changes suggested during submission, peer review and editor-author communications.

Authors can share their accepted author manuscript:

- immediately
    - via their non-commercial person homepage or blog
    - by updating a preprint in arXiv or RePEc with the accepted manuscript
    - via their research institute or institutional repository for internal institutional uses or as part of an invitation-only research collaboration work-group
    - directly by providing copies to their students or to research collaborators for their personal use
    - for private scholarly sharing as part of an invitation-only work group on commercial sites with which Elsevier has an agreement
- after the embargo period
    - via non-commercial hosting platforms such as their institutional repository
    - via commercial sites with which Elsevier has an agreement

In all cases accepted manuscripts should:

- link to the formal publication via its DOI
- bear a CC-BY-NC-ND license - this is easy to do
- if aggregated with other manuscripts, for example in a repository or other site, be shared in alignment with our hosting policy not be added to or enhanced in any way to appear more like, or to substitute for, the published journal article.

Published journal article (JPA): A published journal article (PJA) is the definitive final record of published research that appears or will appear in the journal and embodies all value-adding publishing activities including peer review co-ordination, copy-editing, formatting, (if relevant) pagination and online enrichment.

Policies for sharing publishing journal articles differ for subscription and gold open access articles:

Subscription Articles: If you are an author, please share a link to your article rather than the full-text. Millions of researchers have access to the formal publications on ScienceDirect, and so links will help your users to find, access, cite, and use the best available version. Theses and dissertations which contain embedded PJAs as part of the formal submission can be posted publicly by the awarding institution with DOI links back to the formal publications on ScienceDirect.

If you are affiliated with a library that subscribes to ScienceDirect you have additional private sharing rights for others' research accessed under that agreement. This includes use for classroom teaching and internal training at the institution (including use in course packs and courseware programs), and inclusion of the article for grant funding purposes.

Gold Open Access Articles: May be shared according to the author-selected end-user license and should contain a CrossMark logo, the end user license, and a DOI link to the formal publication on ScienceDirect.

Please refer to Elsevier's posting policy for further information.

18. For book authors the following clauses are applicable in addition to the above:
Authors are permitted to place a brief summary of their work online only. You are not

allowed to download and post the published electronic version of your chapter, nor may you scan the printed edition to create an electronic version. **Posting to a repository:** Authors are permitted to post a summary of their chapter only in their institution's repository.
19. **Thesis/Dissertation:** If your license is for use in a thesis/dissertation your thesis may be submitted to your institution in either print or electronic form. Should your thesis be published commercially, please reapply for permission. These requirements include permission for the Library and Archives of Canada to supply single copies, on demand, of the complete thesis and include permission for Proquest/UMI to supply single copies, on demand, of the complete thesis. Should your thesis be published commercially, please reapply for permission. Theses and dissertations which contain embedded PJAs as part of the formal submission can be posted publicly by the awarding institution with DOI links back to the formal publications on ScienceDirect.

Elsevier Open Access Terms and Conditions

You can publish open access with Elsevier in hundreds of open access journals or in nearly 2000 established subscription journals that support open access publishing. Permitted third party re-use of these open access articles is defined by the author's choice of Creative Commons user license. See our open access license policy for more information.
Terms & Conditions applicable to all Open Access articles published with Elsevier:
Any reuse of the article must not represent the author as endorsing the adaptation of the article nor should the article be modified in such a way as to damage the author's honour or reputation. If any changes have been made, such changes must be clearly indicated.
The author(s) must be appropriately credited and we ask that you include the end user license and a DOI link to the formal publication on ScienceDirect.
If any part of the material to be used (for example, figures) has appeared in our publication with credit or acknowledgement to another source it is the responsibility of the user to ensure their reuse complies with the terms and conditions determined by the rights holder.
Additional Terms & Conditions applicable to each Creative Commons user license:
CC BY: The CC-BY license allows users to copy, to create extracts, abstracts and new works from the Article, to alter and revise the Article and to make commercial use of the Article (including reuse and/or resale of the Article by commercial entities), provided the user gives appropriate credit (with a link to the formal publication through the relevant DOI), provides a link to the license, indicates if changes were made and the licensor is not represented as endorsing the use made of the work. The full details of the license are available at http://creativecommons.org/licenses/by/4.0.
CC BY NC SA: The CC BY-NC-SA license allows users to copy, to create extracts, abstracts and new works from the Article, to alter and revise the Article, provided this is not done for commercial purposes, and that the user gives appropriate credit (with a link to the formal publication through the relevant DOI), provides a link to the license, indicates if changes were made and the licensor is not represented as endorsing the use made of the work. Further, any new works must be made available on the same conditions. The full details of the license are available at http://creativecommons.org/licenses/by-nc-sa/4.0.
CC BY NC ND: The CC BY-NC-ND license allows users to copy and distribute the Article, provided this is not done for commercial purposes and further does not permit distribution of the Article if it is changed or edited in any way, and provided the user gives appropriate credit (with a link to the formal publication through the relevant DOI), provides a link to the license, and that the licensor is not represented as endorsing the use made of the work. The full details of the license are available at http://creativecommons.org/licenses/by-nc-nd/4.0.
Any commercial reuse of Open Access articles published with a CC BY NC SA or CC BY NC ND license requires permission from Elsevier and will be subject to a fee.
Commercial reuse includes:

- Associating advertising with the full text of the Article
- Charging fees for document delivery or access

250

- Article aggregation
- Systematic distribution via e-mail lists or share buttons

Posting or linking by commercial companies for use by customers of those companies.

20. Other Conditions:

v1.8

Questions? customercare@copyright.com or +1-855-239-3415 (toll free in the US) or +1-978-646-2777.

Figure 2.10

252

claims arising out of your use of the licensed material other than as specifically authorized pursuant to this license.

11. No Transfer of License: This license is personal to you and may not be sublicensed, assigned, or transferred by you to any other person without publisher's written permission.

12. No Amendment Except in Writing: This license may not be amended except in a writing signed by both parties (or, in the case of publisher, by CCC on publisher's behalf).

13. Objection to Contrary Terms: Publisher hereby objects to any terms contained in any purchase order, acknowledgment, check endorsement or other writing prepared by you, which terms are inconsistent with these terms and conditions or CCC's Billing and Payment terms and conditions. These terms and conditions, together with CCC's Billing and Payment terms and conditions (which are incorporated herein), comprise the entire agreement between you and publisher (and CCC) concerning this licensing transaction. In the event of any conflict between your obligations established by these terms and conditions and those established by CCC's Billing and Payment terms and conditions, these terms and conditions shall control.

14. Revocation: Elsevier or Copyright Clearance Center may deny the permissions described in this License at their sole discretion, for any reason or no reason, with a full refund payable to you. Notice of such denial will be made using the contact information provided by you. Failure to receive such notice will not alter or invalidate the denial. In no event will Elsevier or Copyright Clearance Center be responsible or liable for any costs, expenses or damage incurred by you as a result of a denial of your permission request, other than a refund of the amount(s) paid by you to Elsevier and/or Copyright Clearance Center for denied permissions.

LIMITED LICENSE

The following terms and conditions apply only to specific license types:

15. **Translation:** This permission is granted for non-exclusive world English rights only unless your license was granted for translation rights. If you licensed translation rights you may only translate this content into the languages you requested. A professional translator must perform all translations and reproduce the content word for word preserving the integrity of the article.

16. **Posting licensed content on any Website:** The following terms and conditions apply as follows: Licensing material from an Elsevier journal: All content posted to the web site must maintain the copyright information line on the bottom of each image; A hyper-text must be included to the Homepage of the journal from which you are licensing at http://www.sciencedirect.com/science/journal/xxxxx or the Elsevier homepage for books at http://www.elsevier.com; Central Storage: This license does not include permission for a scanned version of the material to be stored in a central repository such as that provided by Heron/XanEdu.

Licensing material from an Elsevier book: A hyper-text link must be included to the Elsevier homepage at http://www.elsevier.com . All content posted to the web site must maintain the copyright information line on the bottom of each image.

Posting licensed content on Electronic reserve: In addition to the above the following clauses are applicable: The web site must be password-protected and made available only to bona fide students registered on a relevant course. This permission is granted for 1 year only. You may obtain a new license for future website posting.

17. **For journal authors:** the following clauses are applicable in addition to the above:
Preprints:
A preprint is an author's own write-up of research results and analysis, it has not been peer-reviewed, nor has it had any other value added to it by a publisher (such as formatting, copyright, technical enhancement etc.).

Authors can share their preprints anywhere at any time. Preprints should not be added to or enhanced in any way in order to appear more like, or to substitute for, the final versions of articles however authors can update their preprints on arXiv or RePEc with their Accepted

Author Manuscript (see below).

If accepted for publication, we encourage authors to link from the preprint to their formal publication via its DOI. Millions of researchers have access to the formal publications on ScienceDirect, and so links will help users to find, access, cite and use the best available version. Please note that Cell Press, The Lancet and some society-owned have different preprint policies. Information on these policies is available on the journal homepage.

Accepted Author Manuscripts: An accepted author manuscript is the manuscript of an article that has been accepted for publication and which typically includes author-incorporated changes suggested during submission, peer review and editor-author communications.

Authors can share their accepted author manuscript:

- immediately
  - via their non-commercial person homepage or blog
  - by updating a preprint in arXiv or RePEc with the accepted manuscript
  - via their research institute or institutional repository for internal institutional uses or as part of an invitation-only research collaboration work-group
  - directly by providing copies to their students or to research collaborators for their personal use
  - for private scholarly sharing as part of an invitation-only work group on commercial sites with which Elsevier has an agreement
- after the embargo period
  - via non-commercial hosting platforms such as their institutional repository
  - via commercial sites with which Elsevier has an agreement

In all cases accepted manuscripts should:

- link to the formal publication via its DOI
- bear a CC-BY-NC-ND license - this is easy to do
- if aggregated with other manuscripts, for example in a repository or other site, be shared in alignment with our hosting policy not be added to or enhanced in any way to appear more like, or to substitute for, the published journal article.

Published journal article (JPA): A published journal article (PJA) is the definitive final record of published research that appears or will appear in the journal and embodies all value-adding publishing activities including peer review co-ordination, copy-editing, formatting, (if relevant) pagination and online enrichment.

Policies for sharing publishing journal articles differ for subscription and gold open access articles:

Subscription Articles: If you are an author, please share a link to your article rather than the full-text. Millions of researchers have access to the formal publications on ScienceDirect, and so links will help your users to find, access, cite, and use the best available version. Theses and dissertations which contain embedded PJAs as part of the formal submission can be posted publicly by the awarding institution with DOI links back to the formal publications on ScienceDirect.

If you are affiliated with a library that subscribes to ScienceDirect you have additional private sharing rights for others' research accessed under that agreement. This includes use for classroom teaching and internal training at the institution (including use in course packs and courseware programs), and inclusion of the article for grant funding purposes.

Gold Open Access Articles: May be shared according to the author-selected end-user license and should contain a CrossMark logo, the end user license, and a DOI link to the formal publication on ScienceDirect.

Please refer to Elsevier's posting policy for further information.

18. **For book authors** the following clauses are applicable in addition to the above: Authors are permitted to place a brief summary of their work online only. You are not allowed to download and post the published electronic version of your chapter, nor may you scan the printed edition to create an electronic version. **Posting to a repository:** Authors are permitted to post a summary of their chapter only in their institution's repository.

19. **Thesis/Dissertation:** If your license is for use in a thesis/dissertation your thesis may be submitted to your institution in either print or electronic form. Should your thesis be published commercially, please reapply for permission. These requirements include permission for the Library and Archives of Canada to supply single copies, on demand, of the complete thesis and include permission for Proquest/UMI to supply single copies, on demand, of the complete thesis. Should your thesis be published commercially, please reapply for permission. Theses and dissertations which contain embedded PJAs as part of the formal submission can be posted publicly by the awarding institution with DOI links back to the formal publications on ScienceDirect.

Elsevier Open Access Terms and Conditions

You can publish open access with Elsevier in hundreds of open access journals or in nearly 2000 established subscription journals that support open access publishing. Permitted third party re-use of these open access articles is defined by the author's choice of Creative Commons user license. See our open access license policy for more information.

Terms & Conditions applicable to all Open Access articles published with Elsevier:
Any reuse of the article must not represent the author as endorsing the adaptation of the article nor should the article be modified in such a way as to damage the author's honour or reputation. If any changes have been made, such changes must be clearly indicated.

The author(s) must be appropriately credited and we ask that you include the end user license and a DOI link to the formal publication on ScienceDirect.

If any part of the material to be used (for example, figures) has appeared in our publication with credit or acknowledgement to another source it is the responsibility of the user to ensure their reuse complies with the terms and conditions determined by the rights holder.

Additional Terms & Conditions applicable to each Creative Commons user license:
CC BY: The CC-BY license allows users to copy, to create extracts, abstracts and new works from the Article, to alter and revise the Article and to make commercial use of the Article (including reuse and/or resale of the Article by commercial entities), provided the user gives appropriate credit (with a link to the formal publication through the relevant DOI), provides a link to the license, indicates if changes were made and the licensor is not represented as endorsing the use made of the work. The full details of the license are available at http://creativecommons.org/licenses/by/4.0.

CC BY NC SA: The CC BY-NC-SA license allows users to copy, to create extracts, abstracts and new works from the Article, to alter and revise the Article, provided this is not done for commercial purposes, and that the user gives appropriate credit (with a link to the formal publication through the relevant DOI), provides a link to the license, indicates if changes were made and the licensor is not represented as endorsing the use made of the work. Further, any new works must be made available on the same conditions. The full details of the license are available at http://creativecommons.org/licenses/by-nc-sa/4.0.

CC BY NC ND: The CC BY-NC-ND license allows users to copy and distribute the Article, provided this is not done for commercial purposes and further does not permit distribution of the Article if it is changed or edited in any way, and provided the user gives appropriate credit (with a link to the formal publication through the relevant DOI), provides a link to the license, and that the licensor is not represented as endorsing the use made of the work. The full details of the license are available at http://creativecommons.org/licenses/by-nc-nd/4.0.

Any commercial reuse of Open Access articles published with a CC BY NC SA or CC BY NC ND license requires permission from Elsevier and will be subject to a fee.

Commercial reuse includes:

Figure 2.11

From: **Harsha S Surenahalli** <harsha.surenahalli@cummins.com>
Date: Mon, Nov 28, 2016 at 2:39 PM
Subject: RE: Permission to reuse Fig 6.1 from PhD Dissertation
To: Boopathi Singalandapuram Mahadevan <bsingala@mtu.edu>

Hello Boopathi,
I give you the permission to reuse the Figure 6.1 for your PhD dissertation.

Best Regards
Harsha
Harsha S Surenahalli, PhD
CPI Technologist Sr Engineer
Cummins Emission Solutions
301 Jackson St.
Columbus, IN 47201

Cell: 9063707906

K.3 Letter of Permission for Chapter 3

Permission for re-use of references 1 and 2.

Springer

PERMISSION LETTER

November 29, 2016

Your project

Requestor:	Boopathi Singalandapuram Mahadevan
	bsingala@mtu.edu
University:	Michigan Tech University (MTU)
Purpose:	Dissertation/Thesis

With reference to your request to reuse material in which Springer controls the copyright, our permission is granted free of charge under the following conditions:

Springer

PERMISSION LETTER

- includes use in an electronic form, provided it is an author-created version of the thesis on his/her own website and his/her university's repository, including UMI (according to the definition on the Sherpa website: http://www.sherpa.ac.uk/romeo/);
- is subject to courtesy information to the co-author or corresponding author;
- is personal to you and may not be sublicensed, assigned, or transferred by you to any other person without Springer's written permission;
- is only valid if no personal rights, trademarks, or competitive products are infringed.

This license is valid only when the conditions noted above are met.

Permission free of charge does not prejudice any rights we might have to charge for reproduction of our copyrighted material in the future.

Rights and Permissions
Springer
Tiergartenstr. 17
69121 Heidelberg
Germany

Permission for re-use of reference 3

From: **Boopathi Singalandapuram Mahadevan** <bsingala@mtu.edu>
Date: Mon, Feb 13, 2017 at 6:01 AM
Subject: Permission to use copyrighted Springer materials for my PhD dissertation
To: permissions.springer@spi-global.com

Hello,

I am current PhD student at Michigan Tech University (MTU) located in Houghton, MI. I would like to request permission **to use all or any part of** the following paper that I have authored in Emiss. Control Sci. Technol. Journal. This paper is accepted for publication on 1st Feb 2017 and has gone into production. The details of the paper are

1. Mahadevan, B.S., Johnson, J.H., and Shahbakhti, M., Predicting pressure drop, temperature and particulate matter distribution of a catalyzed diesel particulate filter using a multi-zone model including cake permeability, Journal of Emiss. Control Sci. Technol., Accepted for publication on 1st Feb 2017, doi:10.1007/s40825-017-0062-6,2017.

I will be using the above materials in my PhD dissertation. The dissertation is tentatively titled "Development of a Multi-zone Catalyzed Particulate Filter Model and Kalman Filter Estimator for Simulation and Control of Particulate Matter Distribution of a CPF for Engine ECU Applications". The dissertation will be distributed electronically throughout the various individuals/departments at MTU and MTU Aftertreatment consortium partners and will be printed upon completion with an expected publication date of Feb, 2017.

Thanks and regards

Boopathi S.M

Springer, Permissions   Feb 16 (1 day ago)
to me

Dear Boopathi,

Kindly please fill up the attached questionnaire for manual review and processing. Thank you.

Regards,

Springer

Rights and Permissions
Springer Science+Business Media
Tiergartenstr. 17
69121 Heidelberg
Germany

Request for Permission/Republication

Springer

In order to enable us to process your request as quickly as possible, please complete this form as detailed and accurately as possible. Please note that for some fields it might be necessary to select 2 or more boxes.

---

1. Requestor type: please select – I am or I am asking for:

☐ Author/contributor of the new work for which I am requesting permission

☑ Author/contributor of the Springer work/article/chapter from which I want to use material

☐ Publisher   ☐ Agency acting on behalf of a publisher

☐ Commercial industrial company   ☐ Agency acting on behalf of an industrial company

☐ Pharmaceutical industry   ☐ Agency acting on behalf of a pharmaceutical company

☐ Institute   ☐ Society

☐ University   ☑ Student   ☐ Professor/Lecturer

☐ Hospital   ☐ Medical practitioner

☐ Broadcaster (TV)   ☐ Film/Movie/Theater production company   ☐ Museum

---

2. Please enter your complete contact details - address and e-mail:

Boopathi Singalandapuram Mahadevan.
Michigan Technological University, 815 RL Smith Building, 1400 Townsend Drive, Houghton, MI 49931, USA.
e-mail:bsingala@mtu.edu

---

3. Please include the billing address (if it is not the same as in 2) and VAT (if applicable) for the invoice:

Boopathi Singalandapuram Mahadevan.
Michigan Technological University, 815 RL Smith Building, 1400 Townsend Drive, Houghton, MI 49931, USA.
e-mail:bsingala@mtu.edu

---

4. Please provide the book or journal title, as well as ISBN (for books), page numbers, title of the chapter/article and year of publication from which you would like to use content:

1. Mahadevan, B.S., Johnson, J.H., and Shahbakhti, M., Predicting pressure drop, temperature and particulate matter distribution of a catalyzed diesel particulate filter using a multi-zone model including cake permeability, Journal of Emiss. Control Sci. Technol., Accepted for publication on 1st Feb 2017, doi:10.1007/s40825-017-0062-6,2017.

5. Please select portion/material you would like to use:

☐ Figures/tables - please indicate the original figure or table number(s):

☑ Complete article/book chapter   ☐ Original abstract of the article/chapter

☐ Excerpts – please indicate page number(s) or number of words :

☐ Complete book   ☐ Video/Film

6. Type of use – please select for which product or purpose you would like to use the material:

☐ Book   ☐ Journal   ☐ Supplement to Journal/Newspaper

☐ Book plus Derivatives/Family Products

    Please indicate:

☐ Newspaper/Newsletter/Magazine   ☐ Advertising journal

☐ Inhouse Journal/Newsletter (intercompany)

☐ Cover/Jacket book/DVD   ☐ Cover journal   ☐ MOOC

☐ Customized Coursepack/Reader   ☐ Classroom Materials/Academic Coursepack

☑ Thesis/Dissertation - at University: Michigan Technological University   ⊞

☐ Annual Report   ☐ Conference

☐ Poster – Size:

☐ Presentation/Slide Kit   ☐ Training Materials

☐ Institutional brochure/flyer   ☐ Promotional Material   ☐ Industrial brochure/flyer

☐ Catalogue   ☐ Program Catalogue/Leaflet/Booklet

☐ Web Site   ☐ Touch Screen

☐ Banner ad   ☐ App

☐ Social Media (Facebook, Twitter, YouTube)

☐ Cards/Postcards   ☐ E-Cards   ☐ Calendar

☐ TV/Movie   ☐ Stage property for Movie/TV/Theater

☐ DVD   ☐ Audio Book   ☐ Loose leaf edition

7. Please provide:

- article/chapter title of your publication or product for which you would like to use the material:

Development of a Multi-zone Catalyzed Particulate Filter Model and Kalman Filter Estimator for Simulation and Control of Particulate Matter Distribution of a CPF for Engine ECU   ⊞

- the planned publication date:

22 Feb 2017

8. Please select and provide the name and address of the publisher/company which will distribute your work/product (if not already specified in field 1 or 2):

Name of Publisher: ☐ STM Publisher

Name of pharmaceutical or industrial company you are selling a bulk to or compiling this work for:

Name of company, institution, etc. with regards of types of use:

Michigan Technological University and MTU Diesel Consortium Parners ⊞

9. In which format will your work be published or posted – please select:

☐ Print

☑ Print and e-version intranet/protected website

☐ Print and e-version Internet /Open Access (Creative Commons license)

☐ Print and e-version Internet - protected but freely accessible,

☐ E-version only - intranet/protected website

☐ E-version only – Internet/Open Access (Creative Commons license)

☐ E-version only – Internet – protected but freely accessible

☐ Translation – Language:

10. Information about quantity or duration – please select and specify :

For print version number of copies: 100 ⊞

For bulk and bookstore edition – please indicate both print runs separately:

Bulk: Bookstore:

For e-versions
- Web address/URL: http://www.mtu.edu/library/
- estimated number of users - if not Open Access: 100 ⊞
- estimated number of downloads: 100 ⊞
- expected life of publication/duration: 10 years ⊞

For conference, training, lecture, etc. estimated number of participants:

For TV and movie – number of seconds and broadcasts:

☐ Use in media library: Duration:

11. Additional information:

Your project reference number (if applicable): Not applicable ⊞

Comments:

I will be using the above materials in my PhD dissertation. The dissertation is tentatively titled "Development of a Multi-zone Catalyzed Particulate Filter Model and Kalman Filter Estimator for Simulation and Control of Particulate Matter Distribution of a CPF for Engine ECU ⊞

Figures 3.1,3.2, 3.3 and 3.4

Thank you,

Nikole Aston

IP Compliance Specialist

SAE INTERNATIONAL

400 Commonwealth Drive

Warrendale, PA 15096 USA

o: +1.724.772.4095

e: nikole.aston@sae.org

www.sae.org

K.4 Letter of Permission for Chapter 4

Figures 4.4

Venkata Rajesh Chundru   12/22/16

to me

Hi Boopathi,

You have my permission to use the figure from the " SCR-F model (v1.5) new temperature model and calibration results (Cummins 2007 ISL data), Diesel Engine Aftertreatment Consortium Report, Michigan Technological University dt August 14, 2016" .

Thanks,Venkata

...

On Thu, Dec 22, 2016 at 3:07 PM, Boopathi Singalandapuram Mahadevan <bsingala@mtu.edu> wrote:
Hello Venkata,

May I have permission to use Figure 2 from the " SCR-F model (v1.5) new temperature model and calibration results (Cummins 2007 ISL data), Diesel Engine Aftertreatment Consortium Report, Michigan Technological University dt August 14, 2016" in my PhD Thesis.

Thanks and regards

Boopathi S.M

Figures 4.27 and 4.38

---------- Forwarded message ----------
From: **Ryan Foley** <rkfoley@mtu.edu>
Date: Mon, Nov 28, 2016 at 7:23 PM
Subject: Re: Permissions to use figures from your MS Thesis
To: Boopathi Singalandapuram Mahadevan <bsingala@mtu.edu>

Boopathi,

You have my permission.

Regards,
Ryan

On Nov 28, 2016 3:00 PM, "Boopathi Singalandapuram Mahadevan" <bsingala@mtu.edu> wrote:
Hello Ryan,

May I have permission to re-use Figures K.71 and K.36 of your MS Thesis in my PhD dissertation?. Please leave this text in your reply.

Thanks in advance

Regards

K.5 Letter of Permission for Chapter 5

Refer to Chapter 3 Permissions

K.6 Letter of Permission for Chapter 6

Figure 6.3

Harsha S Surenahalli <harsha.surenahalli@cummins.com>   4:07 PM (11 hours ago)

to me

Hello Boopathi,

I give the permission to re-use the Figure 1 from the quick start guide titled "Quick Start Guide for DOC EKF Estimator Version 4.0" in you PhD Dissertation.

Best Regards
Harsh
Harsha S Surenahalli, PhD
CPI Technologist Sr Engineer
Cummins Emission Solutions
301 Jackson St.
Columbus, IN 47201

Cell: 9063707906

From: Boopathi Singalandapuram Mahadevan [mailto:bsingala@mtu.edu]
Sent: Monday, January 23, 2017 6:39 AM
To: Harsha S Surenahalli <harsha.surenahalli@cummins.com>
Subject: Permission to use DOC Estimator Simulink Diagram

...

Dear Dr. Harsha,

May I have permission to re-use Figure 1 of your quick start guide titled "Quick Start Guide for DOC EKF Estimator Version 4.0" dt 2/7/2013 on my PhD Dissertation. Please level this text in your reply.

Thanks and regards

Boopathi S.M